Power Plant Materials Condition Monitoring and Degradation Assessment

By
Navdeep Singh Kahlon

UNIVERSITY OF BIRMINGHAM

A thesis submitted to
the University of Birmingham
for the degree of
DOCTOR OF ENGINEERING

School of Metallurgy and Materials
College of Engineering and Physical Sciences
University of Birmingham
September 2017

Abstract

Decarbonisation of energy has required fossil fuel power plants to increase operating efficiencies, thus demanding greater performance from critical boiler components. This has raised the scrutiny on power plant operators to be able to non-destructively and accurately characterise component microstructures, particularly those with abnormal surface layers which are unrepresentative of the component's bulk properties. Current techniques (surface replication and hardness testing) have shortcomings since they can only characterise material at the surface, they suffer from inaccuracy and can be time consuming to perform. Electromagnetic (EM) sensors have shown the ability to characterise mis-heat treated (MHT) aberrant microstructures from correctly heat treated (CHT) microstructures based on predominantly lab based research. The work presented in this thesis has addressed some important problems faced by the EM sensor technique for industrial deployment, which have been overlooked in lab-based research and in the literature. The influence of surface roughness, decarburised surface layers and work hardened surface layers on the EM sensor's ability to distinguish CHT from MHT bulk microstructures has been investigated. Results have shown that the EM sensor has the ability to distinguish bulk microstructures, through the presence of an abnormal surface layer. Recommendations have been provided to take advantage of or remove some of these phenomena where appropriate. The results have led to recommendations of two specific applications where the EM sensor can be deployed as a complementary technique in screening service entry material or as a principle technique for screening in-situ components during maintenance outages.

Acknowledgements

First and foremost I would like to thank my eternal guide Sri Guru Granth Sahib Ji Maharaj, without Their blessings I would not have been able to complete my studies.

A special thank you goes to Prof. Claire Davis and Dr Jun Liu for their valuable inputs, guidance and patience, without whom the required progress would not have been achieved.

I would also like to thank the EPSRC and EON for sponsoring the research and my colleagues and dear friends at EON for hosting me and providing training and access to labs and facilities at Ratcliffe Technology Centre. Special thanks go to Dr Craig Degnan, Dr Dave Allen and Dr Colin Brett for their input and technical conversations; Dr Sarah Ogden and Richard Seaton for access to facilities and Dr David Marks, Colin Davis, Paul James and Tim Riley for the jovial atmosphere they created every day in the office. I must acknowledge the self-less support from my friends and colleagues at the University of Birmingham (Aimee and Jas) and Warwick University (Carl, Frank and Mohsen).

I must acknowledge my family. My parents, who provided me with the social securities and life morals to be able to pursue my ambitions with freedom at the expense of theirs – thank you both. And to my nephews, Nirvair and Nishaan, whose frequent visits always provided me with motivation to continue.

And finally to my dear wife Niran and daughter Ajooni, your unfathomable patience and unconditional love and encouragement, even at the darkest of times, kept me motivated and determined – you've always believed in me, even when I didn't believe in myself – this I dedicate to you both.

Preface

This thesis is submitted in fulfilment of the requirements for the degree of Doctor of Engineering in Efficient Fossil Energy Technologies.

The following work describes the research undertaken in the School of Metallurgy and Materials at the University of Birmingham and EON's Technology Centre at Ratcliffe-on-Soar. The work was carried out under the academic supervision led by Prof. Claire Davis and co-supervised by Dr Martin Strangwood. The project was initially commenced under the industrial supervision of Dr David Allen who subsequently resigned. The remaining duration saw industrial support from Dr Craig Degnan.

The research has been presented at the following events:

- Materials Condition Monitoring, Shanghai Advanced Research Institute, Shanghai, China – July 2012

- Power Plant Materials Condition Monitoring and Degradation Assessment, Efficient Fossil Energy Technologies Centre of Doctoral Training, The University of Nottingham, Nottingham – July 2013

- 7th Annual International Energy Association for Green House Gases International Summer School, University of Nottingham, Nottingham – July 2013

- Power Plant Materials Condition Monitoring and Degradation Assessment, EON Technology Centre, Ratcliffe-on-Soar – August 2013

- Power Plant Materials Condition Monitoring and Degradation Assessment, Efficient Fossil Energy Technologies Centre of Doctoral Training, University of Birmingham – July 2014

Table of Contents

List of Figures

List of Tables

Abbreviations

AE – Acoustic emissions
AC – Alternating current
ACFM – Alternating current field measurement
BCC – Body centred cubic
BCT – Body centred tetragonal
CCT – Continuous cooling transformation
CHT – Correctly heat treated
CRT – Cathode ray tube
FCC – Face centred cubic
GMR – Giant magneto resistive
HAZ – Heat affected zone
HP – High pressure
IP – Intermediate pressure
LMP – Larson-Miller parameter
LP – Low pressure
LOM – Light optical micrograph
MBE – Magnetic Barkhausen emission
MBN – Magnetic Barkhausen noise
MFL – Magnetic flux leakage
MHL – Magnetic hysteresis loop
MHT – Mis-heat treated
MPI – Magnetic particle inspection
NDT – Non-destructive testing
NDE – Non-destructive evaluation
NORM – Normalised microstructure
OM – Optical microscope
PWHT – Post-weld heat treatment
SEM – Scanning electron microscope
TEMP – Tempered martensite microstructure
TFS – Taken from service
TTP – Time-temperature parametric
TEM – Transmission electron microscope
UT – Ultrasonic techniques

Nomenclature

Symbol	Description	Units
η	Efficiency of an heat engine cycle	Dimensionless
W	Mechanical work done by typical heat engine system	Js^{-1}
Q_H	Heat flow into the engine system	Js^{-1}
Q_C	Heat flow out of a typical heat engine system	Js^{-1}
T_H	Absolute temperature of the heat engine hot source	°C
T_C	Absolute temperature of the heat engine cold source	°C
Ac_1	Lower critical transformation temperature	°C
Ac_3	Upper critical transformation temperature	°C
M_S	Martensite phase transformation start temperature	°C
M_F	Martensite phase transformation finish temperature	°C
T	Temperature	°C
C	Larson-Miller constant	Dimensionless
t_R	Time to rupture	Hours
F	Vickers hardness indentation load	Kg
d	Arithmetic mean of two diagonal lengths created by Vickers hardness indenter (d_1 and d_2)	mm
d_1	Diagonal length 1, created by Vickers hardness indenter	mm
d_2	Diagonal length 2, created by Vickers hardness indenter	mm
H	Magnetic field strength	Am^{-1}
N	Number of turns in a coil	Dimensionless
I	Magnitude of the current through the coil	A
l	Length of the coil	Mm
B	Magnetic induction/Magnetic flux density/Total magnetic field	Tesla or $Wb.m^{-2}$
B_0	Externally applied magnetic field	Tesla or $Wb.m^{-2}$
B_S	Magnetic induction/magnetic flux density at saturation	Tesla or $Wb.m^{-2}$
B_r	Magnetic induction/magnetic flux density at point of remanence	Tesla or $Wb.m^{-2}$
H_C	Coercivity	Am^{-1}
M^*	Magnetisation	Am^{-1}
L	Mutual inductance	H
Z_j	Trans-impedance (imaginary part)	Ω

ω	Angular frequency	$rad.s^{-1}$
Ra	Arithmetic mean, surface roughness parameter	µm
Rmax	Largest peak-to-valley, surface roughness parameter	µm
ϕ	Magnetic Flux	Wb
m	Net magnetic dipole moments	Am^2
μ	Magnetic permeability	Hm^{-1}
μ_0	Magnetic permeability of free space	Hm^{-1}
μ_r	Relative magnetic permeability	Dimensionless
μ_i	Initial magnetic permeability	Hm^{-1}
V	Volume	m^3
*L**	Self-inductance	H
emf	Electromotive force	V
d_{skin}	Skin depth	m
ρ	Electrical resistivity	Ωm
f	Frequency of the AC current	Hz

CHAPTER 1 BACKGROUND AND INDUSTRIAL CONTEXT

This chapter provides a summary of the research topic and highlights the key points leading to the project aims and objectives concluding with the author's contribution to industry and academia. This chapter is approached from the perspective of a wide audience and it contextualises the academic and industrial motivations to perform this study. A short introduction to the research is given which outlines the materials challenges associated with the development of fossil fuel power plant technologies and how electromagnetic sensor technology can provide an industrial application solution for such challenges by addressing certain issues.

1.1. Development of Fossil-Fuelled Power Generation

Thomas Newcomen made the first commercially practicable steam engine in England, 1712 called the atmospheric-engine for the application of pumping water out of the bottom of coal mines to increase the efficiency of mining (Figure 1-1).

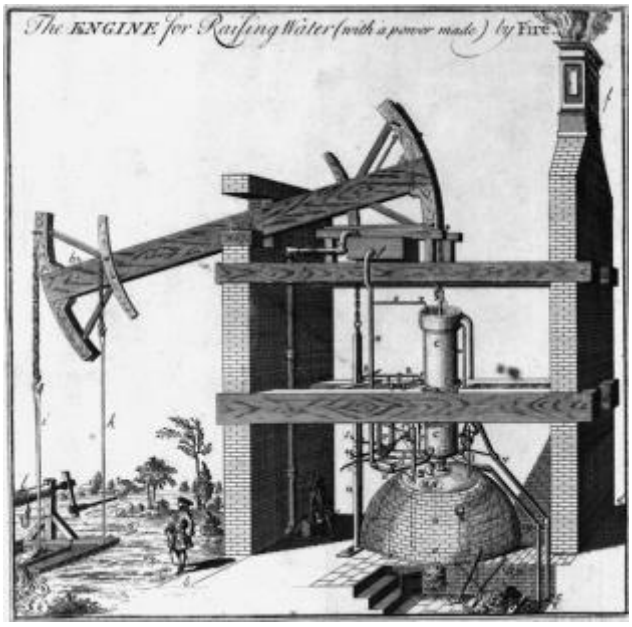

Figure 1-1: Newcomen Engine [1]

Newcomen's steam engine was further developed by James Watt, with the introduction of a separate condenser (1763-1776) [2] and approximately 60 years later in 1831, Michael Faraday discovered electromagnetic induction [3], constructing the world's first

electric generator. These key discoveries contributed to Thomas Edison's, 1882, coal fired power station in London called Edison Electric Light Station, the first of its kind. A pivotal moment came in 1884 when Sir Charles Parsons perfected a radial-flow design of a steam turbine generator which allowed a significant increase in generating capacity making the technology more economical to install and adopt globally [4]. Fossil fuelled electricity generation had rapidly become popular and by the 1890s, hundreds of towns around the world had a coal-fired power station [5]. Between the 1940s – 1960s the energy sector experienced what was known as the 'golden years'. Once the western nations had stabilised after the world wars, economies began to grow and electricity demand (particularly in the US) grew at approximately 7% per year. This led to utility companies designing and manufacturing larger and more efficient coal fired power stations, some with capacities up to 3000MW [6].

1.2. Fundamentals of Steam Turbine Power Generation

The traditional technique to generate electricity from coal is to burn the coal fuel with air, which heats water, transitioning it to steam in a boiler facility, which is then used to power a steam turbine generator. These types of coal fired power stations have been evolving since the early advances of Edison and Parsons, but in principle have remained the same. Coal fired power stations have a number of key components which can be seen schematically in Figure 1-2. Coal, from mines, will be delivered to a plant's site where it will be prepared for combustion. For most coal-fired power stations this entails some form of pulverisation process where the coal is crushed and ground into a fine powder called pulverised coal. Under controlled conditions, the pulverised coal is blown into the combustion unit at the correct fuel-air ratio where it is ignited.

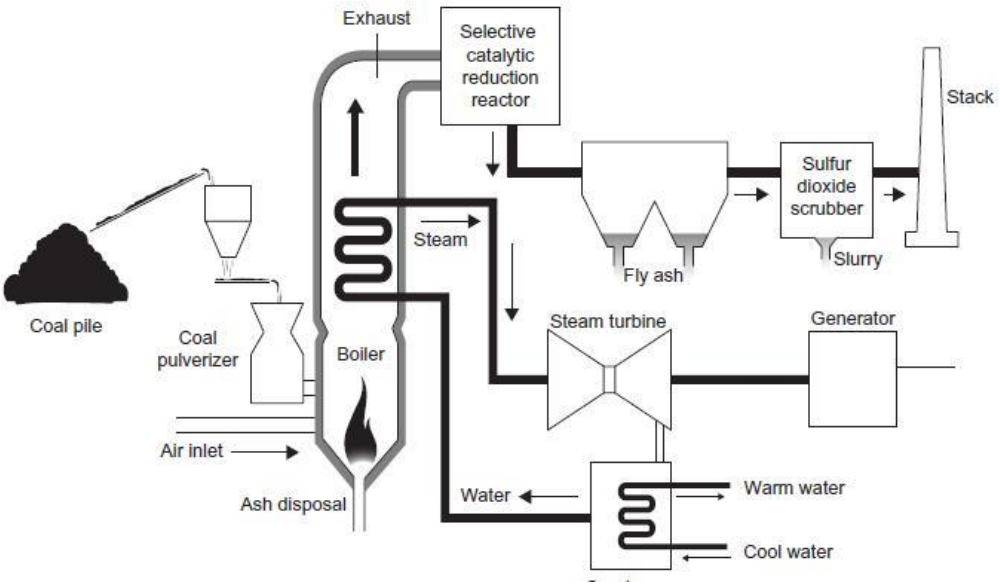

Figure 1-2: Schematic diagram of the typical components in a pulverised coal fired power plant [7]

The heat from combustion is captured by water flowing through numerous steel tubes, within the boiler unit. Here the water within the tubes is converted into steam ready to power the turbines whilst flue gases exhaust to be cleaned and/or released to atmosphere. Ash residue from the coal combustion deposits at the bottom of the combustion chamber ready to be removed as slag. Steam within the steel tubes is routed towards the steam turbine where the heat energy from the steam is converted into mechanical energy within the turbine. Modern day steam turbines are designed to extract as much heat as possible from the steam and so within larger power stations, steam will usually pass through three different turbine stages; low-pressure (LP), intermediate-pressure (IP) and high-pressure (HP). To further increase the efficiency of the cycle, steam exiting certain stages of the turbine is sent back to the boiler into a re-heater stage to be reheated and re-cycled. With stricter carbon emission regulations, the future of fossil fuel burning technology is dependent on the efficiency of the power station [8]. Higher efficiency power stations can reduce the amount of carbon dioxide (CO_2) produced per unit of fuel burned, effectively lowering the emissions of the power

station. The Carnot cycle governs the thermodynamics of the hot steam to electricity conversion process. The efficiency of the conversion is dependent on the pressure and temperature drop between the inlet and outlet of the steam turbine. Therefore, from a thermodynamic perspective, it is in the interest of the power station's efficiency that steam exiting the boiler is at its highest possible temperature and pressure, before it enters the HP turbine. The temperature and pressure of the exiting steam are limited by the ability of the boiler materials and thus making the boiler components critical to the future of coal-fired generation [7].

1.3. Operating Conditions and Material Performance Requirements

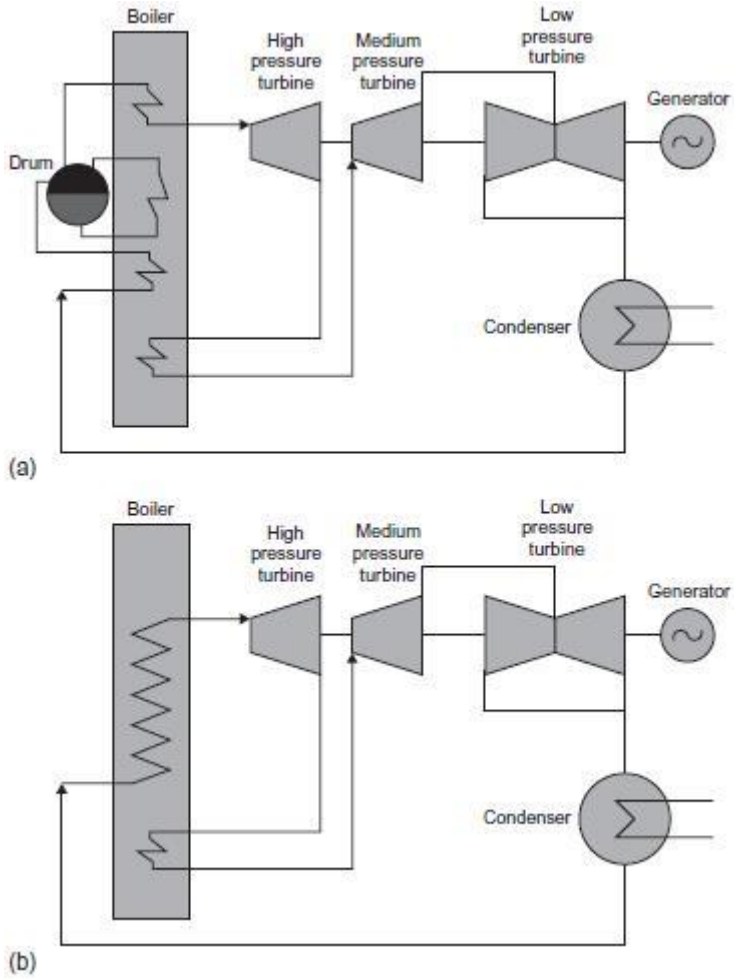

Figure 1-3: Steam cycle boiler arrangements for coal-fired power stations [7]
(a) Conventional subcritical steam cycle with steam drum
(b) Modern supercritical steam cycle

Figure 1-3a shows a typical steam cycle boiler arrangement for a conventional coal-fired power station. Within the boiler unit, pulverised coal and air fuel mixture are burned at temperatures up to 1500 – 1700 °C inside the combustion chamber, releasing energy as radiant and convective heat. Radiant heat is captured by water running through tubes inside the combustion chamber walls and other tubes which are situated within the path of the hot flue gases, as they exit the combustion chamber. Within a conventional boiler, operating temperatures and pressures are such that water

is first boiled in a steam drum and the resulting steam is heated further to produce super-heated steam. This arrangement is referred to as a subcritical boiler and shown schematically in Figure 1-3a [9]. The steam propagates through the high pressure, medium pressure and low pressure turbines to extract mechanical power which is converted into electrical energy via a generator. Steam exiting the turbine is condensed and re-enters the boiler unit for combustion. The temperature and pressure of steam exiting a subcritical boiler varies significantly between different stations with typical figures of approximately 540 °C at 17.5 MPa achieving approximately 38% efficiency [7]. Contrary to the conventional boilers, most modern boilers operate at higher supercritical temperatures and pressures, such that water is heated to produce superheated steam homogenously within the boiler tubes without the need of boiling the water in a steam drum [9]. This arrangement is referred to as a supercritical boiler and the steam cycle is shown schematically in Figure 1-3b. Supercritical steam typically feeds into the high pressure turbine at 540 – 600 °C and at pressures of 23 – 30 MPa. Supercritical boiler power stations can outperform their subcritical conventional counterparts by 2 – 3% achieving efficiencies up to 41% [7]. The efficiency of converting fuel energy into electrical energy is referred to as the heat rate within the fossil fuel energy industry. It is commonly accepted that a percentage improvement in heat rate efficiency is equivalent to an equal percentage reduction in CO_2 emissions [9]. The net efficiency of the turbine is paramount to the life-cycle cost of the power station and by manipulating the operating conditions within the boiler, efficiencies can be enhanced. However, operating conditions are limited to the integrity of critical boiler components and the ability of the materials used being able to withstand the extreme demands supercritical boilers require of them. This makes the materials of critical boiler components the limiting factor to higher efficient coal-fired power stations.

1.4. Critical Boiler Components

Within conventional coal fired power stations, the transformation of water to steam takes place in steam drums (also known, within the industry, as steam headers) and the steam is transported via boiler tubes. Steam tubes and headers are referred to as critical boiler components because they are exposed to strenuous high temperature and pressure environments (as explained in Section 1.3) and are vital to the function of the power station. An example configuration of a typical steam header and tubes can be seen in Figure 1-4.

Figure 1-4: Image of a typical re-heater steam header manufactured by Jiangsu SUNCO Boiler Co. Ltd. [10]

Arduous environments for critical components lead to metallurgical challenges such as the requirement for high temperature creep/fatigue strength, high corrosion/erosion resistance and good weldability [11]. To cope with the challenges, 9% Cr – 1% Mo low carbon alloy advanced ferritic-martensitic steels (Grade 91) have been developed over the past 35 years within the power generation industry [12]. These alloys have allowed critical steam boiler components to be manufactured with the desirable set of mechanical properties to perform under the required conditions.

1.5. Pipe Manufacturing

Alloy technology has paved the way for the development of materials which can perform under harsh conditions. However, this is reliant on the materials being able to attain the correct microstructures that offer the desired mechanical properties. The production of the required microstructure is managed through careful manufacturing processes. There are three main methods to manufacture steel pipe; Spiral-Weld Rolled, Butt-Weld Rolled and Seamless (Figure 1-5).

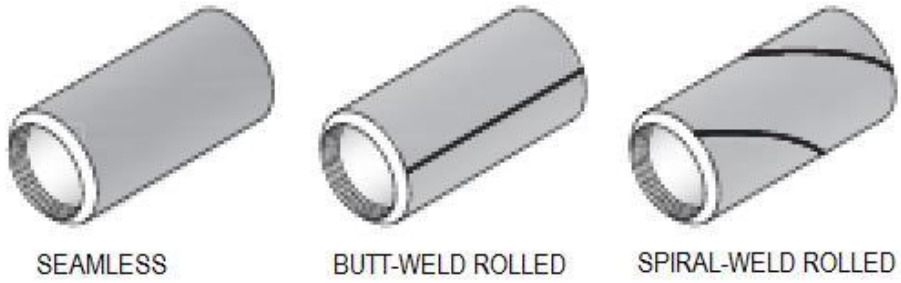

Figure 1-5: Different methods of manufacturing steel pipe [13]

Spiral-weld and butt-weld rolled pipes are more economic for lower pressure pipe systems with thinner walls. However, within power generation, the higher pressure systems require thicker walled pipes and so seamless pipes are preferred, although there can be size restrictions to seamless pipe. Continuously cast round steel billets (Figure 1-6), with the correct compositional chemistry, are produced by the steel manufacturer and shipped to the pipe manufacturer. The pipe manufacturer will cut the round billet to the required length for pipe manufacturing, before placing it into a rotary hearth furnace where the billet is heated uniformly until white-hot. Once at temperature, the hot billet is transferred to a cross roll piercing mill where the billet is pierced (at temperature) using a conical type piercing plug, through the centre of the billet, thus forming a hollow pipe-shell.

Figure 1-6: Example as cast billets. (a) Round Billet (b) Square Billet

The hollow pipe-shell may have an irregular shape and wall thickness at this stage, and so is transferred to a continuous mandrel mill. Here, the piercing plug is removed from the hollow pipe-shell and replaced with a lubricated mandrel before being sent through numerous rolling stages where the pipe-shell's wall thickness is reduced and corrected whilst simultaneously elongating the pipe-shell. The mandrel bar is extracted from the pipe-shell before being transferred to an induction heater, to be reheated for further working in the stretch reducing mill where the final dimensions of the pipe are produced. If it is required, pipes are then cut to length (at temperature) using a rotary cutting saw, and then placed on cooling beds to be air cooled to room temperature. The process as described by the pipe manufacturer Vallourec Group is depicted in Figure 1-7.

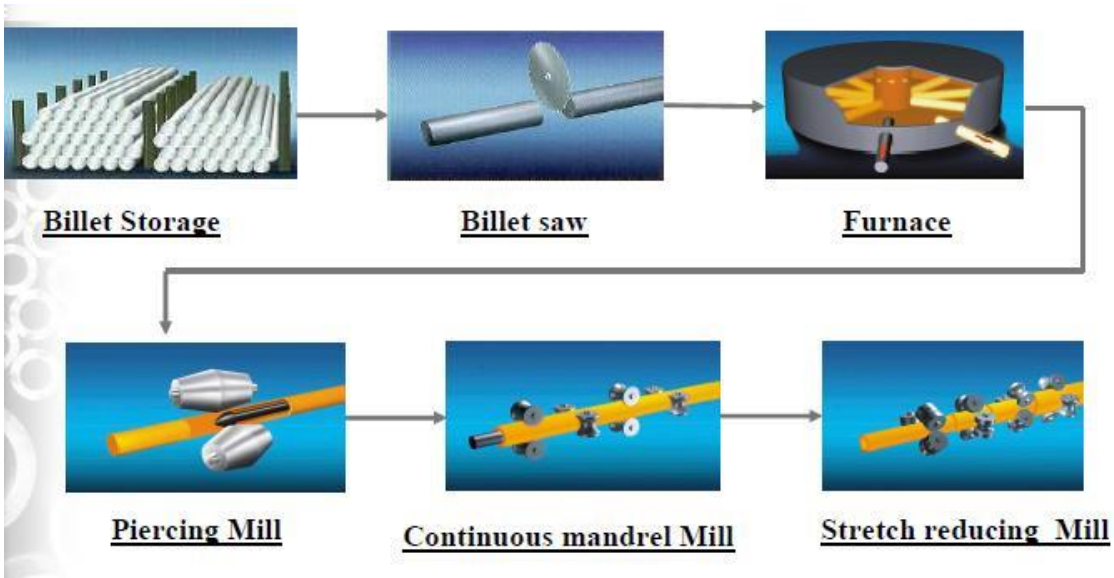

Figure 1-7: Depiction of the process stages for manufacturing seamless steel pipe [14]

1.6. Heat Treatment and Inspection

The heat treatment stage for the pipe is crucial to attaining the correct microstructure which in turn yields the required mechanical properties, such that the component can withstand the operating conditions it will be exposed to.

Material is heated and held for approximately 30 mins between a temperature range 1040 – 1080 °C to austenitise the material. The material is then removed from the furnace and allowed to air cool, transforming into martensite. The martensite is very hard and brittle and so requires tempering at a temperature between 730 – 800 °C, before being allowed to cool in air to form a tempered martensite microstructure. After the pipes have been heat treated, to achieve the desired microstructure, they go through final machining processes where the pipes are ground and turned on lathes to produce a smooth clean surface finish. Finished pipes are then sent for non-destructive testing (NDT) to assure the quality of the finished pipe. ASTM A335 requires Grade 91 pipes to be tested non-destructively using at least one of, or a combination of, ultrasonic, eddy currents and/or magnetic flux leakage to test for surface cracks and rolling defects. The hardness of the pipe is also bound by ASTM A335 to a minimum and maximum range between 196 – 265 HV [15].

1.7. Mis-heat Treatment and Aberrant Material

The high temperature mechanical properties of Grade 91 material are reliant on the material's tempered martensitic microstructure, i.e. finely dispersed carbide and nitride precipitates within a lath martensite microstructure provides elevated temperature creep resistance. Any deviations from this microstructure has historically led to numerous problems and premature failures of Grade 91 components in-service [16]. Careful control measures are taken during the manufacturing and fabrication processes to ensure creation of the correct microstructure; however this is not always achieved

and leads to mis-heat treated (MHT) or aberrant material [17]. Overshooting and undershooting of temperature and time can cause excessively hard or extremely soft material to form, leading to detrimental consequences for in-service operation [18]. In some instances components have not been wholly mis-heat treated, but only in specific local areas on the component due to errors in the air cooling procedure. For example, when hot pipes are air cooled whilst being in contact with one another, this can lead to slower cooling rates at the points of contact between the pipes. This consequently leads to softer material at these positions as the austenite has time to transform into ferrite, which significantly reduces the materials high temperature properties. In some cases, pipe sections may arrive to site in the correct metallurgical condition, however after sections of pipe are welded, they could be given an incorrect post-weld heat treatment (PWHT), which can also lead to aberrant material.

1.8. Industrial Material Screening

EON is an international power generation and energy utility provider and is the industrial sponsor for this research, providing experimental material and research guidance. EON provides coal fuelled power generation as one of its power generating technologies across the globe with particular presence in the UK and Germany. Many power generating companies, including EON, buy boiler components that have tempered martensitic microstructures, typically Grade 91 material. For quality assurance purposes, EON will perform NDT on Grade 91 steam headers to validate the condition of the material before installation. This inspection procedure usually involves a number of portable hardness tests, where micro indentations on the surface of the components reveal the hardness of the material at specific locations. Simultaneously, surface replication is performed in areas of interest; whereby an imprint of the microstructure is taken onto a soft polymer film, which can then be

examined under an optical microscope. These techniques are used to screen and flag any material below the specification requirements; however both techniques come with practical limitations and hence cannot always detect material which is aberrant (out of specification). These techniques are limited to the surface only and cannot provide characterisation of material beneath any abnormal surface layers. Also, due to the large size of steam headers, it is logistically and economically impractical to hardness test and to take replicas of large surface areas of the component due to the length of the testing and processing of results, particularly for surface replications and therefore only a low percentage of the surface area is inspected.

A drawback of portable hardness testing is that it is not as accurate as hardness tests performed in the laboratory and lacks repeatability. Some portable hardness testers use very low loads, especially with thinner walled material and so surfaces must be prepared to higher finishes, almost a mirror finish. Difficulties with portable hardness testing have been experienced and reported by other companies within the industry [19]. Observations have been made such as; the need for experienced operators to recognise device malfunctions and to be manually dexterous so that incorrect measurements are not recorded. Furthermore, surface layers unrepresentative of the component's bulk microstructure need to be removed, i.e. work hardened and decarburised surface layers. Thus the industry's current reliance on portable hardness testing for screening material is not adequate, this can cause material with hardness measurements on the specification borderline, to be incorrectly rejected or accepted.

The quality of the replications of surface microstructure can vary considerably within practise. This can be dependent on a number of factors such as; the availability of consumables, the competence and ability of the operative and the experience and technical judgement of the engineer examining the surface replicas. Even if the replicas have been sufficiently produced, it has been reported by EON that it may not always be

possible to confirm unambiguously the presence of a martensitic microstructure using optical microscopy. This is because carbide precipitation, along previous martensitic lath boundaries, may exist within the transformed ferrite material making it appear under the optical microscope as martensitic lath boundaries. This phenomenon is referred to as “false martensite” within the company and as such presents a risk to EON to be able to assure with confidence, that the Grade 91 steam header components have the correct microstructure before it is put into service. This risk can be addressed by electromagnetic (EM) sensor technology.

1.9. Electromagnetic Sensors

Over the past decade, electromagnetic (EM) sensors have been researched to show sensitivity to the electromagnetic properties of steels [20-30]. EM sensors have been developed with the ability to detect changes in a conductive material’s magnetic relative permeability and electrical resistivity. The electromagnetic properties of Grade 91 are linked to the material’s compositional and microstructural characteristics and hence EM sensors have great potential to assess the condition of the steel microstructures and complement current material screening NDT techniques for EON. EM sensors have proven to be able to distinguish mis-heat treated (MHT) material from correctly heat treated (CHT) material within laboratory environments, based on samples with high quality surface preparation [23, 27, 28]. However, the lab based samples do not fully reflect the environmental and component surface conditions which NDT operators within the utility sector may come across. Therefore understanding the effect that different surface conditions may have on the quality of the EM sensor readings used to characterise the bulk property of the material’s microstructure, will aid with facilitating the transition of the lab based technique into an industrial application.

This can provide EON with the ability to increase their confidence when screening steam header components as part of their quality assurance process.

1.10. Aims and Objectives

The aim of this EngD project is to build upon the encouraging progress of the EPSRC sponsored PowerEMs project at the Universities of Manchester (Prof. Tony Peyton) and Birmingham (Prof. Claire Davis), supported by EON. The PowerEMs project has so far shown that in principle, electromagnetic scanning and measurement of magnetic permeability differences can provide a rapid and effective method of distinguishing normal (martensitic) and mis-heat treated (ferritic) high alloy power plant steels. In order to develop the technique for practical application several materials issues need to be addressed, which form the objectives for this research project.

- Evaluate the ability for a U-shaped EM sensor to screen Grade 91 materials for their bulk microstructural characteristics (i.e. determining whether the material has been correctly heat treated (martensitic) or mis-heat treated (ferritic)

- Assess the effect of surface finish on the EM sensor inductance measurements, particularly the effect of varying surface roughness profiles and hence determine what surface preparation requirements would be necessary for the EM sensor to be used by EON for screening material

- Assess the effect of a decarburised surface layer on the EM sensor inductance measurements, and assess the capability of the EM sensor to determine the bulk microstructure of a material through the presence of a decarburised surface layer

- Assess the effect of a work hardened surface layer on the EM sensor inductance measurements, and assess the capability of the EM sensor to determine the bulk microstructure of a material through the presence of a work hardened surface layer

1.11. Highlights of Contribution

The research carried out as part of this EngD has provided the experimental evidence to determine practical applications for EM sensors as part of EON's NDT regime for Grade 91 boiler components. This has been done by addressing some important problems faced by the EM sensor technique with regards to the presence of abnormal surface layers when determining the bulk microstructure, which has been overlooked in lab-based research and in the literature.

- An evaluation of the ability for a U-shaped EM sensor to determine whether a Grade 91 material has been correctly heat treated or mis-heat treated has concluded that the EM sensor can be used by EON to screen service entry P91 material. EON can purchase and set-up an impedance analyser at their NDT labs and perform low frequency (10 Hz) EM tests, using the sensor (or a similar sensor) as produced in this research to determine whether the bulk microstructure is correctly heat treated (tempered martensite) or mis-heat treated (ferrite). This application will complement the existing NDT performed to screen material (portable hardness testing and surface replication). Using the EM sensor in complement to current screening NDT methods, will give confidence to inspectors when determining if the component should be accepted for service or rejected and returned to the manufacturer.

- The influence of a decarburised surface layer, a work hardened surface layer and various surface roughness profiles on the EM sensor inductance measurements has been made, resulting in recommendations of how these influences can be avoided or removed to allow for the bulk microstructure of the component to be determined, even in their presence. The impact of work hardened surface layers and surface roughness profiles on the inductance values of an EM sensor (for the ranges tested) have not been explored previously in the literature.

- An industrial placement at EON's Technology Centre in Ratcliffe was undertaken as part of the EngD training programme. The placement consisted of various research projects being undertaken and experiences gained as a materials technologist carrying out failure investigations and heat treatments. The heat treatment project was documented as an official EON report and can be found in APPENDIX A.

1.12. Thesis Structure

- Chapter 1 provides a high level introduction to the EngD project and a background to the industrial driving forces for performing the research.
- Chapter 2 provides an examination of published literature (academic and industrial) relevant to this study. It includes a critical review of current NDT and how further research, addressed by this study, is required to translate the EM sensor technique into a practical application for EON.
- Chapter 3 provides details of the materials used in this study and the experimental regimes that were required to carry out the testing and the metallography techniques utilised to capture important data.
- Chapter 4 contains an assessment of the EM sensor's ability to determine correctly heat treated microstructure from a mis-heat treated microstructure by discussing the influence of magnetic permeability on inductance. It also goes on to assess the ability for the EM sensor to determine the bulk microstructure of a material through an aberrant decarburised surface layer.
- Chapter 5 assesses the effect of surface finish on the EM sensor measurements, focussing on the impact of surface roughness profiles.
- Chapter 6 assesses the effect of work hardened surface layers on the EM sensor measurements and the ability to determine the bulk microstructure of a material through a work hardened surface layer.
- Chapter 7 provides recommendations of how EON can use the EM sensor within their organisation to improve their NDT regimes.
- Finally Chapter 8 draws conclusions from the study and highlights potential future work.

1.13. Summary

Fossil fuelled power generation technologies are required to increase their efficiencies in order to become less carbon intensive, but this comes at the cost of higher levels of degradation of the materials for critical boiler components as they will be exposed to higher temperatures and pressures. Therefore it is imperative that the critical boiler components are correctly heat treated to produce the required microstructures which can achieve the high temperature mechanical properties. EON's current NDT regime of portable hardness testing and surface replication for service entry components does not provide the desirable levels of assurance to allow EON to confidently reject or accept components. EM sensor technology has demonstrated that it can be a useful technique to determine correctly heat treated from mis-heat treated microstructures; however the effects on the EM sensor inductance measurements due to the presence of surface roughness, the presence of a decarburised surface layer or the presence of a work hardened surface layer is not completely understood. This research study will evaluate the impact of these surface layers on the EM sensor measurements as well as assess the ability for a U-shaped EM sensor to determine the bulk microstructure of a material through the presence of these surface layers.

CHAPTER 2 LITERATURE REVIEW

This chapter reviews the relevant academic and industrial literature providing an overview of the current methods of determining power generation boiler component microstructures. Firstly, the review details the evolution of power generation boiler steels followed by a review of the current techniques used to determine power generation boiler microstructures as well as research conducted in the field of electromagnetic sensors for their ability to be used as a non-destructive testing method to determine microstructures of boiler components for power grade steels.

2.1. Fossil Fuelled Power Generation

2.1.1. Introduction

The energy trilemma of generating and supplying safe, secure and affordable energy imminently presents itself as one of the most complex problems for any nation. Conflicting factors of global economics, politics and recent upsurges of decarbonisation through the fear of climate change, has added to the complexities of the energy trilemma. The Global Commission on the Economy and Climate was assembled to provide research based advice for governments, local authorities and businesses to aid with decision making, with respect to the challenges faced, and they refer to the challenge as being "…unprecedented…" and "…profound..." [31]. Since the late 20th century, researchers have been suggesting that the combustion of fossil fuels is the significant contributor to all carbon dioxide emissions discharged [32, 33]. Hence, decarbonising fossil fuel power generation has become a worldwide agenda. Britain became the first country legally bound under the 2008 Climate Change Act to set carbon budgets. The target is to reduce UK carbon emissions by 34% by 2020 and at least 80% by 2050 compared to emissions levels of 1991; to be achieved through investment in energy efficiency and clean energy technologies [8]. Governments and research councils are investing in the development of low carbon technologies such as nuclear power, renewable technology and energy efficient fossil plant. However there is yet uncertainty as to how these technologies will develop and then be introduced into a

low carbon and sustainable UK energy economy, a concern which is shared by other researchers [34, 35]. It is for these reasons that The Department of Energy and Climate Change (DECC) have suggested that the UK's low carbon vision will not be realised solely by technological advancements, but will also require changes in economic forecasting, consumer behaviour and global policies [36].

Whilst the complex economic pathways to achieving a decarbonised, reliable and affordable energy economy is modelled and projected, the fossil fuelled power generation industry is reducing its effective carbon emissions by increasing plant operating efficiencies.

2.1.2. Power Plant Operating Conditions

One method of increasing the efficiency of a power station is to increase the top steam/gas temperatures and pressures by adopting ultra-supercritical (USC) steam cycle systems [37-39]. Operating the steam cycles at higher temperatures and pressures leads to an increase in the cycle's efficiency portrayed in Figure 2-1. This means that a greater energy output can be achieved for the same fuel input, and thereby effectively reducing the amount of carbon dioxide emitted from the cycle. However, higher efficiency comes at the expense of higher levels of degradation for the materials used.

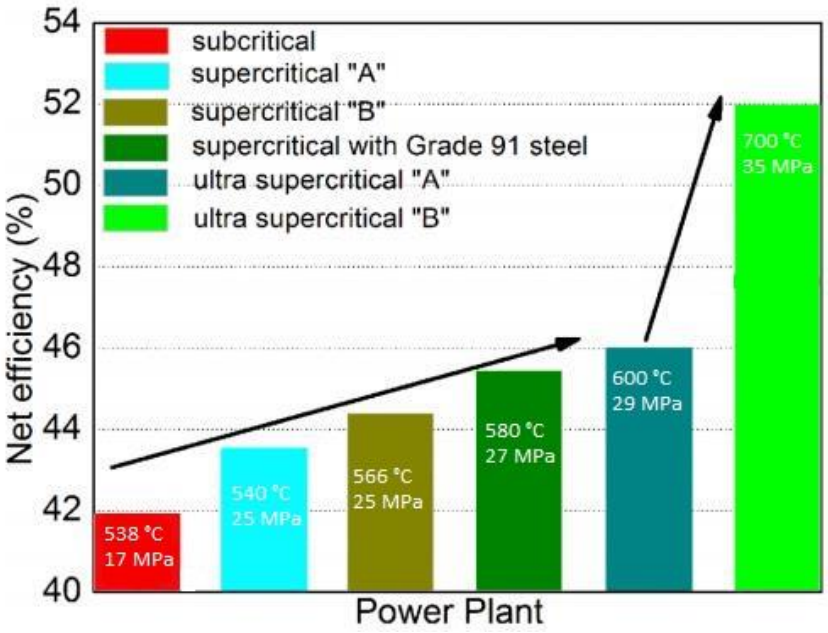

Figure 2-1: Effect of temperature and pressure on net efficiencies of power plants [40]

From thermodynamics, the efficiency of a steam engine cycle is given by [41],

$$\eta = \frac{W}{Q_H} = \frac{Q_H - Q_C}{Q_H} \qquad \textbf{Eq. 2-1}$$

Where η is the efficiency, W is the work done, Q_H is the heat in and Q_C is the heat out. Expressing the thermal efficiency of an ideal heat engine modelled on the Rankine cycle; then the efficiency can be simply written as:

$$\eta = \frac{T_H - T_C}{T_H} = 1 - \frac{T_C}{T_H} \qquad \textbf{Eq. 2-2}$$

Where T_H is the absolute temperature of the heat source and T_C is the absolute temperature of the cold source. From Eq. 2-2 it can be seen that an increase in the temperature of the heat source (T_H) will cause an increase in the efficiency; increasing pressure will have the same effect. Existing typical coal fired power plant steam (built in the 1950s and 1960s) operates at temperatures and pressures approximately 550 °C and 27 MPa respectively. New build advanced ultra-super critical systems (built in the 1990s) are designed to operate at temperatures and pressures between 650-760 °C

and 30 – 35 MPa respectively, having the ability to operate between 45 – 55% efficiency [41-47].

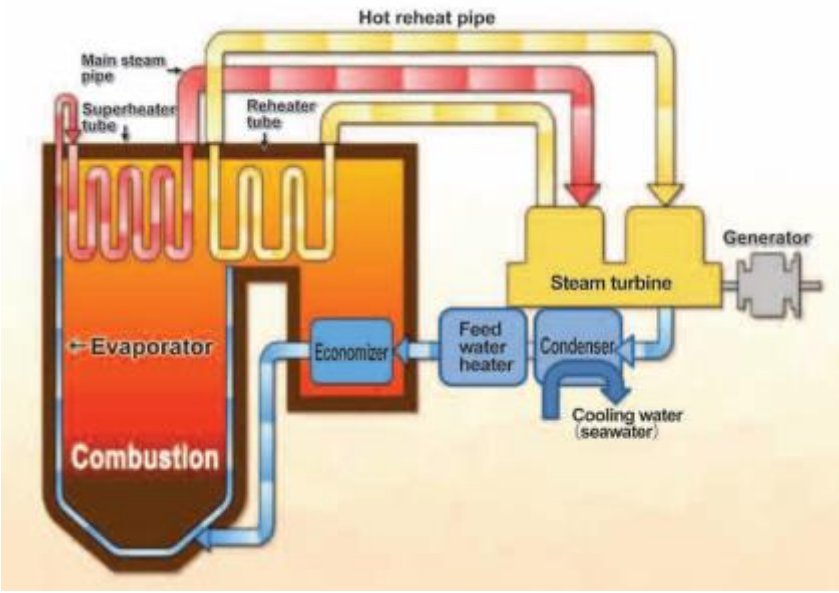

Figure 2-2: Power plant system schematic [48]

Coal fired boiler combustion chambers are extremely aggressive environments and propose difficult operating conditions. This environment is further intensified as operating conditions are elevated to make plant efficiency gains. Figure 2-2 schematically illustrates the location of boiler super-heater and re-heater tubes, which can suffer from hot corrosion on the fire-side (component wall exterior surface) due to their location within the aggressive combustion gas stream, and from oxidation on the steam-side (inner surface in contact with the hot steam) [39, 49]. Fire-side hot corrosion takes place when coal impurities rich in chlorine and sulphur from the combustion gases, combined with the hot temperatures, promote complex reactions between chlorine, sulphur, carbon and oxygen [50]. This leads to liquid salts depositing onto tubes causing non-protective oxide scales to form, exposing them to corrosion degradation. Khanna (2002) [49] highlights the problem of hot corrosion as being one of the key problems responsible for limiting main steam temperatures within

conventional coal fired gas plant to 540 °C. Steam-side oxidation internal to the component may also limit component lifetime. This can be caused directly through metal wastage or indirectly by raising local temperatures at the points of oxide scale formation (due to the oxides lower thermal conductivity) and hence impacting the creep controlled lifetimes [51]. The third limiting factor for high temperature steam cycles is the ability for the material to cope with the high temperature creep. Ennis and Czyrska-Filemonowicz (2003) [38] highlight the necessity to develop improved creep rupture strength steels to facilitate higher plant efficiencies. The maximum steam temperatures operable in conventional UK coal fired boilers are severely limited by the arduous environmental conditions and the need to manage a balance between adequate operational efficiency and unwarranted corrosion/oxidation of the boiler components.

2.2. Development of Power Generation Boiler Steel

2.2.1. Introduction

A clear argument for increasing the efficiency of conventional fossil fuelled power stations has been aforementioned. Sarver and Tanzosh (2004) [39] write of the importance of 'identifying, evaluating and qualifying the materials needed for critical components for coal-fired boilers capable of operating at ultra-supercritical conditions. The main enabling technology in achieving this has been the development of stronger high-temperature materials. Widespread research and development has resulted in the advancement of numerous high strength alloys for power generation plant components over the last 60 years, such as heavy piping and tubing for boilers within conventional and advanced-ultra super-critical coal-fired power plants. Table 2-1 quite clearly displays the material requirements for such components.

Table 2-1: Summary of material requirements for high temperature coal fired power plant boiler materials [52]

Properties		Materials Requirements and Evaluation
High Temperature Strength	Creep	Creep strength at base metal and weldment
	Thermal Fatigue	For a large diameter and heavy wall thick piping when non-steady thermal cycle exerted at start and stop
	Creep Fatigue	For piping thermal expansion at start, steady state operation and stop. For piping thermal expansion at start, steady state operation and stop. Creep fatigue interaction and its life assessment and plant design
Corrosion Resistance	Hot Corrosion	Fire-side corrosion for super-heater tubing
	Steam Oxidation	Scale thickness and exfoliation behaviour of steam oxidation at inner surface of tubing and piping
Weldability		Cracking such as solidification crack, liquefaction, low ductility crack and HAZ crack
Workability		Hot bending
Repair		Weldability of the aged tubing
Inspection and QA		Applicability of inspection testing
Cost Competitiveness		Materials cost and additional cost for working

Viswanathan et al (2006) [43] performed a study aimed at identifying, evaluating and qualifying the materials needed for the construction of critical boiler components for coal-fired power plant; capable of operating with steam temperatures and pressures at 760 °C and 35 MPa respectively. Austenitic alloys (HR6W and SUPER 304H), ferritic alloy (SAVE 12) and nickel based alloys (Haynes 230, CCA 617 and INCONEL 740) were all part of the program of study looking at high temperature creep strength, oxidation resistance and corrosion resistance amongst others. Oxidation tests at 650 °C for 2000 hours showed the high chromium alloys (austenitic) form a chrome-rich oxide layer and that the chromium content in most cases predominantly controls the oxidation resistance. They also concluded that the austenitic alloys were

consistently superior to the ferritic alloys for oxidation resistance [43]; however they suffer from having high coefficients of thermal expansion and lower thermal conductivity offering less operational flexibility than the ferritic alloys. Ferritic alloys are also more economically attractive as they do not contain expensive alloying additions, such as nickel [53].

2.2.2. Austenitic Stainless Steel

Conventional super-heater and re-heater tubes are exposed to temperatures close to 600 °C depending on their exact location within the boiler (shown previously in Figure 2-2). These tubes are subject to hot corrosion dictating the use of austenitic stainless steels or C-Mn/low alloy steels co-extruded with an outer cladding of stainless steel. The higher additions of chromium and nickel, within austenitic stainless steels, provide the high temperature corrosion resistance through formation of protective oxides, which is required within this extremely aggressive environment [50].

Candidate austenitic alloys high in nickel and chromium have been praised by Igarashi et al (2010) [52] after a studying HR6W (23Cr-445Ni-7W) alloy strengthened by the Fe_2W Laves phase as well as $M_{23}C_6$ and MX carbides. It is a good candidate for large diameter heavy thick walled piping such as main steam pipes and hot re-heat pipes as it has been found to be a marginal strength level material with good ductility. Modified versions of HR6W have been studied by Cui et al (2011) [54] where micro-alloying additions of boron and magnesium were added to a typical HR6W steel (Table 2-2).

Table 2-2 Chemical composition of HR6W [54]

Steels	*C*	*Cr*	*Ni*	*W*	*Nb*	*Ti*	*N*	*O*	*S*	*B*	*Mg*	*Fe*
Base steel	0.030	22.980	45.020	7.010	0.200	0.100	0.011	0.032	0.009	-	-	Bal.
+B	0.030	22.970	45.070	6.980	0.200	0.100	0.011	0.038	0.009	0.008	-	Bal.
+ (B, Mg)	0.030	23.020	45.100	7.020	0.200	0.100	0.010	0.010	0.004	0.008	0.005	Bal.

Results of this study further showed the promise of HR6W as a candidate material; complementing the research carried out by Igarashi et al (2010) [52]. The addition of the micro-alloying elements caused a remarkable increase in the stress-rupture life of the material at high temperatures and also displayed excellent creep ductility (Figure 2-3). This was concluded to be due to boron segregating at the grain boundaries decreasing the diffusivity along the grain boundaries and magnesium improving the existing carbides by removing oxygen and sulphur in the form of magnesium-oxide and magnesium-sulphide. This reduced the possibility of strengthening elements (titanium and niobium) to react with the sulphur and oxide to form compounds which would deplete the matrix of the strengthening element. This enhanced precipitation strengthening due to the presence of niobium carbides (NbC) and titanium carbides (TiC) forming at grain boundaries and in the matrix, improving creep life [54]. However, significant additions of nickel make these steels an expensive option.

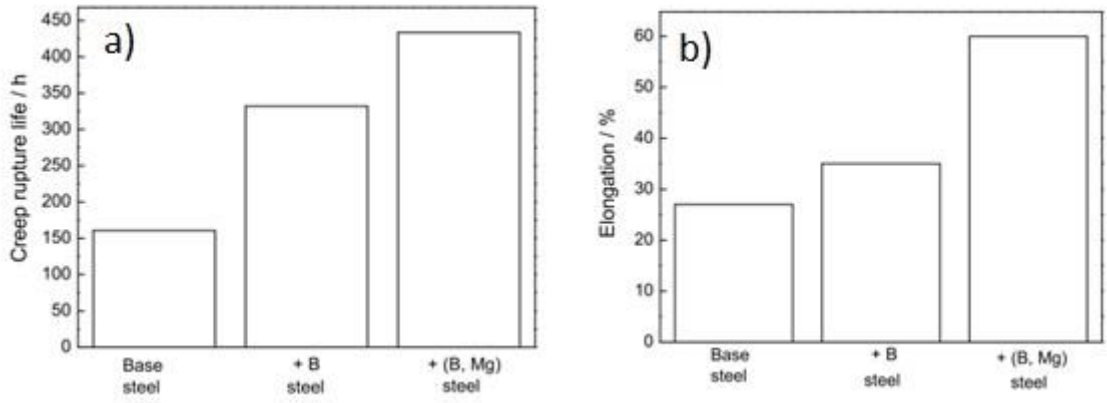

Figure 2-3: (a) Variation of stress-rupture life of the steels tested at 700 °C /180 MPa (b) Variation of elongation of the steels tested at 700 °C/ 180 MPa [54]

2.2.3. Nickel-Cobalt Based Alloys

Interest has been shown in nickel-cobalt based alloy steels such as Alloy 617 and 263 as candidates for high strength super-heater and re-heater tubes. Unlike the iron-nickel based alloys, the material is strengthened by γ' (primary strengthening phase) and has a superior high temperature creep strength than HR6W (Figure 2-4).

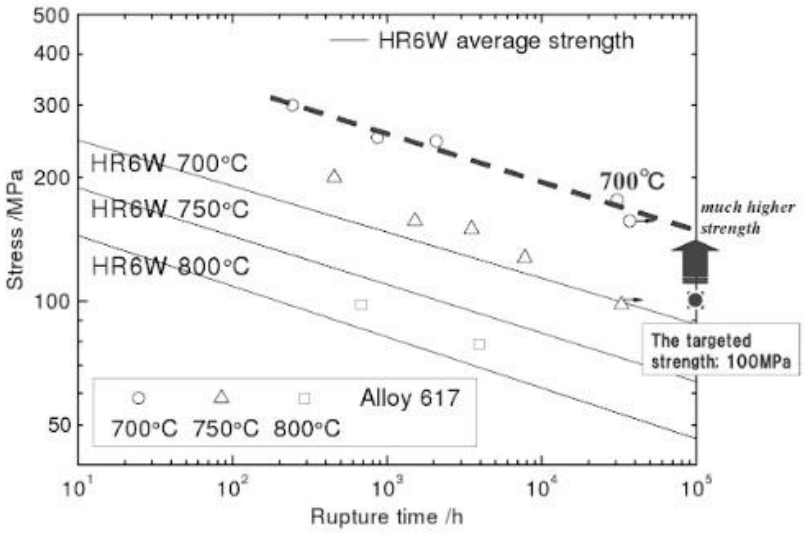

Figure 2-4: Creep strength of Alloy 617 compared with HR6W (Semba et al. 2008 cited in [52])

Although the material has inferior toughness, workability and thermal fatigue properties compared to HR6W, it delivers on the targeted 100,000 hours design creep strength life for 100 MPa at 700 °C, which HR6W marginally falls short of. Alloy 617 and 263 are also prone to grain boundary embrittlement during long term creep exposure and relaxation cracking post welding [52]. However, like the austenitic stainless steel, nickel based alloys are expensive [53].

2.2.4. Ferritic-Martensitic Alloy Steels

Before entering the turbine, steam is typically controlled to temperatures at approximately 550 °C. At this temperature, steam pipes transport large quantities of

high pressure steam from steam headers to the turbines for mechanical power extraction. These steam pipes and headers are not exposed to quite the aggressive environments as the super-heater and re-heater tubes are, albeit operating at high temperatures (550 °C). Therefore they do not come across quite as corrosive conditions but are cycled between different steam temperatures to reflect generation requirements. Ferritic martensitic steels offer operational flexibility whilst remaining cost competitive, especially when compared to other high strength materials such as the nickel based alloys [55]. Steam headers and pipes are generally made from Fe-Cr-C based alloy steels with additional stabilising elements to provide the heightened mechanical properties. At temperatures up to 550 °C, in the UK, steam headers and pipes have typically been manufactured from 0.5% Cr-Mo-V steel (CMV) or 2.25% Cr-1% Mo (T/P22) steel. For steam temperatures above 565 °C, alloyed ferritic-martensitic steels such as 9%Cr-1%Mo-V-Nb (T/P91) and 12% Cr-Mo-V (X20) have been adopted as they provide the higher creep rupture strength; although X20 suffers from fabrication difficulties and so its use has been limited [56]. Improved fracture toughness and creep properties are offered by the 9 - 12% Cr based steels over the low alloyed steels and therefore higher efficiency power generation is possible with higher creep strength materials [55]. As steam temperatures are pushed towards super critical operating conditions (600 °C and above) more expensive austenitic stainless steels may need to be considered, due to their possession of higher fracture toughness and creep properties than ferritic steels. Austenitic stainless steels however, have a lower thermal conductivity and higher coefficient of expansion than ferritic steels [57], making it very difficult to operate thick sectioned austenitic stainless steel boiler components at maximum flexibility, leading to efficiency losses [50, 55].

9 – 12 wt% Cr ferritic-martensitic steels are the typically preferred material for conventional boiler steam pipes and headers as they possess greater mechanical

properties, than CMV and P/T22 steels (Figure 2-5). Properties such as superior corrosion resistance, high temperature creep strength and lower thermal expansion, leads to these steels having good thermal fatigue resistance and they are not as expensive as the nickel alloyed austenitic steels. An example of where these properties are beneficial is that replacing a typical P22 heat recovery steam generator (HRSG) component with P91 can reduce wall thicknesses by 54% and component weight by 65% (Figure 2-6) and increase the thermal fatigue life by a factor of 10 – 12 [58].

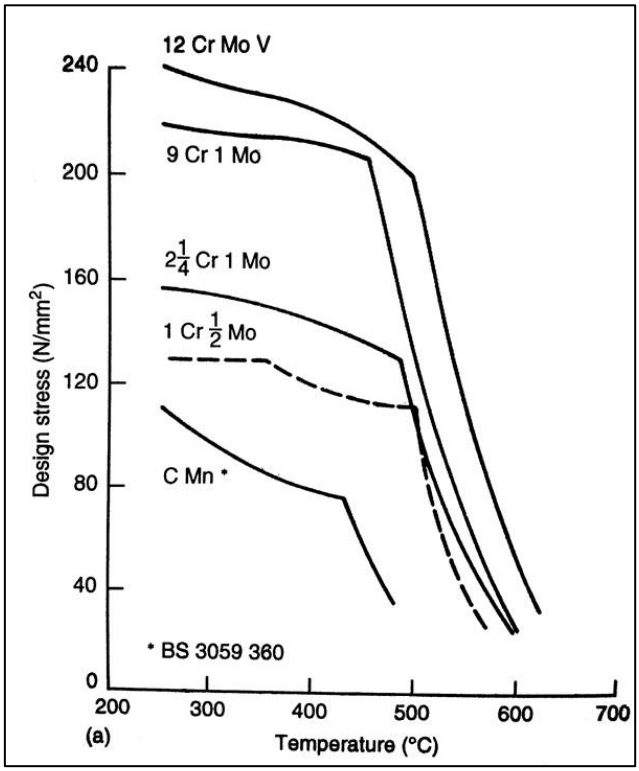

Figure 2-5: Design stress values from BS 1113:1992 cited in [50]

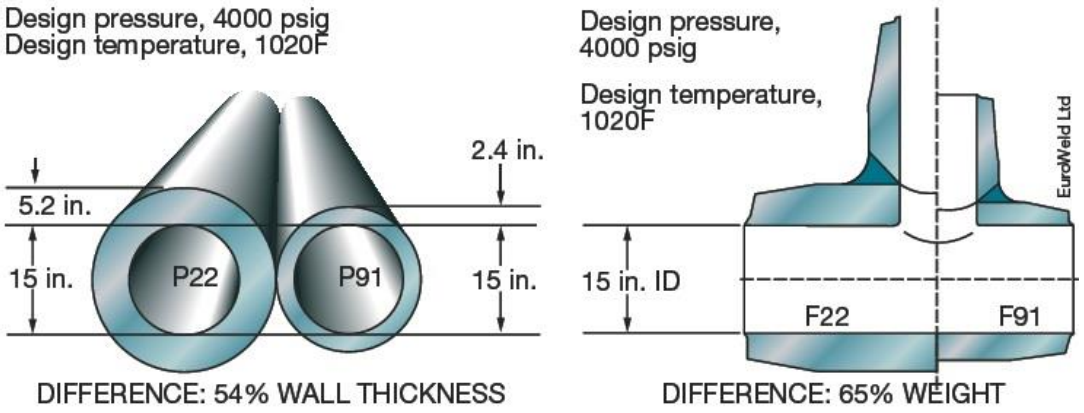

Figure 2-6: Schematic illustration of wall thickness and weight reduction between P22 and P91 material [59].

Enhanced allowable stress values for these materials have contributed to the reduction in their wall thickness sections, in turn making possible the flexible operation of power plant and a reduction in material cost [50, 60]. Highly alloyed ferritic-martensitic steels are the favourable material for boiler components, where applicable, as they have several advantages compared to the austenitic alloys. For example, P91 ferritic martensitic steel has a higher thermal conductivity (improves heat transfer) and lower thermal expansion co-efficient (improves resistance to thermally-induced stress) than austenitic stainless steel. P91 steels have relatively good oxidation resistance and offer more cost effective options than expensive austenitic stainless steels for relevant applications [61].

2.3. 9-Cr Ferritic/Martensitic Alloy Steels

Over the past century, coal-fired power plant temperatures and pressures have seen incredible increases in operating conditions from temperatures below 300 °C rising up to 600 °C and pressures from under 1 MPa to in excess of 30 MPa (Figure 2-7). This outstanding achievement would not have been possible without equivalent advancements in materials technology [62].

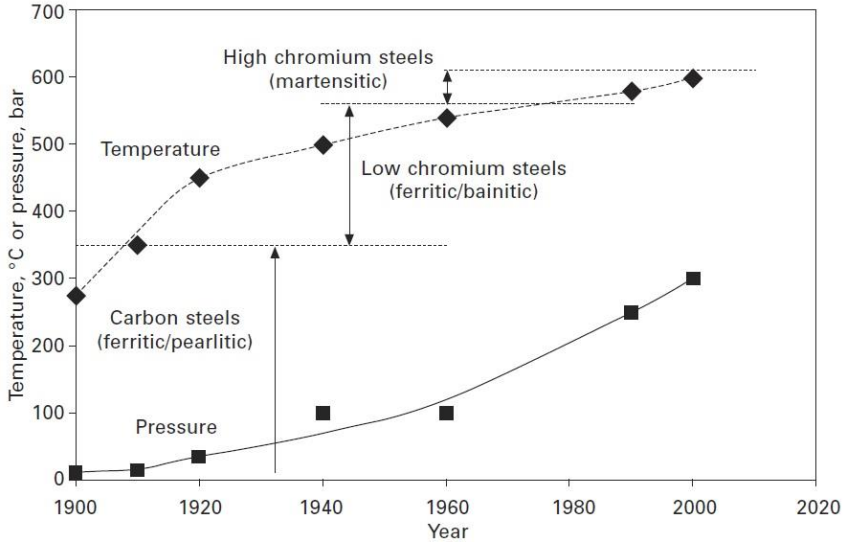

Figure 2-7: The evolution of steam power plant temperatures, pressures and materials. (Mayer and Masuyama, 2008), cited in [56]

The 1950s saw petrochemical plant become familiar with the use of 9Cr-1Mo martensitic steel for its resistance to hydrogen embrittlement, designated P9 under ASTM standards. This was off the back of promising results where Archer et al. (1949) cited in [56] showed how chromium and molybdenum can increase the high temperature creep strength of a material (Figure 2-8). This high chromium alloy was an advancement on the low chromium ferritic steel 2.25%Cr-1%Mo which has inferior high temperature creep strength [63].

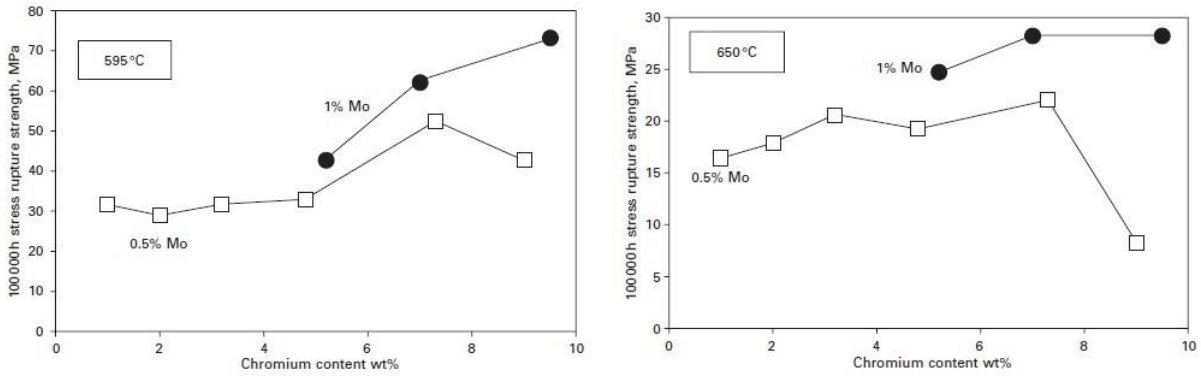

Figure 2-8: Effect of chromium and molybdenum on the 100,000 h stress rupture strength of steel at 595 and 650 °C (Archer et al. 1949) cited in [56])

In a bid to increase creep performance of boiler alloys, the development of enhanced creep rupture life, 9%-chromium ferritic alloys were gaining interest; specifically to provide an economic solution to bridge the gap between low creep life ferritic steels and expensive austenitic stainless steels [38]. By the early 1980s, Oak Ridge National Laboratory developed a low carbon content 9%-Cr ferritic-martensitic steel alloyed with molybdenum designated P91 and T91 where 'P' stands for pipe and 'T' stands for tube (Sikka et al. (1983) cited in [38]). However this material struggled for creep life above 550 °C and was later upgraded with additions of vanadium, niobium and nitrogen (0.2 wt%, 0.06 wt% and 0.05 wt% respectively) [64]. These modifications enhanced creep rupture strength to a temperature range 550 – 600 °C, due to the formation of vanadium and niobium carbides, nitrides and carbo-nitrides, as designated in ASTM 335 for P91 pipes [15] and ASTM A213 for T91 tubes [65]. As well as increasing the creep strength of steam pipe and header components, minimising thermal fatigue has been a major driver hence the focus on 9%Cr ferritic steel development [64]. During a similar period in the 1980s a Japanese steel manufacturer developed the alloy NF616 which is now designated P92 under the ASTM specification [38, 56]. P92 was an advancement of P91 and boasted 20 – 30 % higher creep rupture strength than P91 (at 600 °C). This equated to a maximum steam temperature increase between 15 – 25 °C [66, 67]. The major difference between the alloys is the addition of 1.8 % tungsten (W) and the reduction of 0.5% Mo content. These modifications lead to the formation of a Laves phase Fe_2(Mo, W) above 600 °C further stabilising sub-grain boundaries [68]. At about the same time (1983) alloy E911, similar to P92, was being developed in Europe under Action 501 of the Co-operation in Science and Technology (COST) collaboration. Developing an alloy with creep strength of 100 MPa at 600 °C for 100,000 hours was the target of COST Action 501 [64]. E911 is a 9% chromium ferritic alloy which contains 1 wt% Mo and 1 wt% W (slightly different to P92) but offers similar creep rupture strengths (Staubli et al (1998), cited in [56]). It was originally developed for rotor steel

applications in Round II of the COST activities and later for tubing and piping in Round III [69]. Figure 2-9 highlights the capabilities of the different power generation steels and how they have evolved to accommodate higher operating temperatures. Hence, ferritic-martensitic alloys have been able to provide an economical solution for steam pipes and headers operating at higher temperatures, minimising the need to use expensive austenitic stainless steels.

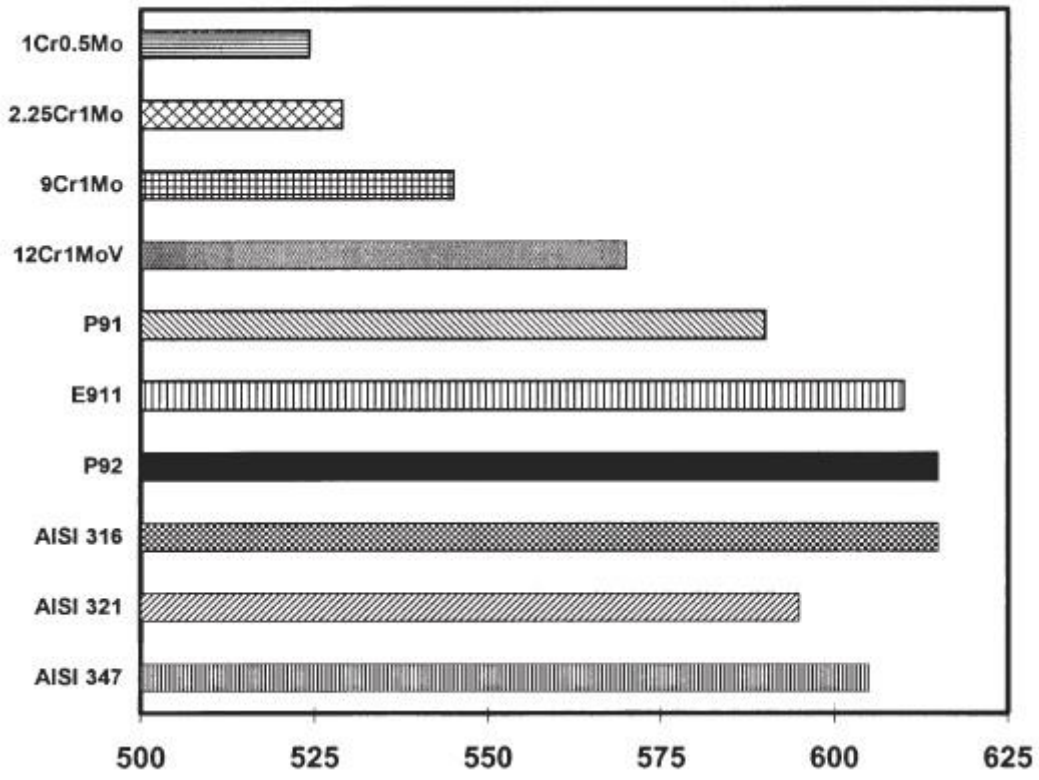

Figure 2-9: Maximum operating temperature (°C), based on a 100,000 h operation and average stress rupture strength of 100 MPa [38]

2.3.1. Physical Metallurgy of 9Cr-1Mo Alloy Steels

The desirable high temperature mechanical properties of 9% chromium material can be attributed to its complex microstructure, which is reflective of the material's chemical composition (given in Table 2-3) and subsequent processing operations.

Table 2-3: Chemical composition in wt% of high chromium steels. Values for P91 from Canonico 1991, for P92 from Watcher et al. 1995, for E911 from Staubli et al. 1998, all cited in [38]

Element	*P9*	*P91*	*P92*	*E911*
C	Max. 0.15	0.10	0.124	0.105
Si	0.20 – 0.65	0.38	0.02	0.20
Mn	0.80 – 1.30	0.46	0.47	0.35
P	Max. 0.03	0.02	0.011	0.007
S	Max. 0.03	0.002	0.006	0.003
Cr	8.5 – 10.5	8.10	9.07	9.16
Mo	1.70 – 2.30	0.92	0.46	1.01
W	-	-	1.78	1.00
V	0.20 – 0.40	0.18	0.19	0.23
Nb	0.30 – 0.45	0.073	0.063	0.068
B	-	-	0.003	-
N	-	0.049	0.043	0.072
Ni	Max. 0.30	0.33	0.06	0.07
Al	-	0.034	0.002	-

Table 2-3 shows the typical compositions for 9% chromium steels and Table 2-4 indicates the mechanical and metallurgical effect of a number of alloying constituents commonly found in such steels. The influences of individual elements can vary for different alloy compositions and therefore Table 2-4 is for indicative purposes only. The base composition of 9%Cr-1%Mo steels allow the material to be hardenable, meaning

the production of a fully martensitic microstructure by normalising is achievable [70]. In contrast, the high chromium content of such steels can lead to the possible formation of δ-ferrite, by austenitising the material at overly raised solution treatment/normalising temperatures (circa 1250 °C) [71]. Therefore it is important to attain a careful balance of ferrite forming and austenite forming elements such that a fully austenitic microstructure is achieved at normalising/tube-making temperatures, a complete martensitic microstructure is achievable upon quenching in air and the correct precipitation strengthening for high temperature creep resistance [55, 70].

Table 2-4: The impact of alloying elements in steel [72]

Element	Impact
Aluminium (Al)	Very strong ferrite former. Used as a deoxidiser, controls austenite grain growth prior to quenching. Carbides difficult to dissolve. Increases tensile strength
Boron (B)	Increases hardenability (most effective in low carbon steels)
Carbon (C)	Strong austenite former. Increases hardness, tensile strength and hardenability
Chromium (Cr)	Increases corrosion and oxidation resistance to improve high temperature strength and hardenability. Strong carbide former, ferrite former
Copper (Cu)	Hot shortness (brittleness at increased temperature). Increases the strength of steel by solid solution strengthening
Manganese (Mn)	Increases hardness, tensile strength and hardenability (less than carbon). Increases surface quality
Molybdenum (Mo)	Increases hardenability, creep resistance and secondary hardening of tempered and quenched steels. Carbide former. Increases the strength of steel by solid solution strengthening
Nickel (Ni)	Does not form carbides in steels, increases hardenability, impact strength, corrosion resistance and strength and toughness of ferrite phase, austenite former
Niobium (Nb)	Increases tensile strength and hardness. Precipitation strengthening, promotes a fine grain structure. Carbide former
Nitrogen (N)	Strong austenite former
Phosphorus (P)	Increases strength and toughness, improves machinability and decreases impact toughness
Silicon (Si)	Deoxidiser, damages surface quality, increases tensile strength and hardness.

	Used to avoid in-service tempering
Sulphur (S)	Reduces ductility and toughness. Increases strength by solid solution strengthening
Titanium (Ti)	Increases ductility and toughness, retards grain growth and improves inclusion characteristics
Tungsten (W)	Carbide stabiliser
Vanadium (V)	Increases tensile strength and creep resistance. Precipitation strengthening of micro-alloyed steels. Carbide former, ferrite former
Other: Hydrogen (H) Oxygen (O)	Additions of hydrogen can also induce hydrogen cracking caused by embrittlement. Oxygen can severely reduce impact toughness.

Carbon takes up the interstitial sites within the atomic structure of the steel providing mechanical strength and forms carbo-nitrides with chrome, niobium and vanadium to improve the materials creep strength in the form of $M_{23}C_6$ and MX type precipitates, where M stands for metal such as Cr or Mo and X stands for C or N (Figure 2-10).

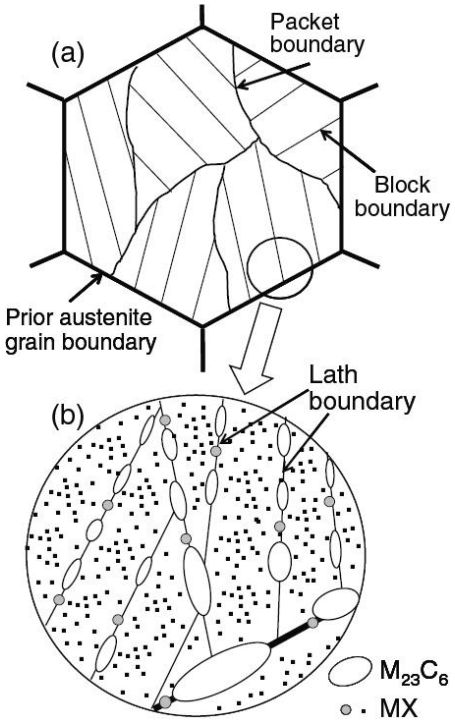

Figure 2-10: Schematic illustration of carbo-nitride precipitate locations within a tempered martensite microstructure for a ferritic-martensitic alloy steel [73]

Niobium and vanadium are the carbide and nitride formers important for creep strengthening [74]. Small additions of niobium (<0.1 wt %) helps achieve a fine prior austenite grain size which promotes high toughness. However for weldments, additions above 0.05 wt% have shown to reduce toughness [75]. Chromium improves the corrosion resistance and steam oxidation by forming protective oxide scales. Molybdenum provides solid solution strengthening and also can be incorporated into the $M_{23}C_6$ carbides [74]. At higher temperature ranges (600 – 650 °C) a Laves phase (Fe_3Mo) can appear, often at the same locations as the $M_{23}C_6$ carbides, achieving a degree of hardening by further stabilising sub-grain boundaries. However, the solid solution strengthening effect of molybdenum is somewhat diminished as molybdenum is removed from the matrix for the precipitation of the Laves phase. Therefore the resultant effect that the Laves phase has on the strengthening of the material can sometimes be difficult to quantify [68, 76]. Nitrogen, like carbon, also provides mechanical strength as it is an interstitial atom and forms fine precipitates within martensitic laths with niobium and vanadium to improve the creep strength [74]. The high temperature mechanical properties of 9%-chromium steels are endorsed by its microstructure. It is the precipitation of carbides and nitrides finely dispersed within a martensitic matrix, to which the high temperature creep properties can be attributed [56]. To achieve this microstructure, components must be put through a carefully controlled heat treatment operation.

2.3.2. Heat Treatment

The heat treatment procedure is critical in producing the microstructure which enables the material to attain its high temperature mechanical properties. A typical schematic representing the heat treatment cycle for 9%-chromium components based on the ASTM International Standard A335 [15] can be seen in Figure 2-11.

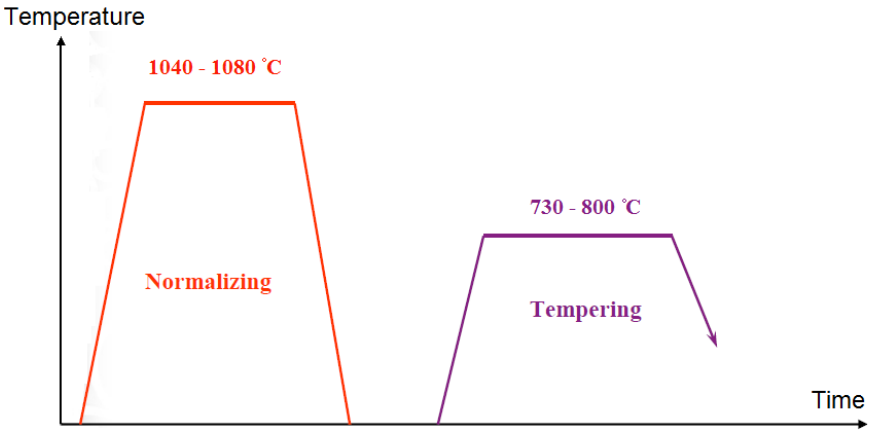

Figure 2-11: Schematic diagram of typical Grade 91 normalising and tempering heat treatment cycle [15]

Pipes are placed within large industrial furnaces and heated to a temperature between 1040 – 1080 °C and held (typically 30 mins) to allow the steel to fully transform to austenite. Once the pipe microstructure has fully transformed to austenite it is removed from the furnace and placed on a cooling bed to cool in air at room temperature to form martensite. This procedure is called normalising. Once fully cooled, the martensitic pipe will be very hard, typically having a hardness value greater than 400 HV. In the as-normalised state, martensite is not only very hard but also brittle and can be weakened by any internal stresses from the normalising procedure. To alleviate these stresses and enhance the ductility and toughness of the martensite; the material is put through a second heat treatment called tempering [77]. The martensite is tempered by re-entering the furnace between 730 – 800 °C and held at temperature (typically 1–3 hours). A typical tempered martensite microstructure can be observed in Figure 2-12a.

The tempering treatment lowers the hardness of the pipe (approximate hardness values ranging between 196 – 265 HV, making it more ductile and brings about the presence and growth of $M_{23}C_6$ and MX type precipitates, where M stands for metals such as Cr, Mo, Nb or V, and X stands for C or N. [15, 78]. These precipitates are what give the material its high temperature creep strength. The Cr-rich $M_{23}C_6$ particles have an elongated block-like formation whilst the finer Nb-rich and V-rich MX particles are almost spherical (Figure 2-12c). A typical 9Cr-1Mo tempered martensite material has shown $M_{23}C_6$ particles to have an average length and width of 285±80 nm and 121±39 nm respectively, whilst the almost spherical MX particles measured an average diameter of 37±15 nm [79, 80]. In Figure 2-12b, $M_{23}C_6$ and MX precipitates can be seen delineating the martensitic packet, block and lath boundaries. Some $M_{23}C_6$ precipitates can be present as small particles along the lath boundaries (0.2 – 0.5 μm) which contribute a dispersion strengthening mechanism, which Abe (2008) [73] refers to as being 'the most important strengthening mechanism for creep' within such alloys [55]. The precipitates produce a hardening effect by preventing the movement of sub-grain boundaries, through the impeding of knitting reactions between free dislocations and sub-grain boundaries, and by pinning sub-boundary dislocations, lending to the materials high creep resistance [81, 82]. Yet it should be mentioned that Callister (2005) [83] has highlighted the concerns around selective leaching when one element (e.g. chromium) is preferentially removed from solution leaving behind depleted zones, which could cause a concern for corrosion resistance. Figure 2-13 schematically illustrates the chromium depleted zones and researchers have begun studies to design precipitates such that chrome-rich $M_{23}C_6$ carbides are preferentially reduced in such steels [73].

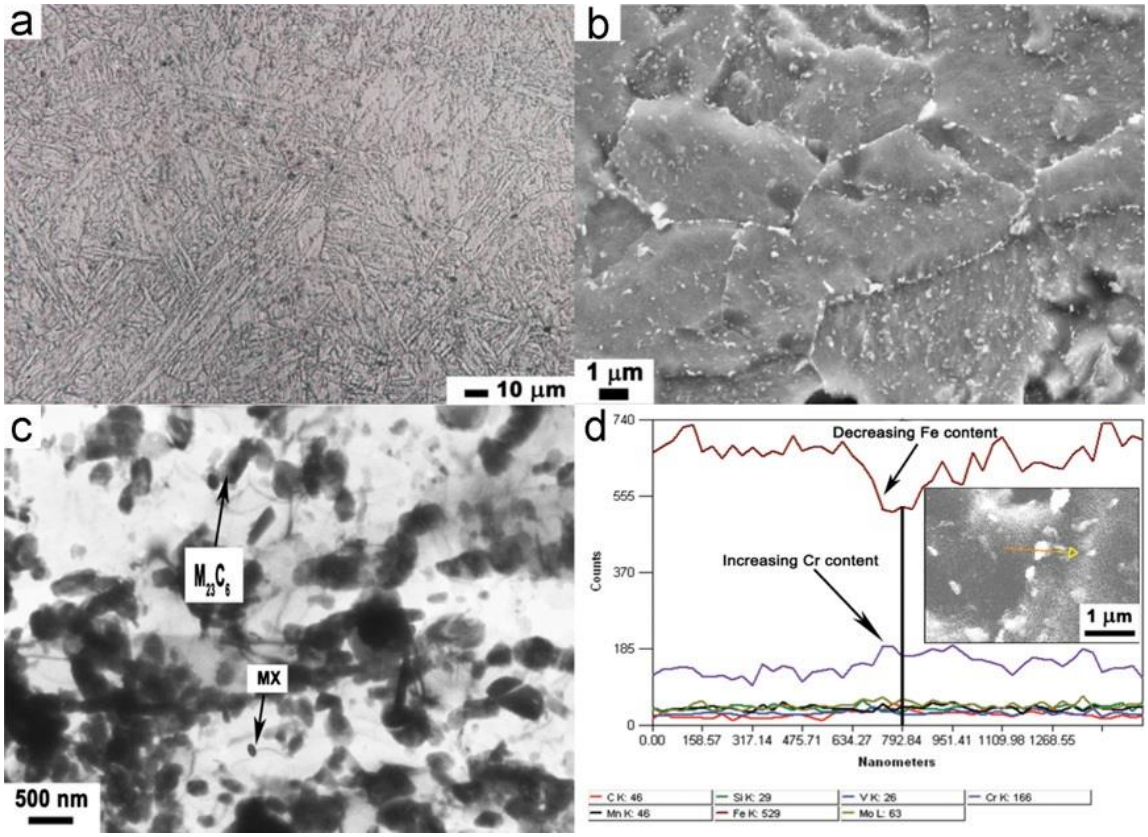

Figure 2-12: Microstructure of Grade 91 Steel: (a) optical micrograph showing the tempered martensitic structure, (b) SEM micrograph showing the distribution of precipitates in the alloy, (c) bright field TEM micrograph showing the various particles and (d) EDS line scan of a $M_{23}C_6$ precipitate [79]

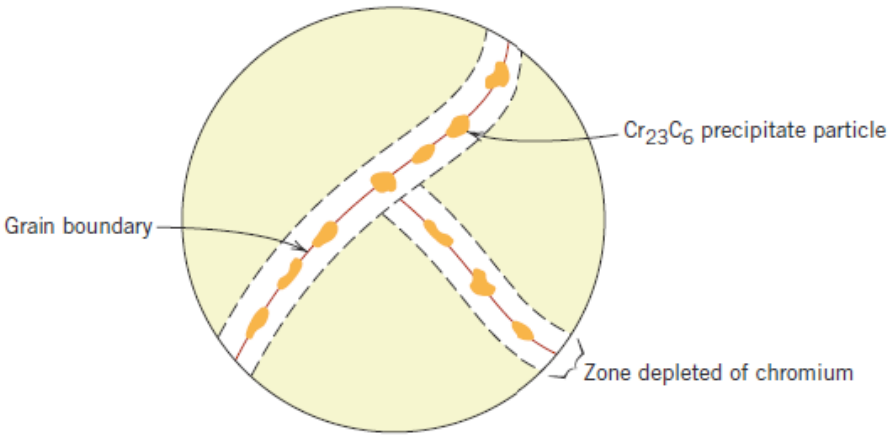

Figure 2-13: Schematic diagram depicts the $M_{23}C_6$ (Cr23C6) carbide precipitation along grain boundaries [83]

2.3.3. Martensite Formation

The ability to produce a tempered martensitic microstructure for 9Cr-1Mo material (e.g. P91) is crucial for its high temperature performance. To produce martensite the alloy must be austenitised to produce a face-centred cubic (FCC) austenitic crystal structure. This is followed by accelerated cooling (often in air) causing the material to form a body-centred tetragonal (BCT) martensitic crystal structure. This heat treatment is also known as normalising. The rapid process of normalising the material causes a diffusionless shear transformation as the alloying atoms do not have time to diffuse to form a body centred cubic (BCC) crystal structure such as ferrite. Based on differential dilatometry performed by pipe and tube manufacturers Vallourec & Mannesmann [78], the temperature at which austenite begins to form, Ac_1, (also known as the lower critical transformational temperature) was found to be between 800 °C – 830 °C and the temperature at which ferrite completes its transformation into austenite, Ac_3, (also known as the upper critical transformational temperature) was between 890 °C – 940 °C [78]. Therefore typical normalising temperatures for P91 are above 1000 °C (Figure 2-11). Orr and Woollard (1997) [70] suggest that the highest possible Ac_1 temperatures should be utilised for components, such as pipes and tubes, which are typically welded and stress relieved before entering service. In this way, the initial tempering and stress relieving can be executed at a temperature range between 750 – 780 °C. Hence, nickel content is typically suppressed below 0.4 wt% as it is an austenite former and will encourage the Ac_1 temperature to decrease. The continuous cooling transformation (CCT) diagram in Figure 2-14 reflects the typical austenitising temperature to be above 1000 °C with the Ac_1 temperature at 810 °C and the Ac_3 temperature at 930 °C [74]. The martensite start temperature (M_S) and martensite finish temperature (M_F) are approximately 400 °C and 100 °C respectively.

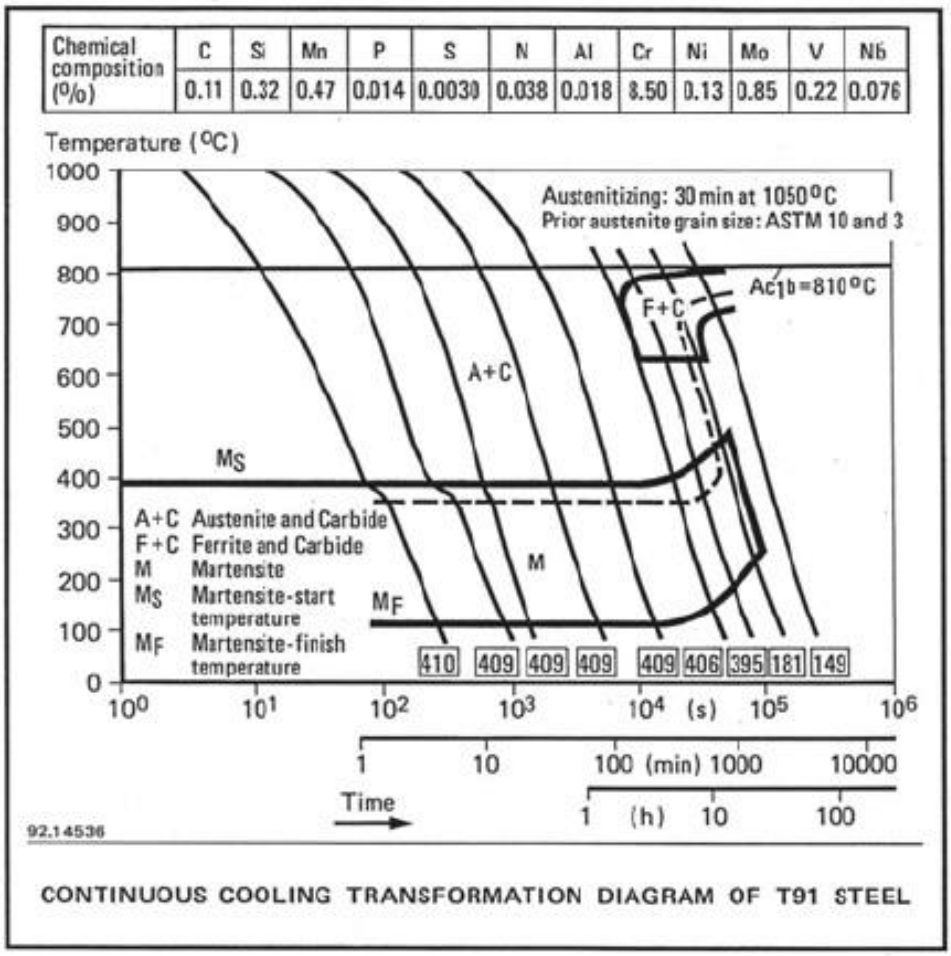

Figure 2-14: Continuous Cooling Transformation diagram for P91 steel [84]

The hardenability of a material has been defined by Siebert et al (1997) [50] as being the capacity of a steel to transform partially or completely from austenite to some percentage of martensite at a given depth when cooled under some given condition. Some P91 header sections can have thick cross-sections and so the hardenability of the material is very important to ensure full martensitic transformation throughout the component. Chromium, molybdenum and nickel increase the hardenability of P91 increasing the chances of through thickness martensitic transformation, although, some thicker sections may require forced air cooling [85, 86]. However, Irvine et al (1960) [87], highlight the need to pay careful consideration to the quantity of chromium and

nickel as they are ferrite and austenite formers respectively, and so will have opposing effects on the M_S and M_F temperatures. In addition, nickel lowers the Ac_1 temperature and has been proven to reduce creep resistance if present in quantities above 0.6 wt%, therefore limiting nickel to 0.3 wt% is recommended [74].

2.4. Material Degradation

The economic return from a boiler component is measured against its life expectancy and operational performance. A component's operational lifetime is significantly affected by its service entry condition and thereafter, the pace and extent to which it degrades. The primary concern of an unexpected component failure is the potential significant risk to life and the environment [30, 88]. The consequence of a failed component also has significant economic ramifications. It is not so much the cost and replenishment of the component that causes concern, but rather the whole boiler unit being unavailable to operate, as the failed component is critical to the boilers operation. A forced outage for a typical 500 MW coal power plant unit in the U.S can cost anything from $500,000 - $750,000 per day, this cost range is reflective for equivalent sized plants in the UK [62, 89]. The major reason for forced outages is the failure of boiler tubes and the high temperature problems faced by critical components such as the thick-walled steam headers. The formation of a specific microstructure, i.e. tempered martensite, and the maintenance of that microstructure throughout its service life is what the superior properties of Grade 91 components rely on. Failing to produce or maintain this precise microstructure during its manufacture or subsequent processing and utilisation can be fatal for the components operational life. Pre-service or in-service inconsistencies can cause the material to change phase, away from 100% correctly tempered martensite, or have a negative effect on the precipitates. In either case, this will significantly deteriorate the mechanical properties of the alloy [59, 90].

2.4.1. Pre-service Degradation

The tempered martensitic microstructure is very sensitive to the high temperature processing and subsequent heat treatment procedures during component fabrication and repair. Grade 91 steels have experienced numerous problems due to the delicate relationship between heat treatment procedures and the achievement of the desired tempered martensitic microstructure [16]. Pipe and tube components are often heat treated in different furnaces depending on the product size, such as, a batch furnace, walking beam furnace or tunnel furnace (Figure 2-15).

Figure 2-15: Image of P91 pipes being heat treated in a batch furnace [14]

However irregularities in procedures can still occur due to human error or equipment failure – such as improperly sealed/shut furnace doors, over/under-tempering temperatures or too slow cooling after austenitising leading to ferrite formation [91-93]. This leads to non-conformance of microstructure and the material falling below specification standards [17]. Slower cooling rates can occur in local regions where hot components are in close proximity to one another whilst air cooling to form martensite, this can lead to mis-heat treated zones. At these locations, the heat in the material takes more time to dissipate, failing to produce martensite, instead forming softer areas of ferrite [91]. Evidence of mis-heat treated components being supplied to industry have been reported by the Electricity Power Research Institute (EPRI) (2009) cited

in [23]. Post-production heat treatment processes (such as normalising to produce martensite), if not managed with caution can cause unwanted results. For example, normalising the material at a temperature excessively (100 – 200 °C) higher than the Ac_3 where complete transformation to austenite occurs (circa 930 °C) [74], can provide an environment where carbon will begin to diffuse. At the surface the carbon atoms can react with the oxygen in the surrounding atmosphere, depleting the surface of carbon and causing a carbon concentration gradient to exist between the surface and the bulk [94, 95]. This phenomenon is known as decarburisation and can considerably reduce the mechanical properties at the surface where carbon has diminished. This is a significant problem for thinner walled sections as the decarburised layer will comprise a significant percentage of the wall thickness as opposed to thicker walled components such as steam headers. However the presence of a decarburised layer within thicker sections is problematic for pre-service product quality inspection. With current inspection techniques such as surface replication and hardness testing, the softer decarburised layer can often mask what may be acceptable bulk property material beneath the surface of the component. This misrepresentation of bulk material properties can lead to incorrect pre-service condition assessments being made [91, 92].

Lack of control over temperature when exposing Grade 91 material to high temperatures for post-normalising tempering treatments or in-service maintenance and welding operations, has been regarded as some of the most significant problems for this type of material [59]. The temperature zone between Ac_1 and Ac_3 is known as the intercritical region (810 – 930 °C) [74]. Within the intercritical region, martensite partially transforms into austenite and carbo-nitride precipitates coarsen. The resultant microstructure is of a dual phased (austenite/martensite) material with coarser precipitates which lack the pinning effect required to achieve the expected high creep

strength properties. Lack of control on tempering time can also be detrimental to the materials microstructure. During tempering, the material is exposed to and held at a temperature below the Ac_1, to increase the toughness and ductility of the brittle martensite. However, if the material experiences prolonged exposure (known as over-tempering); the precipitates will begin to coarsen corresponding to a deficiency in their pinning effect and resistance to dislocation movement [85, 92]. Conversely, under-tempering is when the material does not see sufficient exposure at elevated tempering temperatures to complete the precipitation of carbo-nitrides at the required size and volume, thereby threatening the high temperature properties [59, 85]. Henry (2005) [93] explains the problem of mis-manufactured Grade 91 material as being symptomatic of the industry's 'business-as-usual' nonchalance culture toward the material. An example of this was highlighted where a combined cycle plants' contractor, responsible for heat treating the P91 components, used a treatment with too low a cooling rate, similar to the one they had used for decades with P22 (2.25Cr-1Mo). This resulted in the material being in the over-tempered condition rather than bearing the optimal microstructure of a tempered martensite, leading to significantly reduced creep strength.

2.4.2. In-service Degradation

When correctly tempered martensitic material is installed at service entry, there are still concerns surrounding in-service degradation [96]. The literature highlights several types of service degradation associated with elevated temperature operations.

The degeneration of a tempered martensitic microstructure due to elevated temperature operation is a cause for concern. It has been documented that over the service period of some of these components (10s of years) the microstructure gradually evolves from a desirable structure of fine tempered martensitic laths (Figure 2-16a) into broader ferrite laths and eventually into an equiaxed ferrite grain structure (Figure

2-16b) which has significantly lower creep resistance [27]. Other evolutions noticed were the coarsening of M_2X carbides into larger $M_{23}C_6/M_6C$ carbides and their concentration on ferrite grain boundaries. This would cause the mechanical properties to be weaker than those expected of a tempered martensite microstructure with more finely dispersed smaller precipitates [27, 38, 69, 97].

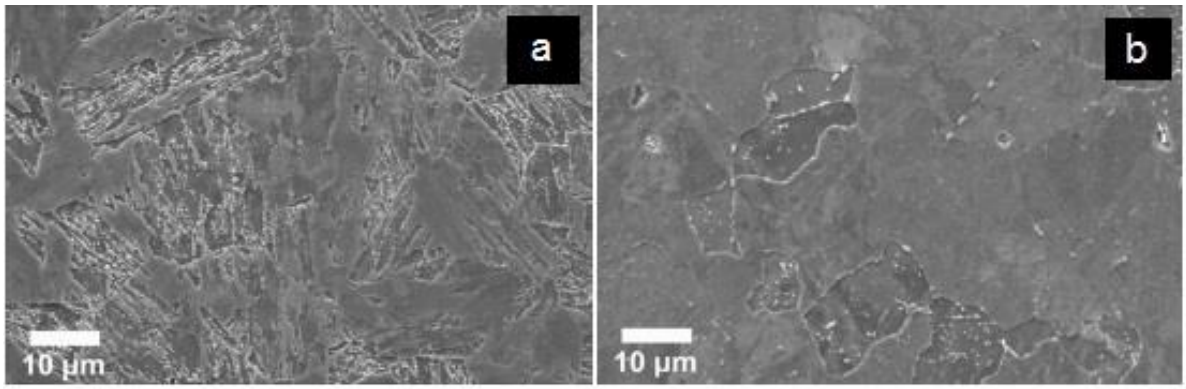

Figure 2-16: Microstructure of P9 (9Cr- 1Mo) in different thermally exposed conditions; (a) normalised and tempered and (b) ex-service [27]

Shrestha et al (2013) [79] discovered identical results of a degraded microstructure over prolonged periods of exposure to high temperatures. The tempered martensitic microstructure had evolved into a polygonised microstructure for a Grade 91 sample which had been exposed to 650 °C at 200 MPa. Studies of the microstructure revealed a decreased dislocation and precipitate density, causing a detriment to the creep resistance as there are no obstacles to dislocation movement within a precipitate free matrix. These findings complement the work done by Zielinska-Lipiec et al (1997, 1999) [98, 99] which investigated the decrease of creep rupture strength of a chromium ferritic-martensitic material (9Cr-0.5Mo-1.8W-V-Nb steel P92). It was identified that the microstructural changes were responsible for the decrease of creep rupture strength, specifically relating to coarsening of the $M_{23}C_6$ precipitates together with the decrease in dislocation density. As well as particle coarsening and microstructure degeneration, Shrestha et al (2013) [79] found the creep strength of Grade 91 to be weakened by the

precipitation of Laves phase (Fe_2Mo). Molybdenum is removed from solution to precipitate the Laves phase and hence abates the solid solution strengthening effect of molybdenum in solution.

Poor oxidation resistance is an issue for boiler components, leading to undesirable degradation and significantly shortened component life. The type of oxide that forms on 9-12Cr wt% alloys has been shown to be dependent on the local temperature, steam conditions and content of major alloying elements (chromium, silicon and aluminium). Small amounts of trace elements such as sulphur have also shown that even at impurity levels, a remarkable improvement of oxidation resistance can be achieved within high chromium ferritic steels. However excessive amounts of chromium, silicon and sulphur will have detrimental effects on the mechanical properties and hence maintaining the correct balance is crucial [100, 101]. Ehlers et al (2006) [46] studied the formation of oxide scales on P91 material under isothermal conditions (650 °C) for various time exposures whilst changing the atmosphere gas type condition between wet and dry. The term ‘wet’ refers to the oxidation reaction taking place with an aqueous solution present in the atmosphere and ‘dry’ refers to no presence of water/aqueous solution present within the material’s environment. As can be seen from Figure 2-17, numerous types of oxides can form on the material. Hematite (Fe_2O_3), magnetite (Fe_3O_4) and complex chrome rich inner spinel region of Fe_3O_4 + $(Fe,Cr,Mn)_3O_4$. The thickness of the oxide scale is dependent on the atmospheric conditions and the time of exposure. Ehlers et al (2006) [46] showed oxide scales on P91 after oxidation in N_2-1vol%O_2-2vol%H_2O at 650 °C for 1 h, 2 hrs, 7 hrs and 16 hrs, to have a total oxide thickness of approximately 1, 8, 50 and 100 µm respectively.

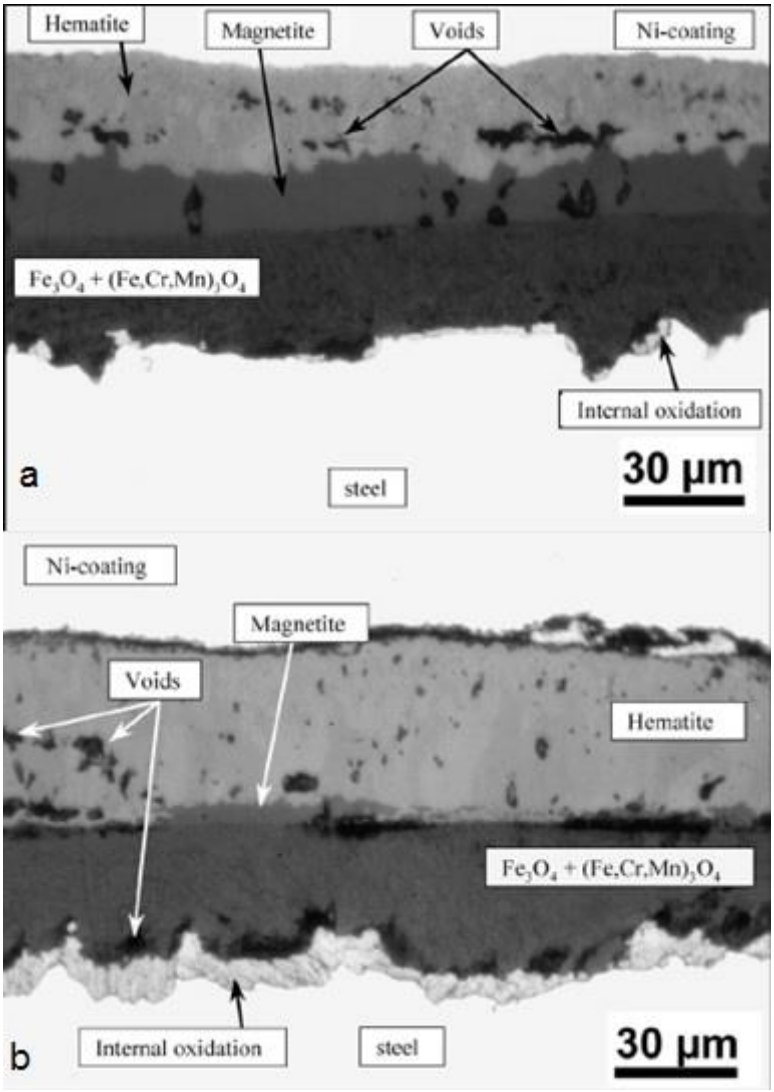

Figure 2-17: Metallographic cross-section of oxide scales for P91 material exposed to 650 °C. Various oxidation stages including in-situ gas changes between wet and dry gas (a) 48 h and (b) 96 h [46]

High temperature creep is a time dependent mechanism by which material permanently deforms when subjected to a constant load or stress. The effect of creep is amplified at elevated temperatures and thus boiler components can become prone to creep [77]. Shrestha et al (2013) [79] have shown that the effect of increasing the stress or temperature on a material will both cause an increasing effect on the minimum creep rate and a decreasing effect on the time to rupture (Figure 2-18).

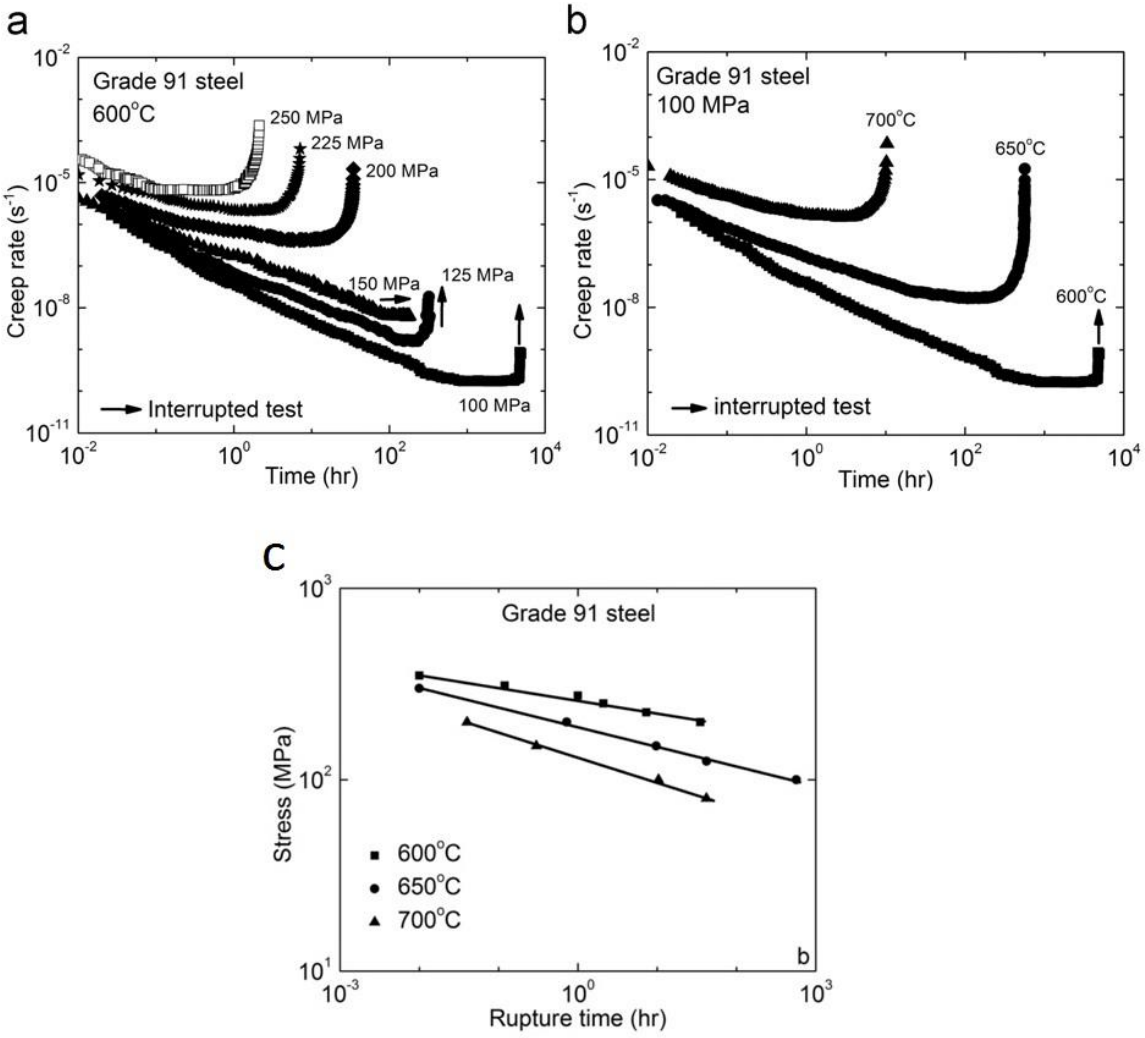

Figure 2-18: The effect of applied stress and temperature on Grade 91 creep behaviour. The variation of creep rates as a function of (a) stress at 600 °C and (b) temperature at 100 MPa. (c) Stress and temperature dependency of creep rupture life [79]

Grade 91 material will lose its inherent creep rupture strength as it creeps over time. This is because creep in Grade 91 will cause the deterioration of, the material's solid solution strengthening, tempered martensitic microstructure, dense dislocation network and precipitates. Shrestha et al (2013) [79] performed tensile tests at varying temperatures and applied stresses to analyse the creep behaviour within a Grade 91 material. They found evidence of creep cavities within the necking region at a position 5 mm along from the fracture surface (Figure 2-19a). However, the extent of creep is insignificant at this point as cavitation depends on the amount of true local strain, which

is lower at a position 5 mm from the fracture surface and increases significantly as it approaches the fracture surface. Further evidence of creep cavitation and damage initiation can be seen in Figure 2-19c and Figure 2-19d, which were tested at an applied stress and temperature of 100 MPa and 600 °C, and 150 MPa and 700 °C respectively. Figure 2-19b shows the variation of localised strain and Vickers hardness with respect to location on the specimen. '0' position on the gauge represents the point of fracture and at this point the localised strain is at its highest. The micro-hardness behaviour shows the material to soften as the necked region is entered and approaching the fracture surface. The point of fracture displayed a severe drop in hardness measuring just 29VHN as opposed to 231VHN at the gripped section of the test specimen and 248VHN of the as-received material. It was concluded that as the number of creep cavities increase, the hardness of the material decreases [79].

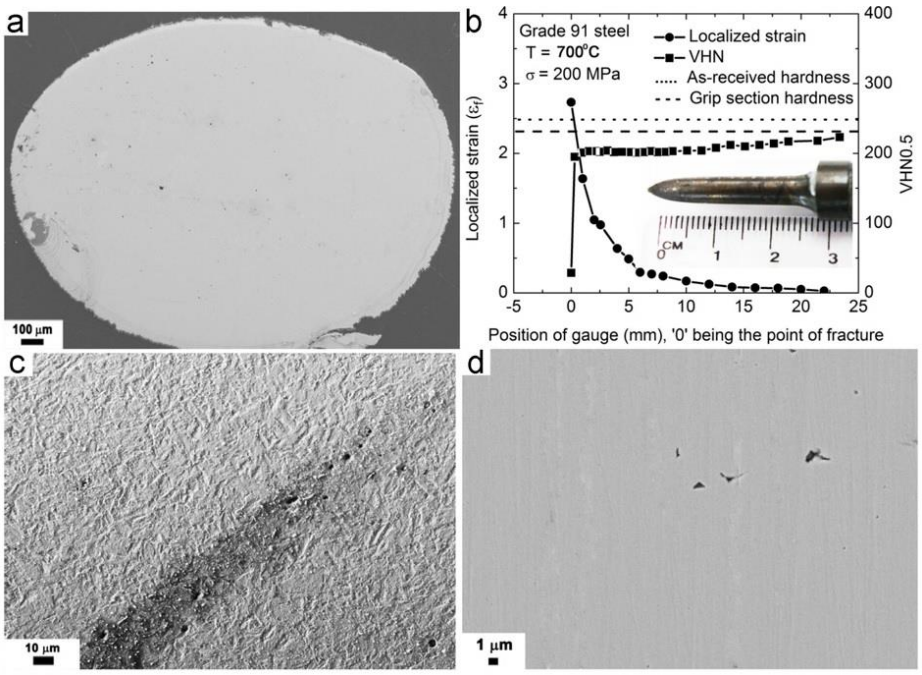

Figure 2-19: Evidence of creep cavitation within Grade 91 material.
(a) Necked area of a creep ruptured specimen (700 °C and 200 MPa), (b) Variation of true local strain and micro-hardness with position, in a specimen fractured at 700 °C and 200 MPa, (c) Nucleation of voids along a straight line in a specimen crept at 650 °C and 100 MPa and (d) wedge cracks seen in a specimen crept at 650 °C and 150 MPa [79]

Time-temperature parametric (TTP) methods are regularly used for the extrapolation of creep life analysis, with the most commonly used parametric approach being the Larson-Miller parameter (LMP) [102]. The LMP is expressed in terms of rupture time and temperature as:

$$LMP = T(\log t_R + C) \qquad \textbf{Eq. 2-3}$$

Where T is the temperature (in K), t_R is the time to rupture (in hours) and C is the Larson-Miller constant, approximately 33 – 35 [79, 102]. Shrestha et al (2013) [79] show in Figure 2-20 that LMP values of Grade 91 steel decreases with increased stress and that discuss how their results are comparable to other studies.

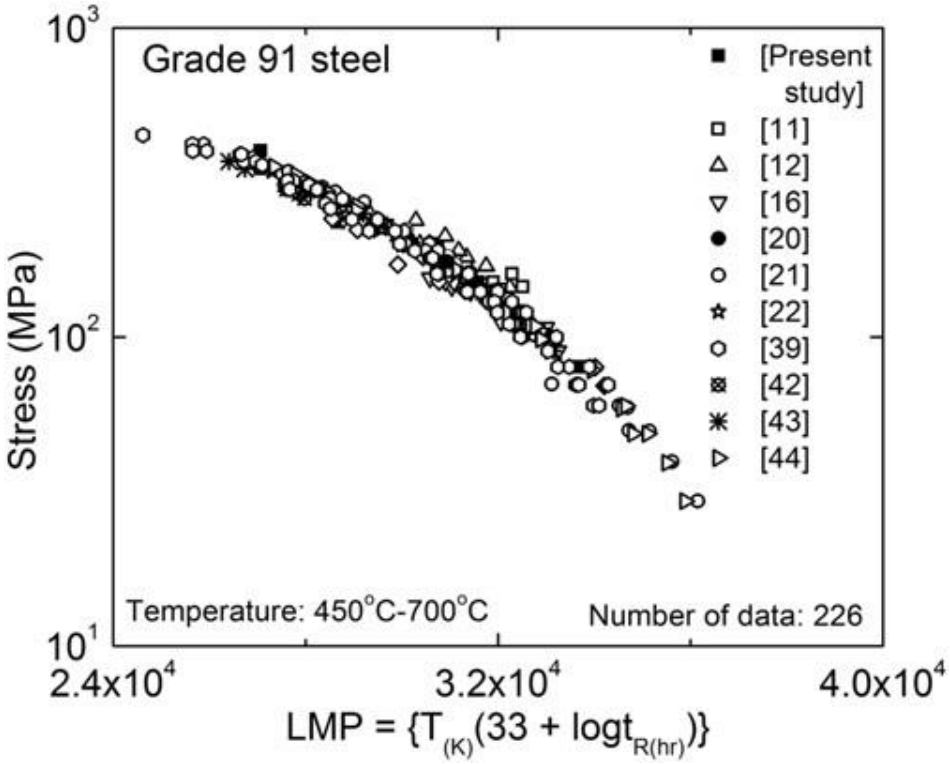

Figure 2-20: Larson-Miller parameter plot of Grade 91 steel [79]

Cerri et al (1998) [82] also performed creep studies to understand what effect microstructure evolution has, due to creep, on the material's properties. Samples were crept at 873 K /175 MPa, 873 K /130 MPa, 923 K /160 MPa and 923 K /115 MPa.

Results clearly showed growth of the subgrains (laths) for crept samples (Figure 2-21b-d) in comparison to the normalised and tempered microstructure which is the common service entry microstructure for Grade 91 (Figure 2-21a). The authors discuss that in general precipitates try to pin subgrain boundaries. However, some of these subgrain boundaries disappear as the subgrains grow, leaving precipitates within the subgrain as opposed to on the subgrain boundaries. This causes a decrease in the percentage of subgrain boundary particles which weakens the effect of subgrain boundary pinning.

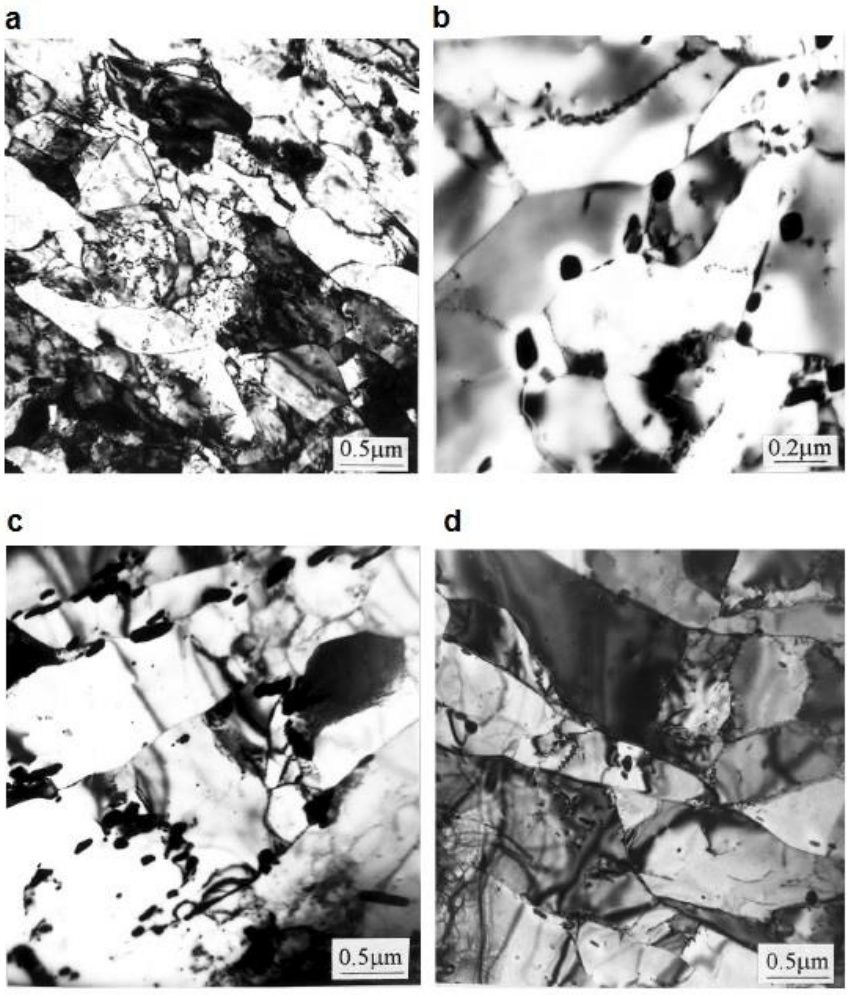

Figure 2-21: TEM micrographs of modified 9Cr-1Mo steel. (a) normalised and tempered state (service entry standard), (b) creep tested at 873 K and 175 MPa, (c) creep tested at 873 K and 130 MPa and (d) crept at 923 K and 160 MPa [82]

2.5. Methods for Material Monitoring and Characterisation

The power generation industry has been experiencing its highest pace of change over the past 15 – 20 years and has seen a shift in driving force from engineering excellence to commercial management and maximising company profits. In this competitive environment, the emphasis on maintaining plant in productivity beyond its original design life has increased. The focus on achieving this without risk to plant safety, workforce or the environment is of paramount importance. This has only been possible with the advances in life assessment and condition monitoring techniques [103]. The importance of producing a specific tempered martensitic microstructure for Grade 91 service entry components has already been highlighted in this chapter. Given what the potential detrimental effects of pre-service manufacturing errors and in-service degradation can have on fossil-fuelled boiler components; it would be beneficial to be able to monitor the change in microstructural features within the material. Raj et al (2013) [104] emphasise the importance of a component's microstructural features as being 'decisive', because they communicate information about the material's physical, mechanical and corrosion performance. Henry (2005) [93] further iterates the significance of material condition monitoring by describing the need to closely monitor Grade 91 alloys throughout their service life as being the 'most important take-away' message from the 2003 Maintenance Workshop on P91/T91.

2.5.1. Microscopy

The conventional method for studying the microstructure of a material is through optical and electron microscopy. An optical microscope can be used to study the different microstructural features such as phase type, grain size and precipitate presence. Optical microscopy (OM) requires the metallographic sample to be carefully prepared via sample mounting, grinding, and polishing to a mirror-like finish followed by chemical

etching. These careful and meticulous surface preparations are necessary to expose the important details of the microstructure, limited to the wavelength of visible light (0.2 μm) [77].

Electron microscopes employ the use of a focused high energy electron beam allowing the examination of microstructures under higher resolution, unlike the use of light radiation as is for OM. The two most common types of electron microscope are the scanning electron microscope (SEM) and the transmission electron microscope (TEM), with the major difference being the type of beam mode employed. Nanoscale levels of resolution can be achieved with electron microscopes and so finer details with respect to grain size, precipitate size/distribution and dislocation structures can be studied [105]. An auxiliary to the SEM is energy dispersive x-rays which allow the elemental analysis of the material under investigation to obtain detailed information about the microstructure. The TEM provides detailed information about the internal composition and characteristics such as morphology, crystallisation or even magnetic domains. It has a much higher resolution than SEM and is not limited to topographic analysis. Both types of electron microscope require significant sample preparations and hence are considered relatively slow. Samples must be sectioned from components and prepared to small scales; a few centimetres for SEM samples and submicron sizes for TEM samples. This restricts the number of samples and locations of material that can be examined due to the lengthy and intricate sample preparation required.

Microscopy processes are innately destructive, time consuming and are limited to small areas of examination. According to Viswanathan (1989) [62] although sacrificial boiler tubes are readily available within boiler units for destructive analysis, there is still a requirement for non-destructive testing to highlight which sections of tube should be investigated destructively. To accurately identify the critical regions for assessment/sampling, amidst miles of tubing, makes a non-destructive evaluation

highly desirable to be able to identify such locations for further destructive sampling. Raj et al (2003) [104] also justify the need to develop techniques which provide the required microstructural information without destroying the component during the analysis. In this manner a non-destructive evaluation (NDE) can be performed enabling structural integrity assessment as either a precursor to destructive sampling or as a tool for complementary information in conjunction with other non-destructive assessment techniques.

2.5.2. Non-destructive Techniques

2.5.2.1. Portable Microscopy

Portable microscopy is a method in which metallographic information can be gathered, without having to section/ destroy the component. It operates in a similar manner to the conventional light reflecting optical microscope with the ability to be taken to the component. In the same manner as OM, the area to be inspected requires a mirror-like surface finish through the processes of grinding, polishing and etching, to reveal the microstructure. Portable microscopes have shown to be able to qualitatively demonstrate the same characteristics of the microstructure as conventional destructive OM [106]. The main disadvantage for this technique comes when it is physically impossible to install a portable microscope, on the surface to be examined, due to geometric constraints. Other issues to consider are component vibrations, low magnification factors of portable microscopes and the surrounding atmosphere with the possibility of high concentrations of dust affecting operability.

2.5.2.2. Surface Replication

The surface replication technique has fewer drawbacks compared with portable microscopy and is therefore one of the more favourable metallographic techniques used within industry. Numerous publications have found the replicas method to have a

lot of applications in non-destructive examination of thermal power plant components as well as having recommendations as a NDE method for thermal power plants [104, 107, 108]. Similar to conventional microscopy, the area of investigation needs metallurgical preparation to a mirror-like finish through grinding and polishing procedures, before etching the surface to reveal the microstructure. The surface to be examined, once prepared to a mirror-like finish, is wetted with a solvent (usually acetone) and a polymer film or foil (usually acetate) is positioned and tightly pressed against the wetted surface. The solvent softens the polymer foil and capillary action forces the foil to conform to the etched surface, reproducing a relief of the microstructure on the polymer foil. Once the solvent has dried, the replica is removed from the surface, mounted on a stable support block and examined using conventional microscopes. Grain structure and size, surface defects such as micro cracks and voids should all be detectable from surface replications [107]. An example of creep cavities being exposed by a surface replica can be seen in Figure 2-22.

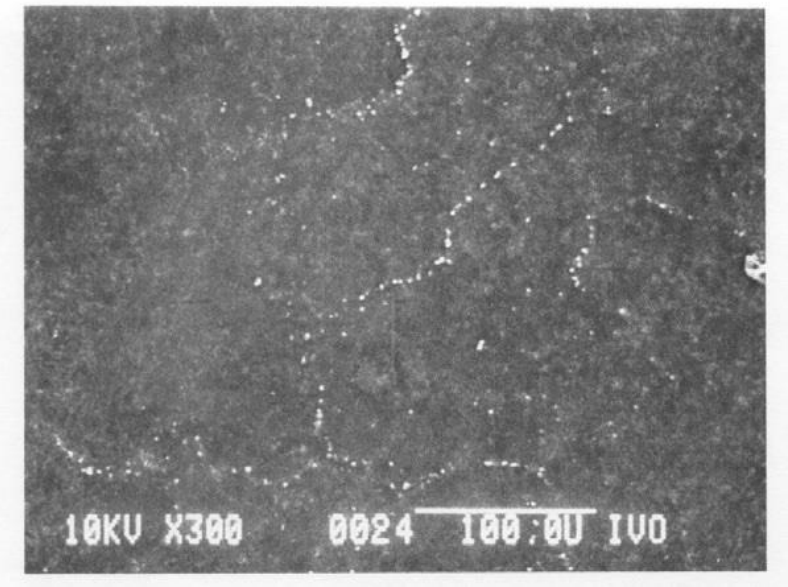

Figure 2-22: Image from a metallographic inspection of a replica of reheat steam mixer (1Cr-0.5Mo steel) after 168,000 h of service at 530 °C, showing aligned cavities [109]

One of the more obvious limitations to this technique is that subsurface defects cannot be detected. Observations by van Wortel (2007) cited in [107] have shown that damage within boiler end caps and headers usually initiate on the inner surface of the component (not available for inspection). This leads to macro cracks growing through over half the wall thickness before any indication of cavities is given at the surface to be seen on the replicas. A less obvious limitation has been reported by Artamonov, V.P. and Artamonov V.V. (2002) [110] based on an investigation where replicas were obtained using early methods of the technique developed by Kan (1968) [111]. The investigation showed the polymer replicas to be prone to low reflectivity under metallographic microscopes. This made it difficult to bring out microstructural features on low-contrast replicas. Although this difficulty can be overcome by a method known as the vacuum deposition technique, it can seldom be used in industrial conditions [110]. Surface replication technique is labour intensive, highly localised and can only be taken on components during maintenance and shutdown periods, which is a significant limitation for non-destructive in-situ evaluation [58].

2.5.2.3. Portable Hardness Testing

“Hardness is a measure of the ease with which solids can be plastically deformed.” This definition given by Gilman (2009) [112] describes the usefulness of hardness testing as it can be correlated to other mechanical properties such as tensile strength [113]. Portable hardness testing is a popular means of carrying out NDT on boiler components because it is a relatively simple, inexpensive and potentially non-subjective means of assessing a material’s mechanical properties [114]. Hardness testing is a surface technique where, depending on the scale of hardness required (Vickers, Brinell etc.); a surface indentation is made which outputs a numerical value for quantifying the hardness of the material, rather than characterising a flaw, discontinuity or phase transformation. The Vickers hardness technique is a popular

method within science and engineering and according to Sposito et al (2010) [107] it has even been considered in many studies as a complementary NDE technique for evaluating creep damage.

A Vickers hardness measurement is gained by indenting the test material with a diamond indenter in the form of a square pyramid with an apex angle of 136˚ (Figure 2-23). A fixed force is applied to the axis of the indenter which makes an irreversible indentation into the surface. The two diagonal lengths indented into the surface after removal of the load are measured using a microscope and their average value calculated (Figure 2-24). This allows the area of the indentation to be calculated using Eq. 2-4, which is a ratio of the indented area to the applied load [112]

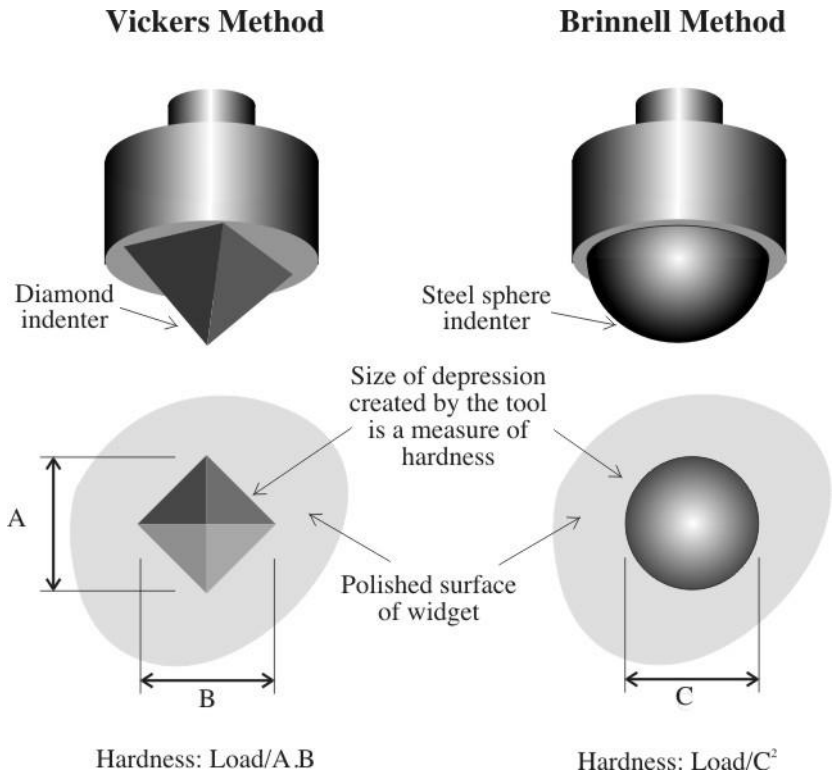

Figure 2-23: Schematic images of the Vickers and Brinell type methods of hardness indentation technique [115]

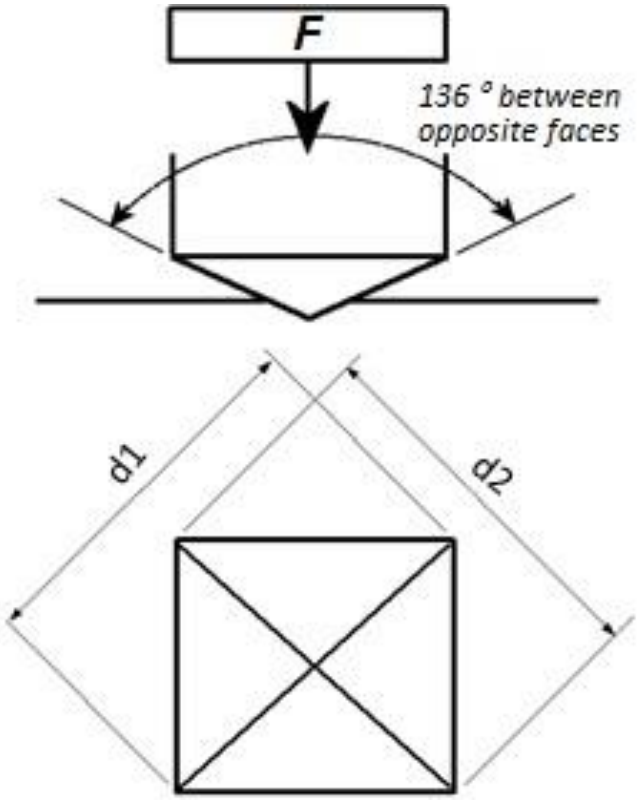

Figure 2-24: Schematic image of a Vickers hardness indentation depicting the diagonal measurements required from the indent to quantify a Vickers hardness value [116]

$$Vickers\ Hardness\ (HV) = \frac{2Fsin\left(\frac{136°}{2}\right)}{d^2} \quad \textbf{Eq. 2-4}$$

Where *F* is the load (in kg) and *d* is the arithmetic mean of the two diagonal indent lines, *d1* and *d2* (in mm).

The microstructural changes associated with thermal aging or creep has a different effect for different materials. A study performed on Grade 91 steel showed the relationship of Vickers hardness and creep life fraction to have a linear decrease between 20 – 90 % of the creep life followed by a sudden drop at rupture (Figure 2-25).

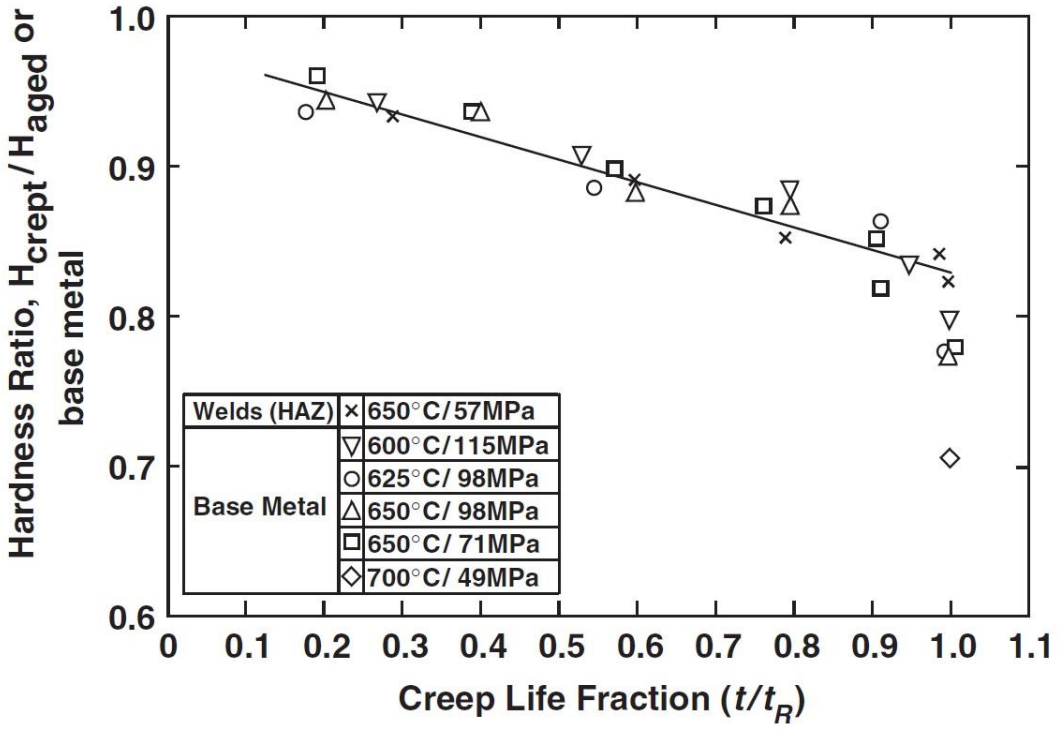

Figure 2-25: Variation of hardness ratio as a function of normalised creep life on several samples of modified 9Cr-1Mo steel tested at various conditions [117]

The observations show a strong correlation between the two features, questioning a stronger case for using hardness testing as a main NDE technique for analysing creep in components. However, like other techniques, portable hardness testing does have its drawbacks. On many occasions the physical limitations of using a portable hardness tester due to the environmental surroundings within a boiler make it impossible to survey some components. Depending on the type of portable hardness tester (Pin Brinell, Equotip etc.) it may be impractical to obtain data. For example, the Equotip tester works on Shore Schleroscope which is a type of indenter rebound technique requiring gravity to assist in the operation of obtaining the indent. Therefore depending on the orientation of components, the gravity dependent technique may not be possible. Therefore it requires a skilled practitioner who has the understanding of such operating procedures to undertake this testing [19].

Surface preparation is another consideration as portable hardness testing is very sensitive to surface condition and thus unrepresentative material like paints and corrosion must be removed before operation. The presence of unknown unrepresentative surfaces such as oxides and soft decarburised layers can produce misleading results. Surface smoothness and flatness is another cause for concern as portable hardness testers are generally low load techniques and the lower the load, the smoother the surface finish must be (almost mirror-like) [19]. The technique is highly sensitive to any variations in the surface condition and the microstructure, resulting in poor reproducibility and large scatter in the data questioning the reliability of the results [107]. For these reasons the technique is considered more of a complementary technique within the field of NDT, but does offer significant value if performed with accuracy.

2.5.2.4. Ultrasound Techniques

Metal fracture due to creep is the process of initiation and growth of microscopic pores and merging of micro-cracks to form macroscopic cracks. A macroscopic crack will eventually propagate and initiate fracture leading to failure of the stressed component. For thermal power generation components it would be preferable to detect microscopic pores, from which micro cracks are generated. Dimensions of creep micro pores are 1 – 4 µm which is beyond the detectable resolution of magnetic particle inspection (MPI), acoustic emissions (AE) and eddy current NDE techniques [110], these will be discussed later. This is where ultrasonic methods have a role within power generation as a NDE technique. Ultrasonic techniques (UT) can be used to determine differences in material structure and physical properties by monitoring the changes in ultrasonic waves. An ultrasonic wave is a high frequency sound wave at frequencies typically greater than 18 kHz (inaudible to humans). These waves can be analysed to study changes in a material's physical dimensions, composition, microstructure and elastic

properties by relating them to changes in the wave's features such as velocity and attenuation. UT testing is a common NDE method employed by industry as it has shown to accurately locate and size defects, achieve a high degree of penetration into the material and has little health or environmental risks [118].

The most common and simplest form of UT testing is the pulse-echo method. Here an ultrasonic transducer (or search unit), coupled with the subject material by surface contact or immersion in a fluid, produces short bursts of high frequency vibrations (sound waves). By exciting a piezoelectric crystal using high-voltage electrical pulses, ultrasonic waves are transmitted into the material to be inspected (Figure 2-26).

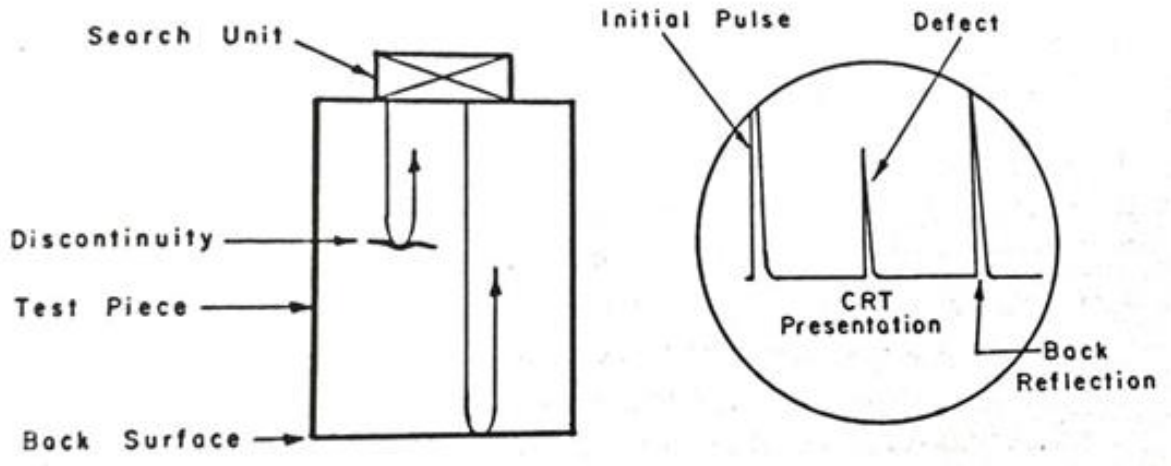

Figure 2-26: Schematic representation of the ultrasonic non-destructive technique depicting the pulse-echo method [119]

The transmitted sound waves will be reflected from a known back surface, usually the edge of the component representing the total distance travelled by the sound wave. If a flaw or discontinuity is present within the material, then some or all of the sound wave will be reflected back before the expected total distance travelled is achieved. The reflected energy arrives back into the search unit where it is converted back into electrical pulses and displayed on an oscilloscope or cathode-ray tube (CRT) monitor. The amplitude of the electrical pulse will relate to characteristics defining the flaw. The

time taken for the wave to arrive back at the search unit after reflection from the flaw is proportional to the distance of the flaw to the contact surface. The ability for UT testing to detect and determine flaw presence, location, size, shape as well as being able to measure wall thicknesses of pipes and vessels has been well documented [118, 119].

Some lab based research has used the fluctuation of ultrasonic wave velocities to investigate and determine microstructure phases in heat treated steels. Wave velocities were found to decrease with phase hardness with highest velocities measured in soft phase pearlite-ferrite and slowest in the hard martensite phases [120, 121]. However, Sposito et al (2010) [107] write in their review of NDE techniques that, the results so far for using UT testing for the early detection of creep damage, have been mixed. This is due the pulse-echo method which by nature examines bulk material giving a result which will average over the entire depth of inspection, rather than highlighting dangerous localised creep. The review goes on to mention that although the sensitivity and reproducibility of ultrasonic testing is improving, the feasibility of the technique at typical power plant operating temperatures is still the subject of research and therefore existing published test data is all based on room temperature experiments. This is most likely due to a limitation of ultrasonics where coupling between the transducer and materials is required; either by contact to surface, or immersion in a fluid such as water, thus restricting its use for in-service high temperature application. In the case of boiler components, insulation layers will need to be removed (and later reinstalled) to attain surface contact adding to the plant-down time. Furthermore the surface condition will strongly affect the results as oxide scale, corrosion and non-flat geometries will interfere with the UT waves [103]. The piezoelectric type transducers also suffer when exposed to high temperature materials (above 327 °C) and do not normally function [122]. These doubts justify the statement made by Artamonov and Artamonov (2002) [110] that “although ultrasonics can detect the small micro pores (1 – 4 μm) in principle,

it has not been recommended by official documents" and rather suggests the use of metallographic techniques for NDE of power generation components as the primary method(s). Thus the method has not been established to characterise material microstructure.

2.5.2.5. Acoustic Techniques

Acoustic emission (AE) technique is a unique NDE method which functions by detecting micro-seismic activity (sound signals) from within a material. Any material subjected to an external load (mechanical or thermal) will generate an AE which can be caused by local disturbances such as micro-cracking, dislocation movement, irregular friction etc. AE is generally used in the application of monitoring crack propagation. As a micro crack generates, the mechanical stress from deformation in the material causes relief waves (high frequency sounds) to be released in various directions. These relief waves are then detected by placing several sensors around the crack, monitoring the time of arrival, frequency of the AE and the amplitude of the event. With this information the nature of micro-cracks can be quantified [103]. The number of detected pulses usually indicates the number of newly formed micro cracks and their size is estimated on the AE amplitudes.

In context to power plant inspection, AE has been investigated as a technique to monitor crack growth in boiler header components, particularly at stub-to-header weld joints (Figure 2-27) [123].

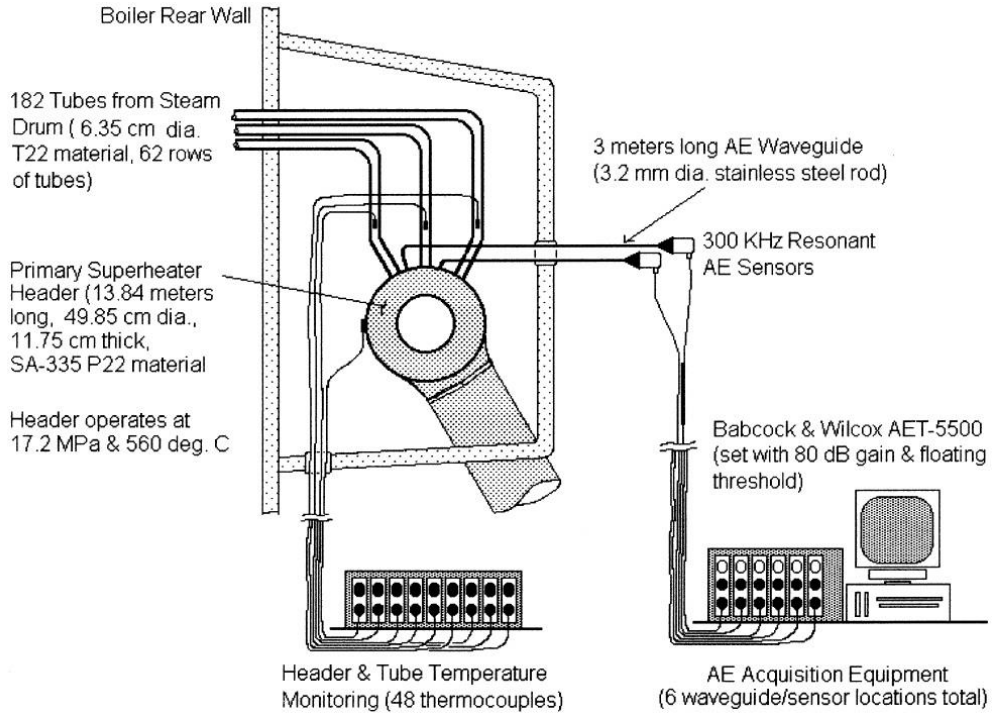

Figure 2-27: Schematic diagram of the AE and thermocouple monitoring setup at Pacific Gas & Electric's Power Plant (Unit 6) in Pittsburgh, California [123]

Results showed that AE activity was related to header/tube temperature changes. As plant operating conditions fluctuated, so did the propagation of the micro-crack and hence associated acoustic emissions were generated. This can be seen in (Figure 2-28) where plant load was cycled over a given period (2 days), resulting in the highest AE rate being correlated with the greatest temperature changes. Other experiences of AE within power plant industry is for similar use in detecting slow crack growth rates, intergranular stress corrosion cracking and leaks in boiler tubes and steam lines [124-126].

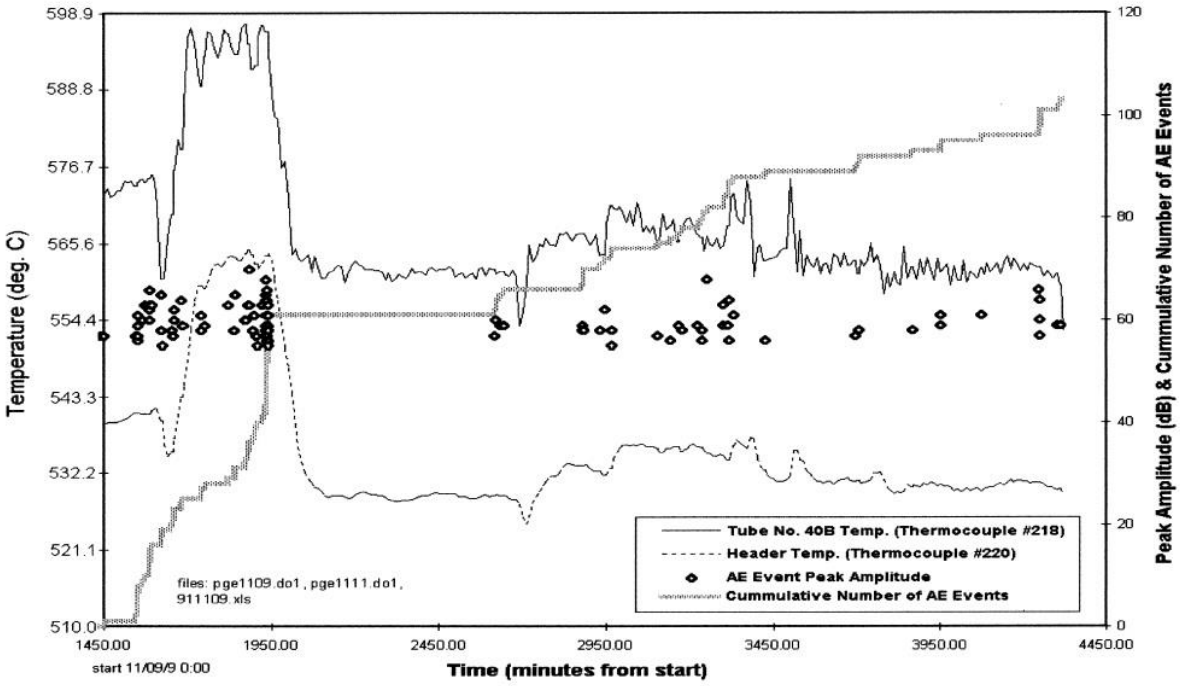

Figure 2-28: Variation of AE activity with respect to plant load change [123]

In more recent studies AE has shown to be able to evaluate hydrogen embrittlement and early stage methane void formation before these voids connect with one another and form micro-fissures [127, 128]. However the technique is complex and as such requires very experienced and skilled operators to be able to measure and interpret acoustic emissions with accuracy. Pulse/signal oscillations arrive at the sensor head at unpredictable times carrying complex waveforms and amplitudes which vary. Background noise from high pressure steam can cause difficulties when interpreting data and so careful surveillance is required when monitoring material with AE technique [124]. The piezoelectric material in the AE transducers suffers in functionality at high temperatures (500 °C and above) and so becomes impractical for high temperature in-situ condition monitoring, although research is being performed to make high temperature AE sensors using advanced ceramics [129]. Similar to UT, AE techniques is not an established method for characterising microstructure.

2.5.2.6. Magnetic Flux Leakage

Magnetic flux leakage (MFL) is predominantly a magnetic NDE method whereby under the application of a magnetic field, any changes to the magnetic flux in the region of interest can be observed. The method works by inducing a magnetic field into the component, which can be generated either by electrical means (AC/DC) or by the use of a permanent magnetic. The distribution of the magnetic flux lines, resulting from the induced magnetic field, is determined by the values of magnetic permeability within the area of interest. The presence of surface or subsurface discontinuities, such as cracks or voids, will cause a sudden change in the permeability of the magnetised material and affect the distribution of the induced magnetic flux lines. The fluctuation in the magnetic flux lines can then be detected through the use of sensing coils or probes (Figure 2-29 and Figure 2-30) [130].

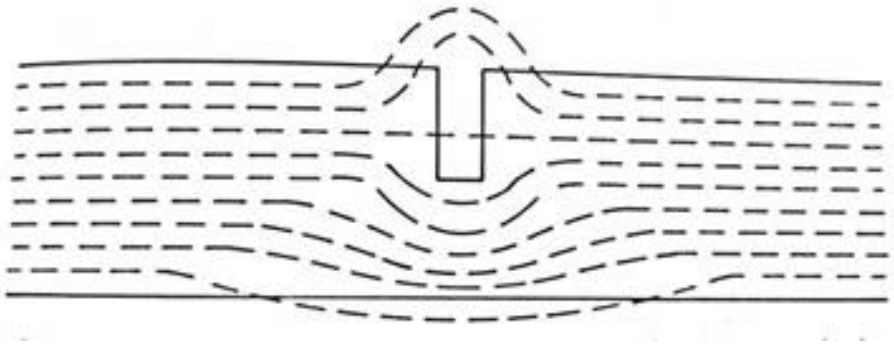

Figure 2-29: Schematic diagram to show magnetic flux leakage at a slot (representing a discontinuity) cut into a magnetised ferromagnetic bar. The dashed lines indicate the magnetic flux lines and diverted (leaked) flux lines can be detected by sensing coils [131]

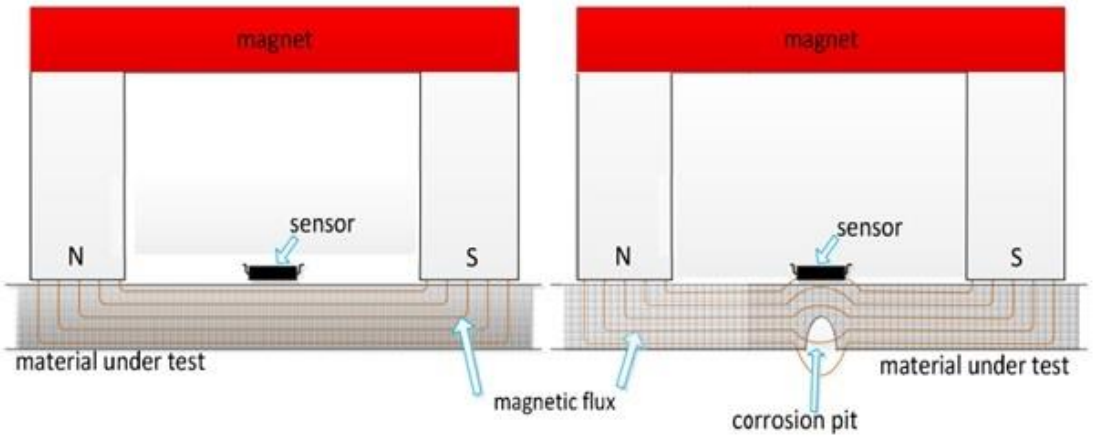

Figure 2-30: Schematic image showing the principle of MFL for detecting wall material loss due to corrosion [130]

9Cr-1Mo power plant tubes have been successfully inspected using MFL technique and show the technology was able to detect notches (discontinuities) on the external tube surface by sending giant magneto-resistive (GMR) sensors through the internal bore of the tube. Figure 2-31 shows the results from the MFL test was clearly able to highlight the location of the notches in the external tube surface. It was also able to correlate the signal to the size of the notch, where the GMR sensor output voltage increased with notch depth [132].

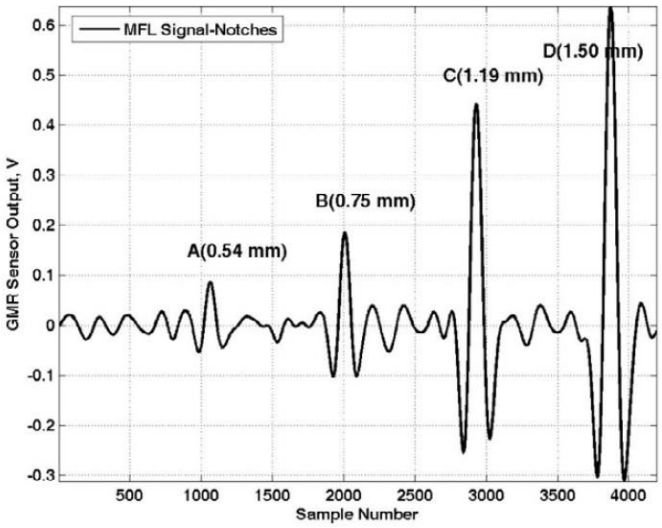

Figure 2-31: Magnetic flux leakage results for outside diameter circumferential notches of depths (A) 0.54 mm, (B) 0.75 mm, (C) 1.19 mm and (D) 1.50 mm [132]

2.5.2.7. Magnetic Particle Inspection

Magnetic particle inspection (MPI) is the most widely used flux leakage technique. It employs the use of fine magnetic particles to be attracted to the flux leakage path to identify the location of discontinuities and defects; instead of magnetic probes or sensing coils as used in MFL. The particles can either be powdered iron fillings dusted onto the surface (dry method) or the more commonly used magnetic iron oxide (Fe_3O_4) suspended in a low viscous liquid such as paraffin to form an ink (wet method). Particles will line up in the direction of the magnetic flux and accumulate at the site of leakage and form a reliable visual indication of the discontinuity [119, 131]. MPI is predominantly used to analyse any defects or discontinuities at welded regions. The conventional method for MPI testing boiler components is through the use of an alternating current (AC) 110V yoke to magnetise the region of interest and then spraying a ferromagnetic ink (iron oxide filings in kerosene) [133].

Blitz (1997) [131] states one of the disadvantages of the flux leakage based techniques is that it is necessary for a sizeable amount of the applied field to cut any discontinuity

perpendicular to the direction of the flux flow, otherwise the amount of flux divergence is too small to be observed. It has also been described as a “messy” technique due to the use of magnetic ink which can require rigorous cleaning after inspection. Cartz (1995) [134] also describes one of the technique’s limitations is the surface preparation required. Surfaces must be sufficiently clean of dust and grease so that the magnetic powder particles can move freely over the surface of the component and concentrate in regions where leakage fields exist; the technique is limited to ferromagnetic materials [107]. This technique is useful for highlighting the presence of surface breaking defects, but is not able to allude to the condition of the microstructure.

2.5.3. Electromagnetic Techniques

Electromagnetic (EM) methods of non-destructive testing have attracted the attention of many researchers [107]. EM techniques operate by detecting changes in the material’s magnetic permeability and electrical conductivity/resistivity and correlating them to the mechanical properties of a material. It has been shown that microstructural changes induced by thermal and mechanical processes affect the electrical and magnetic properties of steels [135, 136]. This relationship has been used to evaluate the condition of steels subjected to various metallurgical phenomena such as; microstructural changes [23, 137-139], decarburisation [140, 141] and creep damage [142-144].

2.5.3.1. Electromagnetic Theory

The movement of electrically charged particles, such as the flow of current in a conductor will cause the generation of an externally applied magnetic field (B_0) measured in Tesla. Magnetic materials themselves also generate an internal magnetic field due to the orbital motions and spins of electrons. The strength of magnetic fields (whether generated internally by a magnetic material or externally by the flow of current

through a coil) is denoted as (*H*) and is measured in amps per metre (Am^{-1}). Both (B_0) and (*H)* in free space or paramagnetic materials are related by the permeability of free space (μ_0), measured in Henries per metre (Hm^{-1}) (Eq. 2-5). However in the case of ferromagnetic materials, the magnetisation within the materials must be considered.

$$B_0 = \mu_0 H \qquad \textbf{Eq. 2-5}$$

The magnitude and direction of a magnetic field can be expressed as lines of force as depicted in Figure 2-32.

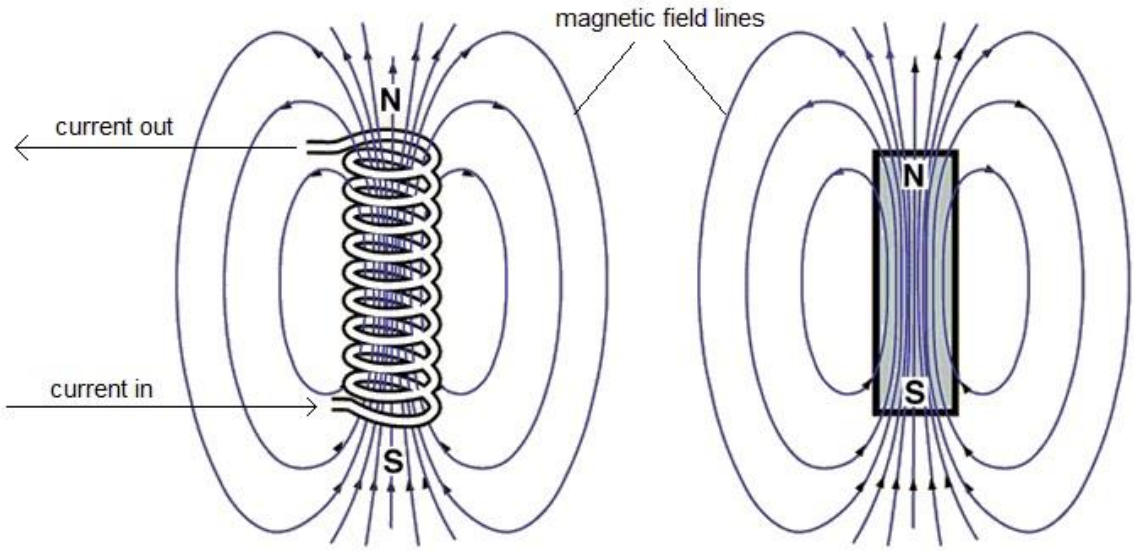

Figure 2-32: Schematic diagram showing magnetic flux lines being generated by a current through a coil (left) and a permanent bar magnet (right). Adapted from [145]

If the externally applied magnetic field is generated by means of current flowing through a cylindrical coil (also known as a solenoid) then the relationship between the magnetic field strength and the coil can be expressed as follows:

$$H = \frac{NI}{l} \qquad \textbf{Eq. 2-6}$$

Where *H* is the magnetic field strength (Am^{-1}), *N* is the number of turns per unit length in the cylindrical coil; I is the magnitude of the current through the coil and l is the length of the coil.

When a magnetic field has been generated within a material by a current, in accordance with Ampère's law, the response of the material is its magnetic induction (*B*), also referred to as magnetic flux density or the total magnetic field. There are two contributing factors to a materials magnetic induction, which is the applied magnetic field (*H*) and the material's magnetization (*M**).

The magnetization of a material can be expressed in terms of the density of net magnetic dipole moments (*m*) per unit volume of material (*V*).

$$M^* = \frac{m}{V} \qquad \textbf{Eq. 2-7}$$

Magnetic induction in the material (*B*) can be given by;

$$B = B_0 + \mu_0 M^* \qquad \textbf{Eq. 2-8}$$

Combining Eq. 2-5 and Eq. 2-8 then the total magnetic field or magnetic induction (*B*) can be written in the equivalent form;

$$B = \mu_0 (H + M^*) \qquad \textbf{Eq. 2-9}$$

2.5.3.2. Relative Permeability

The relative permeability (μ_r), is a dimensionless value of a material representing the measure of ease with which a material can be magnetised in the presence of an externally applied magnetic field [77]. It does this by indicating how it changes the magnetic induction inside a material compared with the induction that would be observed in free space [146]. The magnetic induction (*B*) within a material is related to an applied field (*H*) by:

$$B = \mu_0 \mu_r H$$ **Eq. 2-10**

It should be noted that μ_r can only be treated approximately as a constant for a small applied field and varies with *H* in a larger applied field in ferromagnetic materials.

The relationship of relative permeability, magnetization and magnetic field strength can be seen in Eq. 2-11 (manipulated from Jiles (1991) [146]), which shows that the relative permeability is proportional to the magnetization.

$$M^* = (\mu_r - 1)H$$ **Eq. 2-11**

Combining Eq. 2-6 with Eq. 2-11 we can observe the impact of relative permeability on the magnetization if the magnetic field strength (*H*) was produced using a solenoid (Eq. 2-12).

$$M^* = (\mu_r - 1)\frac{NI}{l}$$ **Eq. 2-12**

Therefore the total magnetic field or magnetic induction (*B*) can be expressed as:

$$B = \frac{\mu_0 \mu_r NI}{l}$$ **Eq. 2-13**

A magnetic flux (ϕ) is caused by the presence of a magnetic field and is measured in Webers (Wb) or volt-seconds in derived units. It can be considered as a measurement of how much magnetic field passes through an area, for example the cross sectional area of a coil carrying current to generate a magnetic field. In this case, for the magnetic flux through a coil (solenoid), the angle between the magnetic flux density (*B*) and the surface of the coil relates the magnetic flux (ϕ) to the magnetic flux density (*B*) as shown in Eq. 2-14.

$$\varphi = BA\cos\theta$$ **Eq. 2-14**

Where ϕ is the magnetic flux, B is the magnetic flux density or magnetic induction, (A) is the area through which the magnetic flux ϕ is being considered and θ is the angle between the direction of the magnetic field lines (generated by the coil) and the direction of the area vector through which the magnetic field lines are traveling; the direction of the area vector is always perpendicular to the cross-sectional face of the coil created by the loops of wire. In this instance, since the magnetic flux travels parallel through the coil, similar to how the magnetic flux flows through the coil shown in Figure 2-32, then $\theta = 0$ and so the magnetic flux can be calculated as:

$$\varphi = BA \qquad \textbf{Eq. 2-15}$$

2.5.3.3. Electromagnetic Inductance

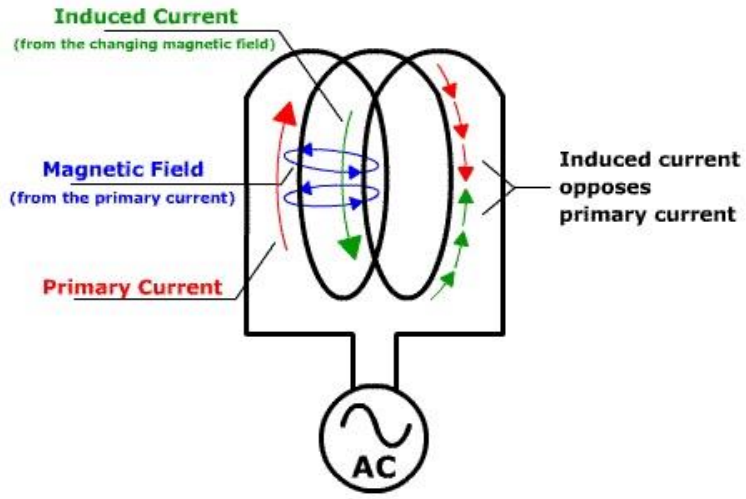

Figure 2-33: Schematic diagram showing a self-induced current (green) created by an alternating magnetic field (blue) driven by a primary AC current (red) [147]

If a solenoid with a coil (coil 1) with N_1 turns is driven with an AC current, then an alternating magnetic field will be produced. The changing magnetic field induces an electromotive force (emf, measured in volts) in the coil in a direction opposite to the applied voltage as shown in Figure 2-33, This effect is called the self-induction (L*),

measured in Henries, and the solenoid can be thought of as an inductor and the inductance therefore being a property of the inductor. *L** can be expressed as:

$$L^*_1 = \frac{N_1 \varphi_1}{I_1} \qquad \textbf{Eq. 2-16}$$

Where *L** is the self-inductance (in WbA^{-1} or Henries), N_1 is the number of turns in the excitation coil (coil 1), ϕ is the magnetic flux (in Wb) and I_1 is the current through the excitation coil (in Amps).

When another coil (coil 2) is nearby to the original coil (coil 1), then when the AC current is driven through coil 1 creating a changing magnetic flux, the changing magnetic flux intersecting coil 2 will induce an emf within coil 2; as a result, an induced electric current will exist within coil 2. Mutual inductance is a measure of how large a change in the current of coil 1 is needed to induce a given change in the voltage in coil 2. For example, in the case of an EM sensor, the soft ferrite U-shaped core has two wires looped around it to produce a ferrite-cored solenoid with two coils (Figure 2-34). The blue wire coil (excitation coil) has an applied voltage to drive an AC current through it generating a changing magnetic field (green dotted lines) through the solenoid giving rise to a changing magnetic flux causing a self-induced current within the excitation coil. As the changing magnetic flux travels through the ferrite core to the red wire coil (sensing coil), by Faraday's law, an emf will be induced inside the red wire of the sensing coil. This is then the mutual inductance (*L*) of the solenoid (inductor), the value of which is the same in both the excitation and sensing coils and given in Eq. 2-17.

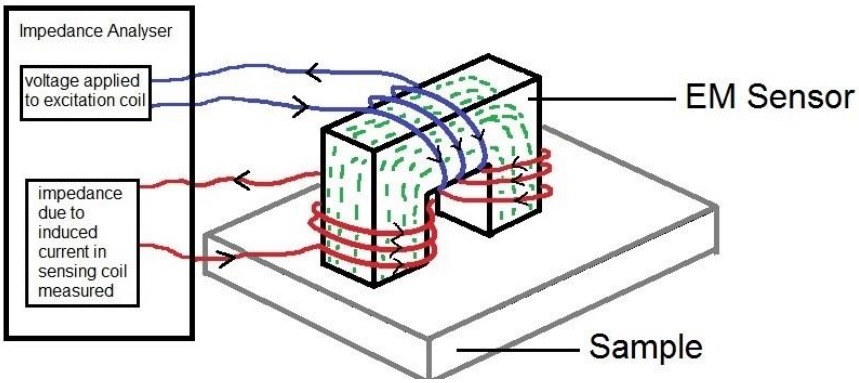

Figure 2-34: Schematic diagram showing how the EM sensor behaves like a solenoid with the presence of two coils; excitation coil (blue loops) and sensing coil (red loops) and a magnetic field (green)

$$L = \frac{N_2\varphi_2}{I_1} = \frac{N_1\varphi_1}{I_2} \qquad \textbf{Eq. 2-17}$$

Where *L* is the mutual inductance in the solenoid/inductor/EM sensor (measured in WbA^{-1} or Henries), N_2 is the number of turns in coil 2 (sensing coil), ϕ_2 is the magnetic flux (in Wb) in coil 2 and I_1 is the current (in A) in coil 1. The induced emf within the sensing coil will generate an induced voltage and it is the impedance to this induced voltage within the sensing coil which is measured by the impedance analyser. When a sensor such as the one shown in Figure 2-34 is in the presence of different materials which have different magnetic properties e.g. relative permeability and conductivity, these materials will cause a change in the sensor's inductance; and it is this change which allows for different materials to be characterised.

2.5.3.4. Magnetic Domains

A magnetic domain is a small volume region in which all magnetic moments are mutually aligned in the same magnetic direction to create areas of strong magnetisation (Figure 2-35a). Any ferromagnetic material (below the Curie temperature) will be composed of such magnetic domains [148]. Domains usually exist on the microscopic scale for polycrystalline materials; each grain can have multiple

magnetic domains with different orientations of magnetisation. Magnetic domains are separated by domain walls, across which a gradual change in the magnetic orientation occurs, usually by either 90 or 180 degrees [148] (shown schematically in Figure 2-35b).

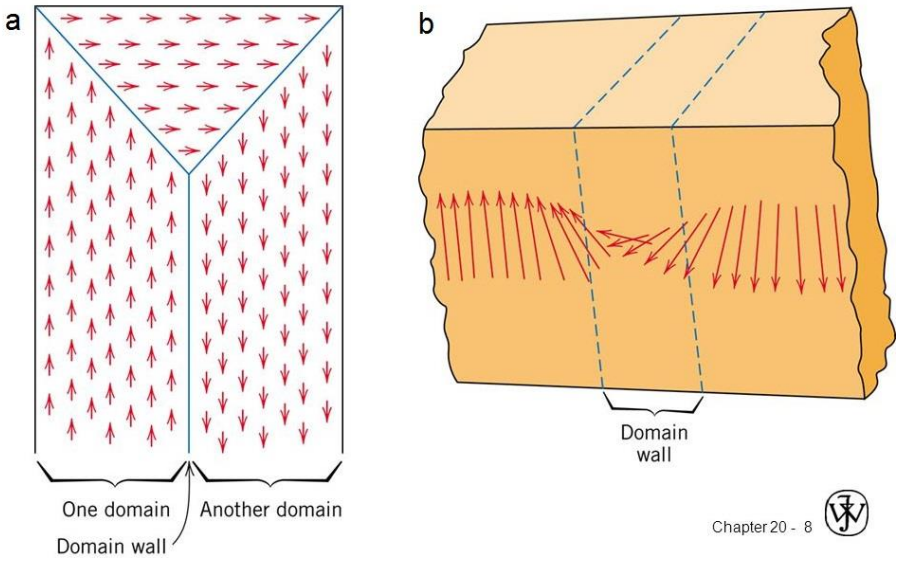

Figure 2-35: (a) Schematic illustration of domains in a ferromagnetic material; arrows reflect the magnetic dipoles. (b) The gradual change of magnetic dipole direction through a block domain wall by 180 degrees [77]

The origin of domains can be understood by considering the structures shown in Figure 2-36, each representing a ferromagnetic single crystal. A single domain configuration (Figure 2-36a) leads to formation of free magnetic poles at the surface and associate with them a significant magnetic energy. Magnetic domains form to reduce this magnetostatic energy within the material (Figure 2-36b); increasing divisions of domains further reduces the demagnetising energy (Figure 2-36c and Figure 2-36d) [149, 150].

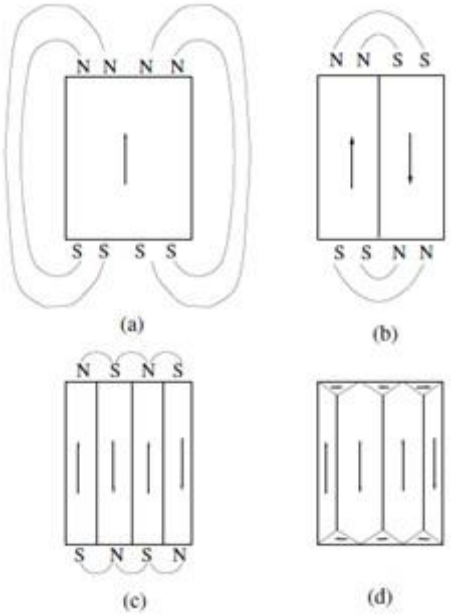

Figure 2-36: Formation of magnetic domains.
(a) a saturated sample, with high demagnetising energy; (b) splitting into two domains reduces the demagnetising energy; (c) subdivision of domains further reduces demagnetising energy; (d) free poles at surfaces are eliminate by closure domains [149]

When a ferromagnetic material is exposed to an applied field, the magnetic domains dynamically react through domain wall motion and domain rotation. At low fields, magnetic domains which are aligned favourably with respect to the applied field will grow and consequently cause a reduction in size of those magnetic domains which are aligned in opposing directions (Figure 2-37). At moderate field strengths, domains will rotate in which the magnetic moments rotate from their original direction and align themselves into a crystallographic ‘easy axes’ direction, nearest to the alignment of the applied field. As the magnitude of the applied field is increased, the domains will coherently rotate to align exactly with the direction of the applied field resulting in a single domain sample [146]. For relatively low magnetic fields, domain wall motion can be considered reversible; meaning that upon application and removal of an applied field, domain walls will move and then return to their original positions [27]. There are many microstructural features that can impede the movement of domain walls with

differing levels of impediment such as; grain boundaries, precipitates and dislocations [151, 152].

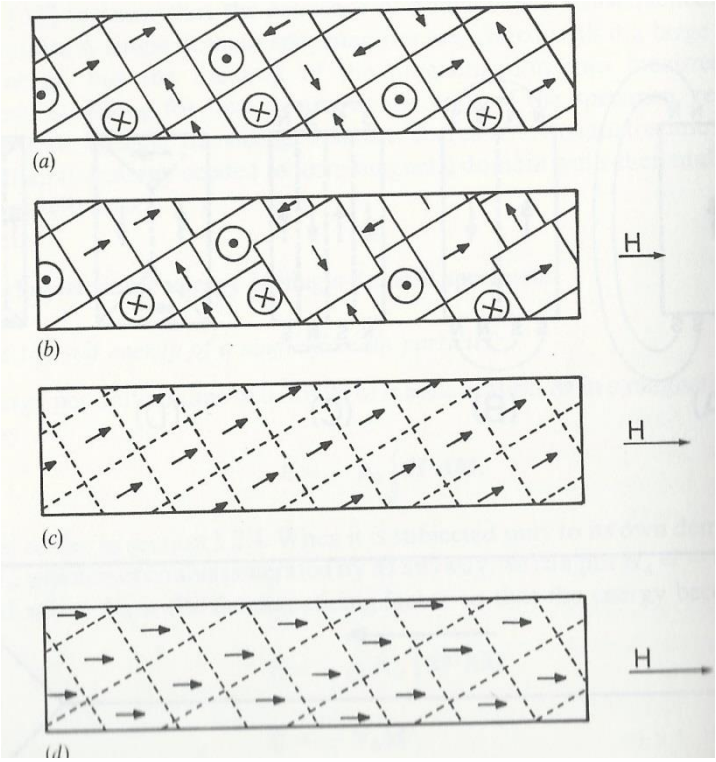

Figure 2-37: Schematic diagram depicting the dynamics of magnetic domain movements. (a) Domains in the unmagnetised state showing random orientation of dipoles. (b) A weak magnetic field (H) is applied leading to domains growing and shrinking depending on direction of dipoles with respect to the applied field. (c) A moderate magnetic field rotates domains to align with their easy axis. (d) A stronger magnetic field causes coherent rotation of domains to align themselves with the direction of the applied field [146]

2.5.3.5. Magnetic Barkhausen Noise

When a ferromagnetic material is subject to a continuously changing magnetic field (*H*), the magnetic domains will begin to rotate and move according to the direction of the applied field. This magnetic domain behaviour causes discontinuous changes in the magnetic flux density (*B*) within the material and can be seen on a magnified magnetisation curve (Figure 2-38). The discontinuous changes are caused by magnetic

domains being pinned and released by microstructural impediments such as precipitates, grain boundaries and dislocations [148, 153].

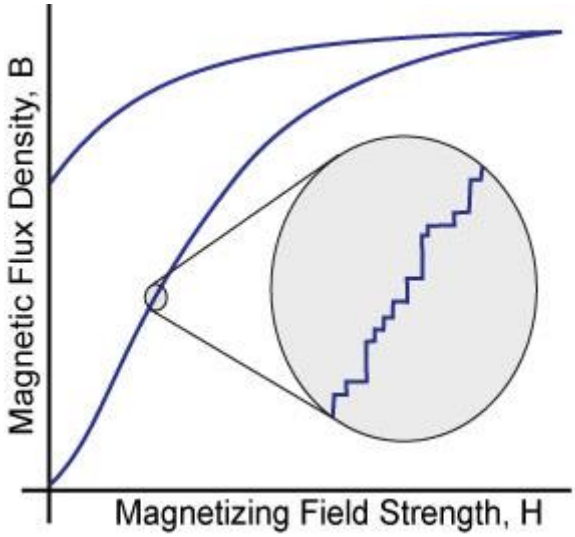

Figure 2-38: Enlargement of the magnetisation curve to show the Barkhausen effect of discontinuous jumps along the initial magnetisation curve [154]

Magnetic Barkhausen noise (MBN), or sometimes known as magnetic Barkhausen emissions (MBE), refers to the noise like voltage impulses produced by each abrupt change in flux density (*B*) due to discontinuous domain movement. MBN is also affected by stress as well as microstructural features and hence has become a valuable materials evaluation tool [146, 155-158], and proven to be a useful technique in providing microstructural information for power plant materials. Das et al (2004) [138] have shown a good correlation between the MBN parameters and microstructural changes. The lamellar carbides (M_3C) within a virgin 1.25Cr-0.5Mo steel spheriodised during initial ageing at temperatures of 500 °C and 550 °C for 100h. This breakdown of carbides increased the number density of pinning sites restricting domain wall movement and resulted in a reduction in the MBN. Ageing for a longer time period or at a higher temperature (600/650 °C) leads some of the spheriodised carbides to combine, causing a change in their composition and morphology and also they begin to

segregate slowly to grain boundaries. This has an inverse pinning effect, reducing the number density of domain wall pinning sites leading to bigger domain wall jumps and hence an increase in the amplitude of MBN signal (Figure 2-39).

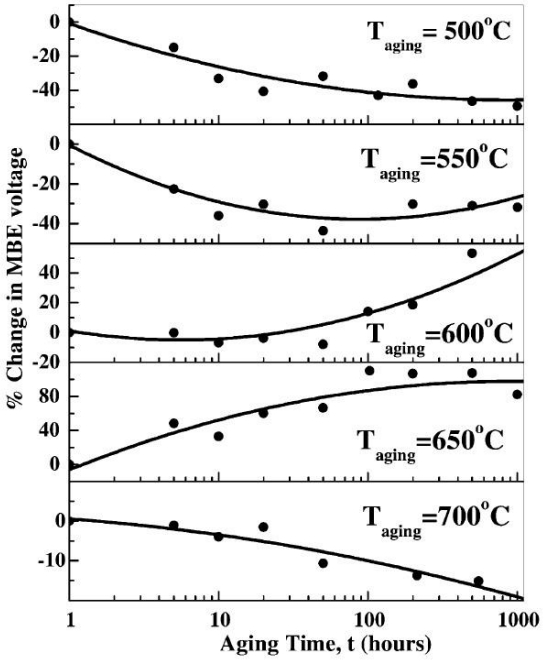

Figure 2-39: Variation of RMS voltage of the MBE signals with ageing time and temperature, adapted from Das et [138]

Moorthy et al (1997) [159] have shown the technique to be useful for distinguishing different microstructures within the heat affected zone (HAZ) in Cr-Mo steel welds. Similarly Kumar et al (2010) [58] have correlated variations in MBN with material experiencing the different regimes of creep and also the effect of tempering temperature. In both cases, microstructural phenomena such as the precipitation and transformation of carbides, heat treatments which cause material to soften or become hard and material deformation affect the manner to which magnetic domain walls are pinned and released which is detectable using MBN. However, these tests were performed in laboratory conditions on small samples. When applying this technique to large power plant components Sposito et al (2010) [107] discuss the impracticalities of

the technique. MBN is limited to only 0.3 mm from the surface of the component because signals from deeper within the sample are significantly attenuated by eddy current shielding. The MBN signal is also strongly affected by the presence of an oxide layer and further by any residual stresses introduced into the surface in an attempt to grind away surface oxidation [107].

MBN was tested to find out whether it would be a valuable technique for non-destructively characterising the depth of decarburisation for a high carbon content spring steel [95]. In some cases, samples were acid pickled or sand blasted to remove surface oxide scales. Results showed a rapid increase in the root mean squared (RMS) voltage value of the Barkhausen signal within the pure ferrite region (up to 100 µm) (Figure 2-40). This then slowly decreases as the pearlite region becomes more prominent over a thicker section (above 200 µm). There was also a distinguishable difference of employing sand blasting to remove the surface oxide compared with no treatment. The sand blasted sample, similar to the no treated sample saw an increase in the MBN signal initially within the 100 µm ferrite region, but then saturated making it unclear to detect the depth at which pearlite is introduced into the decarburised layer.

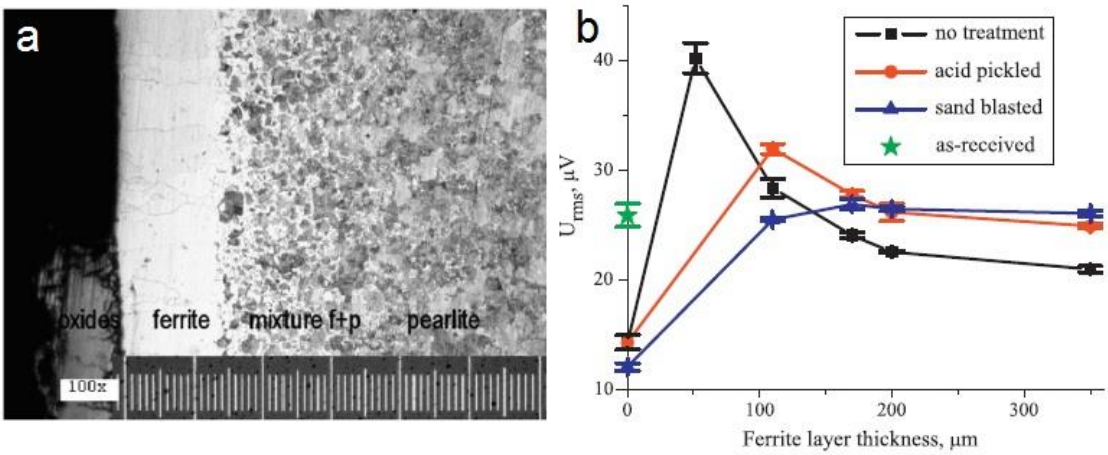

Figure 2-40: (a) Metallographic cross-section of the sample annealed at 4h showing depth of decarburisation, scale division is 100 µm. (b) Variation of RMS value of MBN voltage with ferrite layer thickness [95]

There is a lot of literature where researchers have investigated the ability to characterise microstructural features in steels using MBN [160-164]. Although a promising electromagnetic technique for non-destructive characterisation of microstructural features, it has not been used on operating plant in-situ at temperature or even during maintenance outages due to its credibility with linking the signal to a specific cause, and its sensitivity to surface preparation [107, 165].

More recently Wilson et al (2014) have measured the magnetic Barkhausen properties of thermally treated power plant steels taken from service having been operating at approximately 520 °C for 11 years [137]. P9 (8.4Cr-0.9Mo) and T22 (2.14Cr-1.01Mo) steels were taken from service (TFS) and then normalised and heat treated as per ASTM standards A335 [15] and A213 [65], to obtain three distinct microstructures; normalised (NORM), tempered (TEMP) and the original condition as TFS. MBN peak positions were shown to be indicative of mechanical hardness values (Figure 2-41 and Table 2-5). For P9 material, the softest sample (P9-TFS) peaked at the lowest *H* field and the hardest (P9-NORM) peaked at the highest *H* field. Harder martensitic materials will exhibit broader peaks at higher *H* field values as the domain walls overcome pinning from high density martensitic lath boundaries and dislocation networks. A tempered martensite (P9-TEMP) will develop a less strained microstructure with coarser laths and precipitates yielding higher amplitude peaks at lower *H* field complementing the findings of Saquet et al [163]. The high temperature service exposure leads to a softer microstructure and hence a shift to a lower *H* field peak for sample P9-TFS. The T22 samples did not correlate with hardness in the same manner as the P9 samples. It was noticed that T22-TEMP sample produced two peaks with the major peak peaking at a lower *H* field than the softer (service exposed) T22-TFS and the second peak (labelled Peak 2 on Figure 2-41) peaking at a higher *H* field than T22-TFS. This was interpreted by Wilson et al as domain walls overcoming pinning due to

lath boundaries at the lower *H* field peak and carbide precipitates at the higher *H* field (Peak 2).

Table 2-5: Coercivity and mechanical hardness data for power plant steels exposed to different thermal conditions [137]

	P9-TFS	*P9-TEMP*	*P9-NORM*	*T22-TFS*	*T22-TEMP*	*T22-NORM*
HV	158	212	401	129	203	316
MBN_{PK} (mV_{rms})	0.43	0.70	3.43	0.59	0.66	1.87
H_C (*kA/m*)	0.43	0.70	3.43	0.59	0.66	1.87

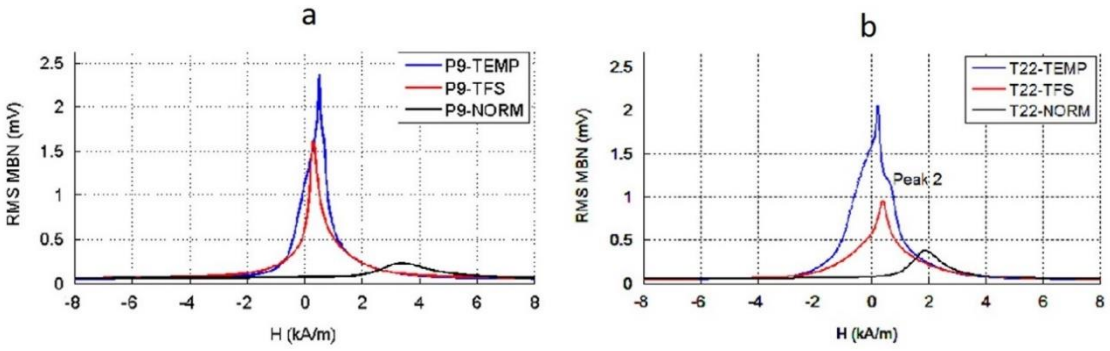

Figure 2-41: MBN profiles for samples in three different thermally exposed conditions for materials (a) P9 and (b) T22 [137]

Mohapatra et al (2007) [144] was able to correlate the RMS voltage of the MBE with the different stages of creep for a bainitic power plant material (5Cr-0.5Mo), concluding the technique to be a suitable one for detecting creep damage non-destructively (Figure 2-42a). During the primary stage of creep, carbide precipitates are forming acting as pinning sites for domain walls, restricting their movement and hence a decrease in the RMS voltage of the Barkhausen signal was observed. As well as the carbide precipitation, the presence of dislocations and grain boundaries combined contribute to the magnetic hardening which causes the retardation of RMS voltage value. In the secondary creep regime, at the high temperatures, carbides are

coarsening at the expense of smaller ones, reducing the carbide density and increasing the inter-carbide spacing leading to a decrease in effective domain pinning sites. Magnetic softening (term given by the author [144] to indicate a reduction of domain wall pinning sites) was clearly distinguishable by the MBN, as an increase in the RMS voltage of the MBE was observed. Further into the tertiary stage of creep, the RMS voltage of the MBE began to reduce as the accumulation of brittle coarse carbides and dislocations at the grain boundary cause the formation of microcracks. A similar trend between the RMS voltage of the MBE signal and the expended creep life was observed by Mitra et al (2007) [143] (Figure 2-42b) for P91 power plant material (9Cr-1Mo).

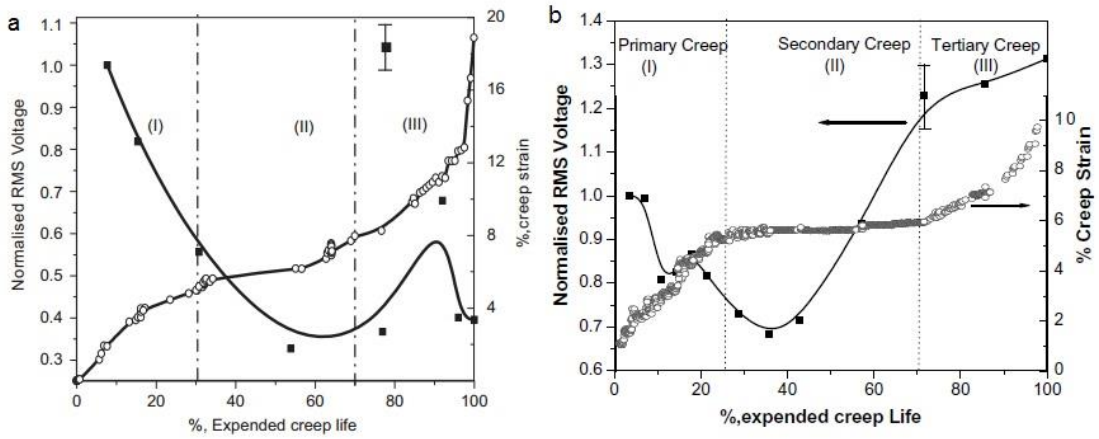

Figure 2-42: Variation of normalised RMS voltage of the MBE with expended creep life in (a) 5Cr-0.5Mo steel [144] and (b) 9Cr-1Mo steel [143]

Similar to other defects, dislocations will interact with domain walls and have an influence on the magnetic properties of a material. A single dislocation is very small in comparison to the domain wall thickness and so will have an insignificant impact on the magnetic properties. However, if a number of dislocations amalgamate, tangling with one another, increasing the dislocation density, then domain walls will face much larger barriers to motion and the magnetic properties will be affected [166-168].

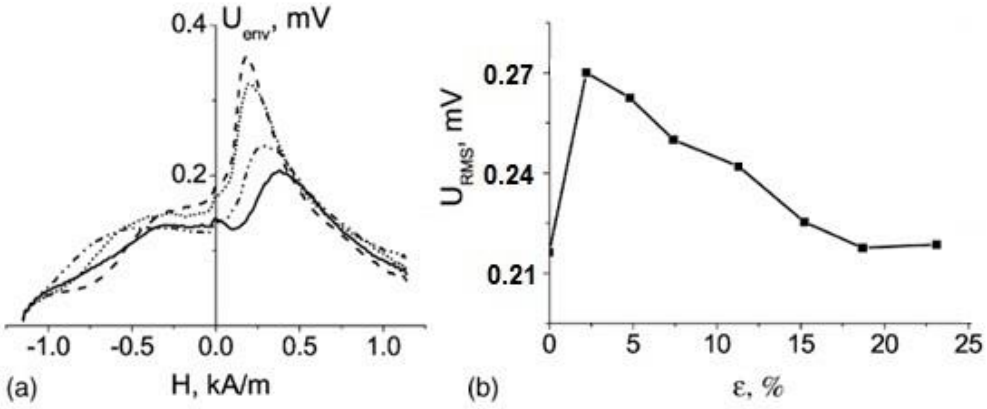

Figure 2-43: (a) MBN envelope for low carbon steel strip samples plastically deformed to 0% (solid line), 2.3% (dashed line), 4.8% (dotted line) and 15.2% (dash-dotted lines) of strain and (b) Variation of the RMS value of the MBN against strain for low carbon steel strip samples, adapted from Stupakov et al [169]

The effect of dislocations on magnetic properties can be seen in Figure 2-43 where Stupakov et al (2007) [169] have plastically deformed low carbon steel strips samples to different magnitudes of strain. The full envelope (Figure 2-43a) and RMS values (Figure 2-43b) of the MBN for the strained samples show a consistent effect. Initially there is an increase in the MBN signal as dislocations begin to form. Dislocations tangles/clusters are separated and small in number at this stage, causing larger MBN jumps. As the sample continues to deform, dislocation density increases which hinders the magnitude of these jumps and so you see a decrease in the RMS signal. The use of magnetic properties to characterise work hardened effects within P91 type material is lacking.

2.5.3.6. Magnetic Hysteresis Loop

The magnetic hysteresis loop (MHL) is a useful tool to measure the magnetic behaviour of a material and hence try to relate such properties to microstructural information for ferromagnetic materials. The magnetic flux density (*B*) and field strength (*H*) are not proportional for ferromagnetic materials and their relationship can be

observed in Figure 2-44; corresponding schematics of the domain configurations at different stages of magnetisation have also been shown. At the origin, the domains are configured such that there is no overall magnetisation at $H = 0$. As H is increased, B responds by initially increasing at a gradient which represents the initial permeability (μ_i) of the material. As H continues to increase, domains which are closely aligned to the direction of the H field, begin to grow favourably at the expense of others. This leads to a rapid increase in the flux density B until the material reaches magnetic saturation at B_s. The gradient of the larger slope gives the maximum permeability (μ_{max}). This behaviour demonstrates that the magnetic permeability changes with H, and is therefore dependent on the applied field strength. [77, 148].

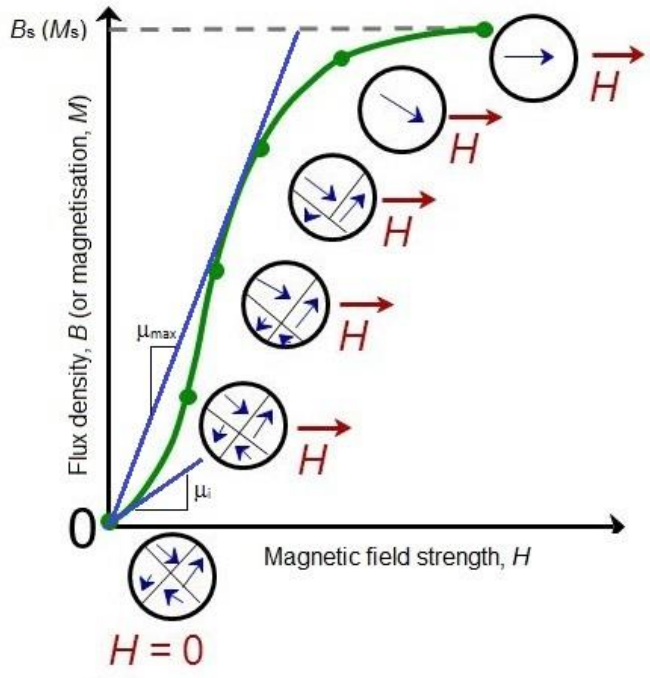

Figure 2-44: Schematic diagram of the flux density (B) vs applied magnetic field strength (H) behaviour when an unmagnetised ferromagnetic material is initially magnetised through to magnetic saturation. The schematic behaviour of magnetic domains during several stages of the magnetisation is also highlighted. Adapted from Callister and Rethwisch [77]

As the applied field *H* is reversed the curve does not trace back its original path. By reversing or removing the *H* field to zero a residual remnant flux density of magnetisation remains, called the remanence (B_r) (point Y on Figure 2-45). This is due to a net volume fraction of domains orientated in the former direction when the material was initially magnetised. In order to demagnetise the material, the strength of the reverse *H* field must be increased to a magnitude of $-H_C$ (point X on Figure 2-45) known as the coercivity [77]. Depending on the magnitude of the coercivity, or coercive force, magnetic materials can be classified as being hard or soft, where a soft magnetic material is easily saturated and demagnetised [148].

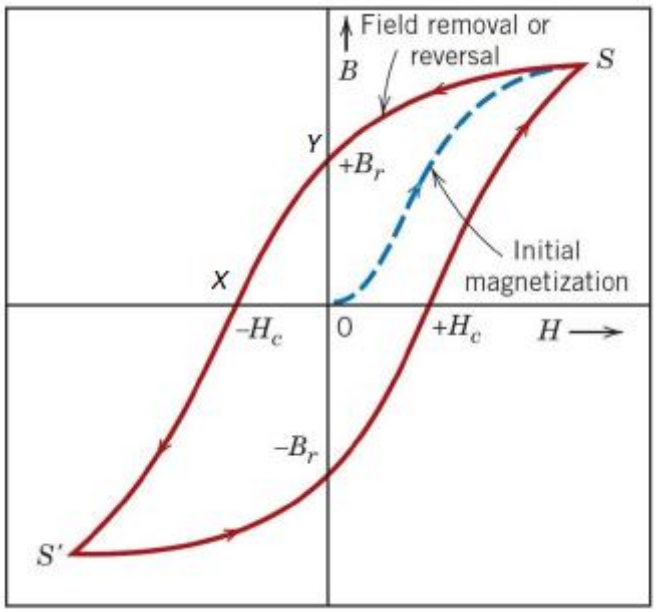

Figure 2-45: Schematic diagram of the flux density (B) vs applied magnetic field strength (H) subjected to forward and reverse magnetic saturations [77]

Govindaraju et al (1997) [142] used the MHL technique to evaluate creep damage in power plant weldments based on the fact that MHL measurements (coercivity and remanence) would be sensitive to the microstructural changes which Chen et al (1994) [170] showed to occur during creep. A portable magnetic inspection system, known as a Magnescope, was employed to measure P22 and CMV hot re-heat and main steam

chest pipe welds. Magnetic measurements were taken at eight locations on a 2.25Cr-1Mo (P22) pipe weld measuring the coercivity and remanence (Figure 2-46a and Figure 2-46b respectively). No significant variations in the coercivity and remanence were indicated, suggesting an absence of creep. However the low remanence at location two suggested possible creep damage, but this was unable to be verified as no replication data was available for location two.

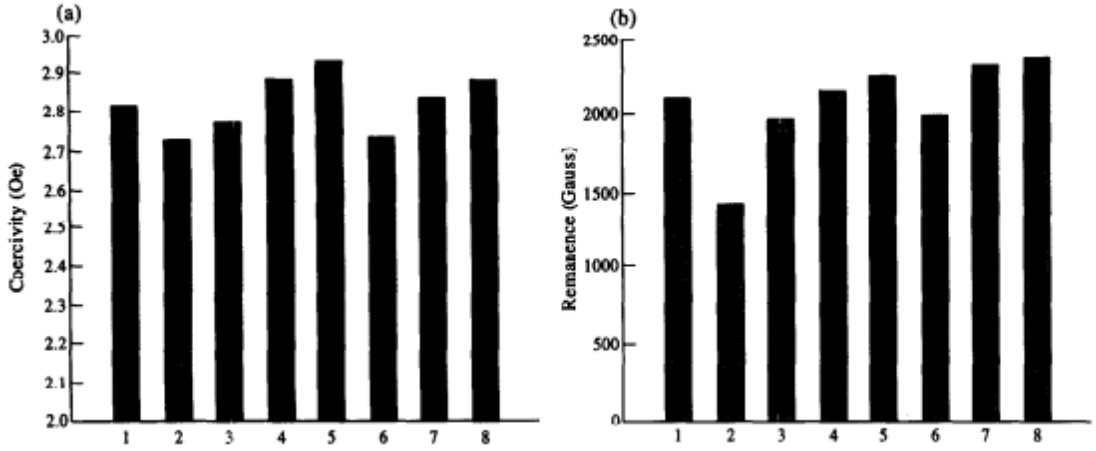

Figure 2-46: Variation of magnetic properties at eight separate locations at the fusion line of a P22 re-heat pipe weldment exposed to 131,563 hours of service. (a) coercivity; (b) remanence [142]

Figure 2-47a and Figure 2-47b show the coercivity and remanence data respectively at different locations (1, 2, 3 and 4) on three different CMV pipes. Consistently low measurements at location one suggested creep damage, which was verified by the replication data. A trend was evident with the reduction in coercivity and remanence when creep damage was present. This was attributed to the reduction in pinning sites within the matrix for domain wall motion, due to voids and dislocations moving to grain boundaries to form grain boundary cavities. Also the presence of cavities will introduce

localised demagnetising fields which assist the reduction in magnetisation as the applied field is removed, thus reducing the remanence [142].

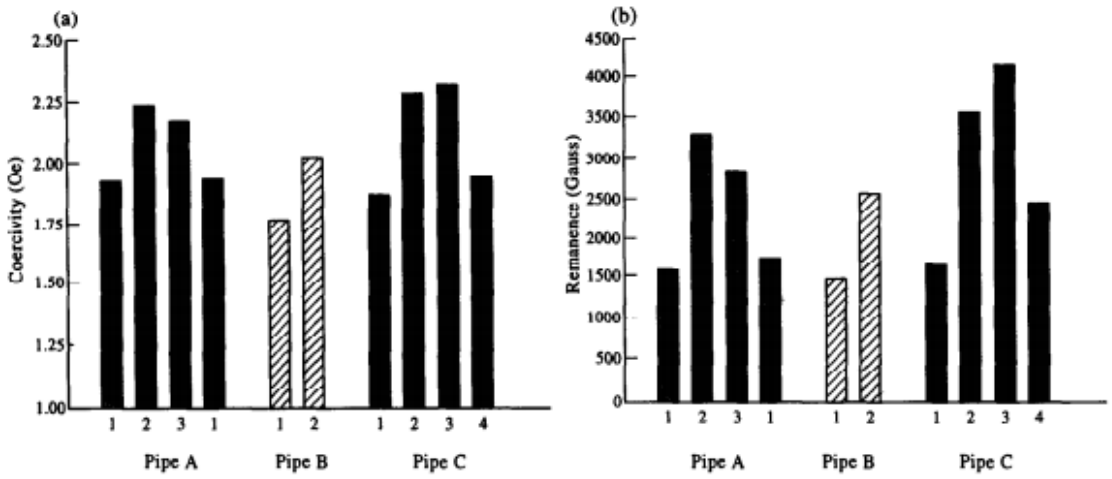

Figure 2-47: Variation of magnetic properties in individual welds on three steam chest pipes (A, B and C) exposed to 131,563 hours of service; (a) coercivity, (b) remanence [142]

A direct comparison of level of creep damage with the measured magnetic properties was also performed by Govindaraju et al (1997) (Figure 2-48) [142]. A discernible trend was distinguished where coercivity and remanence decreased with higher propensity of creep damage. Up to 40% reduction in remanence was observed between undamaged material and level D damage, where micro-cracks begin to form. The advantage of the Magnescope is the capability of measuring magnetic properties without the need to wrap the specimen with a flux coil, however there is considerable scatter in the measured parameters. The statistical variation in measurements was attributed to operational, material and environmental factors such as; surface roughness, local compositional differences, microstructural variations, residual stresses and variations in sensor positioning.

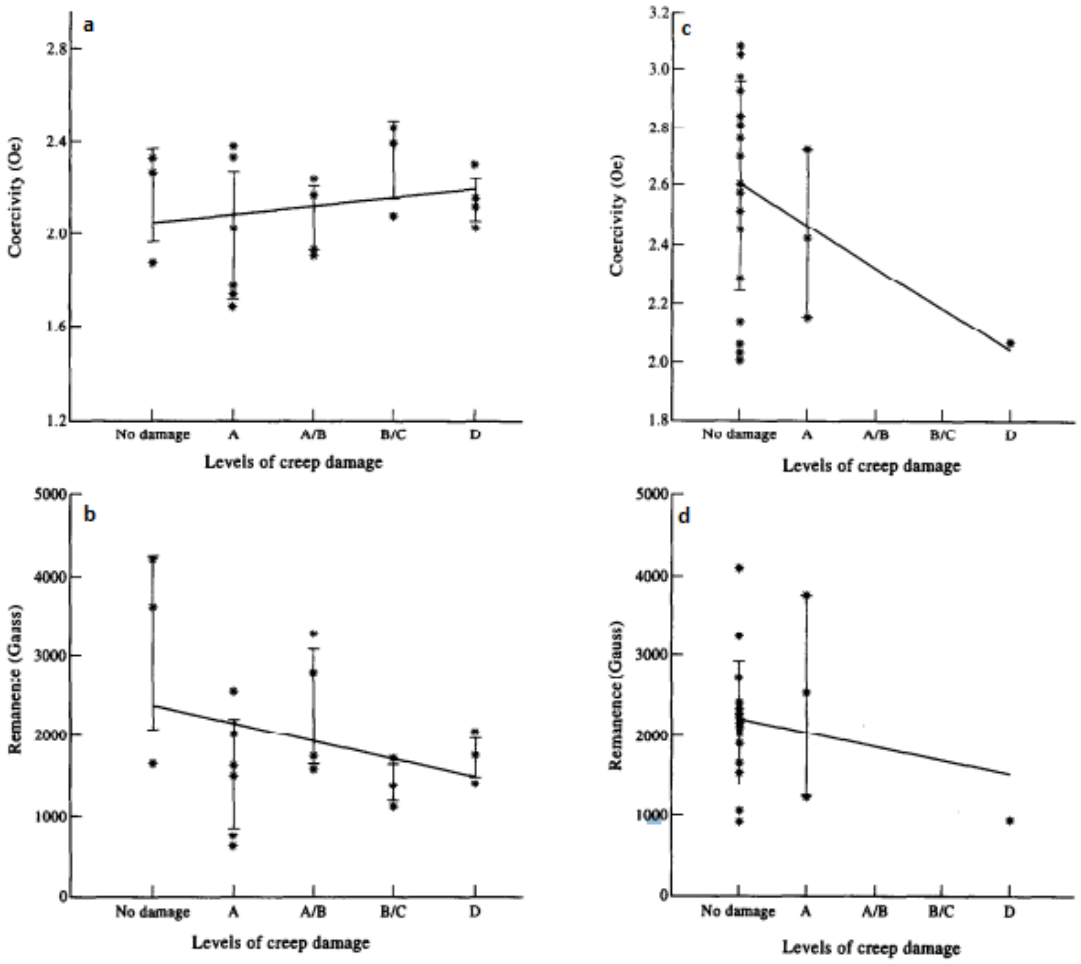

Figure 2-48: Variation of magnetic properties with level of creep damage measuring, (a) coercivity of CMV steel (b) remanence of a CMV steel (c) coercivity of P22 steel and (d) remanence of P22 steel. Level of creep damage varied as follows; level A - creep cavities begin to form, level B - cavities are orientated, level C - cavities begin to link and level D - micro-cracks begin to form [142]

More recently Wilson et al (2014) [137] have used MHL to test different microstructures in power plant steels (Figure 2-49). P9 (8.4Cr-0.9Mo) and T22 (2.14Cr-1.01Mo) steel samples were taken from service (operational for 11 years at circa 520 °C) and heat treated as per ASTM standards A335 [15] and A213 [65] standards to produce three

different microstructures; normalised (NORM), tempered (TEMP) and the original condition as taken from service (TFS).

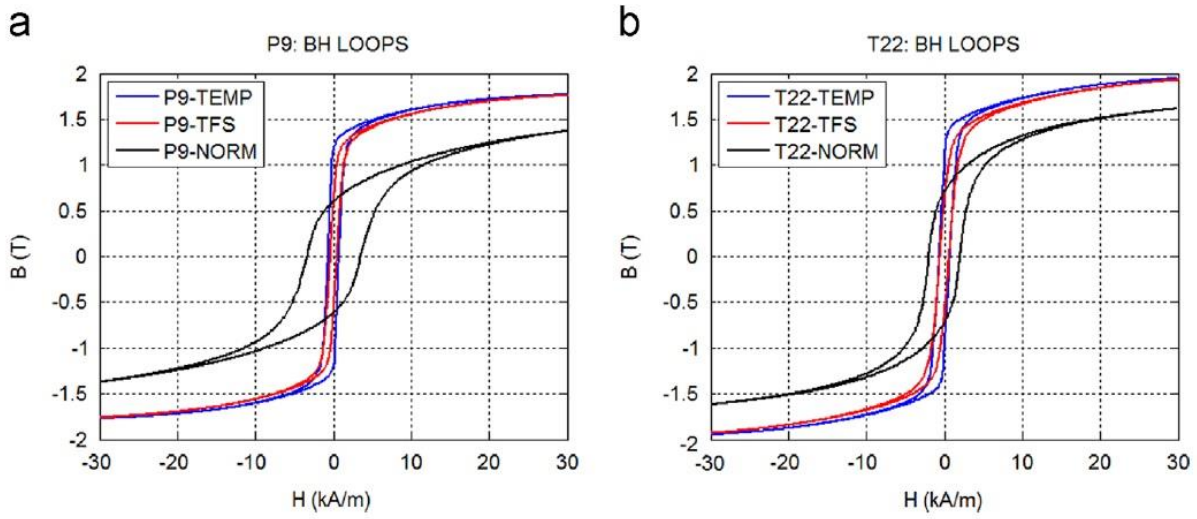

Figure 2-49: Magnetic hysteresis loops for power plant material (a) P9 and (b) T22 showing the material in three different thermal condition samples [137]

MHL analysis demonstrated hysteresis which clearly distinguished between the harder normalised martensite (P9/T22-NORM) and the other samples. The coercivity values measured correlated with the mechanical hardness of the samples as shown in Table 2-5. Mitra et al (2007) [143] used the analysis of the MHL for correlating the different stages of creep in 9Cr-1Mo power plant steel tube (T91) with the materials magnetic properties. 25 mm gauge lengths were cut from the T91 virgin steel tube of nominal composition (see Table 1 in [143]) and creep tested at 600 °C and 125 MPa. The test was interrupted at various stages throughout the creep life and magnetic measurements were taken using a surface probe. The author does not specify if any surface preparation was required before taking the magnetic measurements. Results (Figure 2-50) showed that the coercivity and remanence were both found to increase during the primary stage of creep and decrease during the secondary stage. However, during the tertiary stage of creep, the remanence continued to decrease but the coercive force increased rapidly.

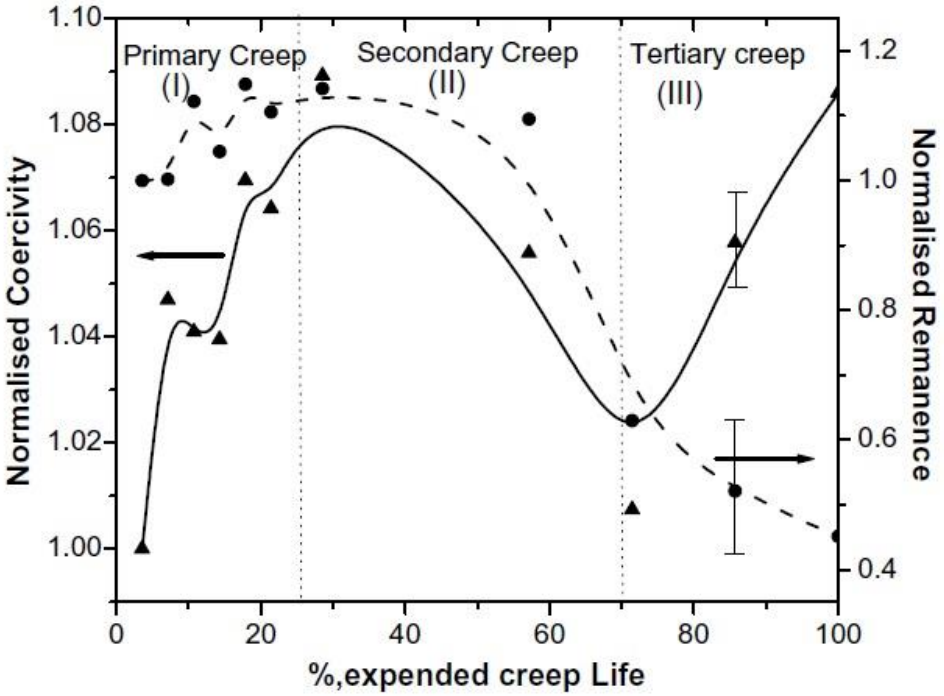

Figure 2-50: Variation of normalised magnetic parameters during different stages of creep. Solid line representing coercivity and dashed line representing remanence [143]

During the primary stage of creep, two conflicting processes with respect to carbon are taking place in the steel; existing carbides coarsen and new finely dispersed carbides precipitate. At high temperature, dissolved carbon within the matrix begins to diffuse to grain boundaries leaving the matrix depleted in interstitial carbon and less strained; under stress (creep) this process speeds up [144]. The carbon interacts with previously existing carbides (M_2C and M_3C_2) altering the composition and causing them to coarsen, leading to a small number of widely spaced pinning points making domain wall movement less constrained resulting in a lower coercive force. Concurrently, the diffused carbon is also interacting with other alloying elements forming new finely dispersed carbides (VC, NbC); here nitrogen also interacts to form nitrides. The precipitation of carbides and nitrides increases the creep strength as well as behave as

pinning sites for magnetic domain wall movement. This causes magnetic hardening and has an increasing effect on the coercivity, which is the dominant effect as shown in Figure 2-50, where coercivity increases in the primary stage of creep. In the secondary stage of creep the coercive force drops because carbides now coarsen at the expense of smaller ones, thereby increasing the spacing between carbides and reducing the number of pinning sites. In the final stage of creep, larger carbides ($M_{23}C_6$) (Figure 2-51a) and brittle phases such as Laves phase (Fe_2Mo) (Figure 2-51b) and complex carbonitride phase (Z-phase) form reducing creep strength leading to micro-cracking. This restricts domain wall movement and hence the increase in coercivity. It was noticed that the remanence in the tertiary stage of creep did not follow the trend of coercivity, as it had done in the previous two stages. This was explained due to the presence of demagnetising fields caused by the large non-magnetic carbides and other brittle phases [143].

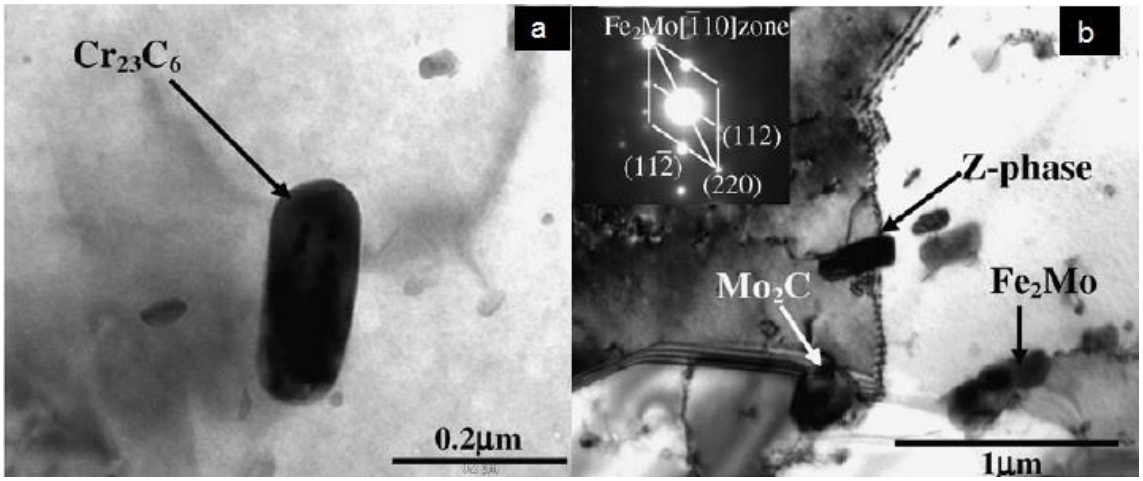

Figure 2-51: TEM micrographs of (a) typical Cr23C6 carbide at the grain boundary and (b) Laves phase Fe2Mo at the grain boundary after creep damage had occurred. Adapted from [143]

A number of authors have highlighted magnetic hysteresis information to be a valuable tool to characterise work-hardening within steels in a non-destructive manner [169, 171-173]. Stupakov et al (2007) [169] strained low carbon steel samples of different

geometries (Figure 2-52) and found that the coercivity of the samples increase with increasing strain as the plastic deformation resulting in dislocation formation causes the permeability of the sample to decrease. These results were in agreement with a previous study performed by Swartzendruber et al (1997) [172] where a similar conclusion was reached. The coercive field increases with plastic deformation tested on ultralow carbon steel and was found to be proportional to the square root of the strain; further enhanced by a number of authors who have shown the coercivity to be proportional to the square root of dislocation density (Vincena (1955),Kersten and Angew (1956) and Dietrich and Kneller (1956) cited in Swartzendruber et al (1997) [172]).

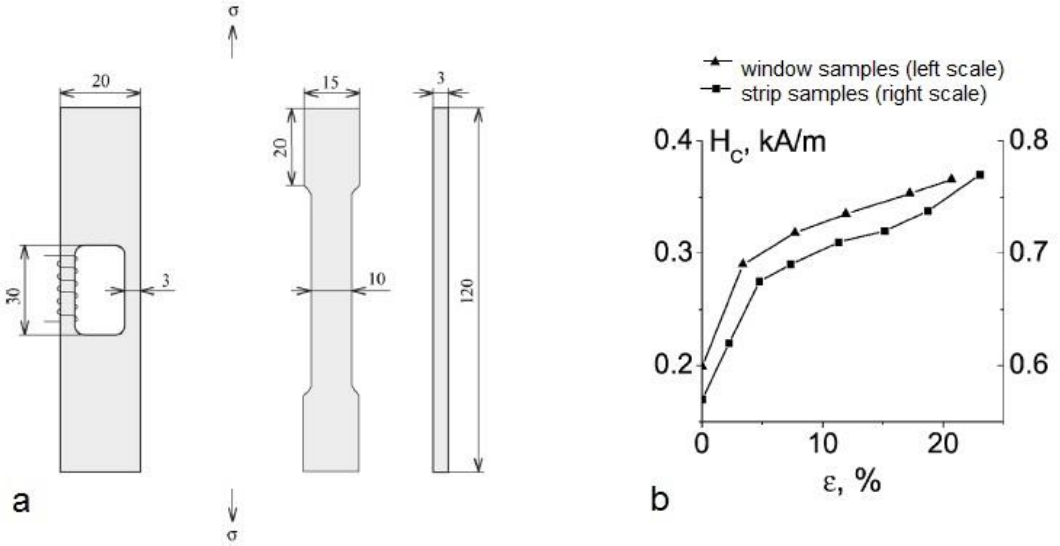

Figure 2-52: (a) Schematic of window (left) and strip (right) samples used in Stupakov et al study [169] and (b) Results of the coercive field measurement (H_C) with strain

2.5.3.7. Eddy Current Testing

Eddy current testing (ECT) involves the use of alternating magnetic fields which can be applied to any conducting material. The basics of the technique is to use an AC current

to excite a conductive coil at a given frequency, which then develops an alternating magnetic field with flux lines concentrated at the centre of the coil. As the coil is drawn closer to the object to be tested, the alternating magnetic flux lines penetrate the material and induce continuous, circular eddy currents (Figure 2-53).

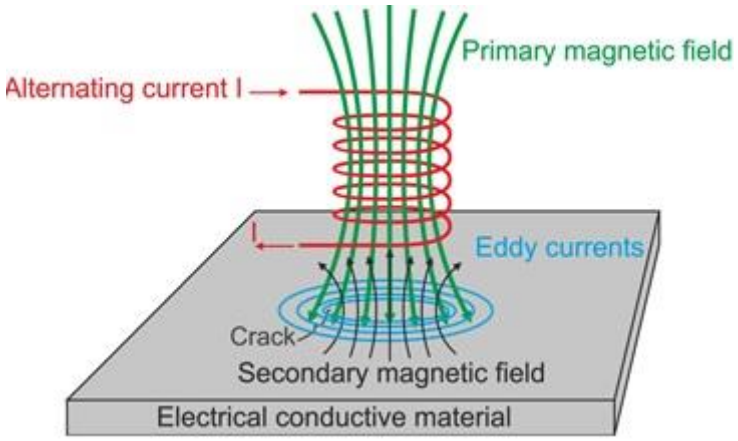

Figure 2-53: Schematic representation of eddy currents being induced into an electrically conductive material [174]

As the penetration of the induced field increases (either by bringing the coil closer to the object being tested or increasing the AC current, the eddy currents become weaker; therefore larger eddy currents will remain near the test surface (Figure 2-54b). The eddy currents which have been induced then produce their own magnetic field which is secondary and opposing to the original alternating magnetic field induced in the coil. This opposing magnetic field, coming from the test material, has an effect on the original magnetic field by weakening it. This change can be sensed by the test coil. In effect, the impedance of the coil is reduced proportionally to the increase of eddy currents in the test material. This relationship is then used to detect discontinuities in the test material. If a crack or other type of discontinuity is present in the test material, this will obstruct the eddy current flow (Figure 2-54c). The path of the eddy currents will be increased, reducing the secondary magnetic field and therefore increasing the coil impedance. This change can be amplified, detected and displayed by electronic

equipment to detect presence of defects [175]. An important factor for NDE techniques such as eddy currents is the distance between the coil and the test piece, known as lift-off. The lift-off distance determines the strength of the eddy currents generated. Ward (2010) [175] mentions the lift-off to affect the amount of flux linkage which is lower with higher lift-off, usually undesirable, as well as being affected by the incident angle between the coil and test material.

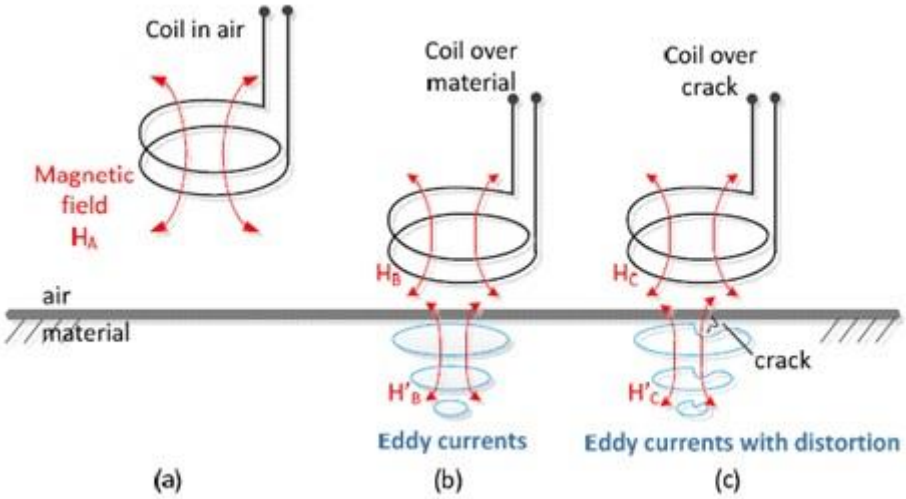

Figure 2-54: Schematic diagram of how a defect can be detected using eddy currents. (a) magnetic field generated around the coil by an alternating current flowing through the coil, (b) eddy currents induced in the material by the magnetic field from the coil, (c) a flaw in the material disturbs the eddy current circulation, the magnetic coupling with the probe changes and a defect signal can be measured [130]

Eddy currents can vary with a range of factors, such as microstructure, surface roughness, hardness, local permeability differences, or variations in chemical composition. This makes ECT a valuable technique for analysing power plant material but it is difficult to distinguish and relate between changes in signal [107]. Industry will use eddy currents to test components such as welds, tubes and wrought material for surface breaking and sub-surface defects [133]. A big advantage the eddy current technique has is that it does not require metal surface contact and therefore components with a surface coating can be inspected without removal of the coating

(usually up to 2 mm paint). It is currently used to assess heat treatments on wrought components and detect thinning, pitting and fretting on tube material. Unlike the flux leakage process, the tested material does not have to be magnetised but the base material to be tested must be electrically conductive offering a wider range of materials to be tested. However the technique is restricted to experienced personnel as displays and charts can be complex to interpret and the surface depth of penetration is limited.

2.5.4. Multi-frequency EM Sensors

Like other electromagnetic techniques, multi-frequency EM sensors work by detecting changes in the material's magnetic permeability (at low frequencies) and electrical conductivity/resistivity (at high frequencies). The EM sensors measure the changes in the inductance, caused by the presence of a conductive material within the vicinity of the EM sensor, interacting with the EM sensor's generated field (more details have been given earlier in Section 2.5.3.3). The changes in inductance can be correlated to the materials mechanical characteristics (such as hardness) and microstructural characteristics (such as phase fraction, grain size and presence of decarburisation) [22, 176]. The advantages of using EM sensors for NDT is that they have a fast response, are relatively inexpensive and have the ability to operate non-contact [176], although, the techniques are confined to ferromagnetic materials [131]. The EM sensor technique, also referred to as impedance or induction spectroscopy [26] is similar to the initial magnetisation stage of the hysteresis loop techniques (see Section 2.5.3.6) when only a small magnetic field is applied such that domain movement is reversible. Thus, the initial relative permeability of the material is an important material property for this technique. A typical EM sensor consists of at least one exciting coil and one sensing coil and can be arranged in different configurations based on application. Figure 2-55 shows a schematic diagram of a typical cylindrical EM sensor made up of a plastic (insulating) air cored body, with two copper coils wound around it (sensing coil and

exciting coil). Such a sensor can be used to assess cylindrical/rod shaped samples small enough to slot into the insulating core of the sensor [23, 27, 94]

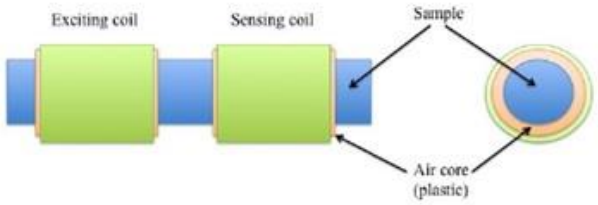

Figure 2-55: A schematic diagram of a typical cylindrical EM sensor [177]

Another configuration (given in Figure 2-56a) is of a typical H-type EM sensor made up of two U-shaped ferrite cores placed back to back forming the shape of the letter 'H'. Such a sensor would be used to assess flat surface material such as strip or plate steel [20, 26]. The excitation coil is wrapped around the centre of the two U-cores (blue wire in Figure 2-56a) with two sensing coils wrapped around either set of the ferrite core feet, one to measure the target material (active side) and the other to measure the atmospheric field as a datum (dummy side), seen more clearly in Figure 2-56b. In instances where a dummy sensor is not required, a simple U-shaped EM sensor has shown to be useful [25].

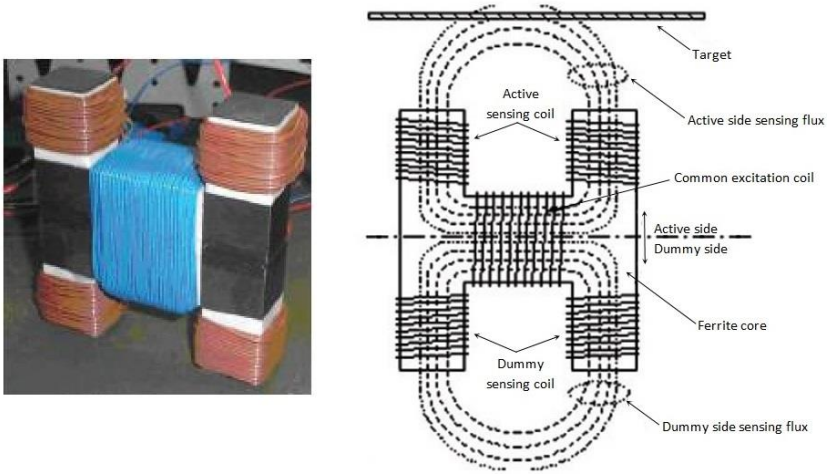

Figure 2-56: (a) Image of a H-type sensor and (b) Cross-sectional schematic of the main elements of the H-type sensor adapted from [26]

The typical operation of an EM sensor begins with an impedance analyser generating an AC current through the exciting coil of the EM sensor, which can be applied at varying frequencies. The generated magnetic field from the exciting coil interacts with the material and is altered with respect to the EM properties of the material. The resultant field is detected by the sensing coil and the inductance/impedance (real and imaginary parts) can be recorded. The changes in real impedance relate to the variation in the actual energy loss element (the resistive component) and the imaginary impedance relates to the energy storage element (inductive component). Changes in the measured impedance/inductance can be used to characterise microstructural changes [26, 178]. At high frequencies, the AC current applied magnetic field induces eddy currents at a depth into the material (skin depth see Section 2.5.4.1) which opposes the applied field. Consequently this decreases the mutual inductance of the sensor. Here the resistivity and conductivity of the material have a more significant impact on the mutual inductance signal than the permeability. At lower frequencies, the magnitude of the eddy currents are small, allowing the applied field to penetrate further into the material as there is less resistance from the eddy currents. In this arrangement the magnetic permeability is the dominant EM property affecting the mutual inductance of the sensing coil. The usefulness of the technique is based on this principle that multi-frequency EM sensors can be useful in gathering depth dependent information [26, 178].

In the past decade impedance spectroscopy (IS) or multi-frequency EM sensors have shown promising results in the ability to characterise steel microstructure in a non-destructive manner. Davis et al (2005) [26] and Haldane et al (2006) [179] have both investigated impedance spectroscopy as a non-destructive technique to monitor the microstructure online for high temperature steel application such as the production of strip steel. Both authors share the opinion that online non-destructive EM sensors will

provide a desirable addition to the current methods of analysing hot strip steel, such as optical/electron microscopy and x-ray analysis.

A number of researchers in this field have used multi-frequency inductance measurements to characterise microstructural information, finding the low frequency data (typically less than 100 Hz) to be independent of frequency (relatively flat) [23, 25, 179-181]. Figure 2-57 shows typical real inductance curves measured at multiple frequencies. In this case Yin et al (2007) [25] were able to distinguish the rolling direction of a steel billet by comparing the magnitudes of the real inductance at low frequencies. There is less magnetic reluctance along the rolling direction as the ferrite is elongated in this orientation allowing easier flux flow. As the relative permeability dominates at low frequencies, the difference in the relative permeability of the two directional measurements is exemplified. As frequency increases the real inductance drops as the eddy currents strengthen (in this instance approximately 300 Hz). Here the resistivity component dominates allowing eddy currents to oppose the applied field (skin effect) and reduces the mutual inductance and hence diminishes the difference between real inductance of the two directions.

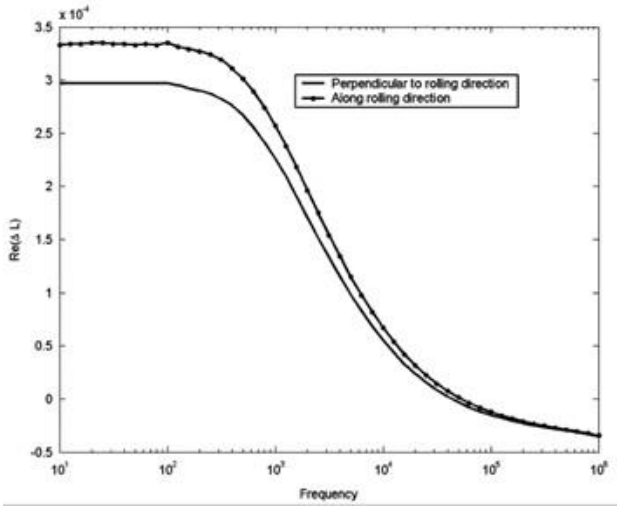

Figure 2-57: Variation of real inductance and frequency differentiating between microstructural anisotropy of rolled steel [25]

Similarly Liu et al (2012) [27] was able to distinguish between different power plant steel microstructures using low frequency real inductance measurements (Figure 2-58). P9 (9Cr -1Mo) and T22 (2.25Cr-1Mo) steels were subjected to different heat treatment processes and small cylindrical samples were machined and tested with a cylindrical sensor similar to the one shown in Figure 2-55. Results proved the sensor to be able to differentiate between the three different microstructures produced by samples that were; normalised, tempered and taken from service. The relative permeability of the samples was shown to have an exponential relationship with the low frequency inductance (shown in Figure 2-59). The low permeability samples yielded lower real inductance values; caused by their microstructures. The normalised sample (Figure 2-60a) had a magnetically hard microstructure consisting of a mixture between some bainite and predominantly un-tempered martensite. The high dislocation density in this microstructure acts as pinning points for magnetic domain movement, restricting the ease to which the magnetic flux flows through the sample. This causes the material to possess a low relative permeability and hence a low real inductance. The tempered martensitic microstructure (Figure 2-60b) contains a significantly reduced dislocation density and larger laths. This produces a magnetically softer microstructure than the normalised sample, with higher permeability, leading to an increase in its real inductance value. The ex-service microstructure (Figure 2-60c) shows a more significant transformation, where the previous martensitic laths have transformed into larger ferrite grains. Any dislocation networks in the tempered martensite have been annihilated, thus reducing the number of pinning points for domain wall movement, leading the material to hold a higher relative permeability [27]. These low frequency inductance measurements would be a suitable methodology to screen the bulk microstructure of EON's Grade 91 steam headers, since the relative permeability of the material will change significantly depending if the material has been correctly heat treated or mis-heat treated.

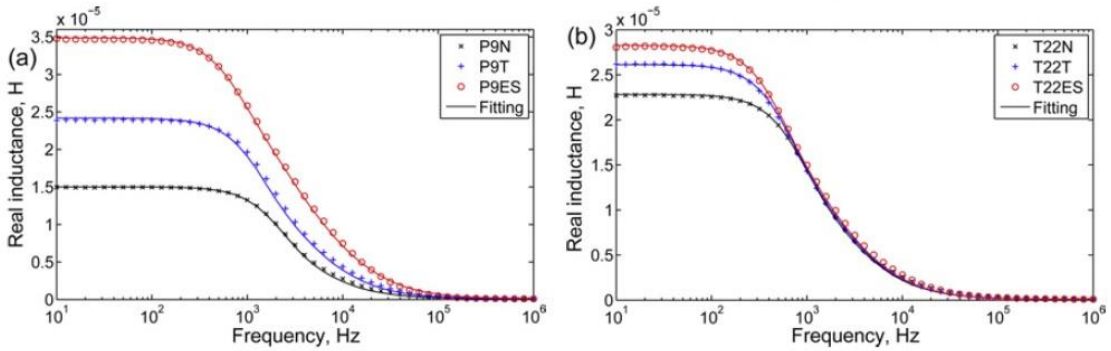

Figure 2-58: EM sensor results for different power plant steels subjected to different heat treatments (a) P9 and (b) T22 [27]

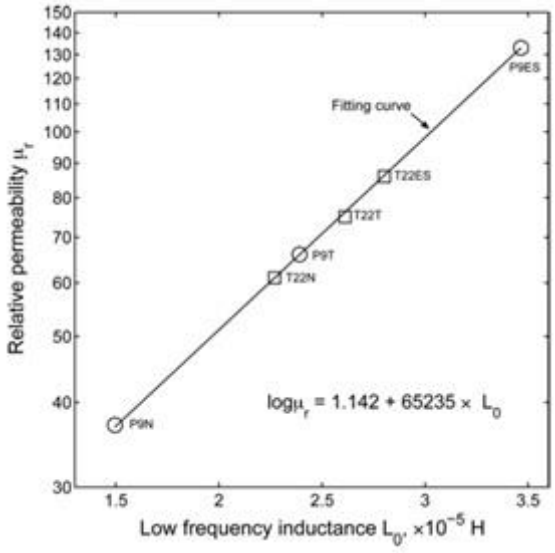

Figure 2-59: Exponential relationship between the relative permeability and low frequency inductance for P9 and T22 heat treated samples [27]

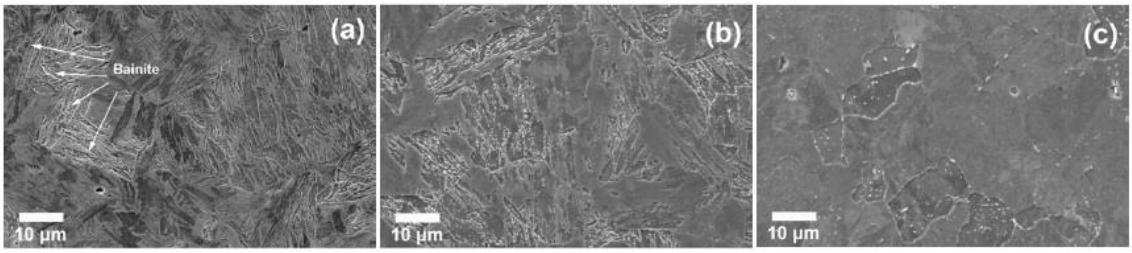

Figure 2-60: Microstructures of the differently heat treated P9 samples. (a) normalised, (b) normalised and tempered and (c) ex-service [27]

2.5.4.1. Skin Depth

When an AC current is induced into a conductive material, the tendency for the current to distribute such that the current density is largest nearer the surface and decreases with greater depths is known as the skin effect. The depth to which the current can be induced into a material from its surface is commonly referred to as the skin depth and expressed as:

$$d_{skin} = \sqrt{\frac{\rho}{\pi f \mu}} \qquad \textbf{Eq. 2-18}$$

Where d_{skin} is the skin depth (in m), ρ is the resistivity of the material (in Ωm), f is the frequency of the AC current (in Hz) and μ is the permeability (Hm^{-1}).

From Eq. 2-18 it can be seen that the frequency has a reducing effect on the skin depth meaning the applied electromagnetic field's depth of penetration into the material decreases as the frequency of the applied AC current increases. An alternating magnetic field (induced in the material from the AC current) will generate circulating eddy currents at the centre of the conductive material which oppose the induced current and forces the conducting electrons to the outside of the conductor, reinforcing the current flow in the skin (near the surface) [182, 183].

2.5.4.1. Impact of Lift-off

The lift-off can be described as the spacing between the EM sensor and the test specimen and has adverse effects on the EM signal [182]. At high lift-offs the sensor signal strength decreases as the electromagnetic interaction between the sensor and sample becomes weak. On the other hand, when the lift is very small (or zero) the sensor signal is very sensitive and prone to significant fluctuation and error [180, 184] due to surface conditions of the sample. Therefore it is generally sensible to understand the relationship between lift-off and EM signal for the specific sensor to

determine the optimum lift-off distance which is high enough to be stable but not so high that the electromagnetic interaction between sensor and sample is too weak to be useful. Wei (2013) [184] found that the EM signal for a U-shaped alternating current field measurement (ACFM) sensor decreased with increasing lift-off following an inverse power law.

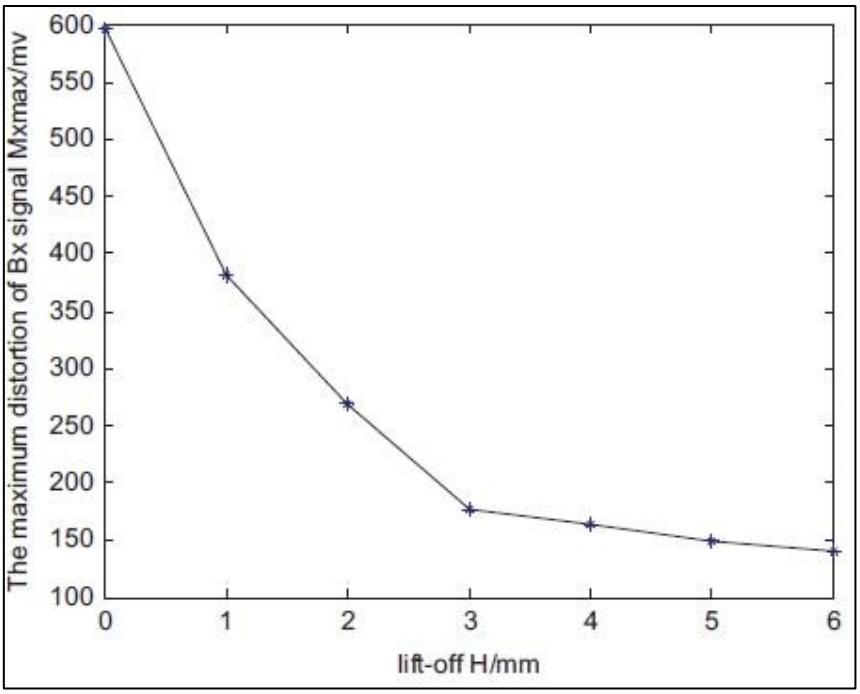

Figure 2-61: Experimental results showing relationship of EM signal with lift-off [184]

2.5.4.2. Impact of Sensor Type

Previous studies have used EM sensors to distinguish the change in percentage ferrite as the microstructure transforms from a paramagnetic austenite phase to the ferromagnetic ferrite phase. Haldane et al (2006) [179] employed an air cored cylindrical sensor to study ferrite/austenite stainless steel disc samples (43 mm diameter, 10 mm thick) and found, that for specimen containing less than 40% ferrite, the ferrite percentage can be measured using low frequency real inductance values (Figure 2-62a). For specimen containing more than 40% ferrite, the low frequency inductance values are less useful and instead the zero-crossing frequency data (the

frequency value at which point the real inductance is zero) (Figure 2-62b) can evaluate the percentage ferrite. At the beginning of the transformation, only small volumes of high permeability ferrite exists in dispersed locations and disconnected from one another by the paramagnetic austenite phases resulting in a low inductance value. As more ferrite is produced the material's permeability is increasing and hence the increase in inductance. As the transformation proceeds (circa 40 % ferrite) it is believed that the microstructure has formed a near fully connected ferrite path and hence the inductance saturates. In this study, the sensor output has been directly correlated to the microstructure. However, Hao et al [180] raised the concern that the EM sensor output is also dependent on sensor geometry and conclusions drawn from different sensor configurations may not always relate to one another. Two EM sensors were deployed to carry out the study; one was an axisymmetric (circular) air-cored coil (inner radius of 20 mm, height of 2 mm and 10 turns) the other being an H-shaped ferrite cored sensor (similar to that shown in Figure 2-56a). The results showed that at low frequencies (10-100 Hz) the real inductance shows different sensitivity to the amount of ferrite within the material depending on the type of sensor; air cored sensor was more sensitive to low volume of ferrite fraction whereas the ferrite cored sensor was more sensitive to higher volumes of ferrite fraction.

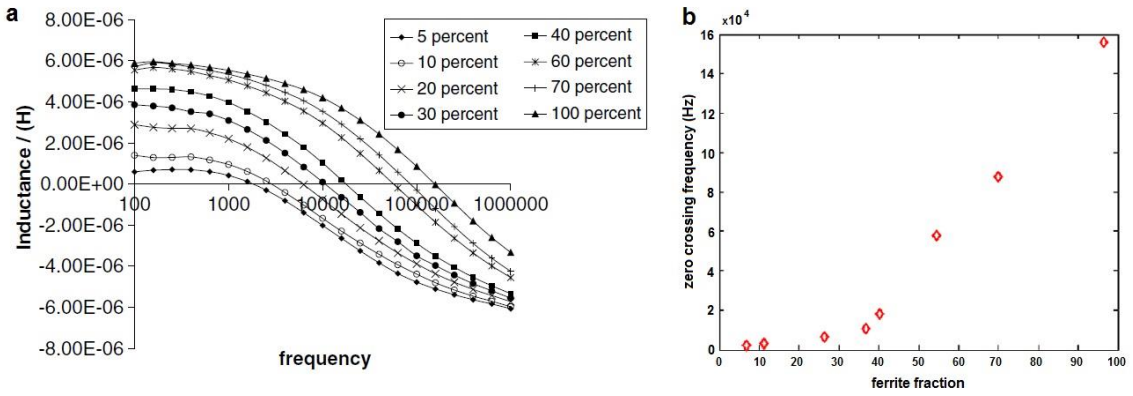

Figure 2-62: Variation of ferrite fraction within a dual phase ferrite/austenite microstructure measured using (a) multi-frequency real inductance values and (b) zero-crossing frequency, adapted from Haldane et al [179]

The axisymmetric type system (e.g. cylindrical air cored sensor with cylindrical sample placed within the sensor, similar to that shown in Figure 2-55) have been deployed in many other studies [23, 27, 176, 181, 185]. One of the main benefits of using the cylindrical sensor and sample arrangement is that it is easier to perform finite element modelling, which enables the fundamental EM properties of samples that are independent of sample and sensor geometry to be inferred. In such a system only a 2D axisymmetric model is required as opposed to a 3D model for the H-type and U-type sensors. The 3D model significantly increases the complexity of designing the model and can also increase the computational running time. However the U-type sensors present a much more pragmatic function as they can measure open samples directly and is more easily deployed for large in-situ components unlike the cylindrical sensors. The disadvantages of the U-type sensor are that it is more sensitive to the surface finish and condition of the components which can significantly impact the EM signal. As such research using U-shaped and H-shaped sensors have generally deployed a constant lift-off between the sensor and sample [24, 29] (to avoid surface effects) at the

expense of sensor sensitivity (since the sensor loses sensitivity with increasing lift-off, explained in Section 2.5.4.1).

2.5.4.3. Impact of Decarburisation

As previously mentioned, pre-service power plant component processing usually requires the steels to be heated into the austenite phase field, where temperatures typically exceed 1000 °C. Such temperatures can cause carbon at the surface of the components to react with oxygen in air and deplete the surface of the material from carbon (decarburisation) [15, 141]. Lack of carbon at the surface of a material can significantly deteriorate the mechanical properties of the component in particular, hardness, strength, fatigue and wear resistance. The international standard for measuring decarburisation within a material as set out by ISO 3887:2003 specifies three distinct methods; micrographic, micro-indent hardness and chemical analysis. The micrographic method entails measurement of microstructural variation due to carbon depletion using microscopy, such as ferrite transformation within a martensitic microstructure. The second method employs the use of micro-hardness indentation along the cross-section of the material from surface to bulk; the hardness will significantly reduce within the decarburised zone. The third method involves the use of chemical or spectrographic analysis to directly measure the carbon content within a specific region [186]. These three methods are destructive by nature and can be relatively time consuming to obtain results. For a power generating plant, the presence of a decarburised surface layer can mislead the bulk property measurement of a component. The typical standard adopted for performing quality assurance on pre-service entry components is to check the material hardness. The decarburised surface layer will significantly lower the hardness for a typical martensitic Grade 91 component and hence lead to misinformed decision making whether to accept or reject the material. In the literature, authors have investigated the ability of multi-frequency EM

sensors to non-destructively evaluate decarburisation within 0.8 wt% carbon steel [94, 141, 187]. Hao et al (2008) [141] decarburised Fe-0.8 wt.% C steel bars (150 mm long and 10 mm in diameter) by heating them in air at 1000 °C for varying times followed by air cooling. The microstructural results from the heat treatments can be seen in Figure 2-63. At the sample core (dark regions) the material is pearlitic. In some cases, near the surface, (white regions), full decarburisation has taken place and the pearlite has transformed into ferrite. Between the two regions a mixed zone exists where the material is said to be partially decarburised.

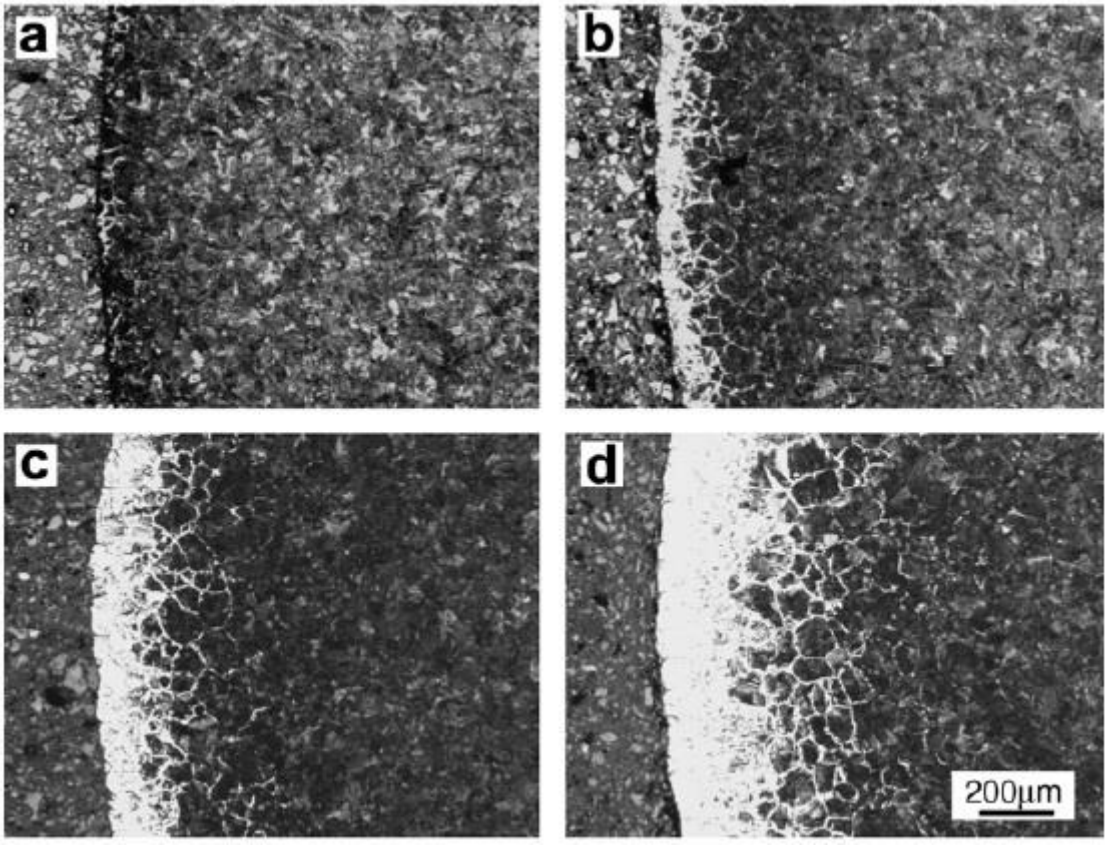

Figure 2-63: LOM images of the decarburised Fe-0.8 wt.% C steel samples heat treated at 1000 °C for: (a) 10 min, (b) 1 h, (c) 2 h and (d) 5 h [141]

The results showed that the longer the heat treatment, the large the depth of both full decarburisation (white regions) and partial decarburisation (mixed region). An air-cored cylindrical sensor was employed to determine variation in inductance as a function of

decarburisation by inserting the rod samples into the central core of the sensor (similar to that shown in Figure 2-55). The low frequency sensor results showed the inductance to rise with increasing decarburisation time (Figure 2-64). It was noted that at really low frequencies (<20 Hz) the samples with least decarburisation were difficult to distinguish from one another, but at a higher frequency of 100 Hz, they could be detected. This was explained by the phenomenon of skin depth (see Section 2.5.4.1 for more information). As frequency increases, this leads to a rise in the eddy currents induced into the sample which oppose the applied field and reduce the depth of penetration to a certain skin depth. At very low frequency, the skin depth is much larger than the decarburised layer and so the ferrite in the decarburised layer contributes less than the bulk pearlite. As the frequency is increased (and the skin depth reduces), a larger contribution to the sampled area comes from the decarburised layer and so a variation can be seen in the inductance. In this way, the frequency can be used to calculate the skin depth and hence correlate to a depth of decarburisation [141].

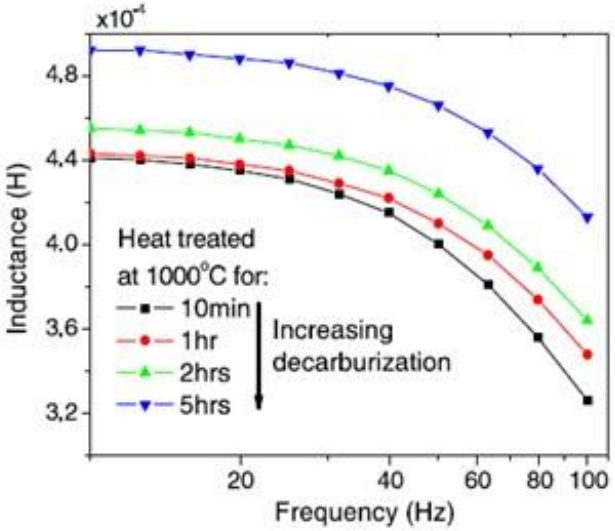

Figure 2-64: Variation of inductance with frequency for decarburised rod samples [141]

The work performed in this study uses a cylindrical sensor which is suitable for rod components, however it would not be suitable for detecting localised decarburisation as

the inductance is measured as an average across the circumference of the rod. For localised measurements, a probe type sensor would be more suited where the sensor probe can be placed specifically over the area of interest, specifically in contact with the sample to increase sensor sensitivity.

2.6. Major Challenges in the Application of EM Sensors at EON for Materials Screening

The conditions within a power plant boiler house can be very arduous and dirty and hence over long service times, the microstructures of a material can change due to operation and also the surface condition of the components can vary from when the component was first entered into service. Power plant boiler components arrive for service entry with a tempered martensite microstructure after being heat treated. If components are mis-heat treated then it is possible that an aberrant bulk microstructure consisting of soft ferrite is produced or that a decarburised ferrite layer at the surface can exist (as explained in Section 2.4.1). To verify that the components going into service have the correct microstructure, NDT is performed (surface replication and portable hardness testing explained in detail in sections 2.5.2.2 and 2.5.2.3 respectively). However surfaces are not always in a condition ready for NDT inspection due to the presence of oxide layers formed during the manufacturing heat treatment processes, which requires removal before application of the NDT. The oxide layer is typically removed using mechanical processes of coarse and fine grinding resulting in machine marks and different degrees of surface roughness on the component's surface.

During elevated temperature service, the service entry tempered martensite microstructure can degenerate whereby the fine laths begin to broaden which, over prolonged service, will evolve into an equiaxed ferrite grain structure (as explained in

Section 2.4.2). Oxide scales can become present during service and require removal before NDT inspection can be performed. Initially surfaces are cleaned using a wire brush which introduces abrasive marks and a surface roughness. Depending on the type and thickness of the oxide it is typically removed with coarse and fine mechanical grinding for small local regions of inspection. Some components are wrapped in insulation and bonded using bitumen which adheres to the surface of the component; others may be painted for corrosion protection. When a large surface area needs to be exposed for NDT testing, then local (small area) mechanical grinding is not efficient and therefore a grit or sand blasting process is used. With grit blasting, stock removal of the oxide layer, bitumen or paint coatings can be achieved. For example, steam headers may be grit blasted to remove any build-up of corrosion or oxides to allow access to the metal surface for surface replication or hardness testing to be performed [89].

The impact of surface roughness layer or a work hardened layer on U-shaped EM sensors has been omitted from the literature and is blocker in creating a practical application for the EM sensor within EON's NDT suite for differentiating correctly heat treated material from mis-heat treated material. These issues have not been considered by researchers for a number of reasons. Firstly sample surface finishes have been kept constant in some research or a lift-off has been used and as such the surface finish has not been a considered variable, i.e. for in-situ rolling mill experiments [24, 28, 29, 185, 188]. In other research cylindrical air-cored sensors have been used where samples have been placed within the coils of the sensor and as such the field floods the entire sample making the surface finish less of a variable [23, 27, 30, 189], this would be an impractical method for the very large boiler components that EON are interested in screening and as such only a U-shaped probe type sensor would be applicable for EON's needs. Finally some researchers, where U-shaped or H-shaped

sensors have been used, have used relatively large sensors compared with any small abnormal surface layers, such that the ratio of the electromagnetic field sampling the bulk of the component dwarfs the very small amount of field which is sampling the relatively small abnormal surface layer [20, 21, 58, 190]. For the EM sensor to be used as a screening technique alongside EON's current non-destructive screening methods of portable hardness testing and surface replication, then the U-shaped EM sensor must be small enough to carry out spot checks on steam header components of a similar surface area that is prepared for portable hardness testing and surface replication, this is typically 100 x 100 mm.

2.7. Summary of Review

EON is a large power generation utility company and like any company with power generating assets is preparing for a transition to a decarbonised energy system. As part of this transition, there will be requirement for fossil fuelled power generation to operate at higher temperatures and pressures to raise efficiencies. In conjunction, fossil plants will also need to operate with more flexibility (as opposed to base load) as renewable technologies are introduced onto the energy grid. This requirement will put a strain on the current operational materials, in particular the critical boiler components exposed to the high operating conditions such as steam headers, pipes and tubes. Grade 91 material is presently the cost effective choice for most existing fossil fuelled power generation plants. The tempered martensitic microstructure of Grade 91 boiler components is critical for the component's to operate under arduous conditions and thus the ability to accurately characterise the condition of these microstructures non-destructively is of huge benefit, as the assets are operated closer to their design limits. EON's current methods for screening material is primarily portable hardness testing

and surface replication and the review suggests that these techniques are time consuming, subjective and can be misinterpreted (detailed in Table 2-6).

Table 2-6: Advantages and disadvantages of current NDT techniques used on power plant components for quality assurance information gathering

Surface Replication	
Advantages	• Attain microstructure image
Disadvantages	• Labour intensive - time consuming and costly • Requires considerable surface preparation • Skilled operator • It can take hours/ days before the replica is analysed with an optical microscope • Unable to characterise bulk material • Dependent on subjective analysis • Very localised technique
Portable Hardness Testing	
Advantages	• Relatively simple • Inexpensive • Non-subjective output
Disadvantages	• Data can be unreliable due to large scatter • Information of surface only is attainable • Unable to characterise bulk material • Limited by gravity dependency – restricted by component geometry.

The majority of research thus far, proving electromagnetic sensors to be able to characterise microstructural changes, has been performed in laboratory conditions where sample surface finish has been controlled and kept consistent. This level of control on surface finish is not achievable in the challenging environments presented within boiler houses. Grade 91 components in service can have a variety of surface finishes with variations in surface roughness, the presence of decarburised surface layers and the presence of work hardened layers. The challenge exists in transitioning

electromagnetic techniques for monitoring and characterising microstructures into a practical application that can be used by EON at their power plant to screen components in determining whether the bulk microstructure of the components has been correctly heat treated or mis-heat treated. The nature of some EM techniques (MBN, MHL and cylindrical EM sensors) are not suitable for larger industrial components where a probe type (U-shaped) sensor is more practical and as such a U-shaped small EM sensor will be the focus of this study. The impacts on a U-shaped EM sensor of surface roughness finish, decarburised surface layers and work hardened surface layers, that may be found on service entry and in-service components, has been overlooked in the literature and therefore require investigation to be able to recommend a practical application for EM sensors to be used by EON. A variety of surface roughness samples will need to be created ranging from very rough surfaces which can be produced by wire brushing or machining, to smoother surface that can be produced using surface grinding. EON's current maximum surface roughness finish for any NDT technique is 3.2 µm (Ra) and a minimum of 1.6 µm (Ra) so a range of samples which encompass this range will be suffice, i.e. samples with surface roughness values ranging from greater than 3.2 µm (Ra) to less than 1.6 µm (Ra) to determine the impact of the surface roughness layers when using a small U-shaped EM sensor to screen correctly heat treated material. EON currently make use of grit blasting to clean surfaces for inspection and so a range of samples, grit blasted using typical grit blasting parameters, will be produced to determine the impact of the work hardened layer when using a small U-shaped EM sensor to screen for correctly heat treated material. EON's current acceptable specification for Grade 91 steam headers and thick walled pipes is a 2 mm aberrant or decarburised surface layer, therefore samples with varying depths of decarburisation will be studied to determine the impact of a decarburised surface layer when using a small U-shaped EM sensor to screen for correctly heat treated material.

CHAPTER 3 EXPERIMENTAL METHODS AND MATERIALS

This chapter details the material used and the different samples that were produced to carry out the research. Details of the different heat treatments to produce the various microstructures are given as well as the various surface finishes including surface roughness patterns and work hardened layers. The chapter goes on to describe how the EM sensor was manufactured and how it was operated, making note of the EM sensors expected function and output with respect to edge effects, sample thickness, sensor lift-off and effect of sample permeability. Details of microscopy techniques, hardness indentation measurements, decarburisation measurements and surface roughness measurements are also given.

3.1. Material

Five pieces of Grade 91 steel were used to prepare various samples within this study. Three pieces were supplied as sections of Grade 91 pipe, designated P91:A, P91:B and P91:C (pipe sections were supplied by EON). Two pieces were supplied as plate sections designated PL91:A (supplied by Tata Steel) and PL91:B (supplied by EON). The as-received condition of all five pieces was representative of the typical service entry condition; tempered martensite with varying hardness values as will be discussed in later chapters. A schematic diagram of P91:A can be seen in Figure 3-1 and the dimensions of all the Grade 91 steel sections are given in Table 3-1. Photographic images of all five bulk pieces of Grade 91 material can be seen in Figure 3-2. The chemical composition has been detailed in Table 3-2. Compositions for, samples P91:A and PL91:A were provided by EON and Tata Steel respectively, samples P91:B and PL91:B were attained through optical emission spectroscopy using a Foundry-Master PRO and WASLAB software and sample P91:C was measured using a Niton x-ray spectrometer.

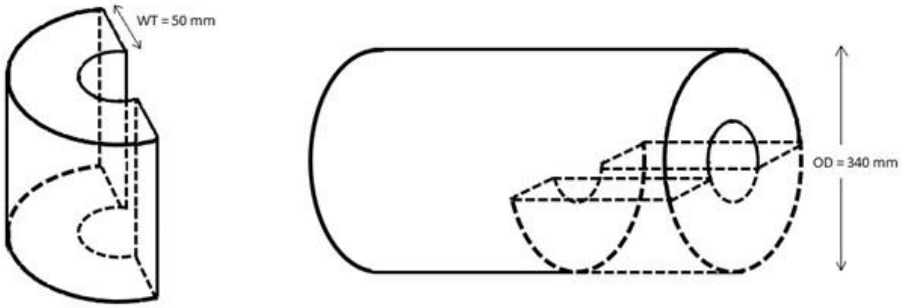

Figure 3-1: Schematic diagram to show the piece (dotted segment) of P91:A as taken from a larger pipe Section with a wall thickness (WT) of 50 mm and outside diameter (OD) of 340 mm

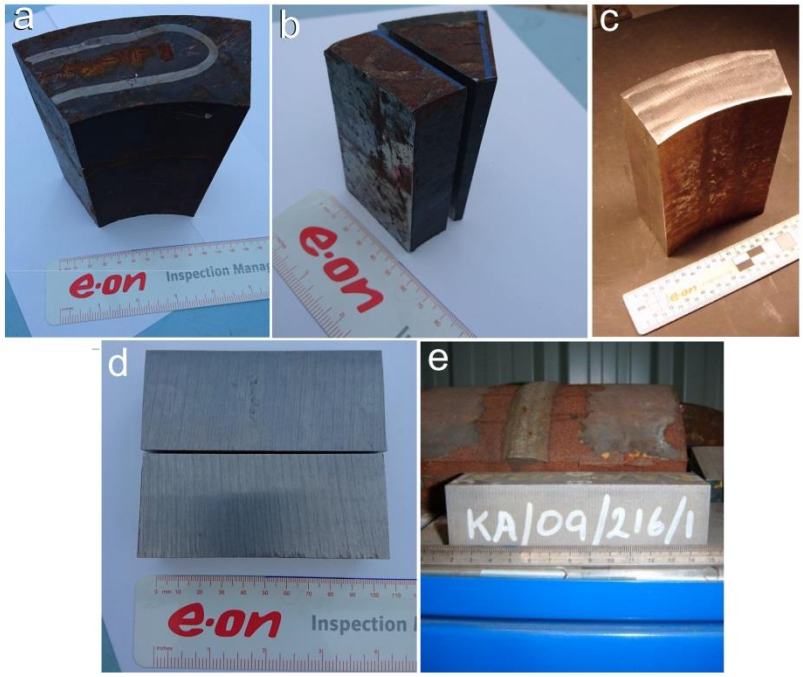

Figure 3-2: Images of Grade 91 material sections showing the as-received geometries (a) P91:A, (b) P91:B, (c) P91:C, (d) PL91:A, (e) PL91:B

Table 3-1: Dimensions of as received Grade 91 pieces

Sample	Type	Wall thickness (mm)	Height x Width (mm)
P91:A	Pipe	50	n/a
P91:B	Pipe	50	n/a

P91:C	Pipe	35	n/a
PL91:A	Plate	40	95 x 130
PL91:B	Plate	50	50 x 130

Table 3-2: Chemical composition of as received Grade 91 material

Element (wt. %)	Cr	Mo	C	Si	Mn	P	S	Ni	Al	Nb	V
P91:A	8.29	1.02	0.10	0.27	0.35	0.016	0.007	0.11	<0.01	0.07	0.22
P91:B	8.65	0.92	0.09	0.28	0.41	0.004	0.006	0.19	-	-	-
P91:C	8.55	0.96	-	-	0.71	-	-	-	-	0.07	0.26
PL91:A	8.84	0.90	0.11	0.21	0.41	0.012	0.006	0.11	0.003	0.08	0.20
PL91:B	8.49	0.89	0.09	0.31	0.42	0.005	0.009	0.19	-	-	-

3.2. Samples and Heat Treatments

The selection of samples used in this study were designed and produced on the basis of two challenges. Firstly, the power generation industry's challenge to non-destructively detect mis-heat treated (MHT) material using a U-shaped EM sensor, particularly on large components where the cylindrical shaped sensor is not practical; and secondly, the challenge that U-shaped sensors are far more sensitive to surface features than the cylindrical shaped sensors, and so the magnitude of the surface effect on the sensors ability to differentiate MHT from CHT material was important. Therefore two sets of samples were produced based on each challenge; a set of samples to study the impact of surface finish (i.e. surface roughness, work hardening, grinding and polishing) on the inductance values of the U-shaped EM sensor and a set

of heat treated samples with alike surface finishes to study the ability of the U-shaped EM sensor to be able to differentiate MHT microstructures from correctly heat treated (CHT) microstructures.

3.2.1. Heat Treatment Samples

In order to study the capability of EM sensors to differentiate aberrant Grade 91 material from correctly manufactured Grade 91 material, samples were heat treated to produce the different microstructures reflective of correctly heat treated (CHT) and mis-heat treated (MHT) material.

3.2.1.1. Correct Heat Treatment

To create a correctly heat treated Grade 91 service entry microstructure the Grade 91 material was normalised by heating samples (typically 50 x 50 x 10 mm) in an electric furnace at 1080 °C for 30 minutes followed by air cooling to produce a hard martensite microstructure. The material then re-entered the furnace for a tempering treatment at 760 °C for 1 hour, before it was air cooled; producing a tempered martensite microstructure, synonymous to that of a power plant boiler service entry material microstructure; a schematic of this heat treatment procedure is depicted in Figure 3-3a. These samples were identified with the acronym ‘CHT’ in the sample title.

3.2.1.2. Mis-heat Treatment

In some instances, rogue or aberrant material can be supplied by the manufacturer to the power plants due to mis-heat treatments leading to partially ferritic microstructures or un-tempered martensite as opposed to a fully tempered martensitic microstructure.

To replicate the aberrant material of a ferritic microstructure (as opposed to correctly heat treated tempered martensite) Grade 91 samples (typically 50 x 50 x 10 mm) were subjected to a heat treatment procedure provided by engineers at EON’s technology

centre (Heywood, 2006 cited in [23]). Samples were normalised at 1080 °C for 1 hour before being subject to a simulated furnace cool of 100 °C/hour down to 760 °C and held for 3 hours, followed by cooling in air. A schematic of this heat treatment procedure is depicted in Figure 3-3b and such samples were identified with the acronym ‘MHT’ in the sample title

Further heat treatment cycles were performed to replicate other manufacturing errors made by heat treatment operatives during the heat treatment stages of boiler component production; these have been detailed below:

- To mistakenly perform a furnace cool instead of an air cool following a typical normalising treatment. To replicate this, a sample (45 x 40 x 18 mm) was correctly normalised (1080 °C for 3 hours) following by a furnace cool (instead of being air cooled); this sample was designated as ‘FC’. A second sample (45 x 40 x 18 mm) was similarly normalised (1080 °C for 3 hours) and incorrectly furnace cooled but followed by a correct tempering treatment (760 °C for 3 hours); this sample was designated ‘FC+T’.
- To mistakenly over-temper the material, following a correct normalising treatment, typical due to operators exceeding the tempering time due to human errors during operator shift changes. To replicate this, two samples (45 x 40 x 18 mm) were correctly normalised (1080 °C for 3 hours and air cooled) followed by tempering for extended periods of time at the typical tempering temperature of 760 °C; one sample was tempered for 24 hours (designated ‘N+T24’) and the other was tempered for 100 hours (designated ‘N+T100’)
- To mistakenly over-normalise by exceeding the typical normalising treatment time and temperature, this can be caused by operators being mis-informed on furnace displays due to damaged or mis-wired thermocouples and extended

times for treatments due to human error. To replicate this, a sample (40 x 40 x 28 mm) was normalised at an incorrect temperature and time (1100 °C for 16 hours) followed by furnace cooling; this sample was designated ‘N1100+FC’.

All heat treated samples have been summarised in Table 3-3.

Table 3-3: Grade 91 thermal history and heat treatment procedures

Sample	Thermal history/ heat treatment	Dimensions (mm) (*l* x *w* x *h*)
P91:A-N	Pipe sample normalised at 1080 °C for 1 hour followed by air cooling	50 x 50 x 10
P91:A-AR	Pipe sample as-received in the normalised and tempered condition (sample is expected to be heat treated to a procedure similar to that shown in Figure 3-3a)	50 x 40 x 10
P91:A-CHT P91:B-CHT	Two pipe samples normalised at 1080 °C for 1 hour followed by air cooling to room temperature – followed by tempering at 760 °C for 1 hour followed by air cooling	50 x 50 x 10 45 x 40 x 18
P91:A-MHT P91:B-MHT	Two pipe samples normalised at 1080 °C for 1 hour followed by a programmed furnace cool down to 760 °C at 100 °C/hour and held at 760 °C for 3 hours before air cooling	50 x 50 x 10 45 x 40 x 18
P91:B-FC	Pipe sample normalised at 1080 °C for 1 hour followed by furnace cooling	45 x 40 x 18
P91:B-FC+T	Pipe sample normalised at 1080 °C for 1 hour followed by furnace cooling to room temperature, followed by tempering at 760 °C for 3 hours	45 x 40 x 18
P91:B-N+T24	Pipe sample normalised at 1080 °C for 1 hour and air cooled followed by tempering at 760 °C for 24 hours	45 x 40 x 18
P91:B-N+T100	Pipe sample normalised at 1080 °C for 1 hour and air cooled followed by tempering at 760 °C for 100 hours	45 x 40 x 18
PL91:A-AR	Plate sample as-received in the normalised and tempered condition	50 x 40 x 10

PL91:A-CHT	Plate sample normalised at 1080 °C for 1 hour followed by air cooling to room temperature – followed by tempering at 760 °C for 1 hour followed by air cooling	45 x 40 x 10
PL91:A-MHT	Pipe sample normalised at 1080 °C for 1 hour followed by a programmed furnace cool down to 760 °C at 100 °C/hour and held at 760 °C for 3 hours before air cooling	45 x 40 x 10
PL91:A-N1100+FC	Plate sample, wrapped in stainless steel foil and normalised at 1100 °C for 16 hours followed by furnace cooling	40 x 40 x 28
PL91:A-CHT:GB	Plate sample normalised at 1080 °C for 1 hour followed by air cooling to room temperature – followed by tempering at 760 °C for 1 hour followed by air cooling	45 x 40 x 10
PL91:A - MHT:GB	Pipe sample normalised at 1080 °C for 1 hour followed by a programmed furnace cool down to 760 °C at 100 °C/hour and held at 760 °C for 3 hours before air cooling	45 x 40 x 10

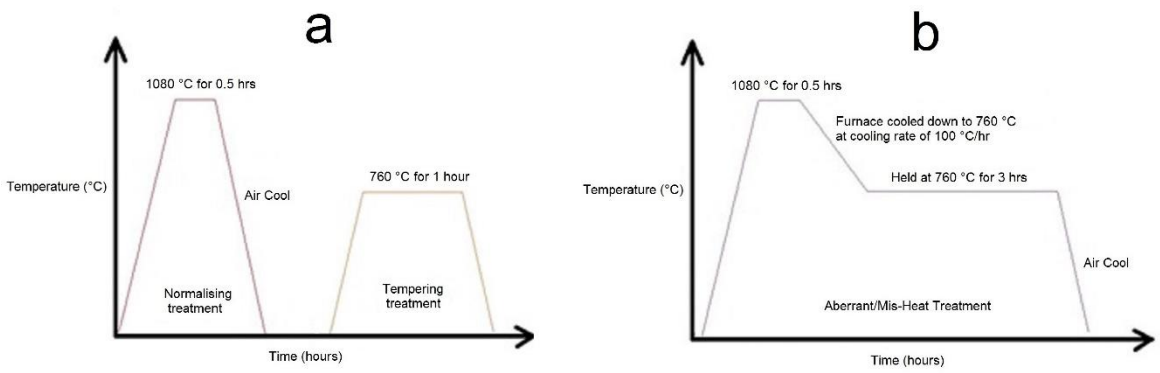

Figure 3-3: Schematic diagram of different heat treatment procedures, (a) Correct heat treatment consisting of 2 stages; normalising and tempering heat treatments to produce tempered martensite service entry microstructure, (b) Mis-heat treatment procedure which allows the generation of an aberrant/mis-manufactured microstructure

3.2.2. Surface Finish Samples

In order to carry out maintenance, repair work or prepare components for non-destructive testing in boiler units, components such as boiler headers and tubes can be exposed to various mechanical processing such as welding, cutting, grinding, wire

brushing, grit blasting etc. To study the impact such surface finishes have on the inductance of a U-shaped EM sensor, as well as the sensors ability to differentiate CHT material from MHT material, a number of samples were prepared with surfaces of varying surface roughness values and various degrees of work hardening.

3.2.2.1. Surface Roughness

To carry out trials on the effect of surface roughness on the EM signal, a total of five samples were prepared. Four samples were sectioned from Grade 91 material pipe section P91:A (Figure 3-2a) and the fifth sample was pipe section P91:C as-received (Figure 3-2c) was used to grind eight different surface finishes (on the same face) using a Transpol surface grinder, EM testing the surface each time a new surface was ground.

The four samples sectioned from P91:A all had similar dimensions of approximately 60 x 50 x 10 mm. Each sample underwent a machining operation to produce two surface finishes (one on either side of the sample's two largest faces), shown in Figure 3-4.

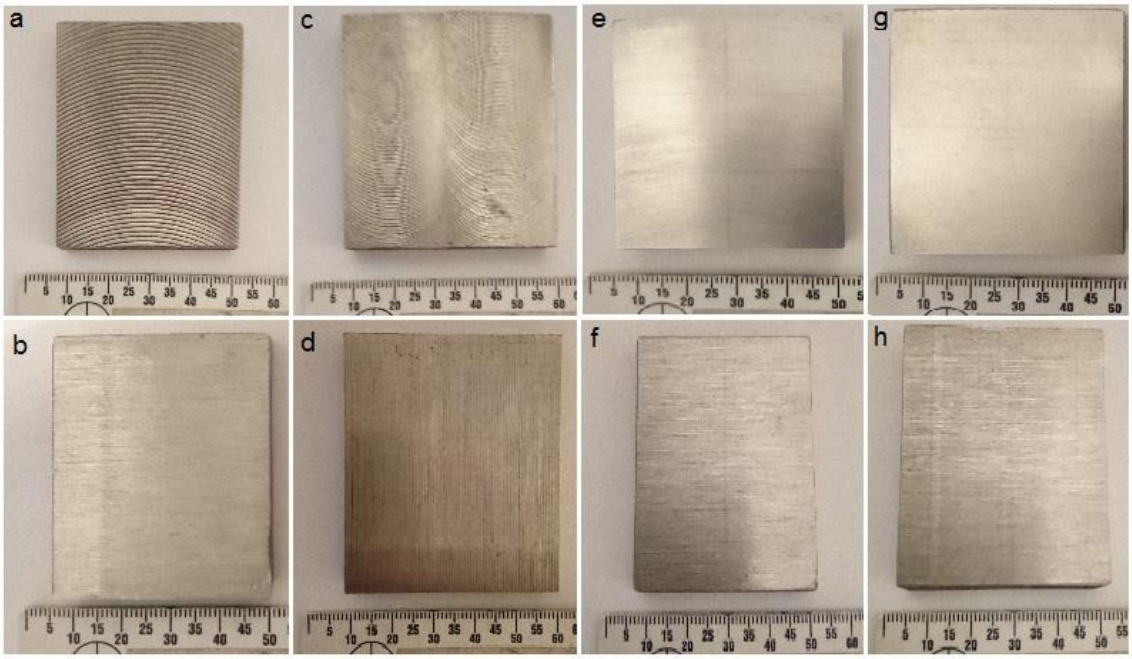

Figure 3-4: P91:A-AR samples machined with different surface finishes. (a) face milled large tool, (c) face milled small tool, (e) mechanically ground with 400 grit SiC paper and (g) mechanically ground using Al_2O_3 surface grinder, are four samples with different surface finishes, Beneath each of these samples [surfaces (b), (d), (f) and (h)] are the opposite surfaces of the samples pictured above them, e.g. surfaces (a) and (b) are opposite faces of the same sample. Sample surface (b), (d), (f) and (h) are prepared with the same horizontal bandsaw cutting process

The two largest surfaces of each sample have been displayed above and below one another in Figure 3-4; (e.g. surfaces displayed in Figure 3-4-a and Figure 3-4b are opposite surfaces of the same sample). Samples were sectioned using a horizontal bandsaw (HB) cutting machine and therefore one surface on each of the four samples had an identical surface finish of bandsaw machine lines, whilst the opposite face on each of the four samples was machined with a unique surface finish. The unique surface finishes were produced to achieve varying degrees of surface roughness profiles across the four samples which would encompass the typical range of surface finishes that may be found on components in a power plant boiler house, these were done using a 5-axis milling machine (to produce samples with coarse roughness values) and grinding papers and surface grinders (to produce samples with smooth

roughness profiles). The HB surfaces were used as a reference to ensure that comparable results could be obtained to confirm there were no microstructural differences between the samples and therefore the only difference between the samples was the surfaces with unique surface roughness profiles. Details of the samples and their corresponding surface finishes have been given in Table 3-4.

Table 3-4: Details of P91:A samples' surface finishes and figure references

Sample I.D.	Surface Finish	Figure Ref.
P91:A-FM1	Face milled using a large tool head spanning the width of the sample	Figure 3-4a
	Cut using a horizontal bandsaw	Figure 3-4b
P91:A -FM2	Face milled using a small tool head spanning half the width of the sample	Figure 3-4c
	Cut using a horizontal bandsaw	Figure 3-4d
P91:A -MG1	Mechanically ground using 400 grit SiC grinding paper until smooth	Figure 3-4e
	Cut using a horizontal bandsaw	Figure 3-4f
P91:A -MG2	Mechanically ground using an Al_2O_3 surface grinder to produce mirror-like finish	Figure 3-4g
	Cut using a horizontal bandsaw	Figure 3-4h

Pipe section P91:C was prepared with different surface finishes (on the same surface) using a Struers TransPol-5 hand grinder (Figure 3-5). This was done to replicate the different surface finishes that are produced on components in service as part of the surface replication NDT procedure. An example of the TransPol-5 hand grinder being

used to prepare a small area on a boiler component for surface replication can be seen in Figure 3-6, notice the small grinding head.

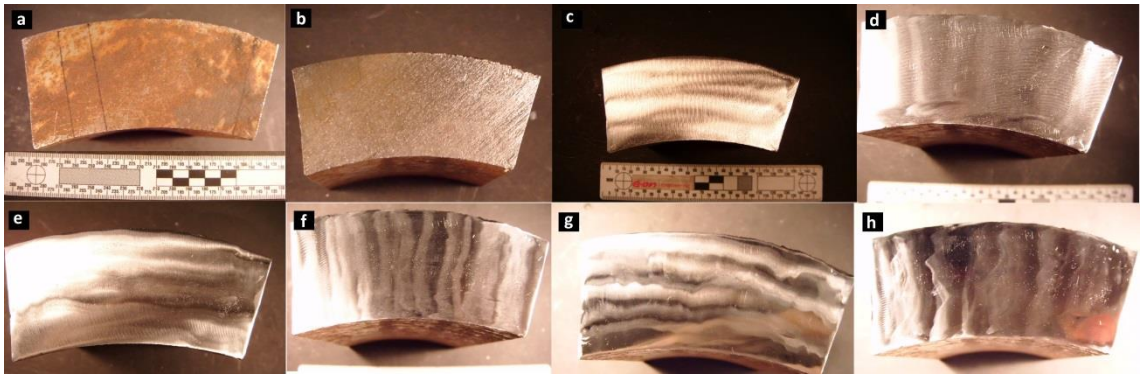

Figure 3-5: Different surface finishes applied to P91:C Grade 91 service entry material; (a) As-received corroded, (b) Wire brushed, (c) 60 Grit ground Transpol, (d) 120 Grit ground Transpol, (e) 240 Grit ground Transpol. (f) 400 Grit ground Transpol, (g) 600 Grit ground Transpol, (h) 1200 Grit ground Transpol

Figure 3-6: Example of TransPol-5 hand grinder being used to prepare a local surface area on a boiler component; typically used to prepare surfaces for surface replication, as it is capable of producing a mirror-like surface finish [191]

There are typically seven to eight surface preparation steps when performing surface replication NDT (detailed in Table 3-5). Therefore steps 1-7 in Table 3-5 were performed to produce different surface finishes on the P91:C pipe section, with EM tests performed on each surface as it was produced. From Figure 3-7 the difference in

surface finish can be noticed; Figure 3-7a shows the surface after it has been ground with the TransPol-5 hand grinder using a grade 60 grit grinding paper disc, from close observation the grinding lines produced by the coarse grit can be seen on the surface. Whereas Figure 3-7b shows the surface of the sample after it had been ground through all the grades of grit grinding paper discs from coarse to fine (60, 120, 240, 400, 600) finishing with the smooth 1200 grade grit grinding disc to produce an almost mirror-like surface finish, so much so that a reflection of the camera can be seen in the sample's surface.

Table 3-5: Different stages of surface preparation to prepare a material for surface replication

Step	Surface Replication Process
1	Wire brush erosion (for removal of surface corrosion or paint)
2	Grade 60 SiC grinding disc
3	Grade 120 SiC grinding disc
4	Grade 240 SiC grinding disc
5	Grade 400 SiC grinding disc
6	Grade 600 SiC grinding disc
7	Grade 1200 SiC grinding disc
8	Etching to reveal microstructure
9	Replication to produce microstructure on glass slide for optical inspection

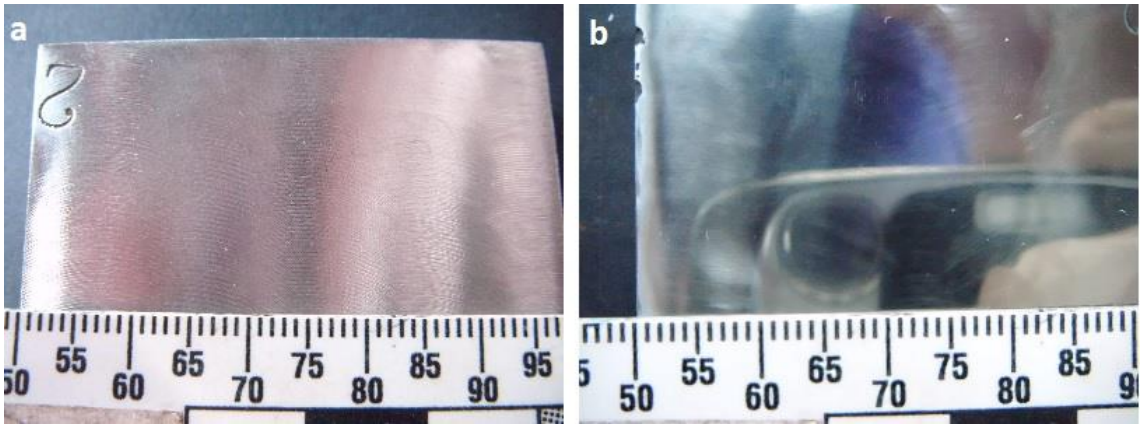

Figure 3-7: P91:A-AR samples with TransPol-5 surface ground finishes using (a) 60 grit disc and (b) 1200 grit disc

3.2.2.2. Grit Blasting

Grit blasting is used in the power generation industry to clean surfaces of corrosion, oxide layers and other refractory debris in preparation for non-destructive testing. Typical grit blasting parameters were adopted to produce samples with grit blasted surfaces similar to those which may be present within the utility power plant industry. A Vacublast machine was used at the University of Birmingham where a 50 x 50 x 10 mm section from P91:A with an as-received microstructure (tempered martensite) was grit blasted (Figure 3-8a) using the parameters identified in Table 3-6.

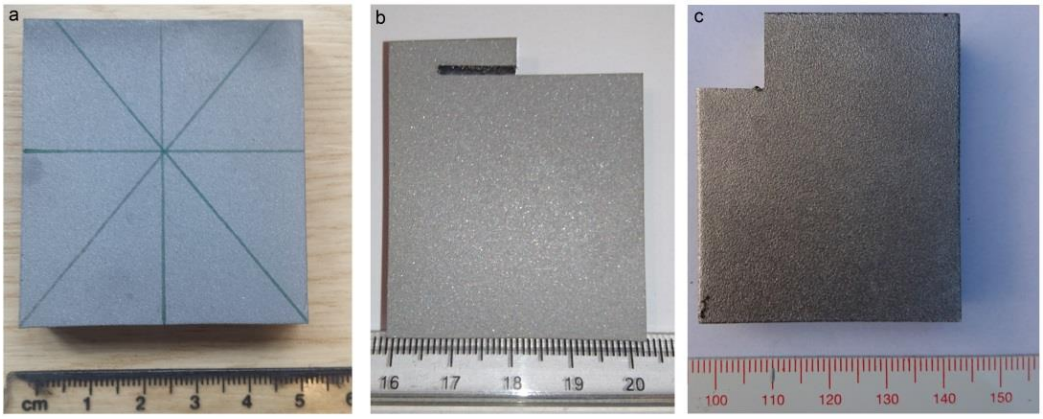

Figure 3-8:Images of Grade 91 samples with work hardened surface layers (a) P91:A-AR:GB grit blasted surface (b) PL91:A-GB grit blasted surface (c) PL91:A-SP shot peened surface

Table 3-6: Grit blasting parameters used to blast sample P91:A-AR:GB

Blasting medium	Alumina grit
Angle of nozzle to sample	90° (just off)
Grit pressure	120 psi
Distance of nozzle to sample	100 mm

To test whether the EM sensor could distinguish between CHT and MHT material with the presence of a work hardened surface layer, four Grade 91 samples of identical dimensions (50 x 40 x 10 mm) were sectioned from PL91:A. Samples were heat treated to produce 2xCHT and 2xMHT samples, which have been designated PL91:A-CHT:GB30, PL91:A-CHT:GB100, PL91:A-MHT:GB30 and PL91:A-MHT:GB100 (details of the heat treatments are given in Table 3-3 in Section 3.2). The designations of 30 and 100 reflect the standoff distance between the sample and the blasting nozzle. The samples were then grit blasted using a Vacublast at the Power Engineering Services workshops where EON's boiler assets are typically overhauled and repaired. The typical parameters for grit blasted Grade 91 components for surface cleaning purposes

have been given in Table 3-7, as identified by grit blasting operatives at the Power Engineering Services workshop.

Table 3-7: Grit blasting parameters applied to grit blasted samples PL91:A-CHT:GB and PL91:A-MHT:GB

Blasting medium	BA80C Alumina grit (ALUMAC BROWN)
Angle of nozzle to sample	90° (just off)
Grit pressure	90 psi
Standoff	30 and 100 mm
Traverse speed	Manual (uncontrolled)

The distance between the grit blaster nozzle and sample (30 and 100 mm) represents the minimum and maximum distances employed. 30 – 100 mm is the nominal distance adopted for grit blasting to remove any unwanted surface layers from Grade 91 components such as corrosion, oxides or refractory material. Below a 30 mm standoff distance between the component and blasting nozzle, the integrity of the material can be impacted as the nozzle and the component are too close, whilst above a distance of 100 mm can make it difficult to clean a component surface evenly. All four grit blasted samples had a similar surface appearance (Figure 3-8b)

3.2.2.3. Shot Peening

Shot peening is a cold working process which is utilised by the manufacturing industry to create the required mechanical properties of a component. Similar to grit blasting, shot peening will introduce a work hardening effect into the surface and near surface region of a component. Sample PL91:A-AR:SP with dimensions 50 x 40 x 10 mm was shot peened (Figure 3-8c) by Curtiss-Wright Metal Improvement Company, Derby, UK to peening parameters (typical within this industry) identified in Table 3-8.

Table 3-8: Shot peening parameters applied to sample PL91:A-SP

Blasting medium	MI230H (cast steel)
Medium diameter	58.5 µm
Medium hardness	610-810 HV
Angle of nozzle to sample	85°
Shot pressure	90 psi
Standoff	254 mm
Traverse speed	12.7mm/s

3.3. Experimental Equipment and Methods

3.3.1. Metallography

To attain microstructural information, small samples, typically 10 x 10 x 10 mm, were cut using a SiC disc (3000 rpm) and a Struers Accutom machine sectioning through the sample at 0.045 mm/s feed rate. Cut sections were mounted in Bakelite, using an OPAL 460 hot mounting press, before grinding the samples through different grit grades of SiC paper (120, 240, 400, 600, and 1200) using water as lubricant and then polishing to a 1µm diamond paste finish using a Struers polishing disc. Samples surfaces were then etched in Villella's reagent (30 second swab) to reveal the microstructures.

3.3.2. Light Optical Microscopy (LOM)

Etched samples were then viewed under an Olympus BX15M optical microscope and images were captured using Olympus Stream software.

3.3.3. Hardness Measurement

A Zwick Roell Indentec hardness indentation machine was used to obtain hardness measurements. For the hardness profiles at the surface, measurements at each depth from the surface were done in triplicate with an average taken of the three indents as well as calculating the error as standard deviation of the three indents. The procedure is schematically depicted in Figure 3-9 for clarity.

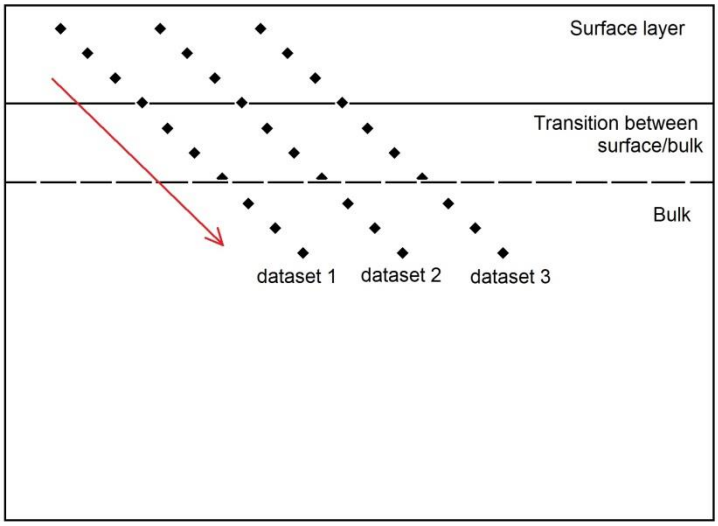

Figure 3-9: Schematic diagram showing three sets of hardness indent profiles such that an average of three measurements at each incremental depth from the surface was taken

Hardness indentation was performed in accordance with BS EN ISO6507-1:2005 which stipulates the required distance between indents (shown schematically in Figure 3-10).

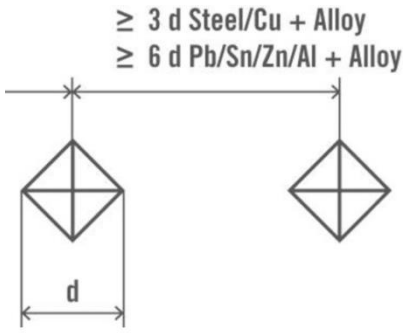

Figure 3-10: Schematic image demonstrating distance between hardness indents

Figure 3-11 shows a micrograph with typical hardness indentations showing the distances between indents and the surface complied with BS-6507. The size (load) of indentation was selected based on the thickness of the surface layer across which a hardness indentation was required. Since surface layers were relatively thin, the smallest indent size/load was adopted (0.2 kg) with typical indent diameters (*d*) of 50 μm.

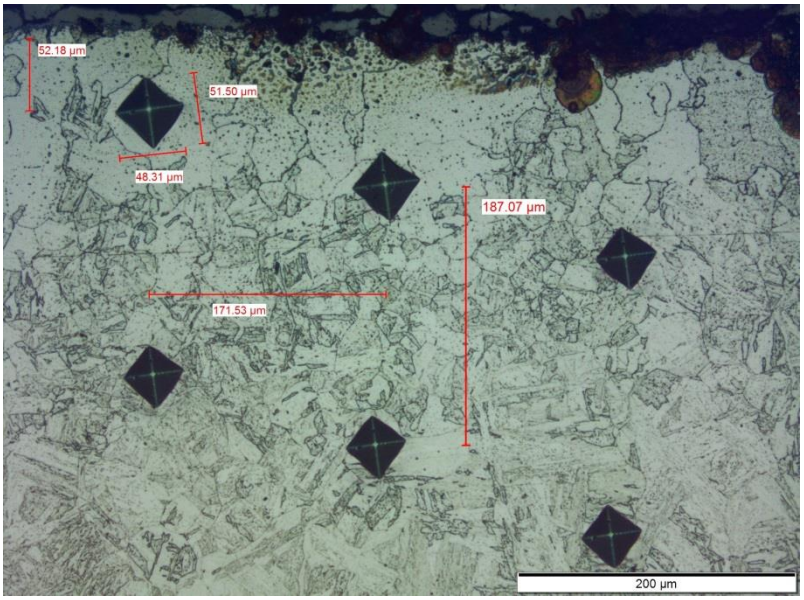

Figure 3-11: Micrograph of sample P91:B-N+T24 surface showing distances between hardness indents ≥ 3*d*

3.3.4. Surface Roughness Measurement

To measure the surface roughness values of samples a Surfcorder SE1700 profilometer was used. The profilometer measures the profile of a surface by traversing a 2 μm diamond talysurf tip, typically up to 8 mm, across the surface of a sample and outputs the amplitude parameters for the surface roughness profile. The arithmetical mean deviation roughness parameter (Ra) represents the average height of the surface profile undulations from the mean line (Figure 3-12). The Ra parameter is the most commonly used parameter within industry and hence the Ra parameter was

obtained for all samples when measuring the surface roughness. For some samples the maximum roughness depth or largest peak-to-valley depth of the profile (Rmax) was obtained. The Rmax surface roughness parameter represents the maximum roughness (i.e. the largest peak-to-valley depth) whereas the Ra parameter represents the average height of the peaks from the mean line, the difference can be observed schematically in Figure 3-12. When considering the impact that the surface roughness profile may have on the EM sensor then it is possible that the roughness profile essentially lifts the EM sensor away from the bulk of the sample and as such the Rmax parameter of the roughness profile may be more useful in exploring the influence of roughness on the EM sensor. It is likely that the magnetic flux will take the 'easy' path as it travels down the EM sensor's legs, into the surface and across the surface of the material (shown schematically in Figure 3-13). When the magnetic flux reaches the surface, the 'easy' path of travel would be through the sample bulk, just below the surface roughness profile (shown schematically in Figure 3-13) as opposed to travelling through the peaks and valleys of the surface roughness profile. This is because the sample bulk (immediately beneath the roughness profile) presents a lower resistance path compared to the roughness profile as there are air gaps between the roughness peaks. In this way, the majority of the magnetic flux is travelling through the sample at a distance (or effective lift-off) of Rmax from the point where the EM sensor is in contact with the surface and hence the Rmax parameter is more representative when considering the impact of the surface roughness on the EM signal.

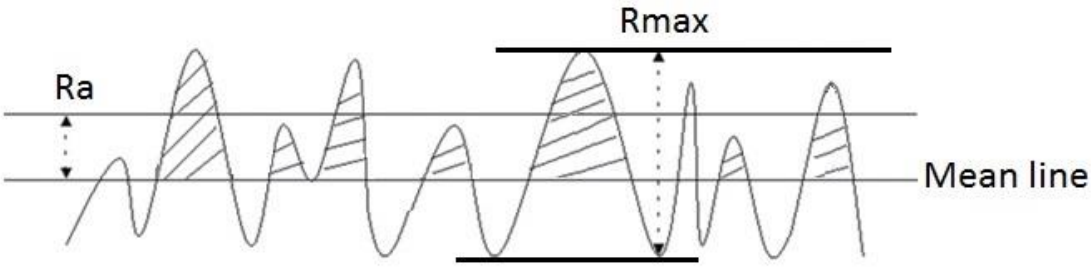

Figure 3-12: Schematic depiction of surface roughness parameters adapted from [192]

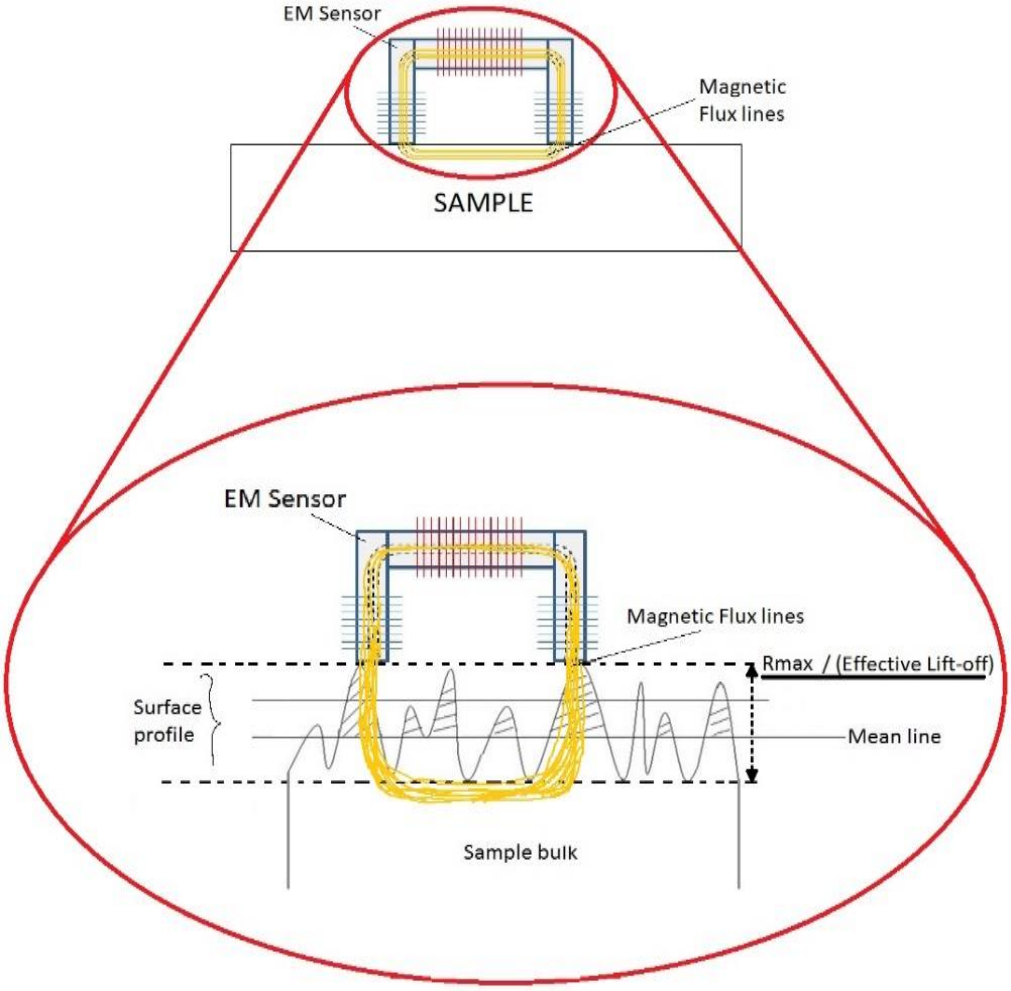

Figure 3-13: Schematic diagram showing EM sensor on sample surface highlighting potential interaction of magnetic flux lines (orange) with sample and influence of surface roughness (Rmax) as an effective lift-off type effect

3.3.5. Producing a Decarburised Surface Layer

Typically, between 1.5 – 2 mm of decarburised surface layer can be found in mis-heat treated service entry components at EON and this usually occurs during the normalising heat treatment at high temperatures (exceeding the specified normalising temperature of 1080 °C), since the carbon is in solution at these temperatures and diffusion of the carbon atoms is more favourable. Therefore to replicate these microstructures, the simplified version of Fick's second law of non-steady state diffusion (Eq. 3-1) was employed to indicatively calculate the time and temperature requirements to produce a certain depth of decarburisation from the surface of the material.

$$x^2 = Dt \qquad \textbf{Eq. 3-1 [77]}$$

Where *x* is the depth to which the non-steady state diffusion (in this case decarburisation) takes place after a time *t* with the diffusion coefficient as *D*. Given the diffusion coefficient for carbon in austenite at 1100 °C is 5.3 x 10^{-11} m^2s^{-1} [77] then the heat treatment time can be calculated for a given target depth of decarburisation. Thus rearranging Eq. 3-1 and entering values for *D* and *x* suggested that the heat treatment should be performed for approximately 21 hours (Eq. 3-2).

$$t = \frac{x^2}{D} = \frac{0.002^2}{5.3 \times 10^{-11}} = 75{,}471.69 \text{ s} \approx 21 \text{ hrs} \qquad \textbf{Eq. 3-2}$$

For practical reasons the heat treatment was performed for 16 hours which should yield a decarburised layer approximately 1.5 – 2 mm deep. A piece of material with dimensions 40 x 40 x 27 mm was sectioned from PL91:A to produce sample PL91:A-N1100+FC (Table 3-3). Initially, the heat treatment was causing the material to oxidise significantly, such that any decarburised surface layer would be consumed by the oxide and spall off upon removal from the furnace. Therefore to reduce the oxidising

atmosphere, the sample was wrapped in multiple layers of stainless steel foil (Figure 3-14a), which protected the decarburised surface layer from significant oxidation, by forming a sacrificial barrier to oxidation (Figure 3-14b).

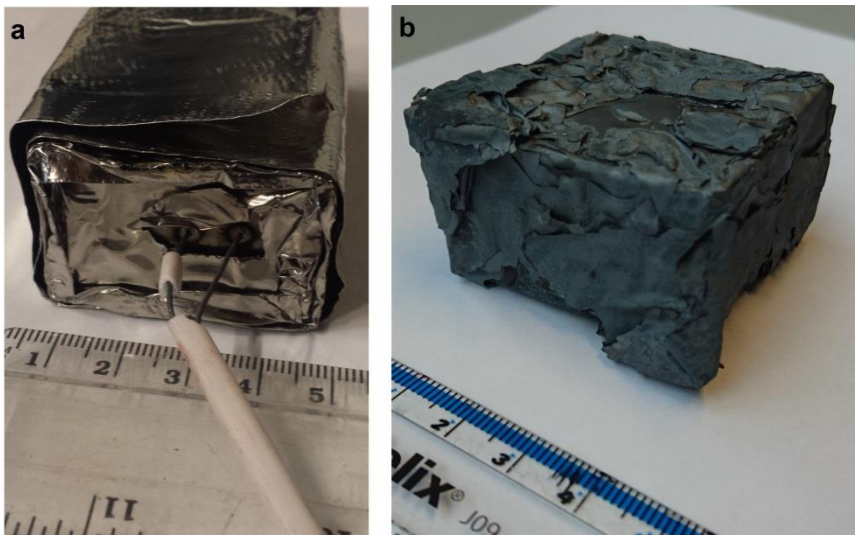

Figure 3-14: Sample PL91:A-N1100+FC wrapped in stainless steel foil, (a) before entering the furnace, (b) post heat treatment and removal from furnace

3.3.6. Measuring Depth of Decarburised Surface Layer

10 x 10 x 10 mm samples were sectioned from samples with aberrant and decarburised surface layers mounted in Bakelite and prepared and etched to reveal the microstructure. Optical micrographs of the aberrant and decarburised surfaces were captured using the Olympus Stream software and used to take measurements of the depth of the aberrant and decarburised surface layers. 10 measurements at approximately 1 mm increments were averaged to obtain a measurement for the depth of the surface layers. An example of two measurements being made can be seen in Figure 3-15.

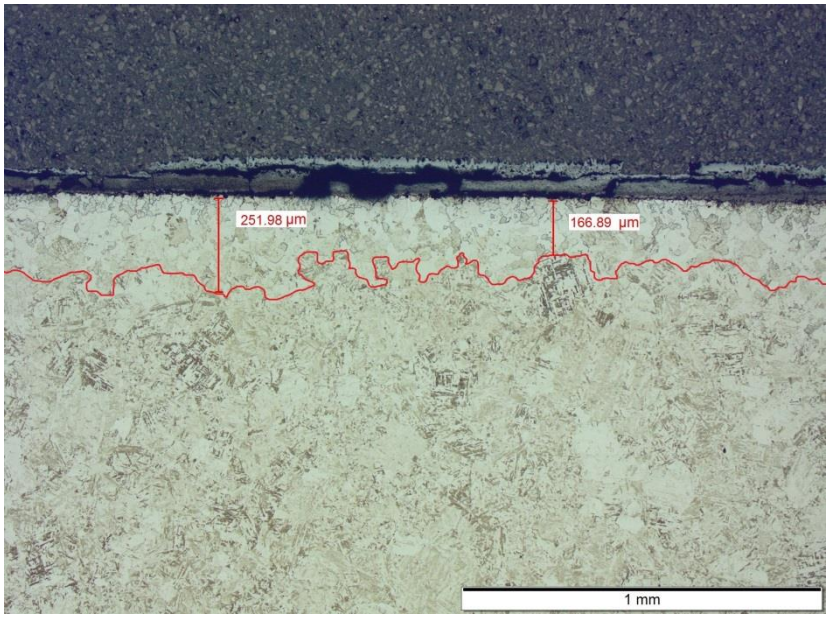

Figure 3-15: LOM image showing the method with which the depth of the aberrant surface was measured using the measuring tools with Olympus Stream software

3.3.7. Progressively Removed Surface Layer Measurements

To measure the inductance value of material with different depths of aberrant surface layers, samples PL91:A-N1100+FC (partially decarburised aberrant surface layer) and PL91:A-SP (shot peened surface layer) were incrementally ground to progressively remove material from the surface. Each newly revealed surface would then be tested using the EM sensor (see Section 3.4 for details of how the EM sensor was used). Samples were manually ground on a SiC grinding wheel using different grades of grit paper (120/240/1200), depending on how much material was due to be removed per increment. To measure the amount of material that had been removed by the grinding process, a micrometer was used to measure the thickness at five different points across the sample to gain an average thickness representative of the sample (shown schematically in Figure 3-16).

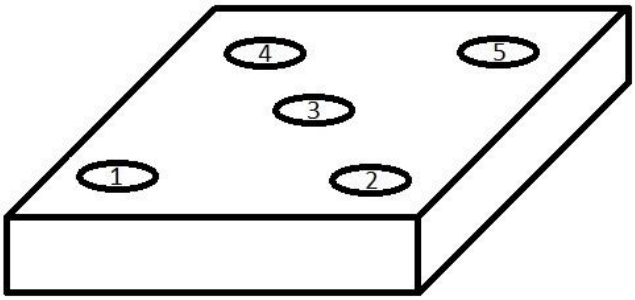

Figure 3-16: Schematic diagram showing five locations where sample thickness was measured using a micrometer for progressively removed surface material test

3.4. EM Sensor

3.4.1. Design and Manufacture

For the purpose of this research a U-shaped sensor was utilised, dimensions of the sensor core are shown in Figure 3-17. A sensor of this size and shape is based on practicality with respect to this technique being used in complement to already existing power generation utility's non-destructive assessment of boiler component microstructures using the surface replication technique. A small surface area, typically 100 x 100 mm on the surface of a boiler component is usually prepared (polished and etched) for surface replica assessment. It would be practical from a non-destructive testing regime perspective to be able to use the EM sensor technique simultaneously on the same prepared surface as the surface replication assessment and as such, a small U-shaped EM sensor is practical and hence used in this study.

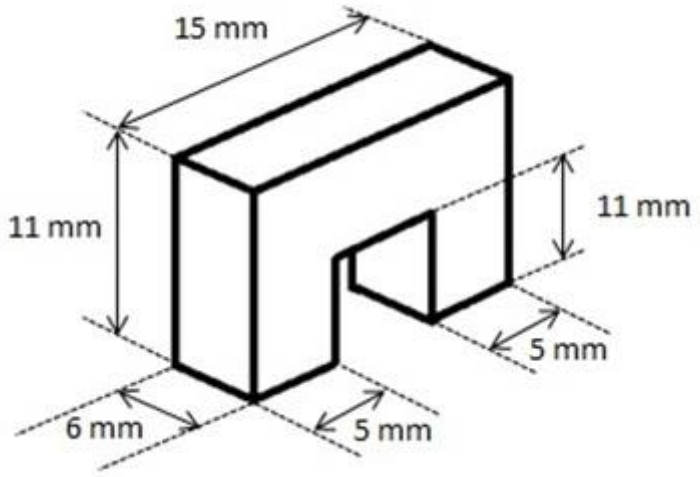

Figure 3-17: Schematic diagram of the U-shaped sensor core with dimensions

The sensor is formed of two components; firstly a ferrite core (purchased from MagDev Ltd.) and secondly, two enamel-coated copper wire windings, to produce coils. One wire is used to wind an excitation coil around the bridge of the sensor and a second wire is used to wind two sensing coils in series around the legs of the core (Figure 3-18).

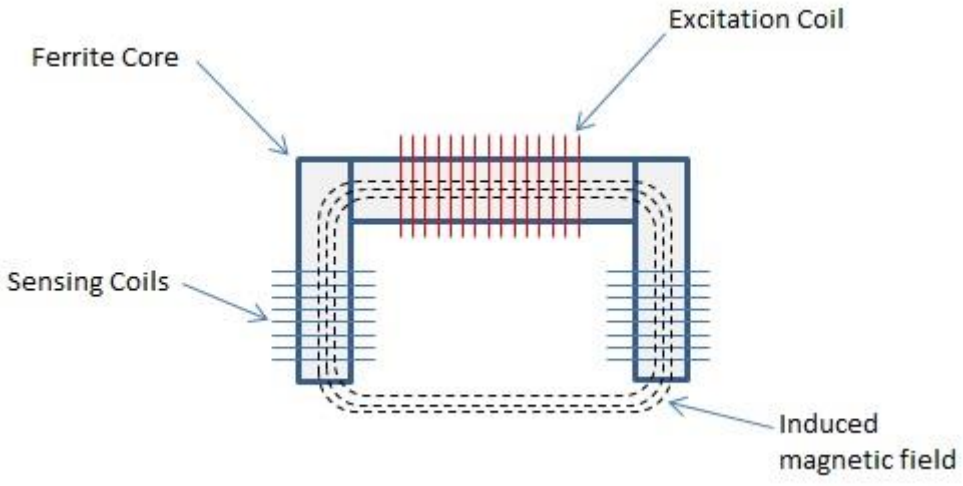

Figure 3-18: Schematic diagram of U-shaped EM sensor

The ferrite core specification is Epcos N30 which is a MnZn based soft ferrite core with typical room temperature initial permeability value of 4000. The ferrite core acts as a medium for the generating magnetic field flux lines to travel through, due to its high magnetic permeability, which increases the induction within the material being tested; shown schematically as red lines of magnetic flux in Figure 3-19.

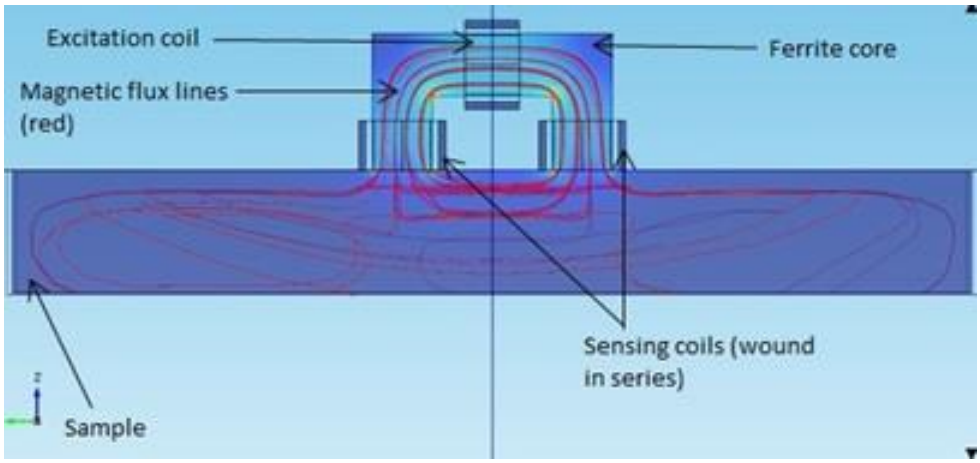

Figure 3-19: Schematic image of the EM sensor on top of sample highlighting the (red) lines of magnetic flux travelling through the sensor and penetrating the sample

Figure 3-20 shows the sensor and wire winding direction; due to the thin diameter wire, they were protected from the sharp edges of the ferrite core by wrapping the ferrite core with PTFE tape before winding the coils. To protect the coils from damage, PTFE tape was also wrapped around the coils (once they were wound). There were 20 turns on the excitation coil wound using 0.5 mm diameter enamelled copper wire and a 0.25 mm enamelled copper wire was used to wind the two sensing coils on each leg of the ferrite core (20 turns on each leg). 20 turns were the maximum number of turns achievable for the ferrite core size, limited by space.

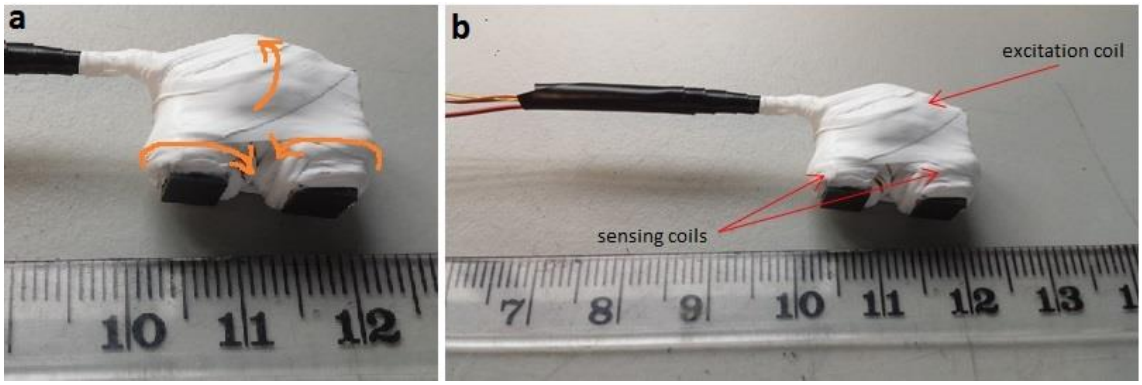

Figure 3-20: (a) Close up of sensor core showing the direction in which the copper coils were wound. (b) Image of sensor core showing location of excitation coil and sensing coils (underneath white PTFE tape) before encasing in epoxy resin encasing

Once the copper coils had been wound on the ferrite core, the whole assembly was encased in epoxy resin. The epoxy resin brought stability to the sensor and acted as protection for the copper coils from external damage. A clean plastic food packaging container was used as a mould within which the ferrite core was placed before immersing it in epoxy resin until it set (Figure 3-21a-b). The bottom of the epoxy base was ground using silicon carbide (SiC) paper on a metallurgical grinding wheel. Due to the small size of the sensor it needed to be hand held for the grinding procedure and significant care was taken to ensure the sensor was held horizontal until the sensor's feet were exposed, therefore the ferrite core feet would come in contact with samples when testing and thereby removing any lift-off and ensuring that the sensor sat flat and level on the test surface (Figure 3-21). The four ends of the two wires on the sensor coils (excitation coil and sensing coil) were each individually soldered onto a 4 mm banana plug, the plugs provided protection for the delicate wires and made the sensor more robust; two of these banana plugs can be seen in Figure 3-21d, with the other two directly beneath them and not visible in the image

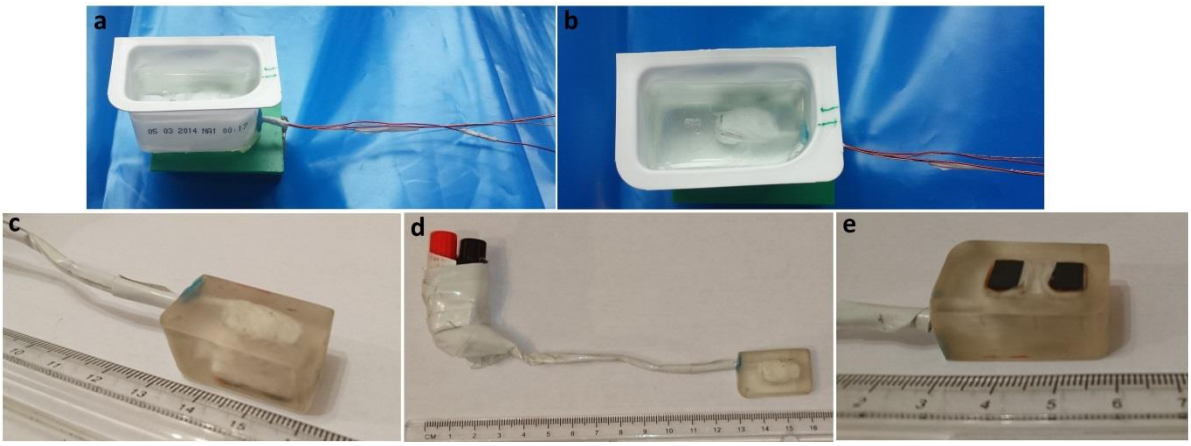

Figure 3-21: (a-b) Images of sensor being encased in epoxy resin, (c) image of EM sensor after epoxy resin had set, (d) EM sensor full assembly with connecting ports to the impedance analyser, (e) underside of sensor to show ferrite core feet flush with the epoxy base

3.4.2. EM Sensor Operation

The EM sensor is connected to a multi-frequency impedance analyser and the EM sensor is placed on top of the sample to carry out tests; as shown in Figure 3-22. The sensor is held in position by hand to maintain good contact between the sensor and the sample and avoid any lift-off between the sample and sensor as it has been previously discussed in Section 2.5.4.1 that a lift-off between the sensor and test sample will have a decreasing impact on the inductance of the sensor due to the non-conductive air gap created by the lift-off, similarly if a surface had significant roughness to cause any degree of air gaps between the sensor and the sample then this may have a similar diminishing effect on the inductance of the sensor. For ease, a nylon weight (280 g) was adopted and positioned on top of the sensor to maintain consistent contact with samples for all EM measurements in this research (shown later in Figure 3-31).

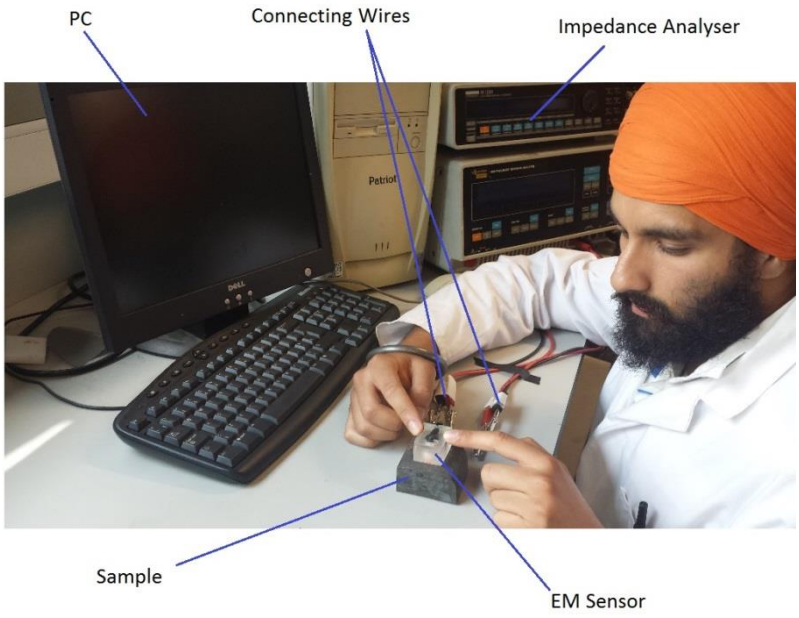

Figure 3-22: Typical sensor sample arrangement for performing an EM test

A multi-frequency Impedance Analyser (Model S1260 made by Solartron Analytical) passes a 3V AC current through the excitation coil at a range of frequencies from 1 Hz to 1 MHz, which in turn induces an AC magnetic field in the test sample. The sensing coils pick up changes in the magnetic field caused by the interaction between the magnetic field and the test sample [20]. Signals detected by the sensing coil were recorded and processed by the impedance analyser to give the imaginary part of the complex trans-impedance *Z*, from which the mutual inductance *L* was calculated using Eq. 3-3; where ω is the angular frequency and *j* is the imaginary unit [27]. The impedance analyser was controlled using a PC. A schematic diagram of the system set-up can be seen in Figure 3-25

$$L = \frac{Z}{j\omega} \qquad \textbf{Eq. 3-3}$$

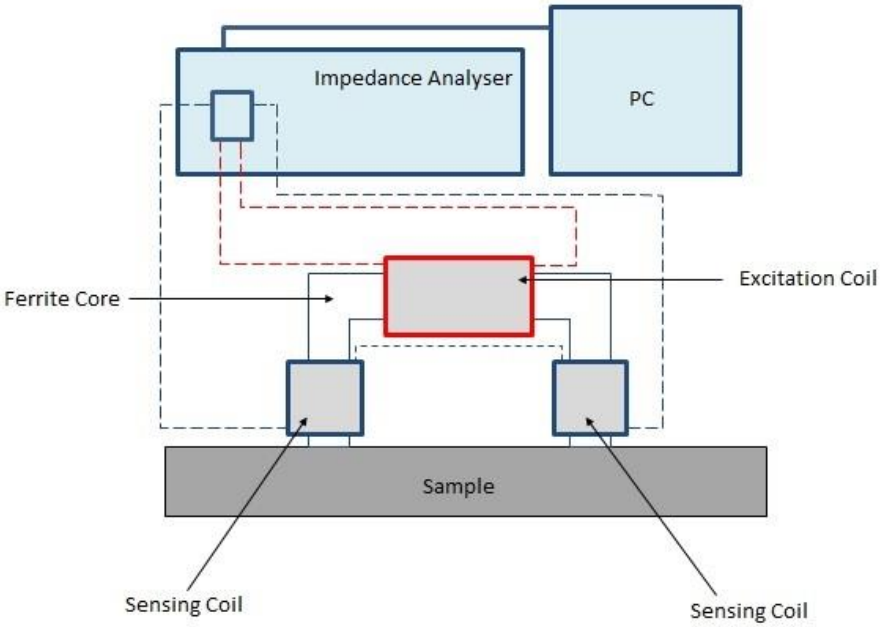

Figure 3-23: Schematic diagram of the system set-up, dashed lines represent connecting wires between the sensor coils and the impedance analyser

There were two formats of presenting data from the EM sensor inductance measurements; one format was a plot of inductance against frequency and the second was a plot of the inductance values at a set frequency. An example plot of an EM sensor measurement showing the multi-frequency inductance curve is given Figure 3-24 where a 50 x 50 x 10 mm Grade 91 sample with a correctly heat treated tempered martensite microstructure. The EM sensor's inductance response is sensitive to the material's electromagnetic properties (permeability and resistivity). A distinct difference can be seen for the EM sensor's inductance response depending on the frequency. At low frequency the inductance is dominated by the test sample's permeability, where typically a plateau region will be seen. As frequency increases the inductance becomes dominated by the test sample's resistivity, this is due to the generation of eddy currents in the test sample with increasing frequency [135].

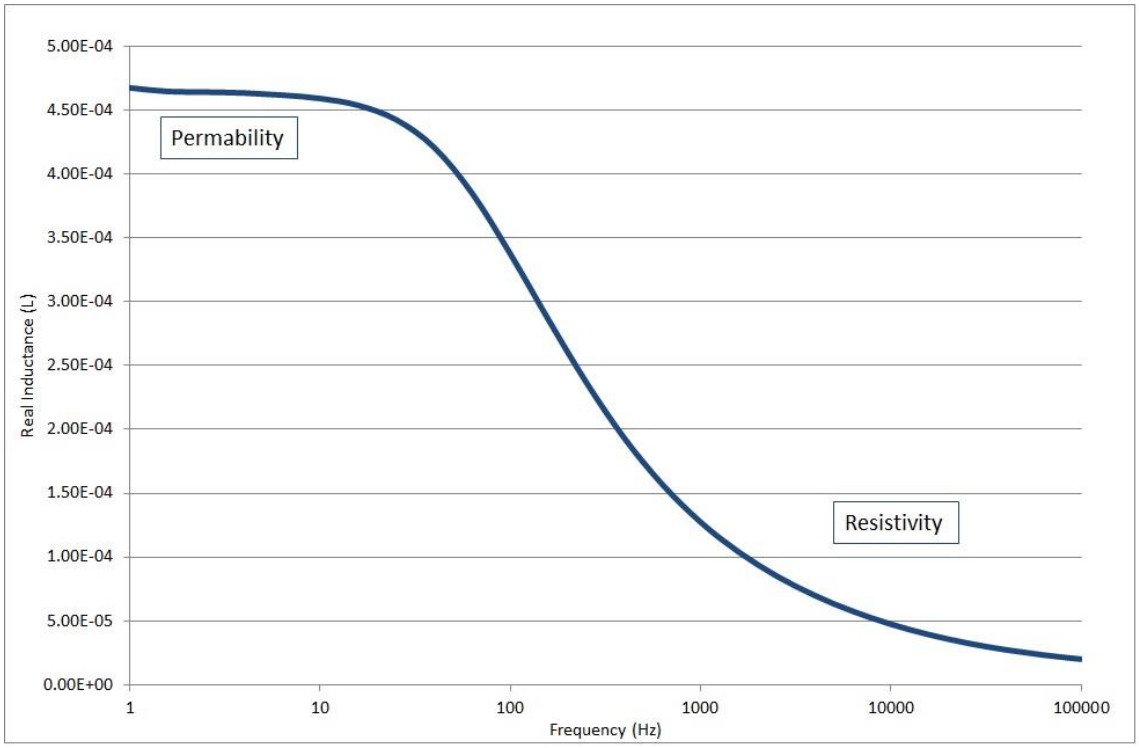

Figure 3-24: Typical EM sensor measurement plot of multi-frequency inductance for a Grade 91 correctly heat treated sample. Low frequency inductance is sensitive to the material's permeability where as high frequency inductance is more sensitive to the material's resistivity

To achieve inductance results representative of the whole sample surface, numerous tests were performed across the sample's surface. The size (surface area) of the sample being tested determined the number of separate tests that were performed on the sample. For larger sample surface areas, typically 50 x 50 mm, eight measurements were made in different orientations and locations over the sample surface (shown in Figure 3-25a), the eight measurements were used to gain an average inductance value and standard deviation. For smaller sample surface areas (typically 45 x 25 mm) only 4 measurements were performed as shown in Figure 3-25b to get an average and standard deviation for the sample.

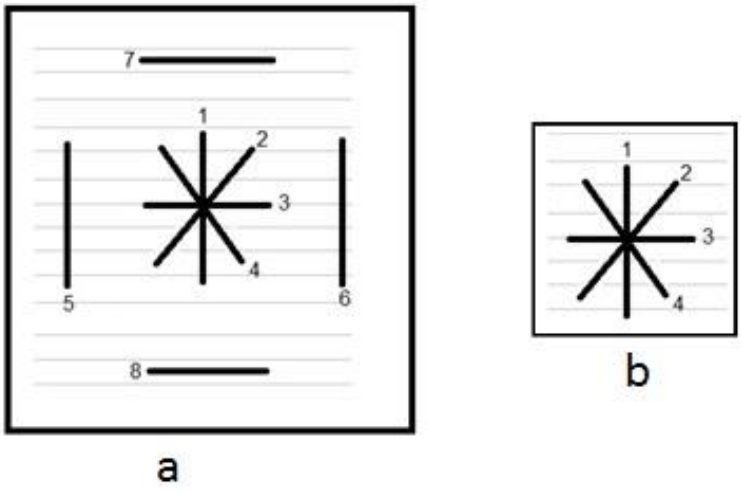

Figure 3-25: : Schematic diagram for EM sensor standard operating procedure to attain standard deviation statistical data (a) 8 different locations and orientations, (b) 4 different locations and orientations

3.4.3. Effect of Sample Edges

Material available for experimentation was limited and as such, required careful sectioning to produce enough samples to fulfil the experimental regime. Therefore it was important to determine minimum sample dimensions (length, width and thickness), below which the dimensions of the sample would significantly affect the EM signal which would make it difficult to compare results for samples with different dimensions.

The proximity of EM sensor to the sample edges has been shown to have an effect on the EM signal; denoted as edge effect [188]. The edge effect will be different for different sensors as it is dependent on the strength of the field applied, sensor geometry, lift off, and sample permeability. The majority of the induced magnetic field is located between the EM sensor's legs; however a significant amount of the field extends beyond the sensor's legs as can be seen from the COMSOL image shown in Figure 3-26 for a typical U-shaped EM sensor. Therefore it was important to understand the impact of edge effects on the EM sensor used for this study. To do this

the EM sensor was positioned parallel and perpendicular to the sample edges and incrementally traversed across the sample measuring the signal at different distances from the edges as depicted schematically in Figure 3-27.

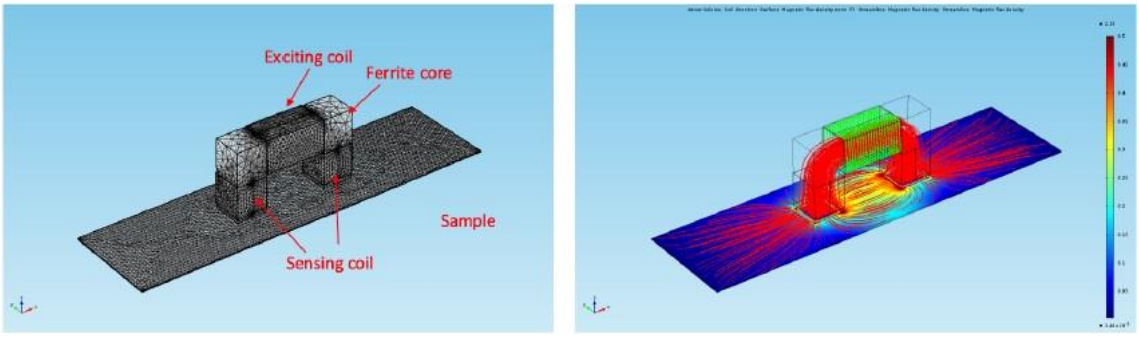

Figure 3-26: COMSOL image showing electromagnetic field distribution within a sample for a typical U-shaped EM sensor [193]

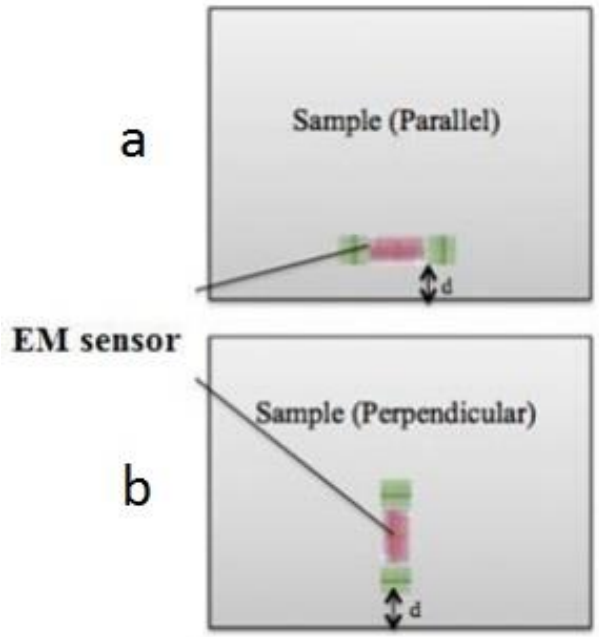

Figure 3-27: Birds eye view schematic diagram showing EM sensor positioned in (a) parallel and (b) perpendicular to the samples edge, image modified from [188]

A Grade 91 sample (P91:A-N) of approximately 50 x 50 x 10 mm in dimensions was used for the study. The material had a normalised martensitic microstructure. The EM sensor was positioned flush with the sample's perpendicular and parallel edges (as shown in Figure 3-27), such that the sensor did not extend beyond the sample edge. Then, inductance measurements were taken from the edge of the sample incrementing towards the centre of the sample at 2 mm increments. A total of three repeat tests per increment were taken to produce the standard deviation error bars. Figure 3-28 clearly shows that a significant edge effect exists for the sensor from both the perpendicular and parallel sample edges. There is a notable decrease in EM signal when the sensor is less than 4 mm from the parallel sample edge, and less than 8 mm from the perpendicular sample edge. This suggests that there is a greater impact on the EM sensor's inductance when the sensor is when the sensor is perpendicular to the sample edge than when the sensor is parallel to a sample edge. This difference is due to the amount of induced field contained within the sample which is greater when the sensor is in closer proximity with a parallel sample edge than a perpendicular sample edge. When the sensor is in closer proximity to a perpendicular sample edge, then a greater amount of induced field is lost beyond the sample edge and hence the decrease in the inductance value. Therefore, considering the sensor dimensions (given in Figure 3-17), the minimum sample surface area to avoid edge effect should be 14 x 31 mm.

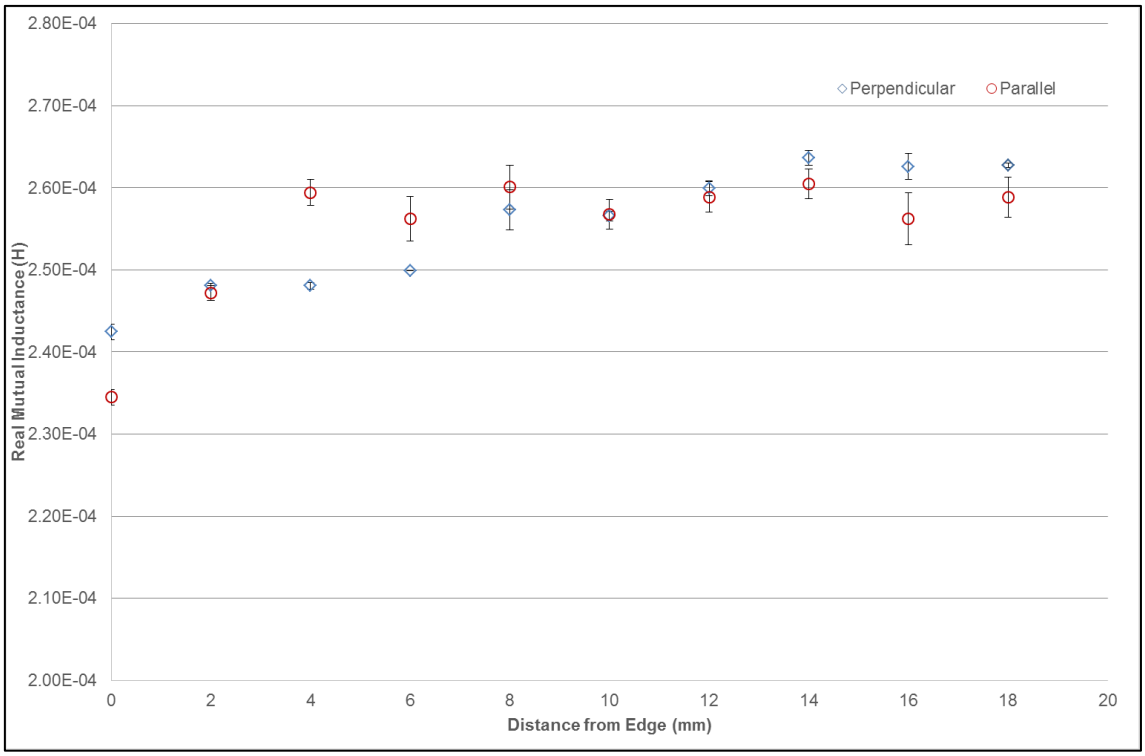

Figure 3-28: Variation of inductance (at single frequency of 10 Hz) with distance of sensor from parallel and perpendicular sample edges

3.4.4. Effect of Sample Thickness

It was important to determine what (if any) effect sample thickness has on the EM signal to deduce minimum thickness dimensions. Nine samples were sectioned from a piece of Grade 91 material designated PL91:B (Figure 3-2e) with equal cross sectional surface area (40 x 40 mm) but varied in thickness between 2 mm and 54 mm. Four measurements were taken per sample to produce standard deviation error bars. The results suggest that a significant thickness effect exists for samples below 5 mm as can be seen in Figure 3-29. The inductance significantly increases as the sample thickness is increased from 2 mm – 5 mm, after which the data plateaus such that there is no significant difference in inductance for samples with thickness between 5 mm and 54 mm. This phenomenon can be explained by the skin depth effect whereby the skin

depth is larger than the thickness of the thin samples (2 – 5 mm) leading to the induced field penetrating the complete depths of the thin samples; hence why there is a sharp increase in the inductance. However, for samples with a thickness of 5 mm and above, the maximum skin depth is not larger than the thickness of the samples and as such the induced field is penetrating to a similar depth (maximum skin depth) within each sample (5 – 54 mm thick) and hence why the inductance values are stable over these thicker samples. Therefore the sample thickness needs to be greater than 5 mm to avoid a thickness effect on the EM sensor signal. If samples less than 5 mm are to be assessed then a calibration curve (or full FE model) would be required to eliminate the effect of thickness.

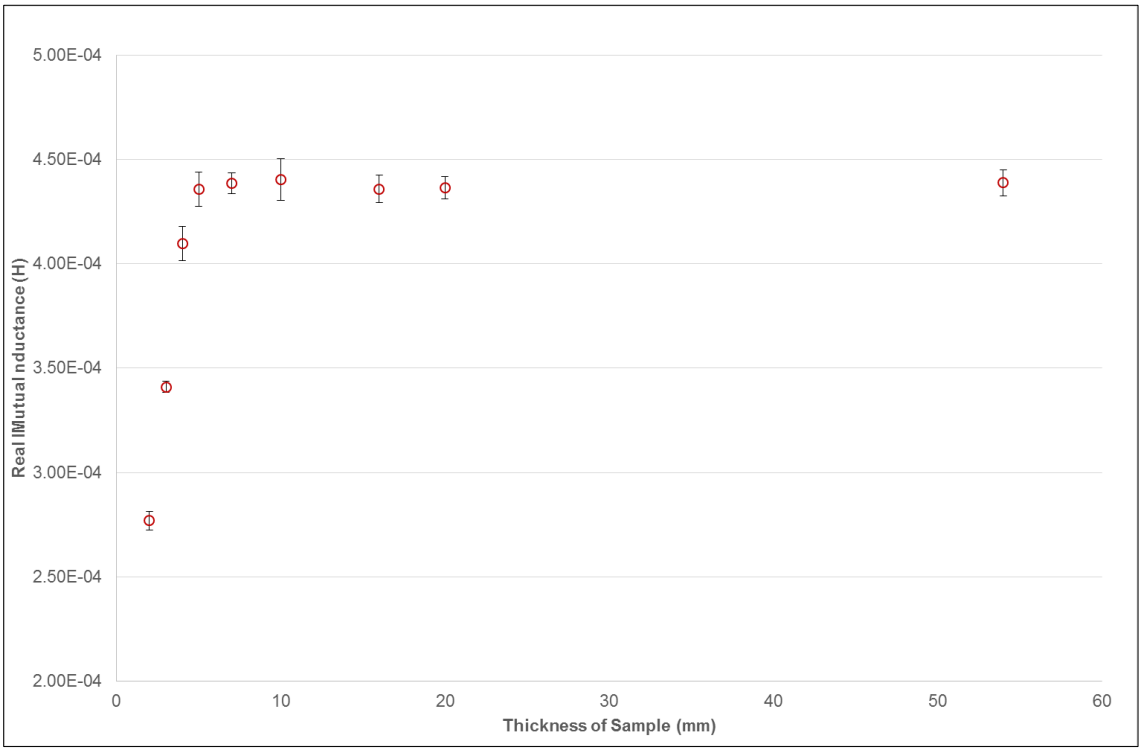

Figure 3-29: Variation of EM signal with sample thickness for Grade 91 steel sample

Taking the results of edge effect and thickness effect into consideration, for this sensor, the minimum sample dimensions to avoid effects of sample thickness and edge effects have been schematically depicted in Figure 3-30. If samples with smaller dimensions

(than those shown in Figure 3-30) are to be considered, then sample geometries must be identical to be able to compare the EM signal.

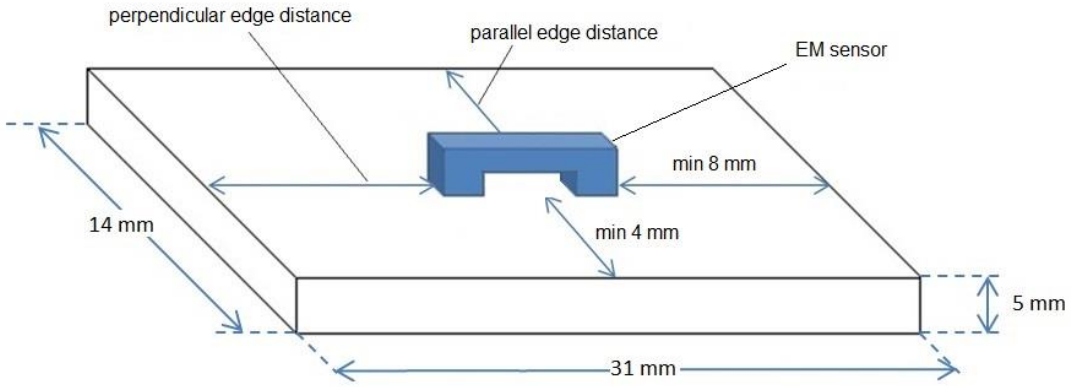

Figure 3-30: Schematic diagram of minimum sample dimensions when using this EM sensor

3.4.5. Effect of Sensor Lift-Off

The lift-off effect has been well established within the literature (discussed in Section 2.5.4.1), so the lift-off behaviour with this sensor was studied to ensure the correct functionality of the EM sensor. A sample from P91:A was sectioned (50 x 50 x 10 mm) which had a tempered martensitic microstructure. The sample was mechanically ground using 400-grit SiC grinding paper producing a smooth surface finish (Ra = 0.38 μm). Non-conductive pieces of thin material, as listed in Table 3-9, were used to create a lift-off gap between the sensor and the sample. Pieces of card, paper and polymer were laid on top of one another to build the lift-off between the sensor and the sample and a nylon weight (280 g) closed any air gaps between the paper, card and polymer spacers, as shown in Figure 3-31. Single frequency (10 Hz) inductance data was obtained at varying increments of lift-off between the sensor and the sample.

Table 3-9: Non-conductive material and associated thickness used to create various lift-offs between sensor and sample, measured using a digital calliper

Material	Thickness (mm)
Polymer sheet	0.05
White paper	0.10
Laminated card	0.25

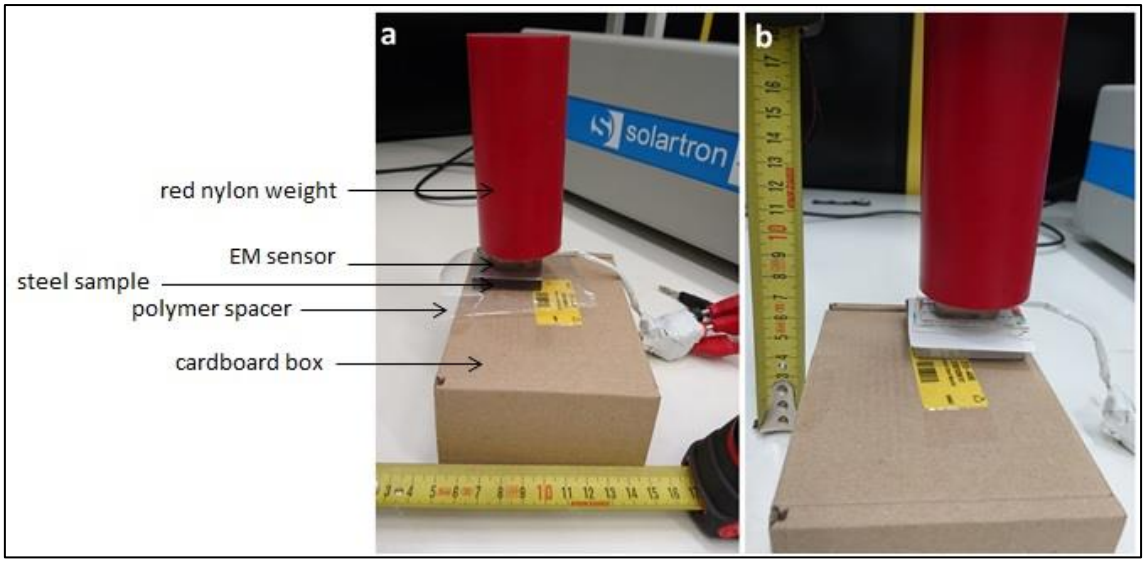

Figure 3-31: (a) EM sensor and sample with polymer spacer causing 0.05 mm lift-off (b) EM sensor and sample with multiple pieces of white card causing 4 mm lift-off

The results from the lift-off trial showed that the EM signal decreases with lift-off, following an inverse power law, which is in line with previous literature [184]. The lift-off curve is given in Figure 3-32 and the standard deviation vertical error bars were based on eight measurements per lift-off value. The trend observed showed that the majority of the decrease in inductance takes place over the initial 500 μm of lift-off. This is due to the magnetic field being strongest (most concentrated) near the sensor feet [174], thus at zero lift-off the magnetic field is penetrating the full depth of the 10 mm thick sample only limited by the skin depth (as discussed with the observations made for

Figure 3-29). As the distance between the sensor and the sample is increased, there is a significant reduction in the amount of magnetic field which penetrates into the sample, caused by the non-conductive gap between the sensor legs and the sample and hence a decrease in the inductance measured. After the initial sharp loss of inductance due to lift-off over the first 500 μm, the effect begins to decay as the proportion of magnetic field penetrating the sample begins to stabilise. It should be noted that although at larger lift-off values the effect of a change in lift-off, on the inductance, is small, the inductance value itself is low and therefore may limit the ability to differentiate between correctly heat treated and mis-heat treated microstructures.

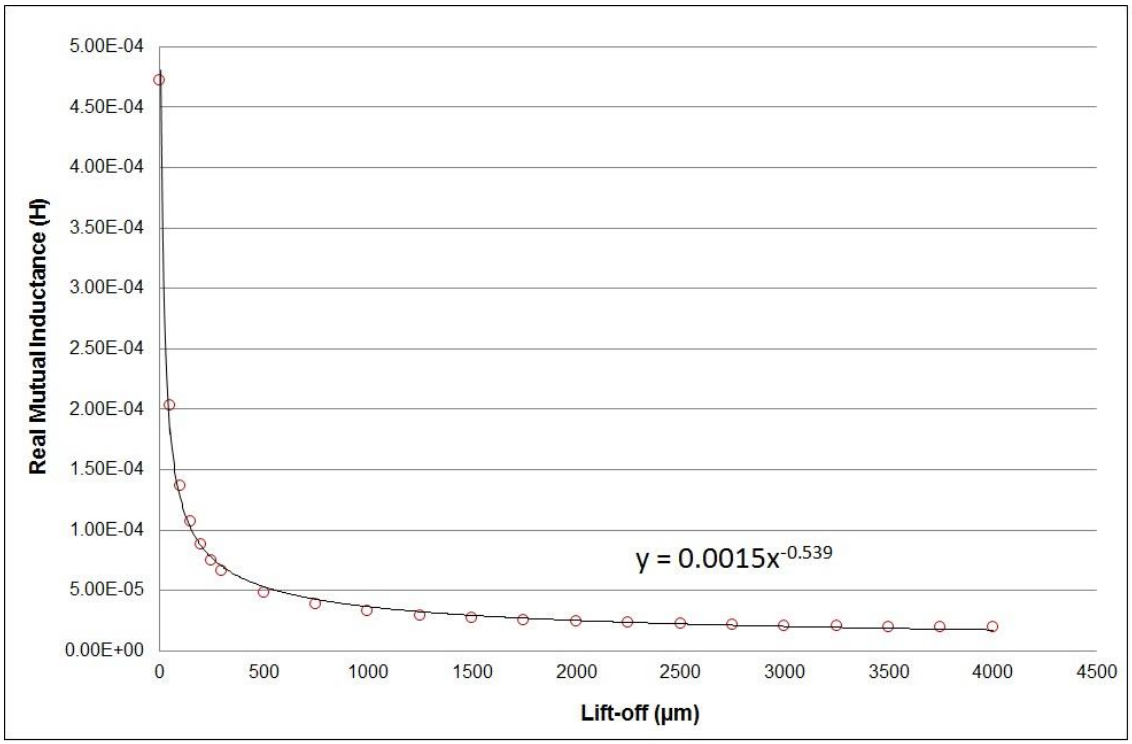

Figure 3-32: Variation of low frequency (10 Hz) inductance with lift-off for Grade 91 (P91:A) tempered martensite material; showing the inductance to decrease with lift-off

3.4.6. Effect of Sample Permeability

Three Grade 91 samples with different permeability values, sectioned into identical geometries (40 x 25 x 10 mm) with identical surface finishes, were provided from a

parallel research project [23]. Sample T91-AR was in the as-received condition with a tempered martensite microstructure and a relative permeability value of 92; T91-T100h sample was tempered for 100 hours and had a measured relative permeability of 161 and T91-M sample was heat treated to create a ferritic microstructure representative of mis-heat treated or aberrant material, with a relative permeability of 177. The three samples were tested with the EM sensor at multi-frequency with the results shown in Figure 3-33 which shows how the low frequency (1 – 10 Hz) inductance values (which are dominated by the samples permeability) correspond to the samples' permeability values in that the high permeability sample (T91-M) has the highest low frequency inductance value followed by T91-T100h and T91-AR. This trend mimics the trend in the multi-frequency inductance results determined by Liu et al (2015) [23], thus suggesting the EM sensor is functioning appropriately.

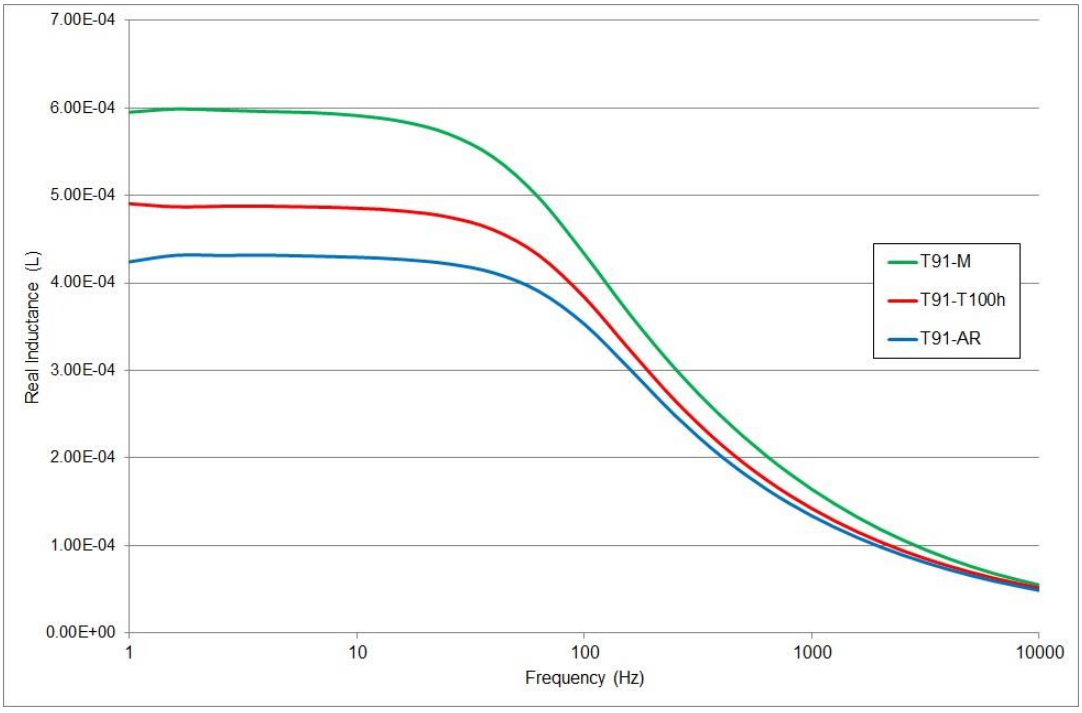

Figure 3-33: Multifrequency inductance curves for Grade 91 samples of identical size and surface finish but varying relative permeability (μ_r) values. T91-M has μ_r of 177, T91-T100h has a μ_r of 161 and T91-AR has a μ_r of 92, permeability values and samples provided by Liu et al (2015) [23]

3.4.7. Skin Depth Calculation

The skin depth is approximately the depth to which the EM signal penetrates the sample and its relevance has been discussed in Section 2.5.4.1. The skin depth can be calculated using Eq. 2-18 (from Section 2.5.4.1). At frequency of 10 Hz the skin depths for correctly heat treated tempered martensite microstructure and mis-heat treated equiaxed ferrite microstructure were calculated and are given in Table 3-10. The resistivity and relative permeability values used in the skin depth calculation have been obtained from Liu et al (2015) [23] where Grade 91 material was exposed to identical heat treatment procedures to produce the same microstructures and hardness values representative of P91:A-CHT and P91:A-MHT samples.

Table 3-10: Skin depth calculations for P91:A-CHT and P91:A-MHT samples based on Eq. 2-18.

Sample	Resistivity, ρ (x10^{-7} Ωm)	Relative Permeability, μ_r	Skin Depth, δ (mm)
P91:A-CHT	5.112	92	11.9
P91:A-MHT	5.085	177	8.5

3.5. Summary

A U-shaped EM sensor has been manufactured to research the potential to differentiate between CHT and MHT microstructures. Initial results presented in this chapter suggest that the EM sensor has correct functionality in terms of outputting the correct shaped multi-frequency inductance curve showing that the low frequency inductance of the sensor is dominated by the sample permeability, this will be further explored in Chapter 4. The materials relative permeability, the presence of a decarburised surface layer, the presence of a surface roughness layer and the presence of a surface work hardened layer are factors which all affect the EM sensor

and will be explored in the results and discussion chapters. Therefore these factors will be investigated to establish how they affect the EM sensor's ability to determine correctly heat treated microstructures from mis-heat treated microstructures. Chapter 4 will consider the impact of a decarburised surface layer and surfaces with varying degrees of roughness on the samples' inductance values and how these surfaces impact the EM sensor determining CHT microstructures from MHT microstructures. Chapter 5 will consider the effect of a work hardened surface layer on the samples' inductance values and how this impacts the EM sensor determining CHT microstructures from MHT microstructures.

CHAPTER 4 SCREENING ABERRANT AND DECARBURISED MATERIAL

This chapter explores the ability for the EM sensor to be able to determine correctly heat treated bulk microstructures from mis-heat treated bulk microstructures and if this ability is inhibited by the presence of a decarburised surface layer. The chapter begins by exploring the relationship between mechanical hardness, magnetic relative permeability and inductance by using samples subjected to different heat treatments to create different bulk microstructures. Using this understanding, the chapter goes on to explore the impact of decarburised surface layers on the sensors ability to determine what the bulk microstructure of the material is, specifically when the microstructure of the surface is not representative of the microstructure in the bulk of the material, since the current NDT techniques are limited to surface characterisation only.

4.1. Introduction

For Grade 91 boiler components it is critical to achieve a correctly tempered martensitic microstructure for the component to attain the desired mechanical properties for high temperature performance. The high temperature normalising heat treatment carried out by the component manufacturer typically consists of exposing the component to a high temperature (1040-1100 °C) followed by air cooling, or quenching for very thick sections; this is critical in achieving the required lath martensite microstructure. Following this, the tempering heat treatment performed at typically 750-780 °C enables creep strengthening precipitates to form and stabilises the microstructure. The mechanical properties of the material are very sensitive to achieving the correct microstructure; hence errors in heat treatment can be serious and sometimes catastrophic. This was exemplified when an erroneous Grade 91 main steam pipe failed in service leading to a violent rupture (Figure 4-1) at Huadian Datong power plant in China in 2006, resulting in the loss of three lives.

Figure 4-1: Grade 91 main steam pipe rupture at Huadian Datong Power Plant, China [194]

4.2. Effect of Permeability

Steel samples with different relative permeability values were sectioned for EM testing to determine the impact of relative permeability on the inductance measured by the EM sensor. The permeability values were determined in parallel projects within the research group using a cylindrical EM sensor and a full finite element (FE) model, described in [27] and [176]. Note that a FE model was not available for the U-shaped EM sensor and sample arrangement used in this study, and development of a fully validated FE model for the sensor was not part of this project. Sample dimensions are given in Table 4-1 and were all prepared with identical surface finishes using a mechanical surface grinder with a grade 60 vitrified aluminium oxide grinding wheel; samples are shown in Figure 4-2. The oxide grinding wheel produced a very smooth surface finish on the samples with an average arithmetic surface roughness (Ra) of 0.08 µm; surface roughness was measured using a SE1700 Surfcorder as described in Section 3.3.4.

The samples were tested using the EM sensor at a single frequency (10 Hz) as the low frequency inductance was shown to be stable at a frequency of 10 Hz and below for the sensor used in this study (shown earlier in Figure 3-24) and that low frequency inductance is more sensitive to changes in permeability than at higher frequencies (above 10 Hz), the reason for this behaviour has already been discussed in 3.4.2. The samples' microstructures are shown in Figure 4-3 and permeability values and inductance results are given in Table 4-3. The inductance results are plotted in Figure 4-4 and shows that the inductance increases with relative permeability. This is expected behaviour since the inductance of a material has been linked with the material's domain wall motion when subjected to a magnetic field, such that a material with high permeability will have less restricted domain wall motion [176] and therefore a greater inductance value. Domain wall motion can be restricted by the pinning effect of microstructural features such as dislocation networks, grain boundaries and the existence of precipitates, the presence of which will make the material magnetically harder and hence reducing its relative permeability and therefore its inductance [27, 58]. The pure iron sample has the highest permeability (330) due to having 100% ferrite fraction (as reported in [176]) and a large ferrite grain structure (as shown in Figure 4-3a) unlike the 0.17C and 0.8C steels which consist of both ferrite (lighter) and pearlite (darker) shown in Figure 4-3b and Figure 4-3c respectively. For the 0.8C steel, the predominant pearlite and 0% ferrite fraction content leads to the material's low permeability (56) and hence low inductance, whereas for the 0.17C steel, although containing some pearlite, it has still has approximately 73% ferrite fraction and hence it has a higher relative permeability (200) than the 0.8C steel. For the Grade 91 materials, the tempered P91 sample has a martensitic lath microstructure (shown in Figure 4-3d) where the dislocations produced during the formation of the martensitic laths and the finely dispersed precipitates will be acting has pinning points to domain wall motion, leading to a reduced permeability (92) and hence a lower inductance value

than the P9 ex-service sample which has an equiaxed ferrite grain structure (shown in Figure 4-3e) with large precipitates distributed within the grains or on the grain boundaries leading to a higher relative permeability (133) and hence higher inductance. The T22 ex-service microstructure (shown in Figure 4-3f) also has a large equiaxed ferrite grain structure similar to the P9 ex-service which would be expected to permit more domain wall motion before the domain wall intercepts a grain boundary and hence would be expected to have a similarly high permeability value. However, the T22 ex-service samples seems to contain more finely dispersed precipitates which would provide the pinning points to restrict the domain wall motion, thus leading to a lower relative permeability (86). However the inductance value was lower than expected (lower than the 0.8C steel which has a relative permeability of 56), but this was due to the thickness of the samples (3 mm), which was thinner than the 5 mm determined to be required to avoid thickness effect on the EM signal as discussed in Section 3.4.4.

The results in Figure 4-4 suggest that the sensor's functionality is correct as inductance is increasing with relative permeability. The standard deviation error bars for the EM signal is based on four EM measurements on all samples except for sample P91 which had eight measurements due to its larger sample size (as explained in Section 3.4.2 with Figure 3-25).

Table 4-1: Dimensions for samples used to determine effect of permeability on inductance

Sample	Dimensions (mm) (length x width x thickness)
0.8C steel	40 x 25 x 10
T22 ex-service	40 x 25 x 3
P91 tempered	60 x 50 x 10
P9 ex-service	40 x 25 x 8
0.17C steel	40 x 25 x 10
Pure iron	40 x 25 x 5

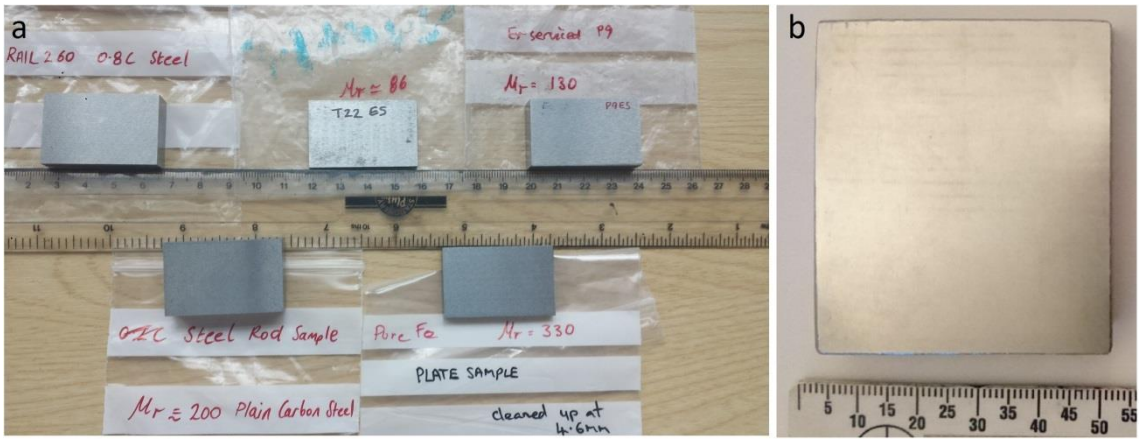

Figure 4-2: Samples for testing the effect of permeability on the EM sensor, (a) (from left to right) 0.8C steel, 0.17C steel, T22 ex-service, Pure iron and P9 ex-service. (b) P91 tempered

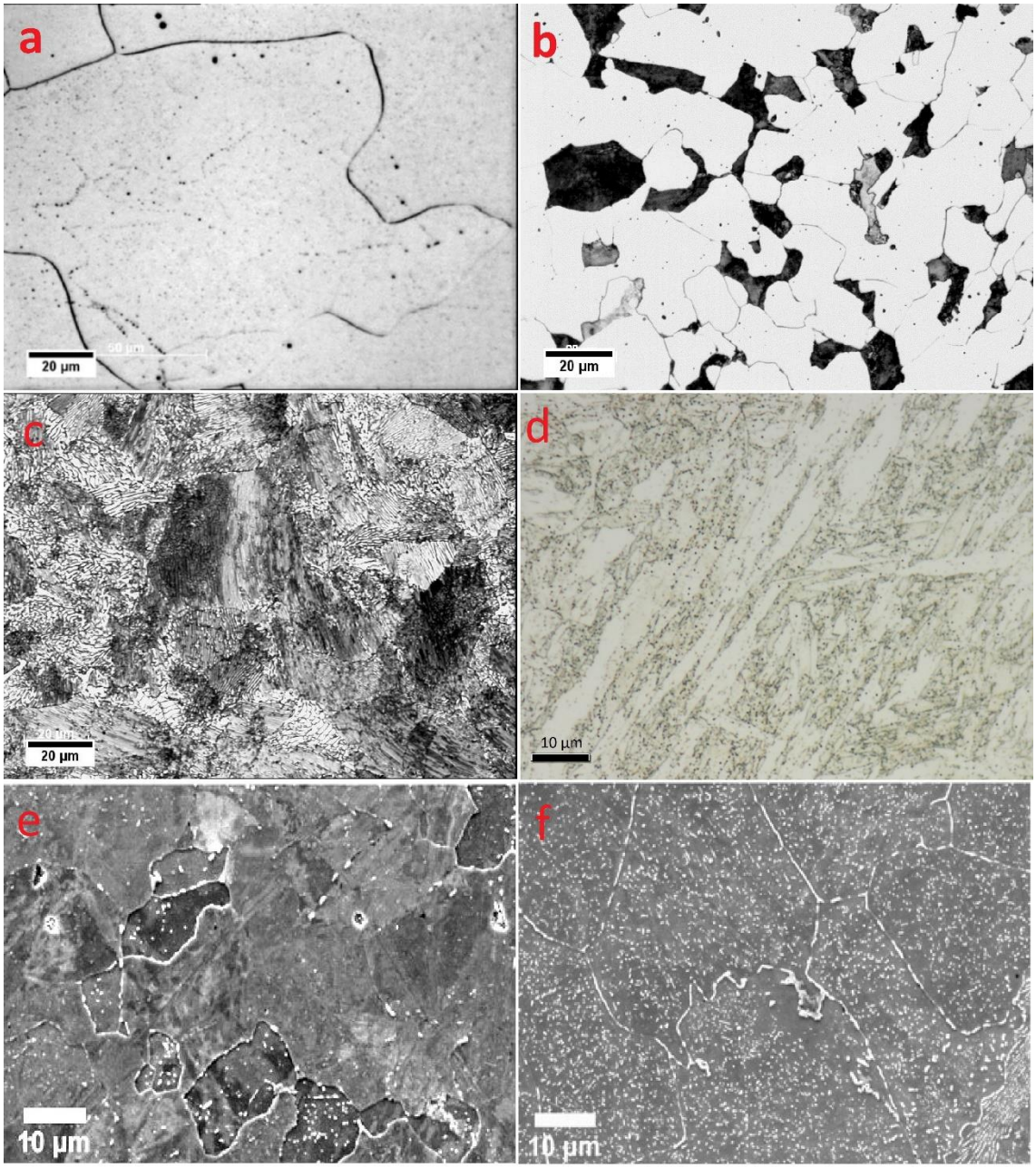

Figure 4-3: Microstructures for samples used to measure effect of permeability on inductance. (a) Pure iron, (b) 0.2C steel, (c) 0.8C steel, (d) P91 tempered, (e) P9 ex-service, (f) T22 ex-service. (a)-(c) were adapted from [176], (e) and (f) were adapted from [27]

Table 4-2: Chemical composition for permeability effect samples, all in wt. %. Compositions for; Pure Fe, 0.2C steel and 0.8C steel were taken from [176] and P9 ex-service and T22 ex-service were taken from [27]

Sample	*C*	*Si*	*Mn*	*P*	*S*	*Cu*	*Cr*	*Mo*	*Ni*	*Al*	*Nb*	*V*
Pure iron	Melting grade pure iron											
0.2C steel	0.20	0.28	0.80	0.01	0.03	0.09	NA	NA	NA	NA	NA	NA
0.8C steel	0.80	0.20	0.96	0.02	0.03	0.02	NA	NA	NA	NA	NA	NA
P9 ex-service	0.12	0.52	0.44	0.01	0.01	NA	8.40	0.97	NA	NA	NA	NA
T22 ex-service	0.15	0.28	0.44	0.02	0.01	NA	2.14	1.01	NA	NA	NA	NA
P91 tempered	0.10	0.27	0.35	0.02	0.01	NA	8.29	1.02	0.11	<0.01	0.07	0.22

Table 4-3: Relative permeability and low frequency (10 Hz) inductance values. Permeability values for samples; 0.8C steel, 0.2C steel and Pure iron were taken from [176] and T22 ex-service, P91 tempered and P9 ex-service were taken from [27]

Sample	Relative Permeability (μ_r)	Inductance ± SD (x10^{-4} H)
0.8C steel	56	2.90 ± 0.09
T22 ex-service	86	3.19 ± 0.02
P91 tempered	92	5.08 ± 0.20
P9 ex-service	133	6.19 ± 0.02
0.17C steel	200	8.29 ± 0.19
Pure iron	330	14.3 ± 0.24

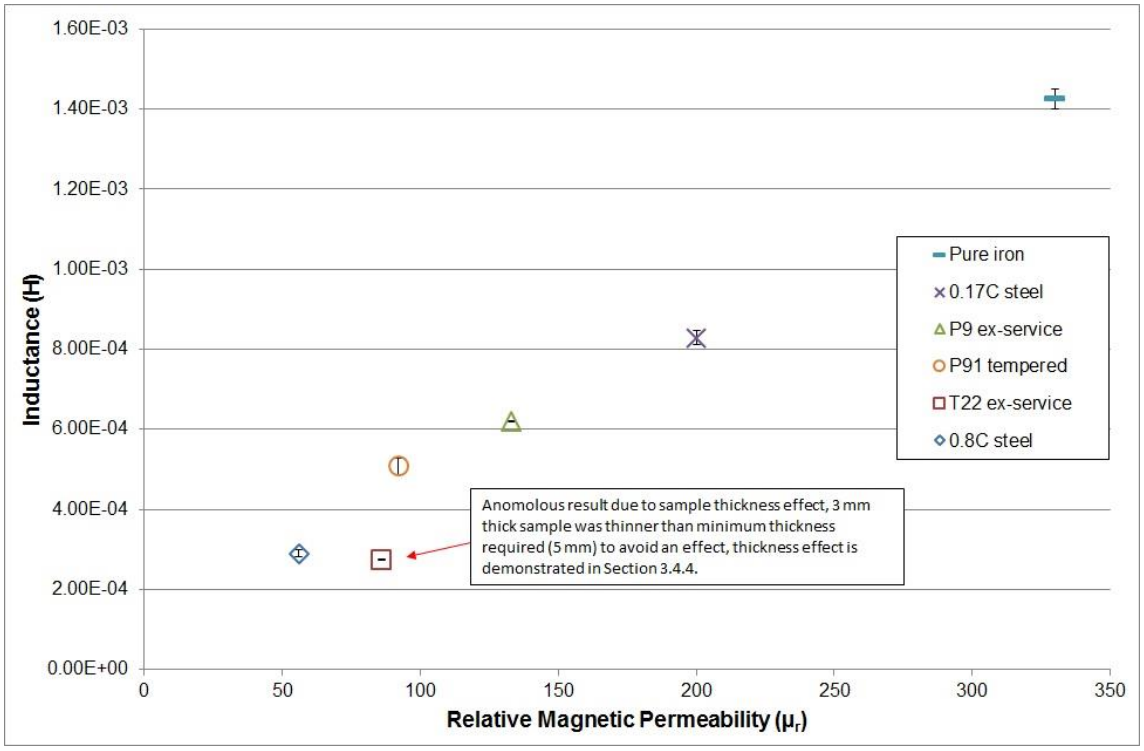

Figure 4-4: Variation of EM response with relative permeability

4.3. Screening Material with an Aberrant Bulk Microstructure

One of the more common heat treatment errors in practise involves gross overheating of the material during the tempering stage which leads to aberrant microstructures as shown in Figure 4-5, i.e. not achieving a tempered martensitic microstructure for Grade 91 components. This is where the component is unintentionally heated above the material's Ac_1 temperature (typically 810 °C), rather than being held at the tempering temperature (typically 750 °C). This mis-heat treatment causes partial re-austenisation of the martensite and is usually caused by erroneous thermocouples which may be broken, incorrectly positioned or incorrectly wired leading to inaccurate readings being displayed and hence operators exceed the tempering temperature set points. Another mis-heat treatment which can lead to the formation of an aberrant microstructure is where the components undergo a slower cooling than required to form the martensitic microstructure. Slow cooling can arise if components are mistakenly left in furnaces to

cool (rather than taken out of the furnace to be air cooled) or when large sections are taken out of the furnace to cool in air but positioned in close proximity to one another. This leads to those areas on the components which are in close proximity to one another to undergo a slower cooling rate than required, resulting in a soft aberrant material with a weak ferritic structure instead of the required tempered martensite [195]. Another form of undesirable microstructure is un-tempered or under-tempered martensite. This is where material is inadvertently heated above the Ac_3 and rapidly cooled (similar to the normalising heat treatment) which will generate a martensitic microstructure with a very high hardness value (400 HV or above). In this highly abnormal condition, the material may be prone to stress corrosion cracking until it becomes tempered by operation in service [196].

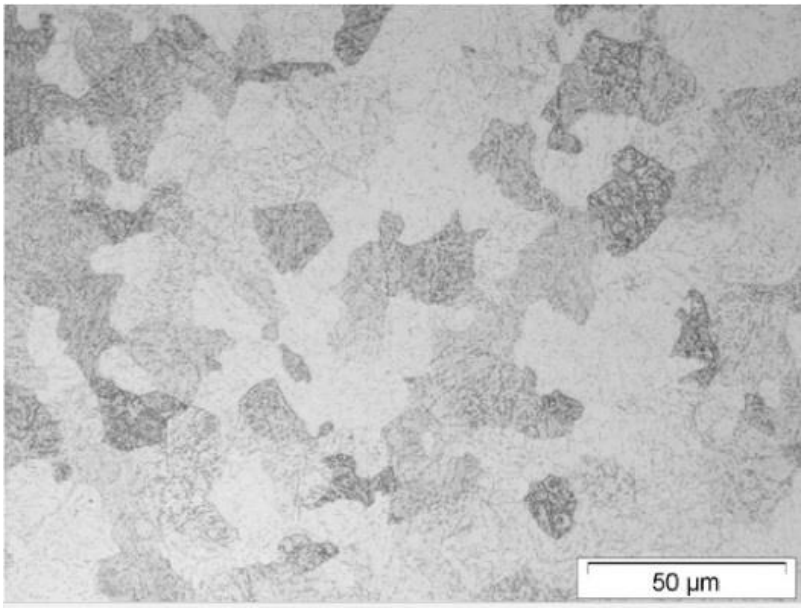

Figure 4-5: Aberrant Grade 91 microstructure showing equiaxed ferrite grains [195]

Experience has shown that serious errors in the manufacturing of Grade 91 components globally is not uncommon and can find their way into power plants. Therefore screening of components before they are installed for service is an important

part of quality assurance for power plant operators [197]. Currently surface replication and portable hardness testing are the techniques employed by power generating utilities to screen service entry material. As summarised in the literature review (Table 2-6), surface replication is a laborious and time consuming process and portable hardness testing suffers from statistical scatter and reliability issues. Furthermore, both these techniques are limited to surface inspection and a typical decarburised or grit blasted (work hardened) surface layer can often mask what can be satisfactory bulk service entry material beneath. Therefore to complement these techniques the EM sensor was investigated for its ability to screen CHT material from MHT aberrant material.

E.ON supplied Grade 91 material designated P91:A which in the as-received condition (P91:A-AR) consisted of a tempered martensite microstructure (Figure 4-6a) with a measured hardness value of 202 HV. The hardness of the as-received material was towards the lower limit of acceptable hardness range for service entry material (ASTM 196-265 HV) [15]. Therefore three sections with identical dimensions (50 x 50 x 10 mm) were heat treated to produce as-normalised (un-tempered), correctly heat treated (CHT) and mis-heat treated (MHT) samples and designated P91:A-N, P91:A-CHT and P91:A-MHT respectively; details of heat treatment are given in Table 3-3 in Section 3.2. P91:A-N consisted of a very hard martensitic lath microstructure (as shown in Figure 4-6b) whilst P91:A-CHT consisted of a tempered martensitic lath microstructure strengthened by alloy precipitates (as shown in Figure 4-6c). P91:A-MHT microstructure (shown in Figure 4-6d) replicated the aberrant P91 microstructure seen previously in Figure 4-5 with an almost equiaxed ferrite grain structure significantly softer than tempered martensite (hardness data is given below in Table 4-4). The microstructure at the surfaces of all four samples was observed to be no different to the microstructures in their bulk, an example is shown in Figure 4-7

whereby the microstructure at the surface and in the bulk, for sample P91:A-CHT, is the same; in this case showing martensitic laths. Ten hardness indents were made over a 1 cm^2 surface area to calculate the standard deviation (SD) for each sample, given in Table 4-4. Instances of aberrant Grade 91 due to faulty heat treatment have been found in dozens of power plant components globally; with hardness values well below 200HV and in some cases as low as 145HV [198]. P91:A-MHT material has a slightly lower but not too dissimilar hardness value and hence is representative of aberrant Grade 91 material found in industry. All four sample surfaces were ground using a grade 60 vitrified aluminium oxide grinding wheel which left a smooth surface finish as seen for P91:A-CHT and MHT samples in Figure 4-8.

Table 4-4: Hardness data for P91:A samples with different heat treated microstructures. Results represent through-thickness hardness values.

Sample	Hardness ± SD (HV_{30})
P91:A-N	405 ± 6.3
P91:A-CHT	224 ± 1.8
P91:A-AR	202 ± 2.6
P91:A-MHT	139 ± 1.2

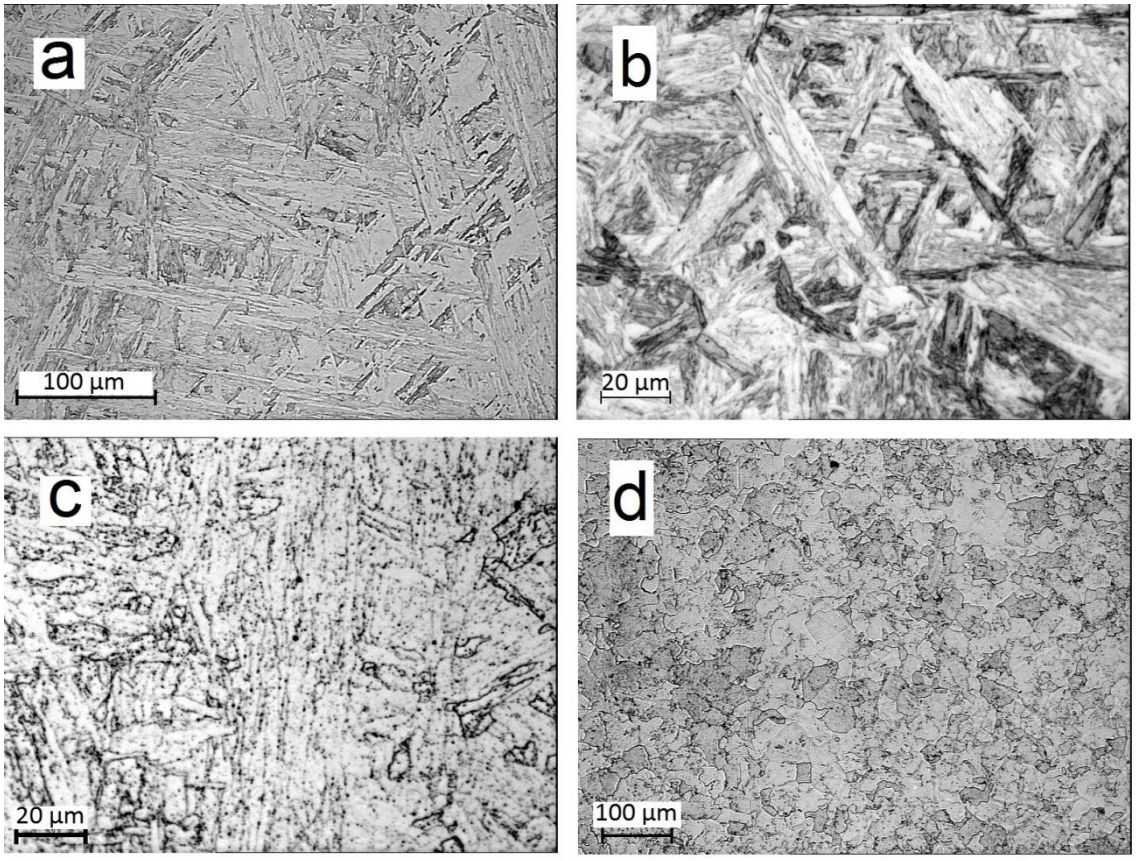

Figure 4-6: P91:A heat treated samples (a) P91:A-AR, as-received tempered martensitic lath microstructure, (b) P91:A-N, normalised (un-tempered) martensitic lath microstructure, (c) P91:A-CHT tempered martensitic lath microstructure, (d) P91:A-MHT aberrant equiaxed ferrite grain microstructure

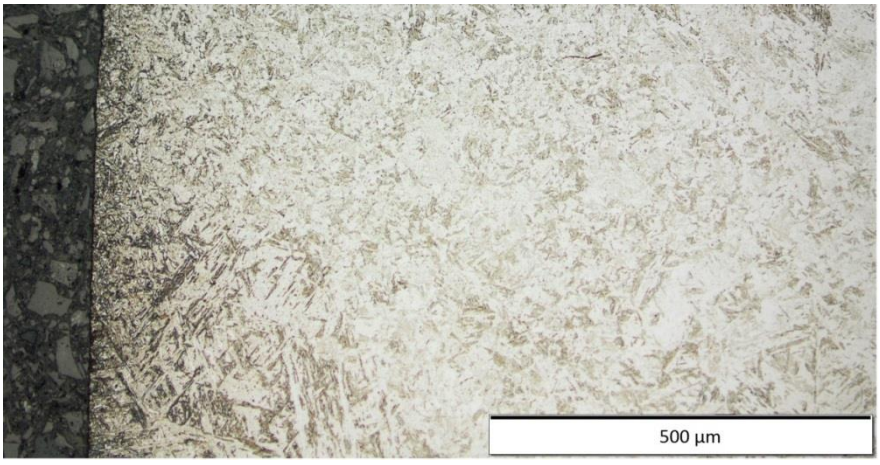

Figure 4-7: LOM image of P91:A-CHT showing that the microstructure at the surface and in the bulk is similar, showing martensitic laths, and hence there is no presence of an aberrant surface layer

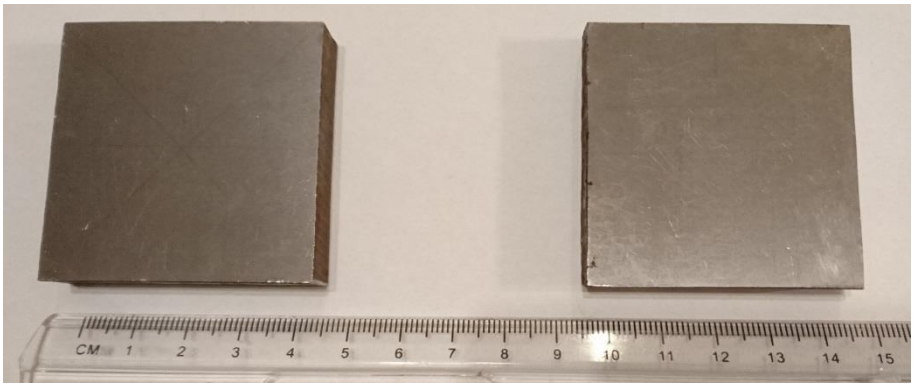

Figure 4-8: (left) P91:A-CHT and (right) P91:A-MHT with identical mechanically ground smooth surface finishes

All four samples were tested with the EM sensor at low frequency (10 Hz), adopting the procedure described in Section 3.4.2 and using Eq. 3-3, to obtain the inductance values given in Table 4-5.

Table 4-5: Low frequency (10 Hz) inductance values for P91:A samples with different heat treated conditions

Samples	Inductance ± SD ($x10^{-4}$ H)
P91:A-MHT	5.99 ± 0.16
P91:A-AR	5.11 ± 0.08
P91:A-CHT	4.59 ± 0.15
P91:A-N	2.54 ± 0.04

The inductance of P91:A-CHT is 81% higher than the normalised sample (P91:A-N) and 23% lower than the mis-heat treated sample (P91:A-MHT). This is expected since the MHT softer ferrite microstructure would have a higher relative permeability than CHT tempered martensite which in turn should have a higher relative permeability than the, un-tempered, normalised sample (P91:A-N). This shows that the MHT softer aberrant material can be easily distinguished from the CHT service entry material using the EM sensor; since there is a significant difference between the inductance values

(the SD error bars do not overlap hence the inductance values for each sample can be considered to be significantly different). Also the CHT material with a tempered martensite microstructure can be distinguished from the un-tempered martensite microstructure (P91:A-N). When the samples' mechanical hardness is compared against inductance values, a linear trend is observed, such that Figure 4-9 shows the inductance decreases with the mechanical hardness. At low frequencies the relative permeability, which dictates the extent of domain wall motion (i.e. higher permeability equates to easier domain wall motion as discussed earlier in this chapter, Section 4.2) dominates the EM signal. For P91:A-CHT, domain wall motion is restricted by the martensitic lath width and probably the number density of the very fine carbonitride precipitates within the laths as well [199]. However the high density of dislocations within the normalised hard martensitic material (P91:A-N) play a dominating role of pinning domain wall motion and causing a far smaller mean free path to domain wall movement, effectively lowering the material's relative permeability and hence a lower inductance value of 2.54E-04 H is observed. Conversely, P91:A-MHT has a large, almost equiaxed, ferrite grain structure and so the domain walls can move further before they become pinned by the widely spread ferrite grain boundaries as opposed to the thin martensitic lath boundaries seen in P91:A-CHT, hence increasing P91:A-MHT sample's relative permeability and the higher inductance value of 5.99E-4 H being observed. Furthermore the carbonitride precipitates in the MHT material are coarser and less finely dispersed than in the CHT material (shown in Figure 4-10), comparable to what was observed by Liu et al (2015) for a similar MHT microstructure [23], thus adding to the increased mean free path of domain wall motion for sample P91:A-MHT.

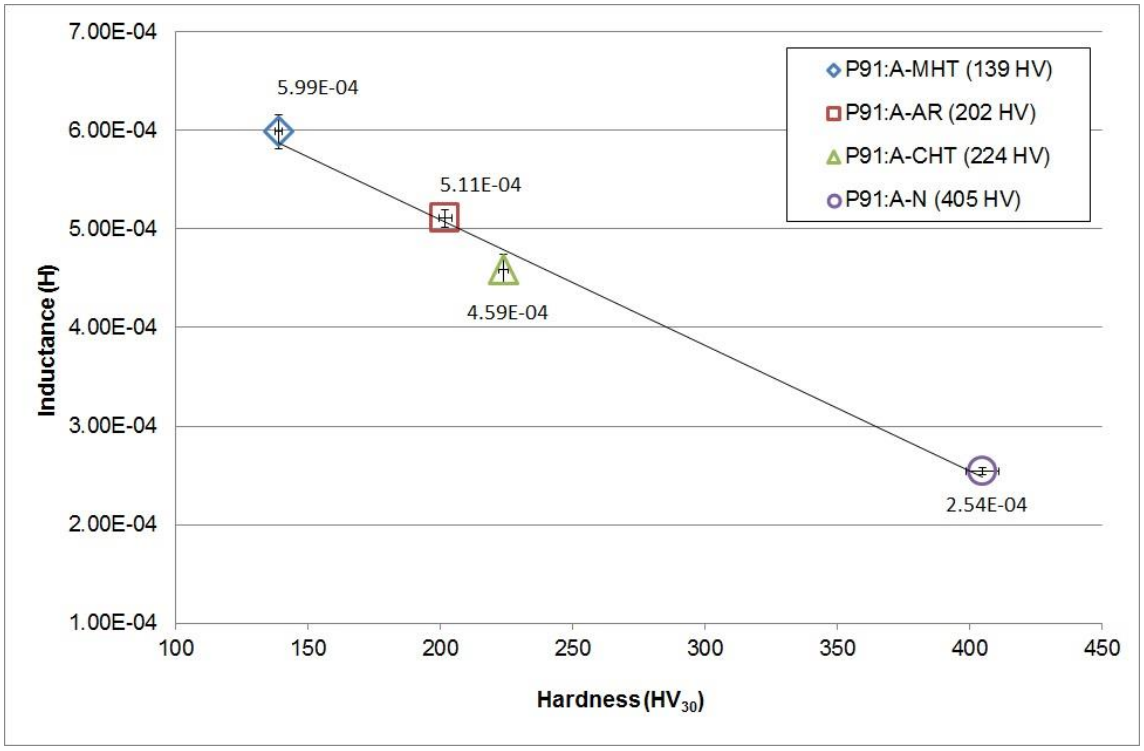

Figure 4-9: Variation of low frequency (10 Hz) inductance values with hardness for heat treated P91:A samples

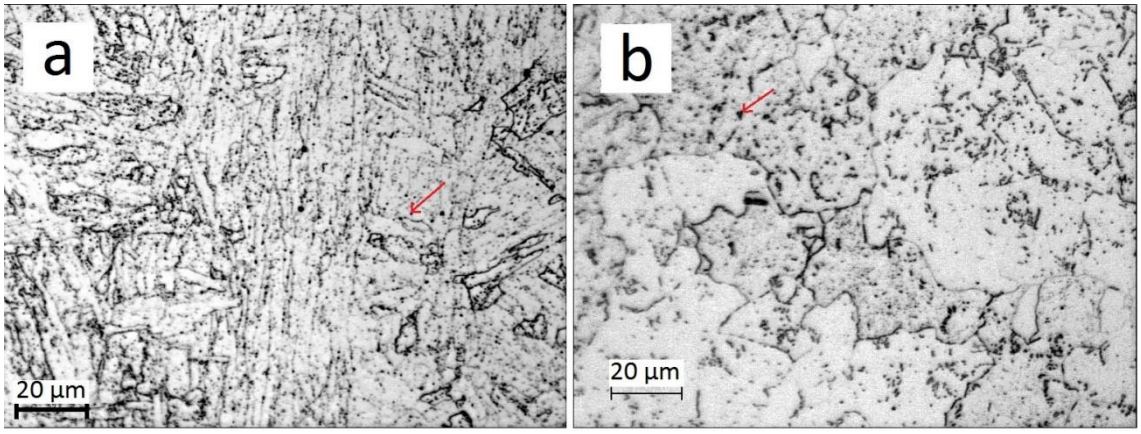

Figure 4-10: High magnification LOM images of (a) P91:A-CHT and (b) P91:A-MHT showing coarser precipitates in P91:A-MHT sample compared to P91:A-CHT sample, example precipitates highlighted by the red arrows

4.4. Screening Material with a Decarburised Surface Layer

The U-shaped EM sensor has shown in Section 4.3 that it has the ability to distinguish Grade 91 correctly heat treated tempered martensite from a mis-heat treated ferrite microstructure. However, in some cases EON have come across components that have a correctly heat treated tempered martensite bulk microstructure but with a thin decarburised surface layer, typically up to 0.5 mm thick, which is not representative of the bulk material [200]. This can be caused by over-normalising or over-tempering, whereby components are left in furnaces for longer than scheduled when they are receiving normalising or tempering heat treatments. Bad practise in industry can lead to mis-information between operators during shift handovers leading to components being exposed to heat treatments for extended periods of time at high temperatures (e.g. the normalising temperature) creating soft decarburised surface layers. Decarburised surface layers cause significant difficulty for operators to obtain accurate characterisation of the material, since surface replication and portable hardness testing, which are the current preferred techniques for screening material, are limited to surface only characterisation (as discussed in Sections 2.5.2.2 and 2.5.2.3 respectively).

To investigate the ability of the EM sensor to determine if a component's bulk material is correctly heat treated or mis-heat treated, through the presence of a decarburised surface layer, six samples were sectioned from P91:B with similar dimensions (45 x 40 x 18 mm) and identified as;

- P91:B-CHT (correctly heat treated sample)
- P91:B-MHT (mis-heat treated sample)
- P91:B-FC (furnace cooled sample)
- P91:B-FC+T (furnace cooled and tempered sample)

- P91:B-N+T24 (tempered for 24 hours sample)
- P91:B-N+T100 (tempered for 100 hours sample)

Two samples were heat treated to produce, a correctly heat treated sample (P91:B-CHT) and a mis-heat treated sample (P91:B-MHT) where the microstructures at surface of the samples and in the bulk of the samples were identical. The remaining four samples were heat treated to replicate some of the incorrect processes which can take place in industry leading to material with a decarburised surface layer on top of a different bulk microstructure (either correctly heat treated or not). To reproduce the erroneous practise of slow cooling after normalising at high temperature; sample P91:B-FC was normalised at 1080 °C followed by furnace cooling. This replicated the erroneous normalising heat treatment when a component is subjected to a slower cooling rate, instead of the required fast cooling rate during the air cooling stage of the treatment after the component exits the furnace. This is caused by components, which are set for air cooling, being taken out of the furnace after being correctly normalised but then placed in close proximity to one another to cool, hence the heat dissipates from components at a slower cooling rate. Sample P91:B-FC+T is similar to P91:B-FC in that it has been furnace cooled (instead of being air cooled) but is followed by the regular tempering process, to replicate a component which has received a faulty normalising heat treatment (slow cooling) followed by a correct tempering heat treatment. To replicate the erroneous practise of over-tempering, samples P91:B-N+T24 and P91:B-N+T100 were over-tempered at the regular tempering temperature (760 °C) for 24 hours and 100 hours respectively, after both samples had been correctly normalised.

P91:B-CHT and P91:B-MHT sample microstructures can be seen in Figure 4-11 showing that the correctly heat treated P91:B-CHT sample has a tempered martensitic lath microstructure and the mis-heat treated P91:B-MHT sample has an equiaxed

ferrite grain microstructure. The hardness tests revealed the P91:B-MHT sample to have a lower average hardness value of 180 HV than the P91:B-CHT sample with an average hardness of 257 HV, standard deviation error is given in Table 4-6.

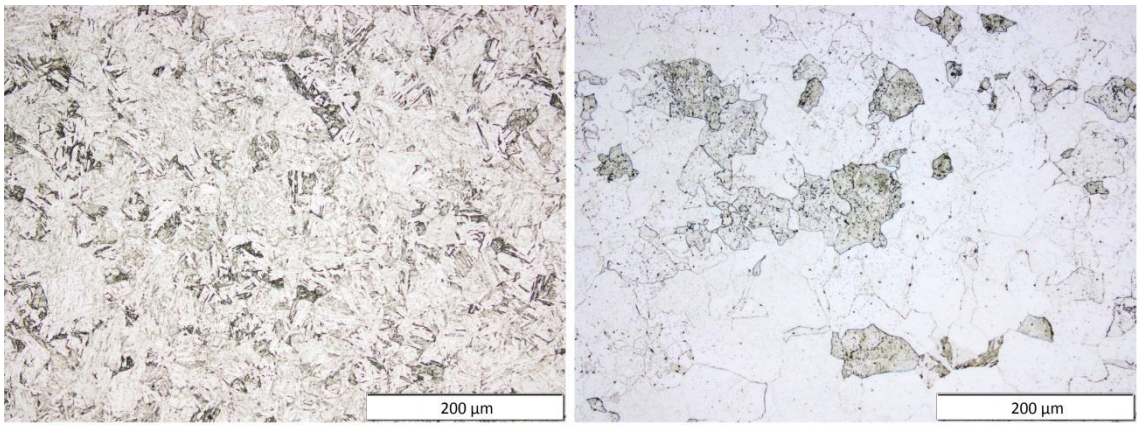

Figure 4-11: LOM images of P91:B samples with (left) CHT microstructure consisting of tempered martensitic laths and (right) MHT microstructure of equiaxed ferrite grains

Detailed microstructure images showing the surface and bulk microstructures for samples P91:B-FC, P91:B-FC+T, P91:B-N+T24 and P91:B-N+T100, can be seen in Figure 4-12, Figure 4-13, Figure 4-14 and Figure 4-15 respectively and the hardness data was also collected for these samples showing a hardness profile between the surface and the bulk and these are given in Figure 4-16, Figure 4-17, Figure 4-18 and Figure 4-19 respectively.

The optical micrographs in Figure 4-12 show that sample P91:B-FC has a martensitic bulk microstructure (Figure 4-12c) with the presence of a coarse grain ferrite surface layer with patches of martensite (Figure 4-12d). An overview of the sample microstructure is given in Figure 4-12a showing the lighter ferrite surface compared to the darker bulk martensite. The depth of the surface layer is approximately 200 µm shown in Figure 4-12b and the transition between the ferrite surface region and the bulk martensite can be seen at higher magnification in Figure 4-12e where packets of martensite and ferrite grains are present at the same depth from the surface. High

magnification reveals the equiaxed ferrite grains with carbides dispersed within the grain and along the grain boundaries shown in Figure 4-12f. Hardness indents were taken on sample P91:B-FC from the surface edge (approximately 50 μm from the surface as shown in Figure 4-12d) to a depth of 2 mm – the results of which are displayed in Figure 4-16. Each data point is the average of three values and the error was calculated as the standard deviation of the three measurements; details of how hardness profiles were obtained for the decarburised surface layer are given in Figure 3-9 in Section 3.3.3. The hardness data (Figure 4-16) shows that at the surface the material is significantly softer, with a typical hardness value between 160 – 170 HV, than the bulk (typically 410 HV). The hardness begins to increase approximately 200 μm from the surface which is the approximate depth of the soft surface layer as depicted in Figure 4-12b. Indents made approximately 300 – 500 μm from the surface show large scatter; this is because at this range the material transitions from soft ferrite grains to martensitic laths and both martensite laths and ferrite grains are present at the same depth from the surface. Therefore some indents were made in the harder martensite regions whilst others, albeit at the same depth from the surface, were made in the softer ferrite regions, this is clearly demonstrated in Figure 4-20.

Figure 4-13 displays various optical micrographs for sample P91:B-FC+T showing a ferrite coarse grain surface layer with a martensitic bulk microstructure similar to P91:B-FC. From Figure 4-13a, a low magnification image, shows the difference between the surface and bulk microstructures depicting the softer white ferrite region at the surface compared to the darker martensite in the bulk; an example of the hardness indentation profile can also be seen in Figure 4-13a. The surface layer is approximately 250 – 350 μm deep in places (averaging circa 300 μm) as shown in Figure 4-13b. At higher magnification the bulk and surface microstructures can be seen more clearly in Figure 4-13c and Figure 4-13e respectively. The transition between the coarse ferrite

grains and the martensite can be seen in Figure 4-13d and at higher magnification in Figure 4-13f. The hardness data for sample P91:B-FC+T (given in Figure 4-17) shows that a hardness gradient exists between the surface and the bulk. The ferrite region demonstrates a soft layer (approximately 155 HV) similar to sample P91:B-FC, however the bulk microstructure, which has an approximate hardness of 210 HV, is much softer than the bulk microstructure in sample P91:B-FC (circa 410 HV), this is because the bulk microstructure of sample P91:B-FC is un-tempered martensite which is hard and brittle compared with the tempered martensite of the P91:B-FC+T sample which is softer and tougher. The hardness profile suggests that the soft ferrite region is approximately 300 μm thick which is similar to what was observed under the optical microscope (Figure 4-13b). Similar to P91:B-FC, there is a slightly larger scatter for indents made between 350 – 550 μm depth from the surface, compared to other indents, because the indents with large scatter were made in the ferrite/martensite transition region.

Figure 4-14 displays the various micrographs for sample P91:B-N+T24 which show a martensitic bulk microstructure with a coarse ferrite grain surface layer. A low magnification overview of the ferrite surface and the bulk martensitic lath microstructure is shown in Figure 4-14a, as well as the hardness indents taken for this sample. Higher magnification images of the bulk martensitic laths and the coarse ferrite grain surface layer can be seen in Figure 4-14c and Figure 4-14e respectively. The transition from ferrite grains to martensitic laths are shown in Figure 4-14d and can be seen more clearly at higher magnification in Figure 4-14f. Figure 4-18 shows the hardness indentation profile for sample P91:B-N+T24 confirming the soft ferrite surface layer (typically 150 HV) spanning to depth of 50 – 150 μm from the surface which is in agreement with those depths observed in Figure 4-14b. The transition area of ferrite grains to martensitic laths was relatively small for sample P91:B-N+T24 compared to

sample P91:B-FC and also the difference between the bulk hardness and surface layer hardness for sample P91:B-N+T24 (circa 50 HV) was smaller than the difference between the bulk hardness and surface layer hardness for sample P91:B-FC (circa 250 HV), hence smaller error bars were observed for hardness indents made in the transition region as shown in Figure 4-18, compared to larger error bars observed for the hardness indents made in the martensite/ferrite transition areas for sample P91:B-FC (shown in Figure 4-16). The bulk microstructure has a hardness of 197 HV which is slightly softer than a typical tempered martensite which usually has a hardness value of 220-240 HV, this is due to the over-tempering of the material as it was held at tempering temperature for 24 hours instead of the typical 3 hours allowing the martensite to soften.

Figure 4-15 displays the various micrographs for P91:B-N+T100 sample, which show a martensitic bulk microstructure with the presence of coarse ferrite grains at the surface. Figure 4-15a, shows a low magnification overview of the different bulk and surface microstructures with Figure 4-15b suggesting the surface ferrite grains exit to an average depth of 200 μm from the surface. Figure 4-15c and Figure 4-15e respectively illustrate, in high magnification, a martensitic lath microstructure in the bulk and a coarse ferrite grain microstructure at the surface. The ferrite/martensite transition region is depicted in Figure 4-15d (along with some of the hardness indents); the transition region can be seen more clearly at higher magnification in Figure 4-15f. Figure 4-19 displays the hardness indentation results showing the hardness gradient between the soft surface ferrite (approximately 130 HV) and the harder tempered bulk martensite (approximately 185 HV). Both the surface and bulk hardness values are lower than that observed for P91:B-N+T24 in Figure 4-18, since the longer tempering time (100 hours) has allowed the material to soften further. The transition area, similar to P91:B-N+T24 is relatively small and therefore there is not as much scatter for the

indents in the transition area as has previously been seen on sample P91:B-FC (shown in Figure 4-16).

The error bars for hardness indents taken in the martensite/ferrite transition region in sample P91:B-FC (shown in Figure 4-16) are much larger than the error bars observed for the hardness indents taken in the martensite/ferrite transition regions in samples P91:B-FC+T, P91:B-N+T24, P91:B-N+T100 (shown in Figure 4-17, Figure 4-18 and Figure 4-19 respectively). This is because the bulk microstructure of sample P91:B-FC is un-tempered martensite (circa 410 HV) whereas the bulk microstructure for samples P91:B-FC+T, P91:B-N+T24, P91:B-N+T100 is tempered martensite (circa 200 HV). Hence the difference in the hardness values between the surface layer (circa 160 HV) and the bulk microstructure (circa 410 HV) for sample P91:B-FC is approximately 250 HV, which is much larger than the differences between the surface layers (circa 150 HV) and bulk microstructures (circa 200 HV) of samples P91:B-FC+T, P91:B-N+T24, P91:B-N+T100 which is approximately only 50 HV.

EM tests were performed on all six samples and the results are tabulated in Table 4-6, alongside their hardness values (bulk and surface) as well as the average depth of the decarburised surface layers (details of how they were measured is given in Section 3.3.6). The low frequency (10 Hz) inductance values were plotted against the samples' bulk hardness values to observe the impact of the decarburised surface layer on the samples' inductance values, and can be seen in Figure 4-21. The data reveals a linear trend in which the samples' bulk hardness is proportional to the inductance suggesting that the decarburised surface layers in this set of samples (which were approximately 200 – 600 µm thick including the transition zones) had no significant impact on the samples' inductance value. This result is similar to the trend observed in Section 4.3 where Figure 4-9 showed the sample's inductance to linearly increase with mechanical hardness. Sample P91:B-N+T100 has a softer surface layer than P91:B-

N+T24 by 9 HV and it also has a slightly softer bulk microstructure by 11 HV (see Table 4-6); this difference causes sample P91:B-N+T100 to only have a 3% higher inductance value than P91:B-N+T24. However, although the difference between the surface hardness for samples P91:B-FC and P91:B-FC+T (difference of 10 HV) is similar value to the difference between the surface layer hardness values of P91:B-N+T24 and P91:B-N+T100 (which is 9 HV), the difference between the bulk hardness of samples P91:B-FC and P91:B-FC+T is much higher at 101 HV, compared to the difference between the bulk hardness values of samples P91:B-N+T24 and P91:B-N+T100 (which is 11 HV). This results in sample P91:B-FC+T having an 82% higher inductance value than sample P91:B-FC, suggesting that the low frequency inductance is more sensitive to the bulk material than the aberrant surface layer since the un-tempered martensite bulk microstructure is having a significant effect on the inductance value of sample P91:B-FC compared to the tempered martensite bulk microstructure of P91:B-FC+T. This would be expected since the decarburised surface layers are much smaller than the low frequency skin depth which dictates the approximate depth to which the EM signal penetrates the sample (the phenomenon of skin depth is discussed in Section 2.5.4.1). The skin depth's for CHT and MHT samples were calculated at approximately 11.9 mm and 8.5 mm respectively, (details are given in Section 3.4.7), and given these skin depths, it would dictate that a larger proportion of the EM signal is interacting with the bulk material than the relatively thin decarburised surface layers; hence the bulk material has a greater impact on the EM signal and as such the low frequency inductance values are more useful for determining the bulk microstructure. Figure 4-21 also shows that the through thickness mis-heat treated material (P91:B-MHT) with a hardness of 180 HV has a 10% larger inductance value than sample P91:B-FC+T which has a decarburised surface layer (155 HV) but an acceptable tempered martensitic bulk microstructure (212 HV). Using EON's current inspection methods (portable hardness and surface replication) samples P91:B-MHT

and P91:B-FC+T would have both been determined as aberrant since the hardness data would show soft material and the surface replicas would show an equiaxed ferrite grain structure depleted of carbon. However, given that the current techniques have determined both samples to have a decarburised surface layer, the EM sensor is able to differentiate the two samples from one another and suggest that the bulk microstructure of P91:B-FC+T is harder than the bulk microstructure of P91:B-MHT. Furthermore, samples P91:B-N+T24 and P91:B-N+T100 which have below specification bulk material (<200 HV) have a significantly higher inductance value (similar to P91:B-MHT sample) than both the acceptable P91:B-FC+T and P91:B-CHT samples which have bulk material hardness values at 212 HV and 257 HV respectively. Therefore in the instance that a component has a relatively thin aberrant surface layer compared with the bulk (up to circa 500 μm for components with a minimum of 18 mm wall thickness), then the EM sensor is able to distinguish the samples based on their bulk microstructures. Surface replication and portable hardness testing would mistakenly conclude P91:B-FC+T as aberrant material even though the bulk microstructure is within specification, whereas the EM sensor can differentiate P91:B-FC+T from the P91:B-MHT based on their bulk material microstructures.

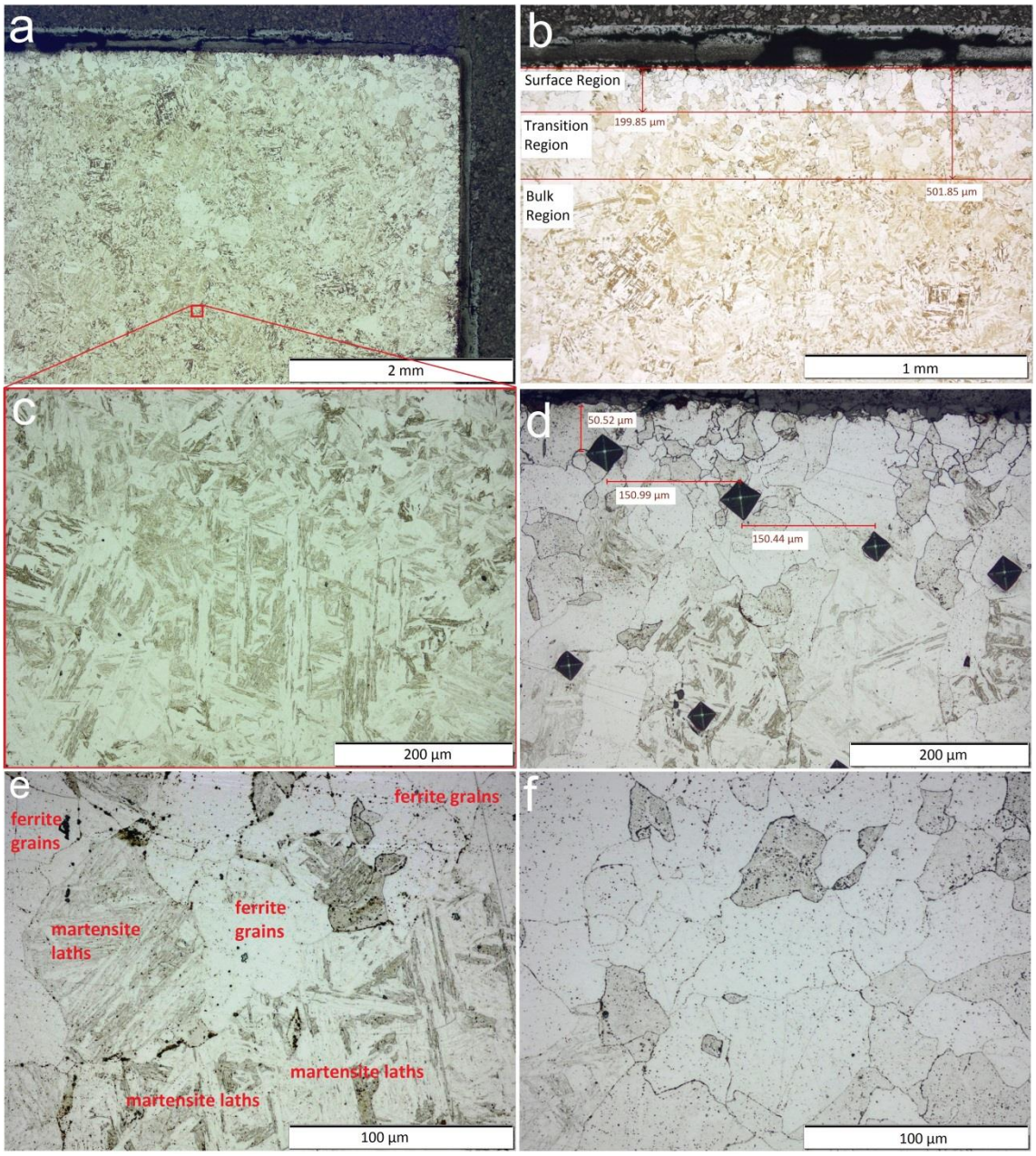

Figure 4-12: Various LOM images for sample P91:B-FC,
(a) low mag. showing coarse ferrite grains at the edges, (b) low mag. showing depth of ferrite from edge, (c) high mag. showing bulk martensite, (d) high mag. showing ferrite at surface, (e) higher mag. showing transition between ferrite and martensite regions (f) higher mag. showing ferrite grains with carbides

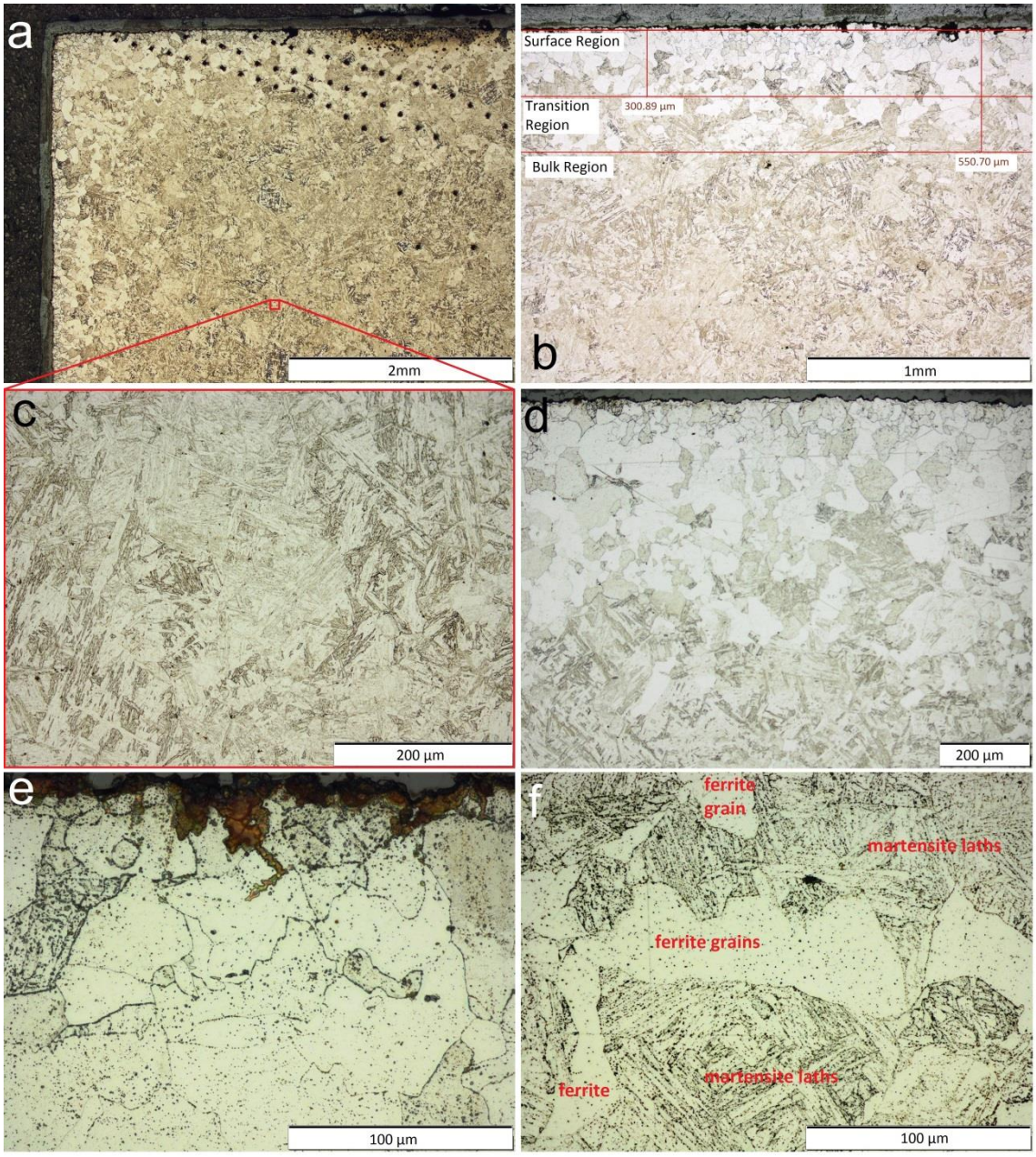

Figure 4-13: Various LOM images for sample P91:B-FC+T, (a) low mag. showing coarse ferrite grains at the edges as well as hardness indents, (b) low mag. showing depth of ferrite from edge, (c) high mag. showing bulk martensite, (d) high mag. showing ferrite at surface transitioning to martensite, (e) higher mag. showing transition equiaxed ferrite grains at the surface (f) higher mag. showing ferrite/martensite transition region

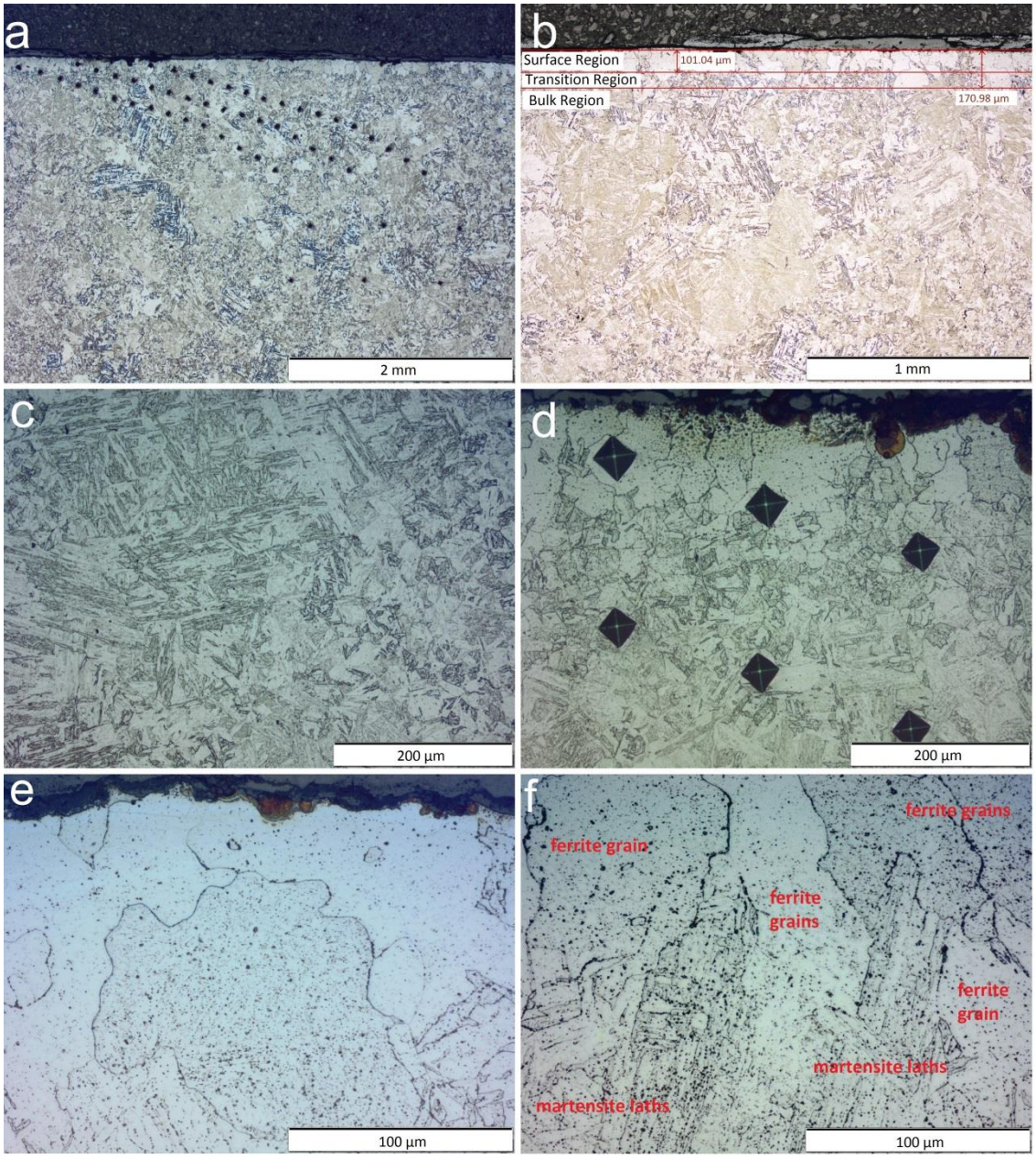

Figure 4-14: Various LOM images of sample P91:B-N+T24,
(a) low mag. showing coarse ferrite grains at the surface as well as hardness indents, (b) high mag. showing depth of ferrite from surface, (c) high mag. showing bulk martensite, (d) high mag. showing ferrite at surface transitioning to martensite as well as hardness indents, (e) higher mag. showing equiaxed decarburised ferrite grains at the surface (f) higher mag. showing ferrite/martensite transition region

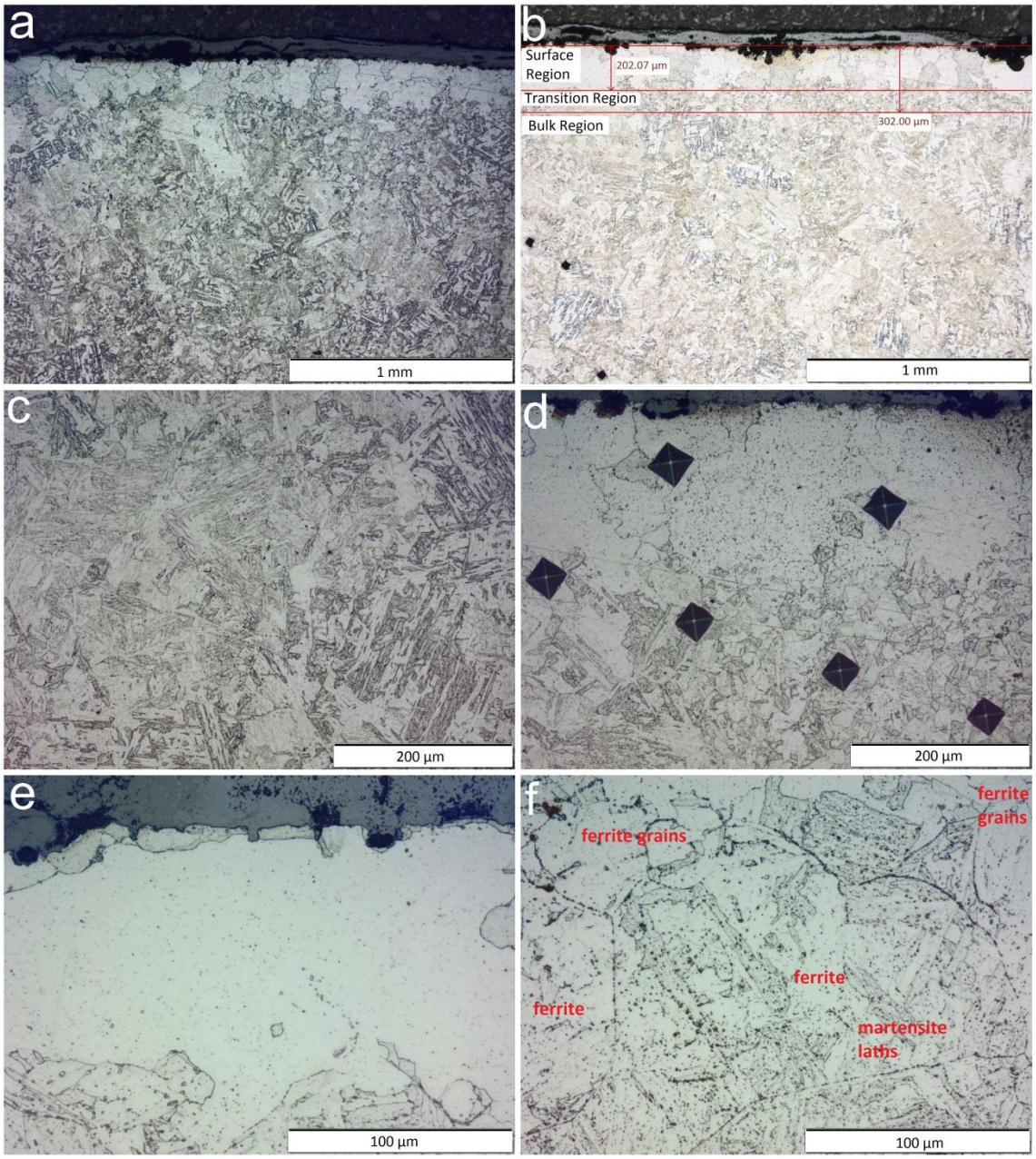

Figure 4-15: Various LOM images of sample P91:B-N+T100,
(a) low mag. showing coarse ferrite grains at the surface, (b) high mag. showing depth of ferrite from surface, (c) high mag. showing bulk martensite, (d) high mag. showing ferrite at surface transitioning to martensite as well as hardness indents, (e) higher mag. showing decarburised ferrite grain (f) higher mag. showing ferrite/martensite transition region

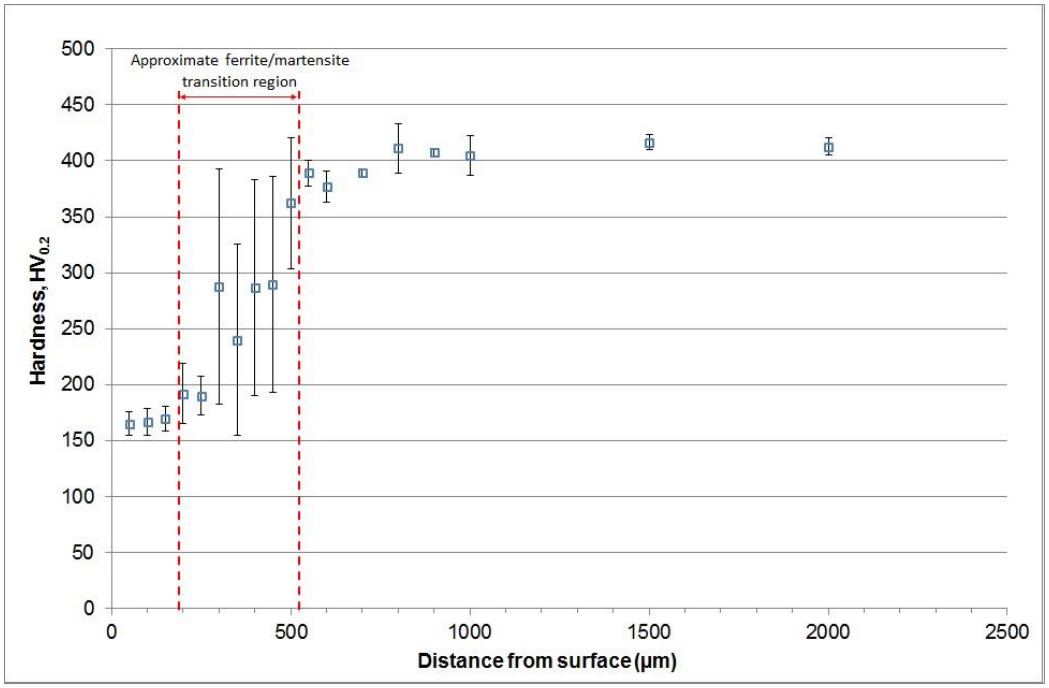

Figure 4-16: P91:B-FC hardness profile between sample surface and 2 mm into the bulk. Each data point and standard deviation error bars are based on three indentations per incremental depth.

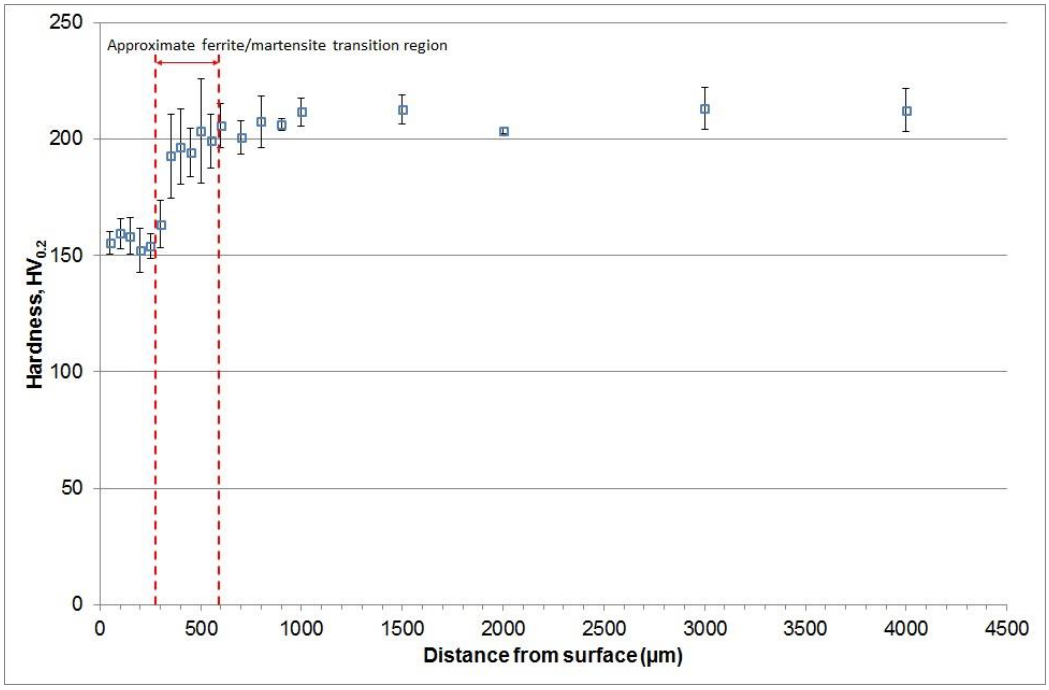

Figure 4-17: P91:B-FC+T hardness profile between sample surface and 4 mm into the bulk. Each data point and standard deviation error bars are based on three indentations per incremental depth.

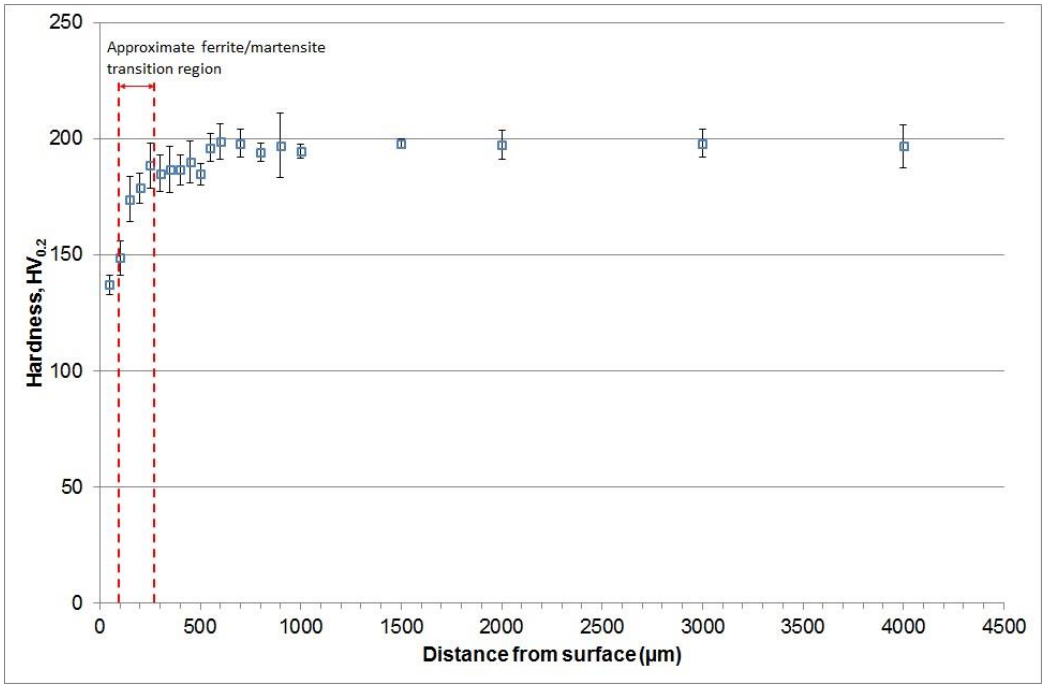

Figure 4-18: P91:B-N+T24 hardness profile between sample surface and 4 mm into the bulk. Each data point and standard deviation error bars are based on three indentations per incremental depth.

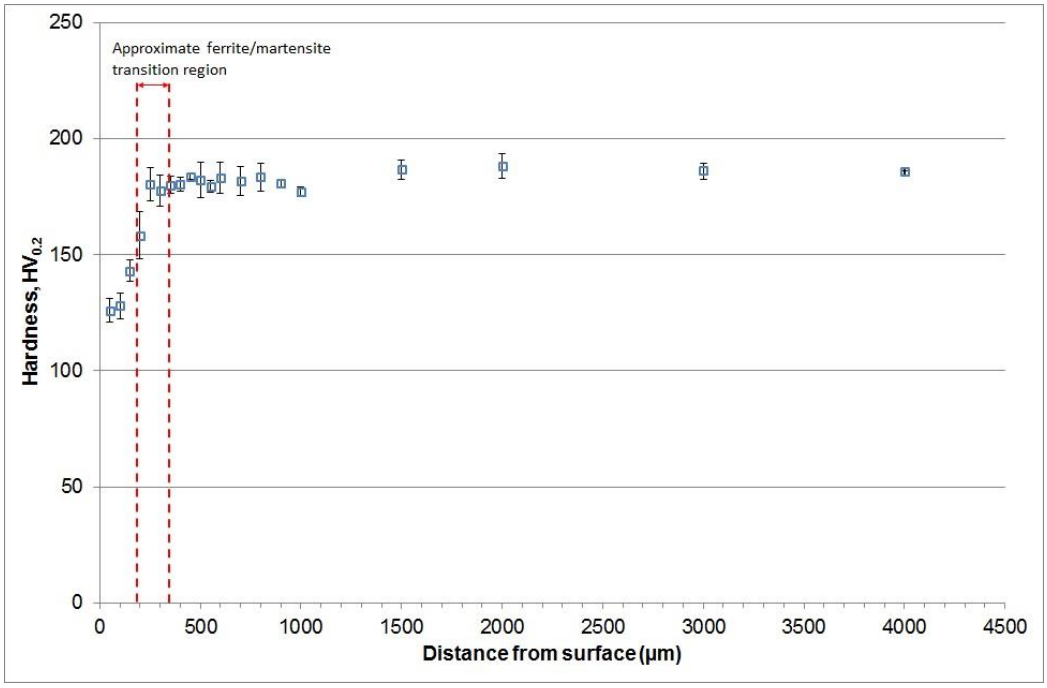

Figure 4-19: P91:B-N+T100 hardness profile between sample surface and 4 mm into the bulk. Each data point and standard deviation error bars are based on three indentations per incremental depth.

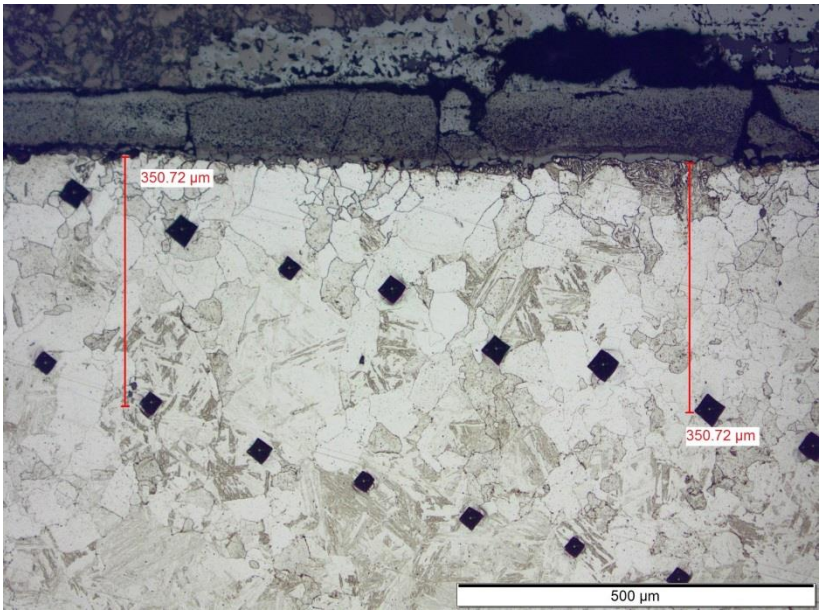

Figure 4-20: P91:B-FC high mag. micrograph of surface region showing hardness indents. At 350 µm from the surface, indents can be seen made in different phases; (left) indent in martensite packet and (right) indent in ferrite grains

Table 4-6: Hardness and low frequency (10 Hz) inductance results for various heat treated P91:B samples. Surface and bulk hardness values were taken at depths of 50 µm and 2000 µm from the surface respectively.

Sample	Average depth of decarburised layer (µm) +SD	Surface Hardness ± SD ($HV_{0.2}$)	Bulk Hardness ± SD ($HV_{0.2}$)	Inductance ± SD ($x10^{-4}$ H)
P91:B-CHT	No decarb layer	No decarb layer	257 ± 5	5.04 ± 0.21
P91:B-MHT	No decarb layer	No decarb layer	180 ± 4	6.09 ± 0.12
P91:B-N+T100	202 ± 7	126 ± 5	188 ± 5	6.20 ± 0.15
P91:B-N+T24	101 ± 21	137 ± 4	197 ± 9	6.01 ± 0.31
P91:B-FC+T	301 ± 23	155 ± 5	212 ± 9	5.50 ± 0.96
P91:B-FC	200 ± 27	165 ± 10	413 ± 8	3.05 ± 0.16

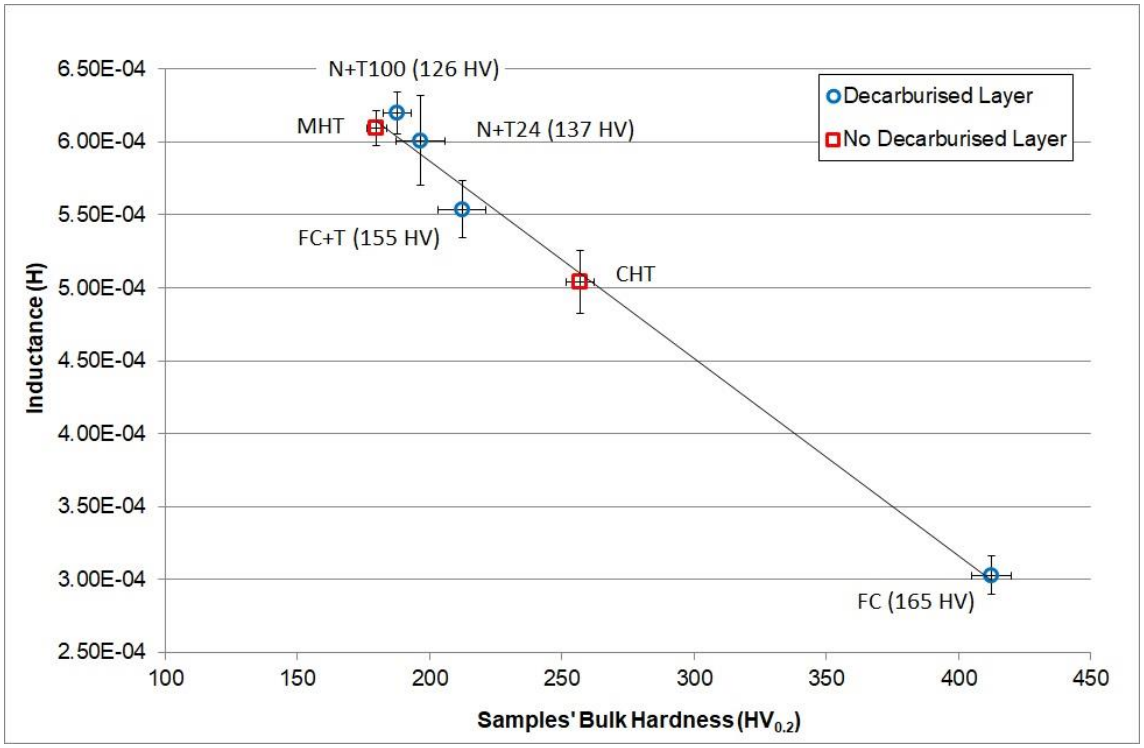

Figure 4-21: P91:B samples' inductance results at 10 Hz varied with the samples' bulk hardness value, samples' decarburised surface layer hardness values are given in brackets

4.5. Impact of Progressively Removed Decarburised Surface Layer

To be able to understand the impact of a decarburised surface layer in isolation on the inductance value, a trial to progressively remove the decarburised layer incrementally and test the sample using the EM sensor at each increment of removed surface layer was performed. Tata Steel supplied Grade 91 plate material identified as PL91:A which in the as-received condition (sample PL91:A-AR) consisted of a tempered martensitic lath microstructure shown in Figure 4-22, with a measured hardness value of 222 HV.

To create a significant decarburised surface layer (1.5 – 2 mm thick decarburised layers typically seen by EON in practise), sample PL91:A-N1100+FC was generated by over-normalising the material followed by slow cooling. The sample was heat treated for 16 hours at a normalising temperature of 1100 °C (more details can be found in the

experimental chapter, Section 3.3.5). Using Fick's second law equation (Eq. 4-1), a decarburised surface layer of 1.75 mm would be expected.

$$x = \sqrt{Dt} = \sqrt{(5.3 \times 10^{-11}).(57600)} = 1.747 \times 10^{-3}\ \mathrm{m} \qquad \textbf{Eq. 4-1}$$

$$= 1.75\ mm$$

Where *D* is the diffusion co-efficient in m^2s^{-1} and *t* is the time in seconds.

The sample's microstructure can be seen in Figure 4-23 which exhibits a decarburised surface layer made of equiaxed ferrite grains, highlighted in Figure 4-23b and a bulk microstructure made up of martensitic laths highlighted in Figure 4-23c. The depth of the decarburised surface layer is approximately 1.6 mm (shown in Figure 4-23a) which is not too similar from the approximation of 1.75 mm based on Fick's second law (Eq. 4-1). Higher magnification shows the white carbon depleted ferrite grains at the surface in Figure 4-23d. The hardness profile, between the surface and to a depth of 6 mm into the bulk, is given in Figure 4-24. The hardness profile confirms a soft surface layer (which is expected for a decarburised layer due to the depletion of carbon), with an average hardness of 200 HV to a depth of approximately 350 μm. The hardness increases as the indents go deeper into the bulk until about 1.7 mm from the surface, where the hardness value surpasses 400 HV stabilising at approximately 430 HV in the bulk. There is a larger scatter in the hardness data at a depth from the surface between 400 – 1500 μm, similar to what was observed in Figure 4-16. This is because, within this range, a mixture of soft ferrite grains and hard martensitic laths co-exist and hence some indents are made in the soft ferrite grains, whereas others are made in the harder un-tempered martensite. This is demonstrated more clearly in Figure 4-25 which shows two hardness indents at similar depths from the surface (1440 μm) having distinctly different sizes, since one is made in a ferrite grain whilst the other in martensitic laths.

After the heat treatment, sample PL91:A-N1100+FC was ground using 120 grit SiC paper to remove the surface oxide and produce a smooth surface finish as can be seen in Figure 4-26a. Later in Chapter 5 it will be shown that the surface roughness produced by grinding using 120 grit SiC paper, does not have an impact on the inductance value, and as such the surface roughness created at each incremental grinding stage was similar, and hence had a negligible impact on the inductance results. The sample was also sectioned using a Struers Accutom cutting disc to expose a cross-sectional smooth surface which comprised of the 1.6 mm thick decarburised surface layer above the un-tempered martensitic bulk microstructure, as shown in Figure 4-26b. Multi-frequency EM tests were then performed; firstly on the 120 grit SiC ground decarburised surface, followed by on the exposed cross-sectional surface keeping the sensor on the un-tempered martensitic bulk material approximately 18 mm away from the decarburised surface cross-sectional layer (>4 mm to avoid a parallel edge effect – see Section 3.4.3). This arrangement has been shown schematically in Figure 4-6c. The results, given in Figure 4-27, show that at low frequency (10 Hz) the bulk microstructure's inductance value is 2.41E-04 H, this seems correct for an un-tempered martensitic microstructure with a hardness value of 430 HV, since it is similar to the inductance value of sample P91:A-N (2.54E-04 H) which also had an un-tempered martensitic microstructure with a hardness of 405 HV. The inductance of the bulk microstructure is significantly lower than the inductance measured by the sensor when positioned on top of the decarburised surface layer. This is expected since the depleted carbon coarse ferrite grains in the decarburised surface layer provide less resistance to domain wall motion than the hard martensitic lath bulk microstructure, thus the relative permeability of the surface layer would be higher than the bulk microstructure and resulting in the inductance at the surface being higher than in the bulk.

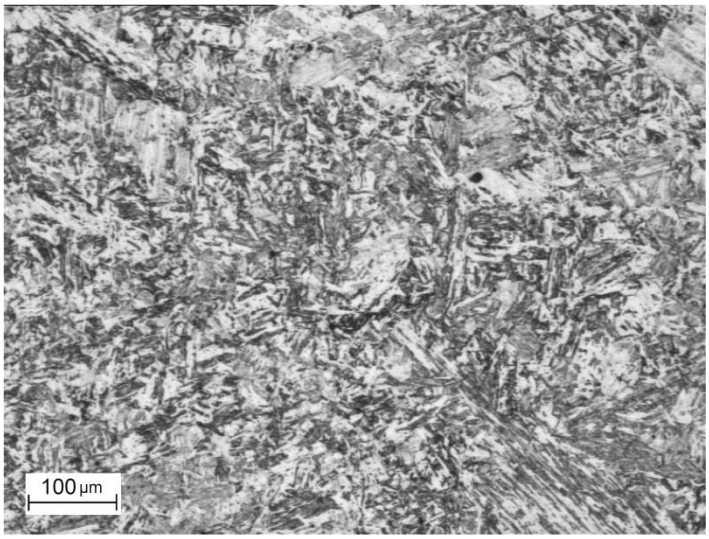

Figure 4-22: LOM image of sample PL91:A-AR in the as-received condition with a tempered martensite lath microstructure

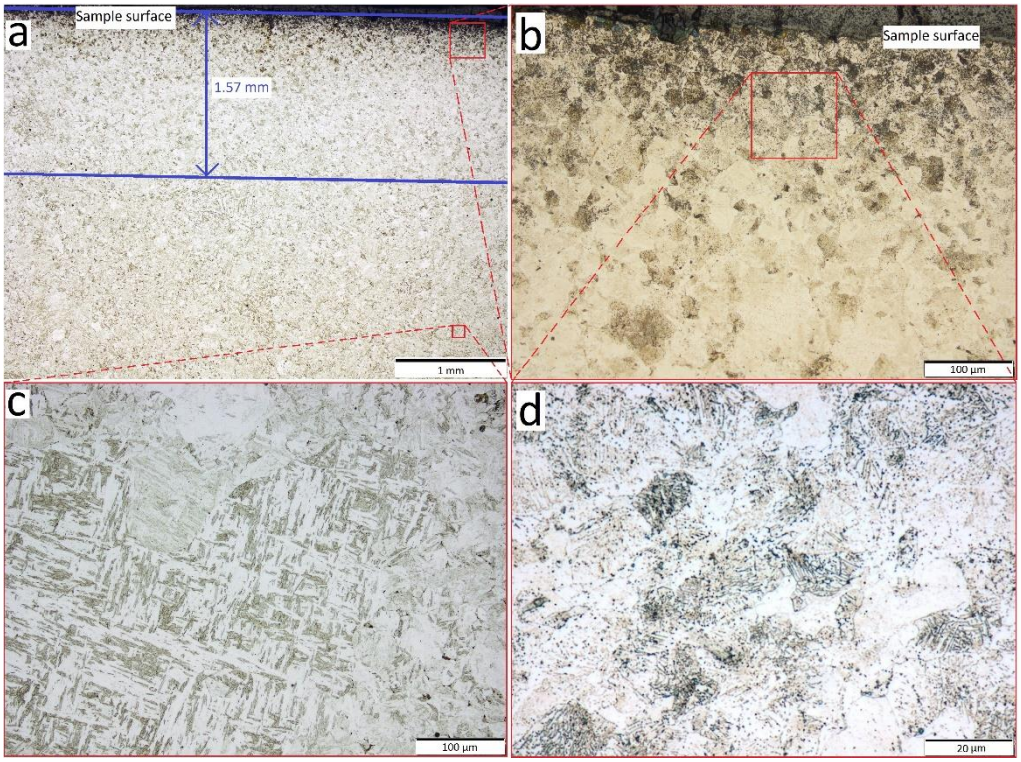

Figure 4-23: Various LOM images displaying sample PL91:A-N1100+FC, (a) low mag. image showing the depth of the equiaxed ferrite grains, (b) high mag. of the ferrite grain

surface layer, (c) high mag. image portraying the bulk martensitic lath microstructure, (d) high mag. image demonstrating the equiaxed depleted carbon surface layer

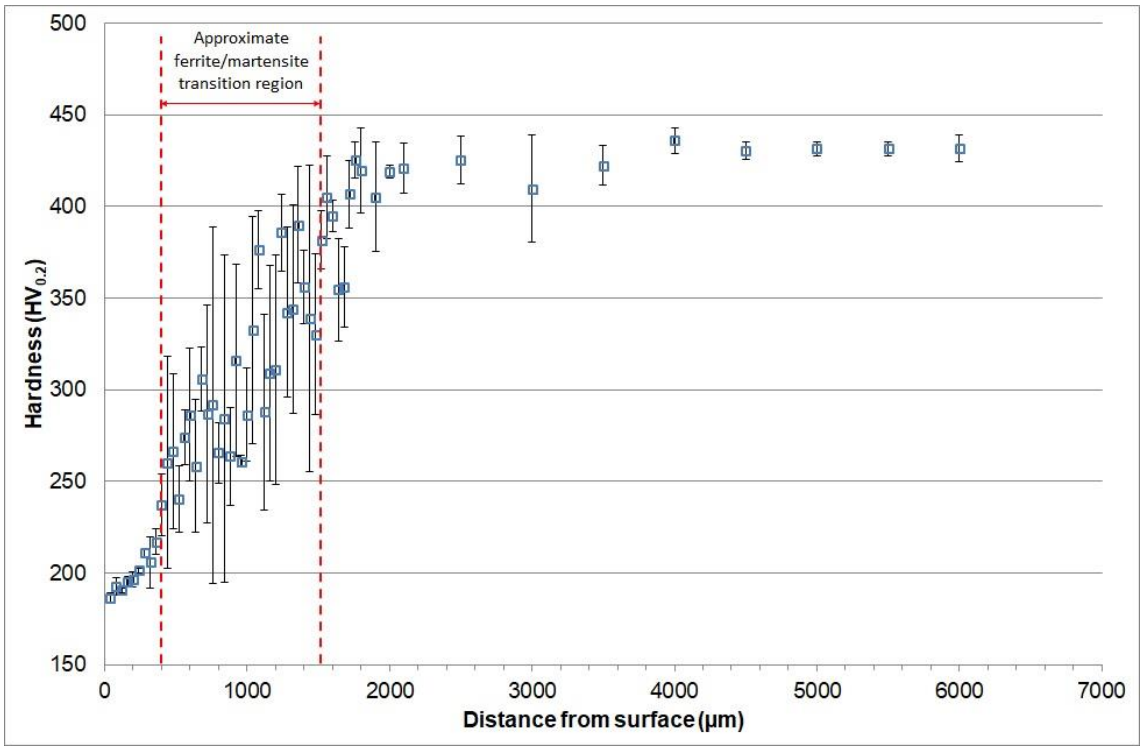

Figure 4-24: PL91:A-N1100+FC hardness profile between sample surface and 6 mm into the bulk

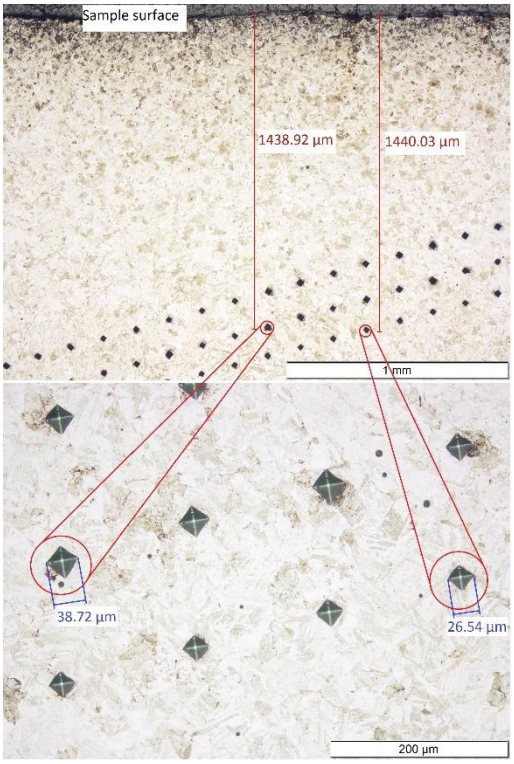

Figure 4-25: Sample PL91:A showing two hardness indents of different size but at similar depths from the surface, (left) large indent made in ferrite grain and (right) small indent made in martensitic laths

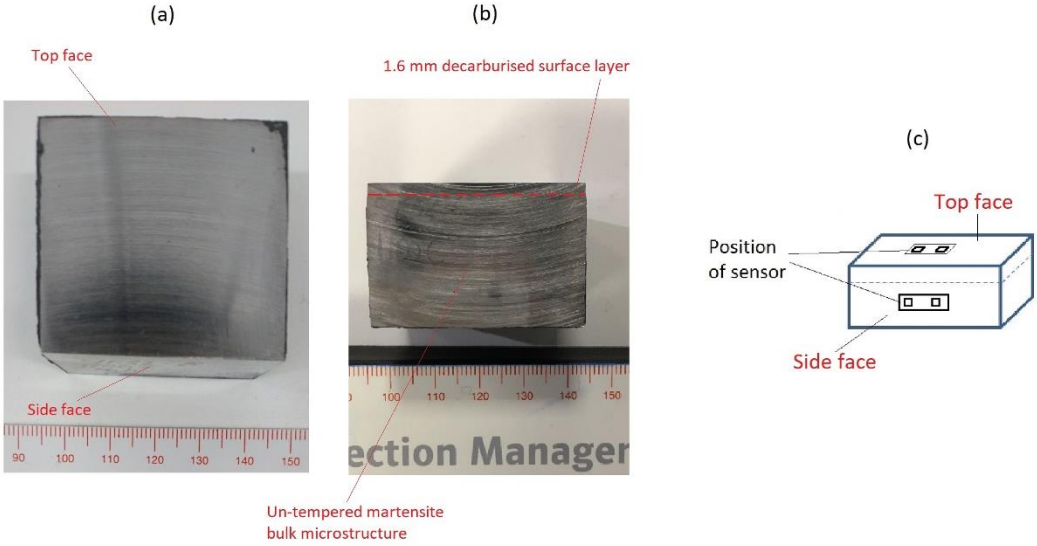

Figure 4-26: Sample PL91:A-N1100+FC, (a) showing top face (decarburised surface) with a smooth 120 grit SiC ground surface finish, (b) showing cross-sectional side face, (c) schematic image showing position of sensor with regards to surfaces

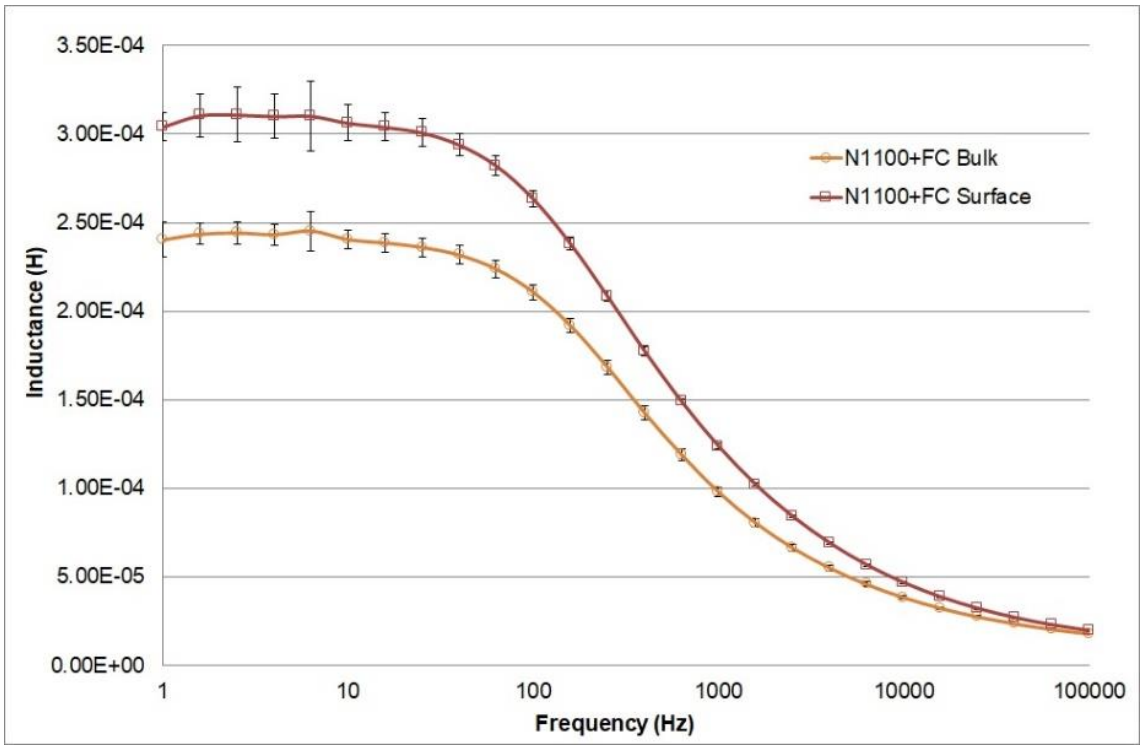

Figure 4-27: Multi-frequency EM signal for PL91:A-N1100+FC sample comparing the results for placing the sensor on the soft ferrite grain surface with the martensitic bulk

The decarburised surface layer was then progressively removed using SiC grinding paper and a low frequency (10 Hz) EM test was performed on each newly exposed surface, the results for which are given in Figure 4-28. The sample thickness was measured, after each incremental layer of the decarburised surface layer was removed, using a micrometer to determine how much of the layer had been removed (details of this procedure are given in Section 3.3.7). As the soft decarburised surface layer is removed, a larger proportion of the EM signal is interacting with the harder bulk material. Since the bulk material (in this case, un-tempered martensite) is mechanically harder than the softer decarburised surface layer (equiaxed ferrite), this causes the inductance to progressively decrease as the soft surface layer is progressively removed. The low frequency inductance (at 10 Hz) is equal to 3.06E-04 H, with the

presence of a 1600 µm decarburised surface layer. This is 25% higher than the inductance measured for the un-tempered martensitic bulk microstructure in (2.45E-04 H). 70% of this decrease (3.06E-04 H down to 2.63E-04 H) takes place over the removal of the first 400 µm of soft aberrant surface layer which can be seen between in Figure 4-28 as the decarburised surface layer is reduced from 1600 µm to 1200 µm. The remaining 30% decrease of signal gradually reduces down to 2.45E-04 H over the removal of the remaining 1200 µm of the decarburised surface layer. This occurs because at the surface, before any of the decarburised layer is removed, the microstructure is predominantly equiaxed ferrite grains with a hardness of 187 HV (as shown in Figure 4-28) measured at a depth of 40 µm from the surface. The material within the ferrite region will have a higher relative permeability compared to the bulk material which has a mechanical hardness of 432 HV. Progressively removing 400 – 500 µm of the decarburised surface layer leads to a significant decrease in the EM signal as most of the ferrite only region is removed, after which the microstructure begins to transition from equiaxed ferrite grains to martensitic laths, effectively decreasing the relative permeability. At these depths (beyond 400 µm from the surface) the majority of the EM signal is now interacting with a martensitic microstructure as opposed to ferrite grains and therefore the difference between the relative permeability of the ferrite/martensite transition region and the bulk will be relatively smaller than the difference between the relative permeability of the equiaxed ferrite grains (within the first 400 µm from the surface) and the bulk. Thus the rate, at which the EM signal decreases with progressively removed surface layer, reduces after removing the first 400 µm of surface layer which is predominantly equiaxed ferrite grains. From Figure 4-28 it can also be seen that the effect of the surface layer when less than 600 µm thickness of the layer remains (after 1000 µm of the decarburised layer had been removed) has an insignificant effect on the EM signal, this was also seen earlier in the chapter in Table 4-6 and Figure 4-21 where the presence of a thin decarburised

surface layer (up to 500 µm), had an insignificant effect on the inductance value. This is because, by removing a significant proportion of the soft ferrite decarburised grains, the majority of the EM signal is now interacting with the un-tempered martensitic microstructure and so the presence of the remaining 600 µm of the surface layer (which is now a mixture of ferrite grains and martensitic laths) is not soft enough to significantly impact the inductance value.

It would be useful to know whether the influence of a 1.6 mm aberrant decarburised surface layer on the EM sensor is adequate to prevent the EM sensor from differentiating an over-normalised and slow cooled un-tempered bulk microstructure from a CHT tempered martensite through thickness microstructure. To examine this, samples PL91:A-CHT and PL91:A-MHT were produced and EM tested to compare with PL91:A-N1100+FC, details of sample dimensions and heat treatments are given in Table 3-3 in Section 3.2. PL91:A-CHT sample consisted of a typically tempered martensitic microstructure (given in Figure 4-29a) with an average hardness of 230 HV and PL91:A-MHT displayed an aberrant equiaxed ferritic soft microstructure (given in Figure 4-29b) with a hardness of 150 HV. EM tests were performed on all three samples sectioned from PL91:A with the results tabulated in Table 4-7, along with the samples' bulk and surface hardness values, where applicable.

The low frequency inductance has been plotted (Figure 4-30) against the samples' bulk hardness values, and as seen in previous results (Figure 4-9 & Figure 4-21), the EM signal is linearly proportional to the samples' bulk hardness values. The inductance value for sample PL91:A-N1100+FC is significantly lower than PL91:A-CHT. This results shows that the EM sensor can differentiate CHT material, which has a tempered martensite bulk microstructure, from material with an un-tempered martensitic bulk microstructure even with the presence of a 1.6 mm decarburised surface layer. Although the decarburised layer increases the EM signal for sample PL91:A-

N1100+FC (Surface), the increase is insignificantly low such that the inductance value cannot be misinterpreted as CHT material.

In practise, if hardness testing the surface of a thick walled component (≥ 35 mm wall thickness) leads to results which indicate that the surface is soft and below specification (i.e. <200 HV), then current quality assurance (for a typical power generation utility) dictates that the surface is ground back 0.5 mm and re-tested. If the material is still soft and below specification, then a further 0.5 mm is ground and re-tested – this continues to a maximum depth of 2 mm. If at a depth of 2 mm the microstructure is still soft, then the component is determined aberrant and rejected. Under current NDT screening methods, hardness testing and surface replication would be employed to assess material integrity and would reveal that samples PL91:A-MHT and PL91:A-N1100+FC have soft decarburised microstructures at the surface (151HV and 187 HV respectively). This would then require technicians to grind the surfaces on both components four times, removing 0.5 mm at each stage, and re-perform the hardness and surface replication tests at each stage, to eventually determine that PL91:A-MHT has an aberrant microstructure through thickness and PL91:A-N1100+FC has a un-tempered martensitic microstructure, ultimately leading to the rejection of both components. In other words, the current NDT screening practice requires grinding of up to 2 mm to correctly indicate the bulk microstructure, however, with the aid of EM sensor measurements, PL91:A-MHT and PL91:A-N1100+FC samples can be separated as soft aberrant through thickness materials and hard aberrant bulk materials respectively without further grinding, thus saving time.

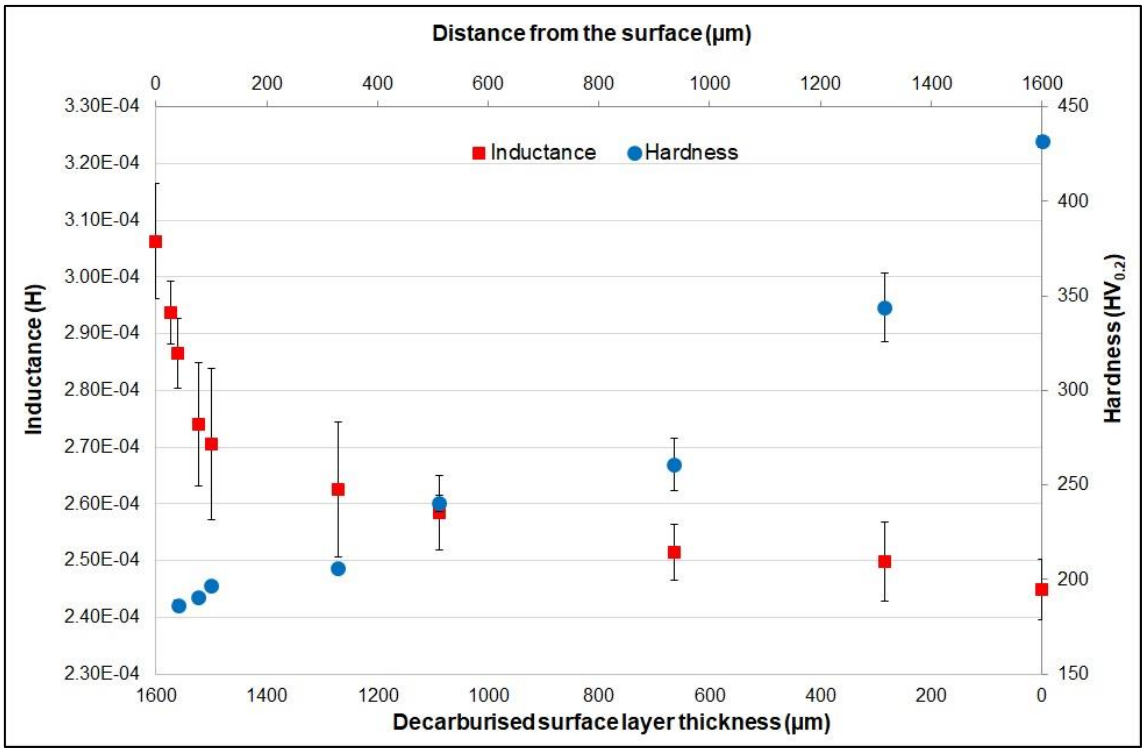

Figure 4-28: PL91:A-N1100+FC sample low frequency (10 Hz) inductance variation with progressively removed decarburised surface layer

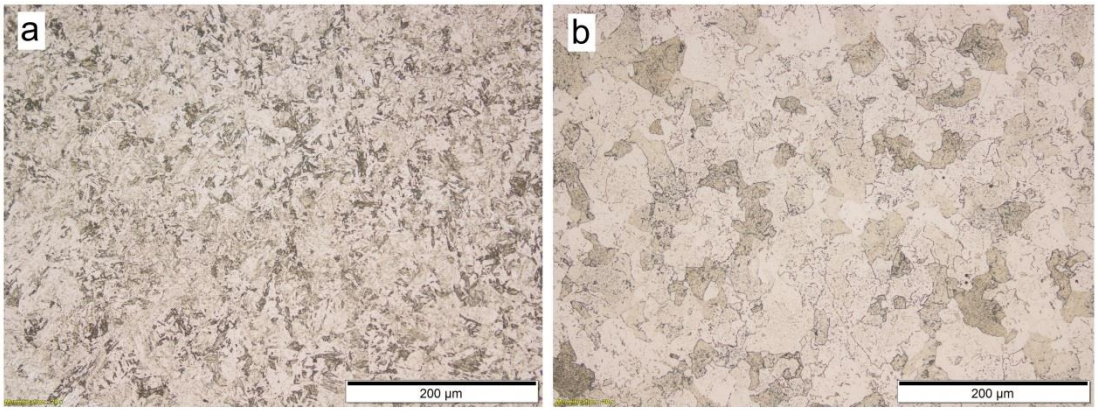

Figure 4-29: PL91:A heat treated samples (a) PL91:A-CHT, tempered martensite, (b) PL91:A-MHT aberrant ferritic microstructure

Table 4-7: Hardness and low frequency (10 Hz) inductance results for heat treated PL91:A samples. Bulk hardness values were taken at depths of 1000 μm for samples CHT and MHT. Bulk and surface hardness values were taken at depths of 5000 μm and 40 μm from the surface respectively for samples N1100+FC Bulk and N1100+FC Surface

Sample	Surface Hardness ± SD ($HV_{0.2}$)	Bulk Hardness ± SD ($HV_{0.2}$)	Inductance ± SD ($x10^{-4}$ H)
PL91:A-MHT	NA	151 ± 1	5.77 ± 0.08
PL91:A-CHT	NA	230 ± 0	4.87 ± 0.06
PL91:A-N1100+FC (Surface)	187 ± 2	432 ± 4	3.06 ± 0.10
PL91:A-N1100+FC (Bulk)	NA	432 ± 4	2.41 ± 0.05

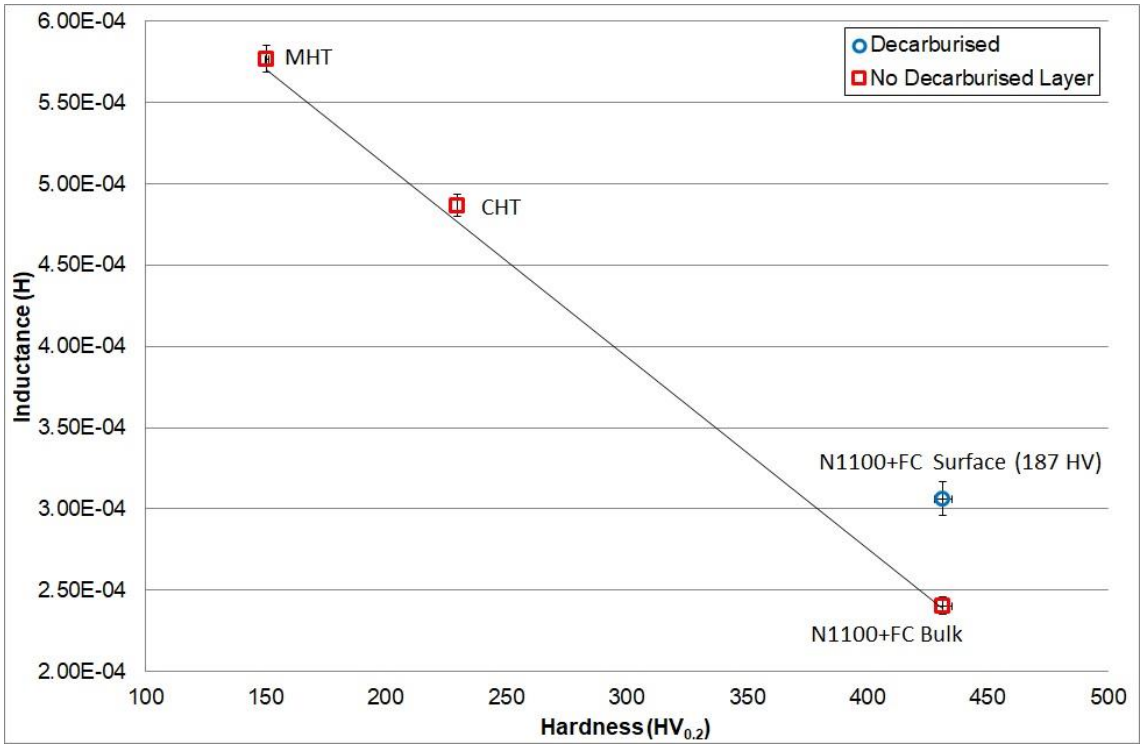

Figure 4-30: Single frequency (10 Hz) Inductance variation with bulk hardness for samples PL91:A MHT, CHT, N1100+FC Bulk and N1100+FC Surface. Decarburised surface layer hardness value is given in brackets.

4.6. Summary

Different Grade 91 microstructures that can be present in industrial power plant boiler components (soft mis-heat treated ferritic, correctly heat treated tempered martensite and hard as-normalised un-tempered martensite) were assessed using an EM sensor. The EM sensor has shown that at low frequency (10Hz) it has the ability to differentiate different microstructures by measuring their inductance which correlates linearly with the material's bulk hardness value. The correlation between the different microstructures and the relative permeability, which determines the inductance, has been discussed.

Samples were heat treated to replicate components which have different microstructures at the surface compared to their bulk, commonly caused by mis-heat treatments in industry, typically over-normalising and under-tempering. The influence of the decarburised surface layer caused inductance values to increase since softer equiaxed ferrite grains will have a higher relative permeability than harder martensitic microstructures. However, the influence on the inductance for the range of samples tested, was not significant enough to deter the EM sensor from distinguishing through thickness aberrant soft material (which would be out of specification for service entry material) from acceptable tempered martensite bulk with the presence of a thin (300-500 µm) decarburised surface layer microstructures (which would be within specification for service entry material). It was also able to distinguish acceptable tempered martensite material from unacceptable un-tempered martensite bulk material with the presence of a larger (1.6 mm) decarburised surface layer.

For the range of samples tested, the EM sensor would be a valuable technique for EON to deploy as part of their NDT assessment of service entry components, since the EM sensor was able to differentiate correctly heat treated bulk microstructures from

mis-heat treated bulk microstructures, even with the presence of up to 1.6 mm decarburised surface layers. EON's current techniques of portable hardness and surface replication would require significant grinding and re-testing before similar determinations could be made.

CHAPTER 5 EFFECT OF SURFACE ROUGHNESS ON THE EM SENSORS ABILITY TO DETERMINE MICROSTRUCTURES

This chapter explores the significance of the surface roughness finish with respect to the EM sensor inductance values. The chapter studies the impact of various surface finishes created by different machining and surface preparation methods and testing these surfaces with the EM sensor to determine their influence on the measured inductance. The results are discussed with respect to the EM sensor's ability to differentiate CHT from MHT bulk microstructures on samples with varying surface roughness profiles. The chapter also determines the minimum surface roughness finish requirement to avoid any influence of the surface roughness on the components' inductance value, for the EM sensor used in this study.

5.1. Introduction

In the power generation industry there are requirements for minimum surface roughness finishes to carry out certain NDT, since the surface finish can have a significant impact on the integrity of the NDT test [201, 202]. Table 5-1 highlights a typical power generation utility's surface roughness requirements when performing certain NDT [203]. In practise the cost for surface preparation can be significant since thousands of individual NDT tests (which will all require surface preparation) may be required for a single boiler unit during a typical outage. With the commercial benefit of reducing the amount of time a boiler unit is non-operational due to routine inspection, there is a drive to reduce the ratio of the time spent on surface preparation to time spent performing NDT. Therefore it is useful to know what the minimum surface roughness finish requirement is, for the EM sensor used in this study. A surface roughness (Ra) of 3.2 µm is the most common standard of finish that accommodates most NDT inspection methods (used by EON). The dye penetrant and replication techniques require better surface finishes as they are heavily dependent on the surface to be able to provide accurate results, unlike eddy-currents and ultrasonics. Surface undulations can restrict the flow of dye over a surface hampering the dye penetrant

technique [204] whereas surface replications require the material to be etched to reveal the microstructure, and hence a mirror-like polished finish is required is time consuming and laborious. Ultrasound and magnetic particle inspection have less stringent requirements as they are not as dependent on the surface finish, although ultrasound requires a coupling medium between the probe and component surface. Eddy currents however can be more sensitive to the surface finish, since it is an electromagnetic technique, depending on the depth of the defects, e.g. if a defect 0.2 mm beneath the surface is to be detected reliably using eddy currents, then the surface undulations ought to be ten times smaller. If the surface is too rough then the signal, due to variations in the surface, could mask any defects [205]. The surface roughness of a component can vary depending on how the surface has been processed e.g. machining, cutting, grinding, polishing, surface damage from handling, or oxidation and corrosive operations. Clearly the surface finish of a component has an impact on the ability to carry out different NDT, hence the requirements in Table 5-1.

Table 5-1: Power generating utility's typical surface roughness specification for certain NDT techniques

NDT technique/ Surface preparation	Minimum arithmetic mean surface roughness, Ra (µm)
Surface Replication Portable Hardness Testing	Mirror-like finish <1.6
Dye-Penetrant	1.6
Ultrasound Eddy Current Magnetic Particle Inspection Ground Surface Finish Machined Surface	3.2
Shot Blast Surface Finish	6.3

For EM techniques, the surface roughness can prevent perfect contact between the EM sensor and the material. Kalyanasundaram and Nagy (2004) [202] have described the effect of surface roughness to be equivalent to that of a constant lift-off for an eddy current application, but this has not been studied for the U-shaped EM sensor used in this research. The effect of lift-off on EM sensors has been acknowledged by some authors in their works and hence an in-built lift-off (millimetres) has been used in some cases to accommodate for the effect of the surface finish [24, 180, 206, 207], since the lift-off reduces the sensor's sensitivity to the surface finish. This effect has been discussed in more detail in the literature review Section 2.5.4.1. Therefore the effect of surface roughness shall be considered for the EM sensor and whether it can be equated to a lift-off type effect and understand the impact on the sensor's ability to distinguish between CHT and MHT material. Also a recommendation will be provided for what the minimum surface roughness finish should be for this particular EM sensor, in line with Table 5-1. It is worth noting that all the samples tested in Chapter 4 had a similar surface finish to one another and hence the surface finish could be discounted as a variable from the experiments in Chapter 4.

5.2. Effect of Surface Roughness on Inductance

In this study Grade 91 material samples (sectioned from pipe P91:A) were prepared with various surface finishes via different mechanical processes as shown in Figure 5-1 (and detailed in the experimental chapter Section 3.2.2.1). This achieved eight surfaces, with varying degrees of surface roughness, on four samples. Surface roughness was measured using a Talysurf Surfcorder SE1700 (details can be found in Section 3.4.2 of Chapter 3). Eight surface roughness measurements were made on each sample surface in different orientations (shown schematically in Figure 5-2) to achieve an average. The software would calculate and output an arithmetic mean (Ra)

surface roughness value. The surface roughness results (given in Table 5-2) shows significant differences, particularly for measurements at locations 3, 7 and 8 (from Figure 5-2) compared to those measured at locations 1, 2, 4, 5 and 6. This was noticed on all sample surfaces where an anisotropic roughness profile existed. For example, with the horizontal bandsaw surfaces (shown in Figure 5-1b, d, f and h) the machined lines quite clearly can be seen in the images. When the Talysurf measuring tip is traversing parallel to the machined lines, the roughness value is lower; as the tip either traverses along the peak or along the valley of a machined line, (hence little variation in the roughness profile) however, when the Talysurf tip is traversing perpendicular to the machined lines, the tip is profiling over the peaks and valleys of the machined lines leading to a larger roughness profile. The only sample where this was not the case was sample P91:A-MG2 - Ground Surface (shown in Figure 5-1g), since this surface has an isotropic surface finish. Therefore it can be deduced that the surface roughness profile anisotropy causes large scatter in the data. This phenomenon can be clearly seen in Figure 5-3, where two 8000 data point plots show the surface roughness profiles for the Bandsaw Surface on sample P91:A-FM1 (the sample's surface is shown in Figure 5-1b), with roughness measurements taken perpendicular to the machined lines (blue plot) and parallel to the machined lines (red plot). As expected, the roughness measurement perpendicular to the machined lines (blue plot), reflects a rough profile of the tip traversing over the large peaks and valleys of the machined lines whereas the roughness measurement parallel to the machined lines (red plot), highlights an almost flat smooth profile in comparison. Consequently, it is important to understand if this directional effect of surface roughness has any influence on the EM sensor inductance values, i.e. if the EM sensor probe was positioned perpendicular or parallel to the surface machined lines, would there be a difference in the inductance value. Therefore sample P91:A-FM1 Bandsaw Surface (surface shown in in Figure 5-1b), was EM tested at multi-frequency with the sensor positioned in parallel and perpendicular to the

machined lines, shown schematically in Figure 5-4. The multi-frequency inductance results, given in Figure 5-5, show that the inductance values are not significantly impacted by the orientation of the sensor, since the difference between the perpendicular and parallel inductance curves is less than the standard deviation error bars, unlike the surface roughness measurements, where there is a significant directional effect when measuring surface roughness. The inductance values begin to drop significantly as the frequency is increased due to the formation of eddy currents dictated by the sample's resistivity, as described in the experimental chapter Section 3.4. Figure 5-6 magnifies the high frequency inductance behaviour (10 – 100 KHz) and shows that, similar to the low frequency results, the inductance values for the two orientations are almost identical. Therefore, for the remainder of the research, surface roughness measurements, for samples with an anisotropic roughness profile, were made in the orientation in which the maximum roughness could be captured; (an example shown schematically in Figure 5-7).

All eight surfaces in Figure 5-1 had their surface roughness profiles measured and EM tested at multi-frequency. Four surface roughness measurements were made on each surface yielding the arithmetic mean surface roughness (Ra) and maximum surface roughness (Rmax) parameters; a description of these parameters and their significance in for this study, is given in Section 3.3.4 of the experimental chapter. The roughness parameters and low frequency (10 Hz) inductance values are given in Table 5-3 and the multi-frequency inductance results are given in Figure 5-8. The multi-frequency curve shows that the surface roughness has a significant impact on the inductance values such that samples with smoother surfaces have a higher inductance than those with rougher surfaces. Magnification of the low frequency (10 – 100 Hz) inductance results, given in Figure 5-9, shows the smoothest samples, MG1-Ground Surface (Rmax = 3.01 µm) and MG2-Ground Surface (Rmax = 5.72 µm), to have an almost

identical inductance inseparable by their error bars. There is a grouping of the four Bandsaw Surface samples which all had a similar surface roughness, Rmax between 24 – 30 µm and had similar inductance values to each other with overlapping error bars. The Bandsaw Surface samples all had significantly lower inductance values than the smooth Ground Surface samples due to their higher surface roughness. The two samples with milled surfaces (FM2-Milled Surface and FM1-Milled Surface) had the highest surface roughness with Rmax = 47.23 µm and 53.12 µm respectively. Consequently, they both had lower inductance values than the smooth Ground Surfaces and the Bandsaw Surfaces, again suggesting that the inductance decreases with surface roughness. It is also observed that as the frequency is increased, all samples' inductance values begin to converge, as seen previously in Figure 5-5 and in Figure 3-24 of the experimental chapter. This is due to the samples' resistivity causing eddy currents to form and reduce the skin depth to which the magnetic flux is penetrating the sample. The observation of inductance decreasing with surface roughness is also seen for all the samples at higher frequencies as shown in Figure 5-10, which magnifies the frequency range 1-10 KHz. At a frequency of 10 KHz, the skin depth has been reduced from 12 mm at 10 Hz down to approximately 400 µm, (methodology for calculating skin depth has been given in Section 3.4.7). Although the amount of magnetic flux interacting with the sample at this frequency is very small (due to the eddy currents produced by the skin effect), the ratio of magnetic flux interacting with the surface roughness profile, relative to the sample's bulk material, has increased. At even higher frequencies (10 – 100 KHz), the inductance values can still be distinguished by their surface roughness such that smooth surfaces have a distinctly higher inductance than the rougher surfaces, shown in Figure 5-11. However, at approximately 40 KHz, where the magnetic flux is only penetrating the sample to a depth of approximately 200 µm, the Bandsaw Surfaces and Milled Surfaces inductance curves converge such that they can no longer be separated by their error bars;

however, the smoother Ground Surfaces are still distinguishable. This is most likely due to the significance of the samples' resistivity within the thin skin layer, such that the Ground Surfaces being smoother, will have a lower resistivity compared to the rougher surfaces, across the 200 µm surface skin layer. The variation in resistivity in this thin surface skin layer will be caused by the air gaps created by the large peaks in the roughness profiles of the rougher sample surfaces (Bandsaw and Milled Surfaces) compared to the smoother sample surfaces (Ground Surfaces), and hence a lower inductance is observed for the Milled and Bandsaw surface samples compared to the smooth Ground Surface samples at 40 KHz.

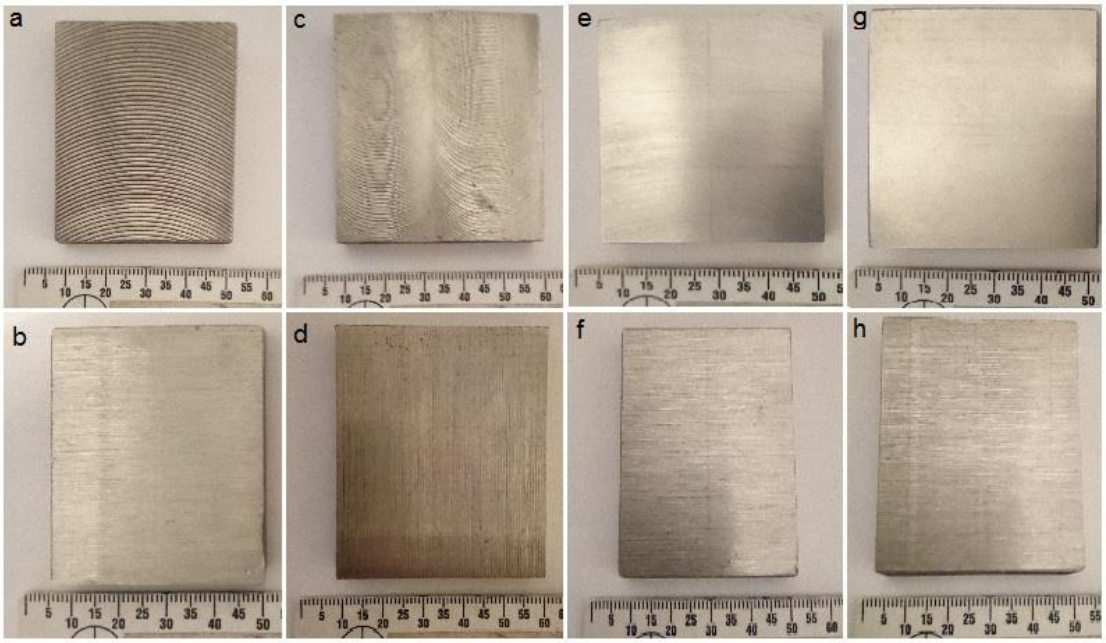

Figure 5-1: Four P91:A-AR samples machined on opposite faces with different surface finishes to produce eight surfaces on four samples. The images above and below one another belong to the same sample, e.g. images (a) and (b) are opposite faces of the same sample. (a) sample P91:A-FM1, surface face milled with a large tool, (b) sample P91:A-FM1, surface cut with a horizontal bandsaw, (c) sample P91:A-FM2, surface face milled with a small tool, (d) sample P91:A-FM2, surface cut with a horizontal bandsaw, (e) sample P91:A-MG1, surface mechanically ground with 400 grit SiC paper, (f) sample P91:A-MG1, surface cut with a horizontal bandsaw, (g) sample P91:A-MG2, surface mechanically ground using Al_2O_3 surface grinder, (h) sample P91:A-MG2, surface cut with horizontal bandsaw.

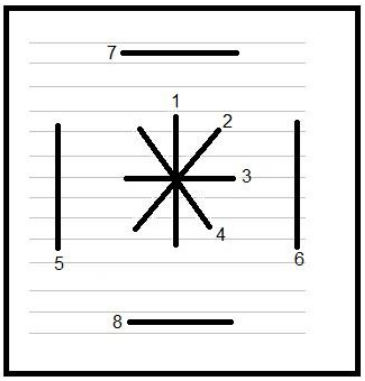

Figure 5-2: Schematic diagram of 8 locations and orientation of surface roughness measurements. Black lines represent surface roughness measurements and grey lines represent the pattern machined into the surface

Table 5-2: Surface roughness measurements at 8 locations and orientations for 8 surfaces on samples P91:A-FM1, P91:A-FM2, P91:A-MG1 and P91:A-MG2

Samples (P91:A-)	Surface Finish	Fig Ref	Surface Roughness, Ra (µm) at 8 locations							
			1	2	3	4	5	6	7	8
FM1 – Milled Surface	Milled with large tool head	5-1a	39.01	52.62	27.62	38.23	42.32	42.21	23.57	26.24
FM1 – Bandsaw Surface	Cut with horizontal bandsaw	5-1b	6.41	4.33	1.78	5.48	5.03	4.98	2.53	1.36
FM2 – Milled Surface	Milled with small tool head	5-1c	10.39	8.19	6.06	9.52	9.97	13.69	4.13	6.30
FM2 – Bandsaw Surface	Cut with horizontal bandsaw	5-1d	6.09	5.11	1.38	5.62	6.48	5.69	2.86	1.02
MG1 – Ground Surface	Ground with 400 SiC paper	5-1e	0.47	0.34	0.24	0.28	0.58	0.52	0.45	0.28
MG1 – Bandsaw Surface	Cut with horizontal bandsaw	5-1f	5.09	4.45	3.09	4.49	5.09	4.80	2.61	1.60

MG2 – Ground Surface	Ground with Al_2O_3 grinding wheel	5-1g	0.09	0.10	0.07	0.08	0.09	0.07	0.06	0.07
MG2 – Bandsaw Surface	Cut with horizontal bandsaw	5-1h	6.33	4.51	1.57	3.79	6.42	4.30	1.77	1.22

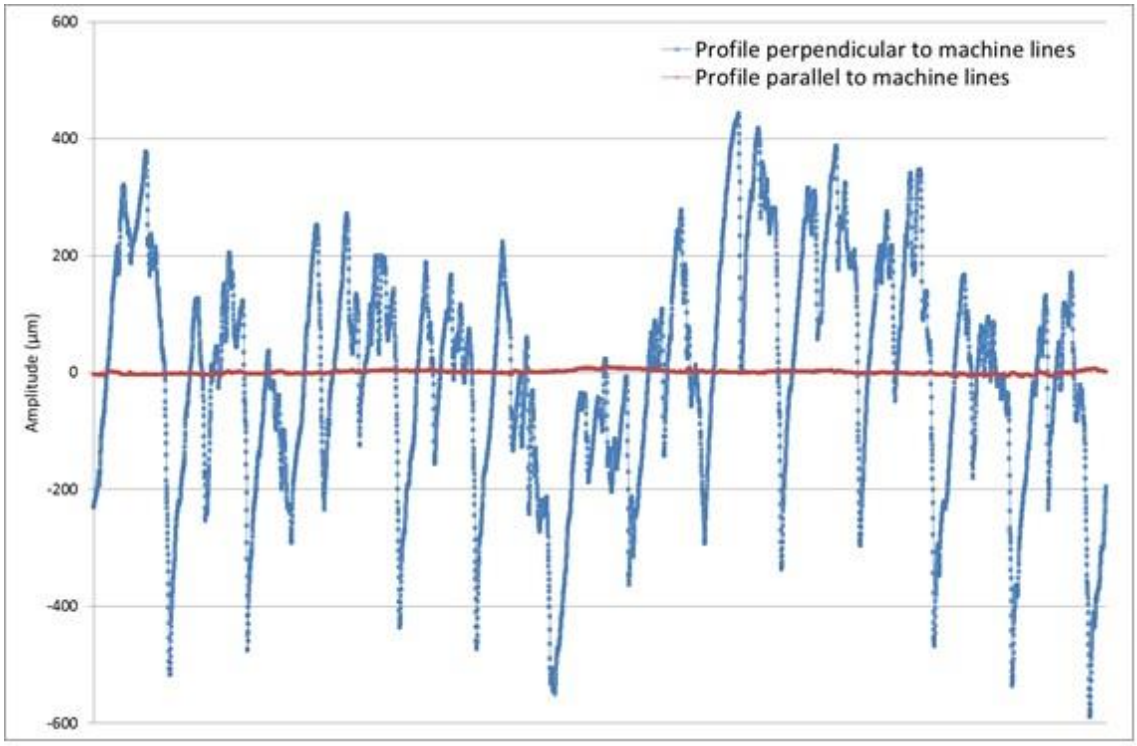

Figure 5-3: Surface profile of sample P91:A-MG1 bandsaw cut surface showing surface roughness profiles measured perpendicular (blue plot) and parallel (red plot) to the bandsaw surface machine lines

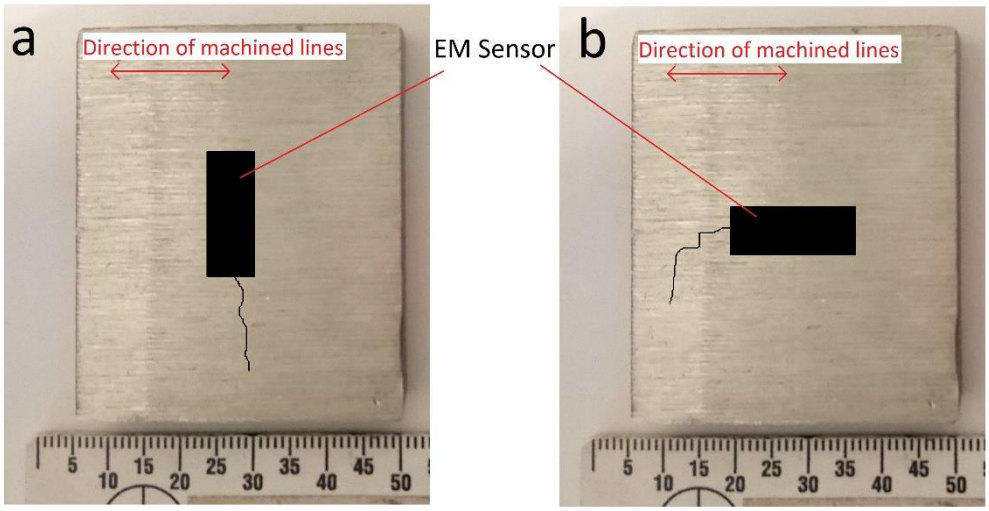

Figure 5-4: Schematic diagram of the EM sensor positioned in, (a) perpendicular and (b) parallel to the machined lines on the Bandsaw Surface on sample P91:A-FM1

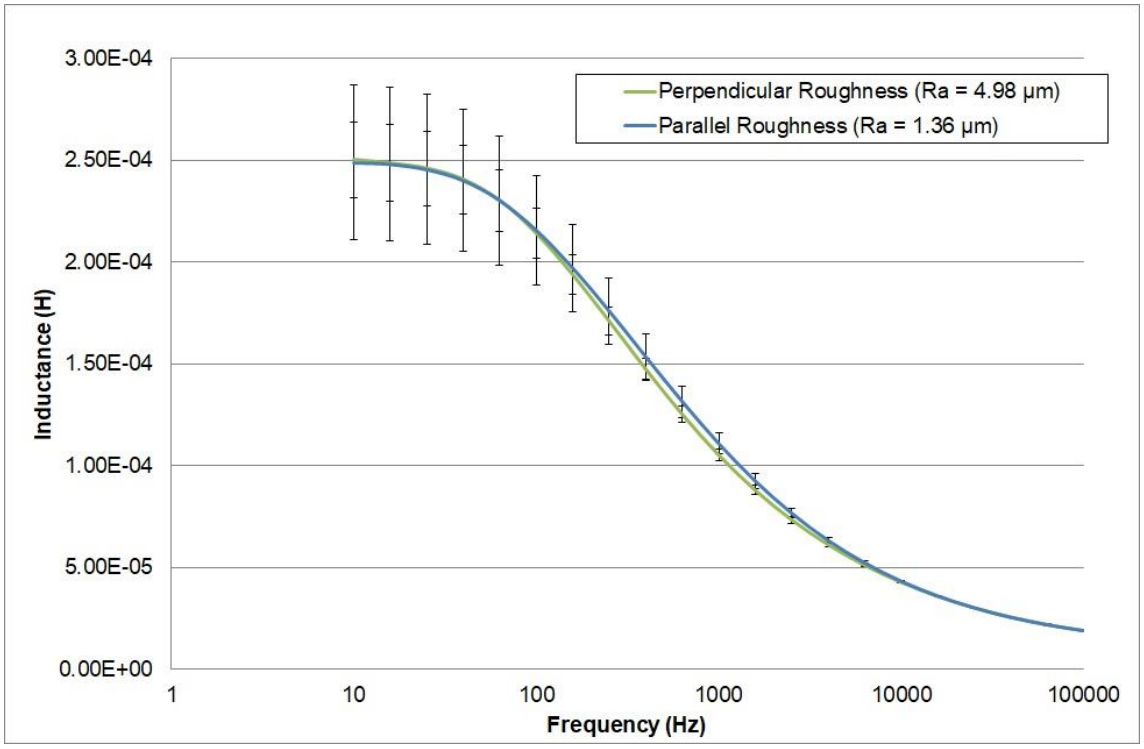

Figure 5-5: Multi-frequency variation of inductance for sample P91:A-FM1 Bandsaw Surface with the sensor positioned perpendicular and parallel to the machined lines

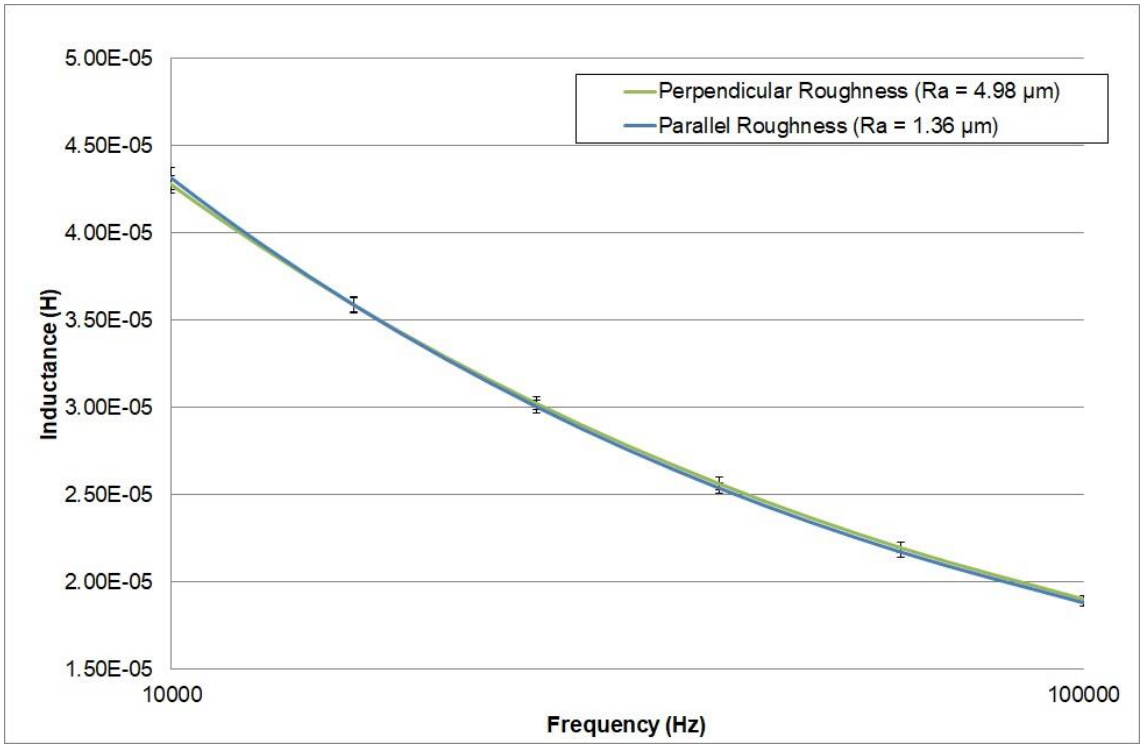

Figure 5-6: High frequency variation of inductance for sample P91:A-FM1 Bandsaw Surface with the sensor positioned perpendicular and parallel to the machined lines

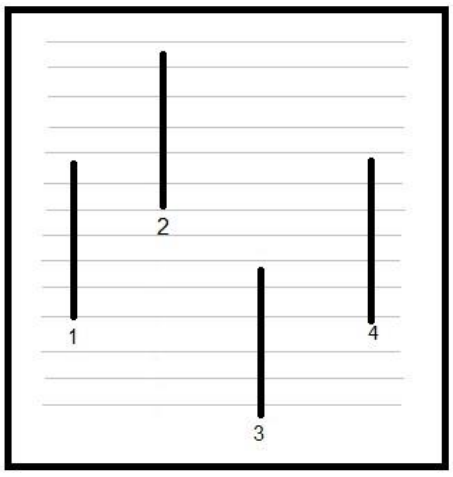

Figure 5-7: Schematic diagram showing how surface roughness measurements were made to yield the highest roughness profile for a given sample. Black lines represent the path taken by the Talysurf profiling tip and the grey lines represent the machined lines

Table 5-3: P91:A samples' surface roughness and low frequency (10 Hz) EM results

Sample (P91:A-)	Surface Finish	Fig Ref	Surface Roughness (µm)		Inductance ($x10^{-4}$ H)
			Rmax (Avg ± SD)	Ra (Avg ± SD)	Avg ± SD
FM1 – Milled Surface	Milled with large tool head	Figure 5-1a	53.12 ± 3.26	40.31 ± 1.77	1.74 ± 0.03
FM1 – Bandsaw Surface	Cut with horizontal bandsaw	Figure 5-1b	27.75 ± 4.58	5.04 ± 0.77	2.50 ± 0.19
FM2 – Milled Surface	Milled with small tool head	Figure 5-1c	47.23 ± 4.29	13.40 ± 1.83	1.82 ± 0.14
FM2 – Bandsaw Surface	Cut with horizontal bandsaw	Figure 5-1d	30.40 ± 6.44	5.94 ± 0.20	2.49 ± 0.38
MG1 – Ground Surface	Ground with 400 SiC paper	Figure 5-1e	5.72 ± 1.80	0.38 ± 0.10	5.02 ± 0.04
MG1 – Bandsaw Surface	Cut with horizontal bandsaw	Figure 5-1f	23.80 ± 2.24	4.68 ± 0.15	2.56 ± 0.34
MG2 – Ground Surface	Ground with Al_2O_3 grinding wheel	Figure 5-1g	3.01 ± 0.24	0.08 ± 0.01	5.00 ± 0.06
MG2 – Bandsaw Surface	Cut with horizontal bandsaw	Figure 5-1h	24.50 ± 2.23	4.39 ± 0.20	2.64 ± 0.42

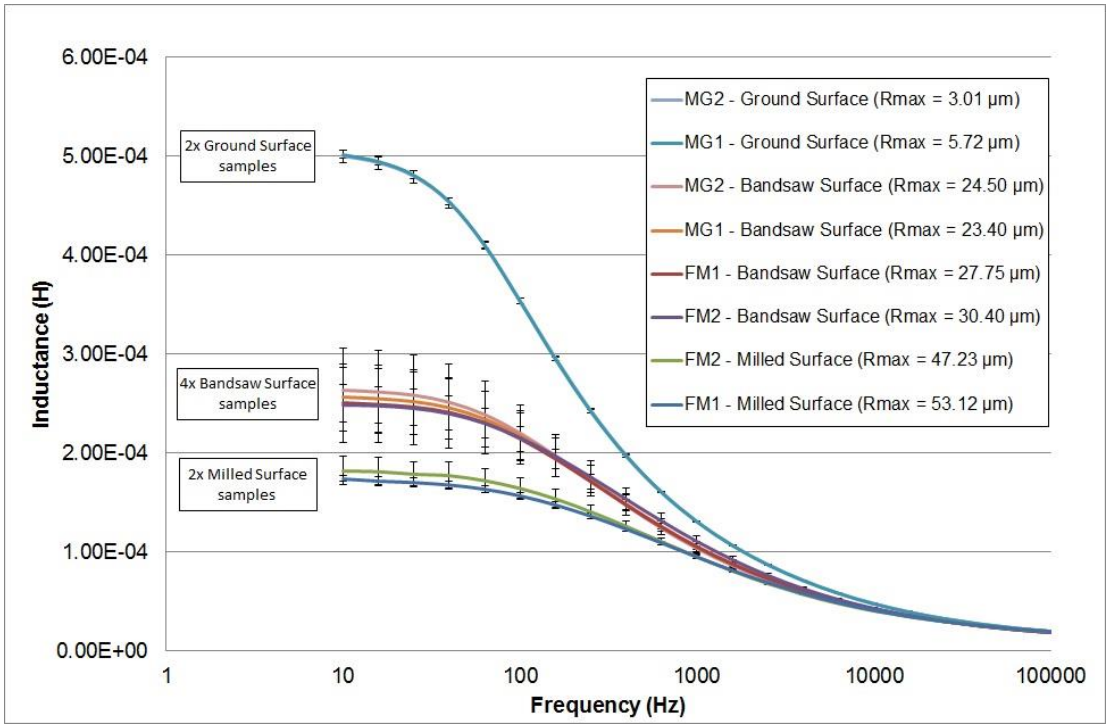

Figure 5-8: Variation of multi-frequency EM inductance with surface roughness (Rmax) for P91:A samples with various surface finishes

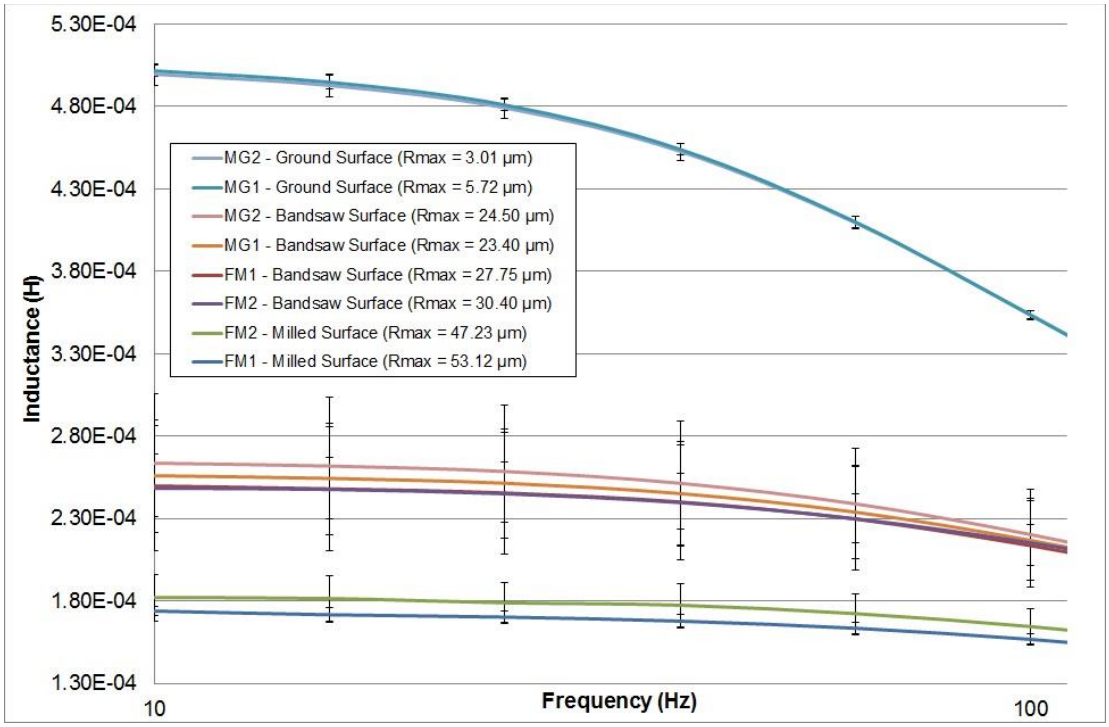

Figure 5-9: Variation of multi-frequency (10 – 100 Hz) EM inductance with surface roughness (Rmax) for P91:A samples with various surface finishes

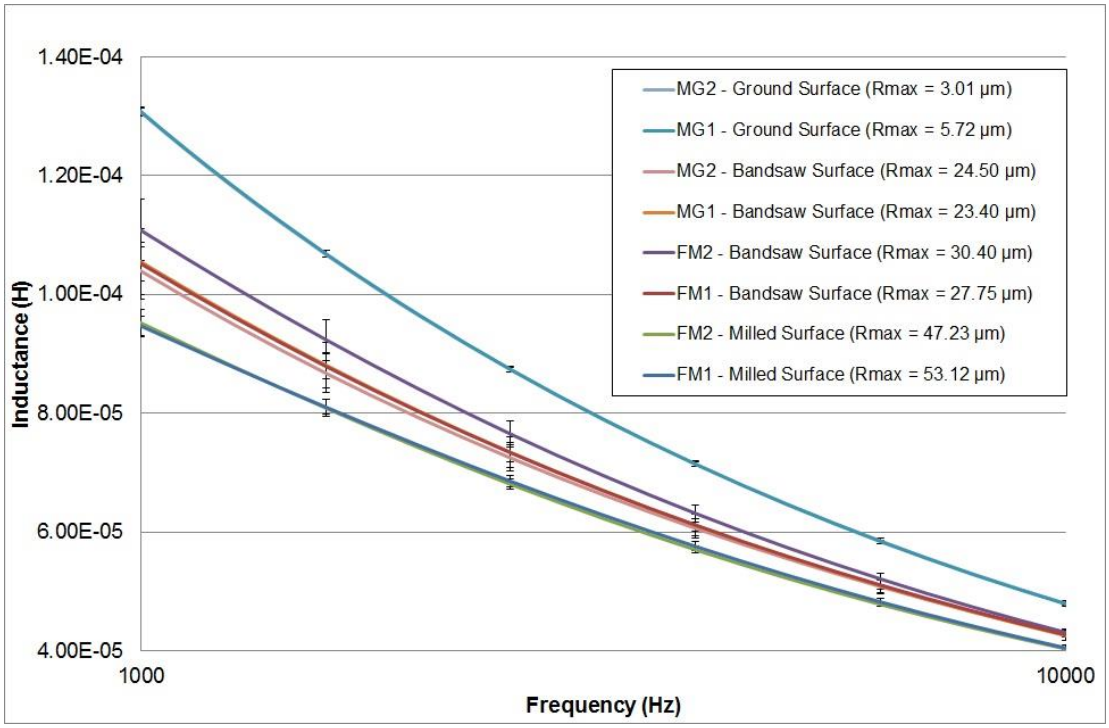

Figure 5-10: Variation of multi-frequency (1 – 10 KHz) EM inductance with surface roughness (Rmax) for P91:A samples with various surface finishes

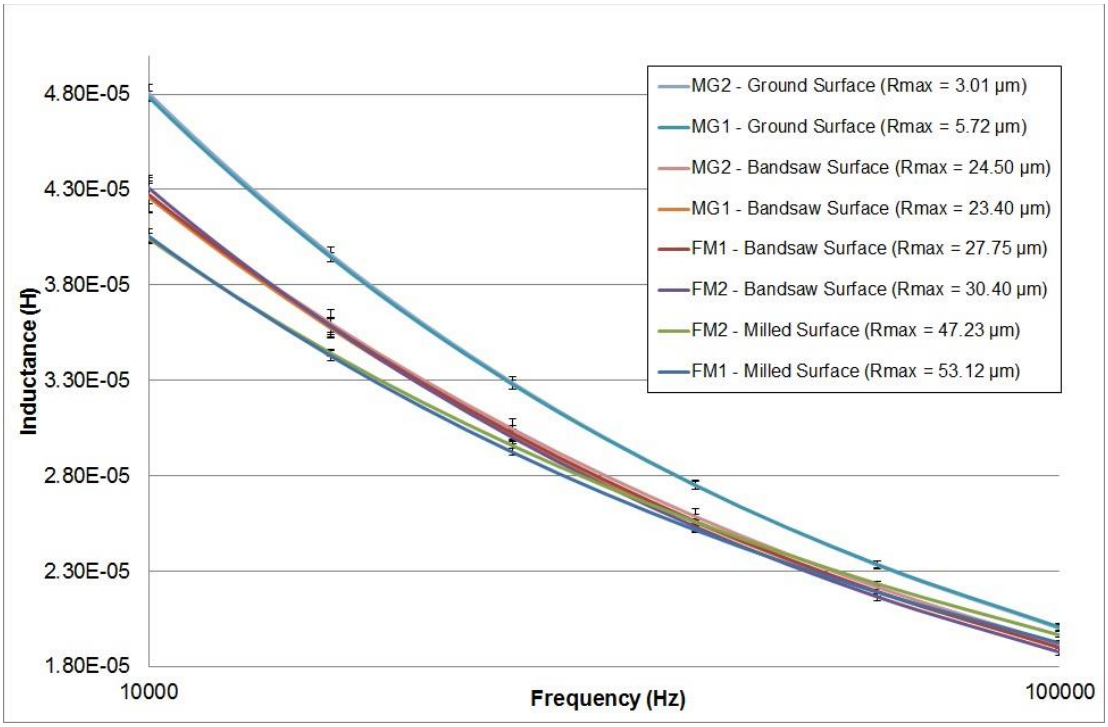

Figure 5-11: Variation of multi-frequency (10 – 100 KHz) EM inductance with surface roughness (Rmax) for P91:A samples with various surface finishes

The inductance values at single low frequency (10 Hz) are plotted against the surface roughness (Rmax) in Figure 5-12 and the results suggest a power law relationship exists between the inductance and the surface roughness, similar to that seen between the inductance and lift-off in Figure 3-32 of the experimental chapter. When the data is plotted on a log-log scale (as shown in Figure 5-13) it can be seen that the data points for the Milled and Bandsaw Surface samples (rougher surfaces) closely fit with a power law function governed by Eq 5-1 which confirms that the low frequency inductance is proportional to the inverse square of the surface roughness (Rmax) which is the same relationship between the inductance and lift-off as described in 3.4.5. However the Ground Surface samples (MG1- Ground Surface and MG2-Ground Surface) do not appear to following this power law trend as the inductance value for these surfaces appears to plateau; suggesting that below a certain surface roughness value, the inductance is unaffected.

$$y = 0.0013x^{-0.505} \qquad \textbf{Eq. 5-1}$$

Where *y* is the inductance at 10 Hz in Henries and x is the Rmax value in micrometres.

Other than the surface roughness of the sample, the only other component that can affect the contact between the sensor and sample is the roughness of the base of the sensor, which comes in contact with the sample. The bottom face of the sensor consists of the two ferrite core feet mounted in epoxy resin as detailed in the experimental chapter Section 3.4.1; the sensor feet are flush with the epoxy resin base such that the epoxy resin base and ferrite core sensor feet are simultaneously in contact with the sample. A total of twelve surface roughness measurements were made on the sensor's base, four on the epoxy resin mount (two perpendicular and two parallel to the sensor's length) and four each on the sensor's front and back feet (two perpendicular and two parallel to the sensor's length); shown schematically in Figure

5-14. The roughness data can be seen in Table 5-4 and shows that the surface roughness of the sensor's ferrite core feet and the epoxy resin mount is similar (such that the standard deviation error overlaps). Therefore an average of all twelve surface roughness measurements was used to produce an overall surface roughness for the EM sensor's base surface; yielding approximately 9.29 µm Rmax (given in Table 5-4). Figure 5-14 compares the surface roughness of the sensor's base with the other surface roughness sample results from Figure 5-13 and suggests that samples that have a smoother surface finish than the sensor's base are unaffected by the sample's surface finish, whereas those that have a rougher surface finish than the sensor's base will be affected by a lift-off type effect. Therefore to negate the impact of the surface roughness on inductance, samples should be prepared such that the surface roughness of the sample surface is less than the surface roughness of the EM sensor base surface which for this particular sensor is 9.29 ± 2.09 µm Rmax or 1.02 ± 0.32 µm Ra. Therefore taking the standard deviation error into consideration, to negate the impact of surface roughness on the inductance measurements when using this particular sensor, surfaces should be prepared to a minimum of 11 µm Rmax or 1 µm Ra.

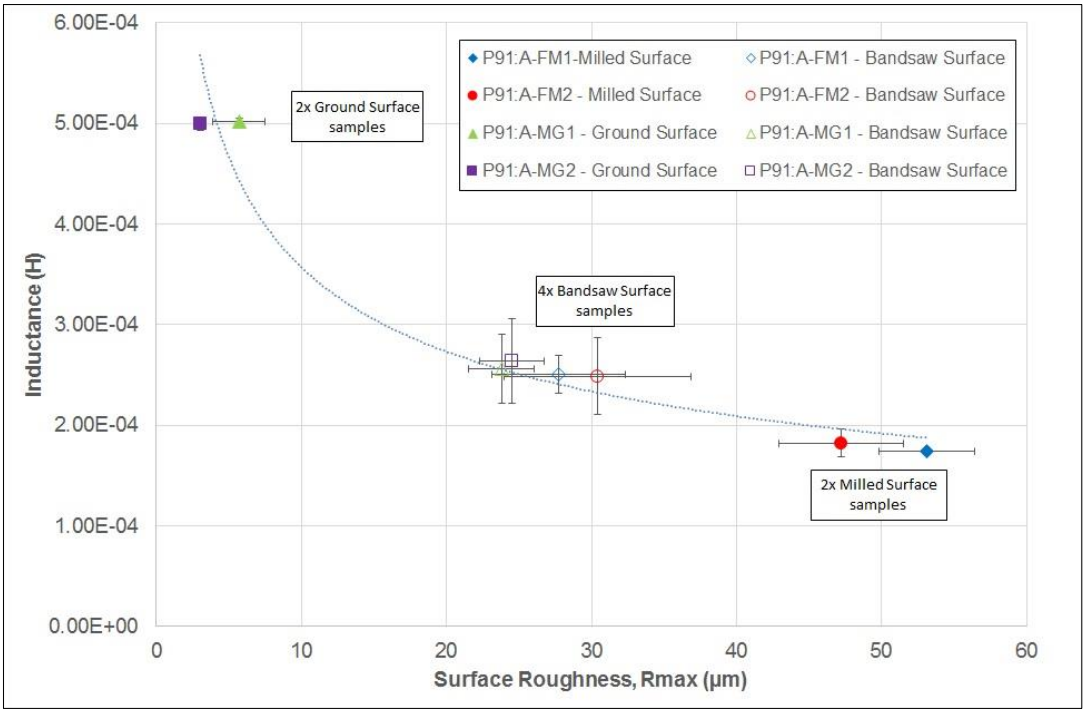

Figure 5-12: Variation of single low frequency (10 Hz) inductance with surface roughness (Rmax) for P91:A samples of varying surface finish

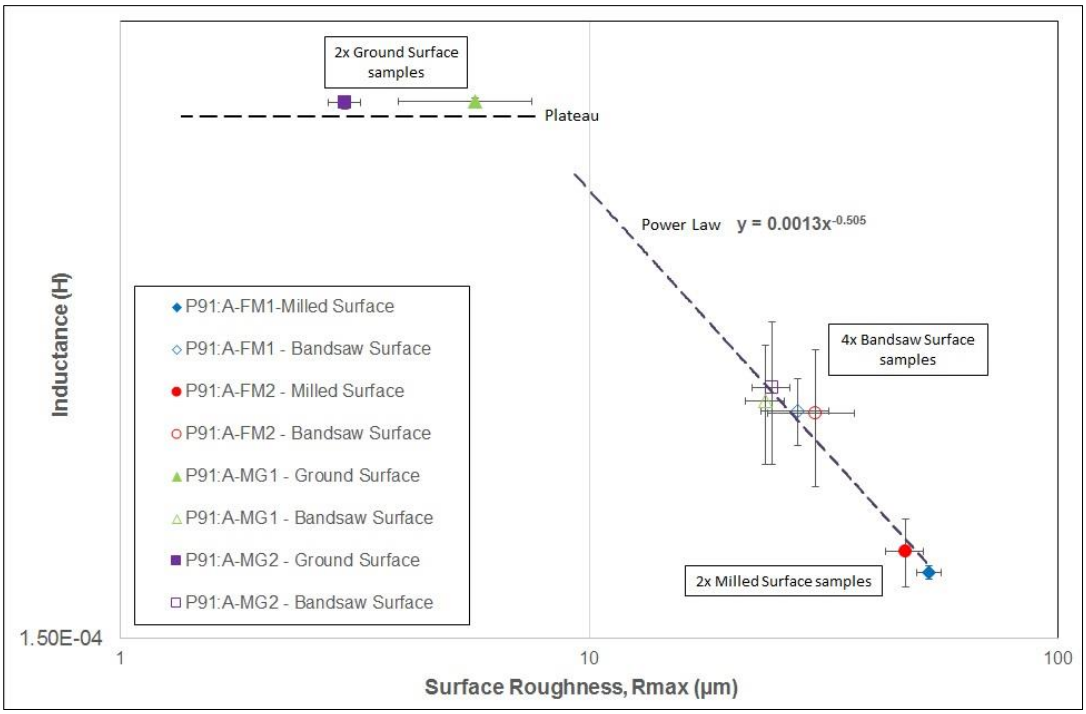

Figure 5-13: Variation of inductance with surface roughness (Rmax) for all P91:A samples with varying surface roughness finishes plotted on log-log scale

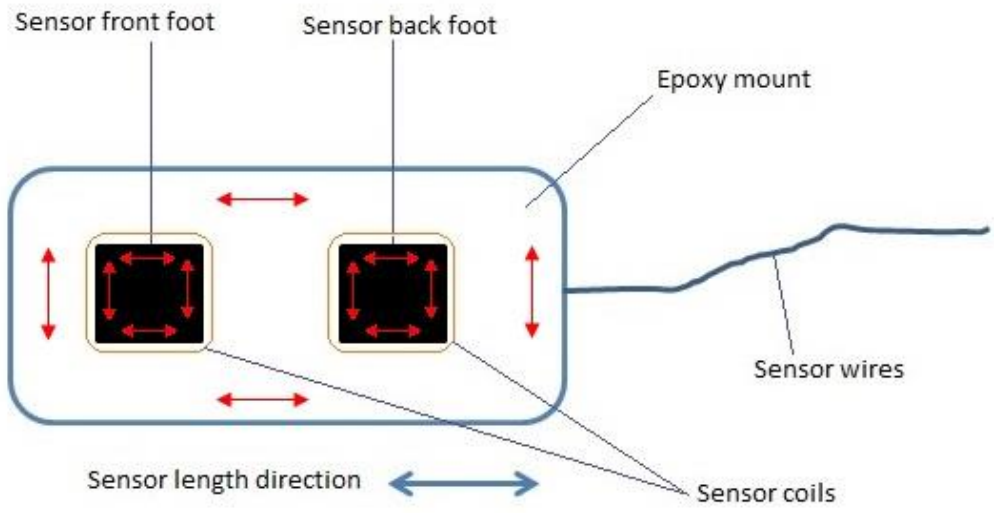

Figure 5-14: Schematic plan view of underside of the EM sensor showing two sensor feet (black squares) and the red arrows show where the surface roughness measurements were taken

Table 5-4: Surface roughness values (Rmax and Ra) for the EM sensor base surface (the surface which contacts the sample)

Surface (orientation)	Surface Roughness, Ra ± SD (µm)	Surface Roughness, Rmax ± SD (µm)
Sensor Back Foot (Parallel)	1.19 ± 0.48	9.04 ± 1.83
Sensor Back Foot (Perpendicular)	1.01 ± 0.17	10.38 ± 2.61
Sensor Front Foot (Parallel)	0.85 ± 0.23	8.34 ± 1.34
Sensor Front Foot (Perpendicular)	1.01 ± 0.28	9.41 ± 2.51
Epoxy Resin (Parallel)	0.67 ± 0.36	5.23 ± 1.72
Epoxy Resin (Perpendicular)	0.74 ± 0.33	4.90 ± 0.69
Average Roughness for Sensor Base Surface	**1.02 ± 0.32**	**9.29 ± 2.09**

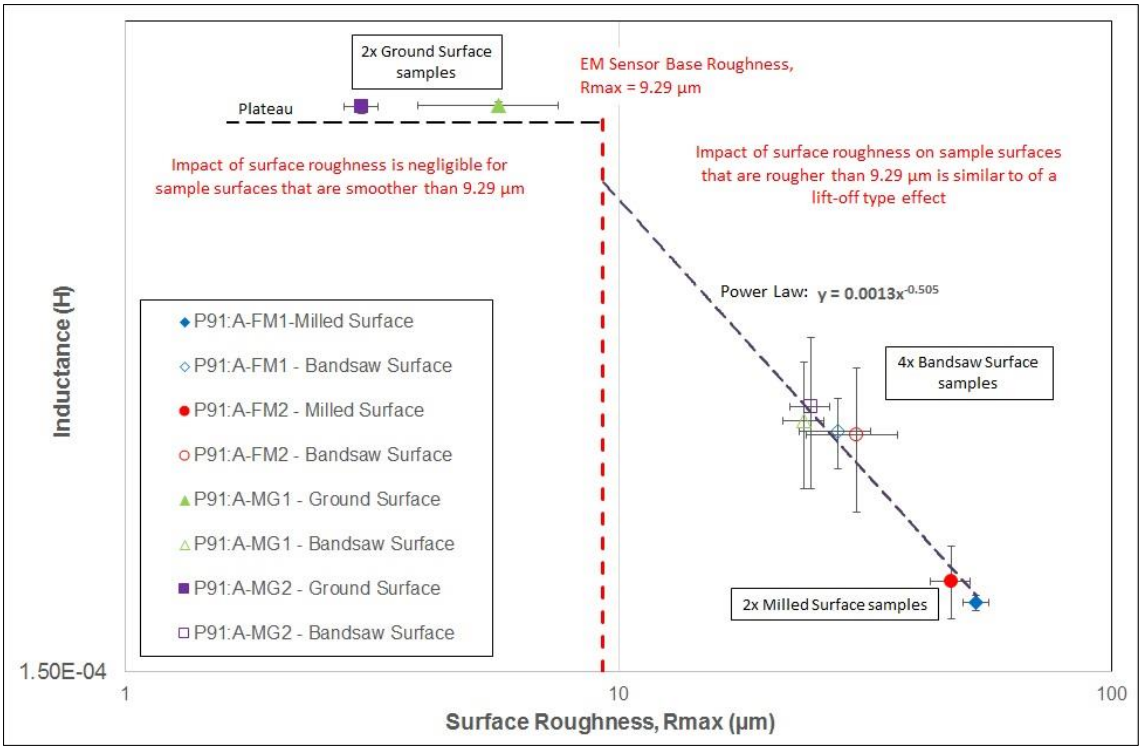

Figure 5-15: Variation of inductance with surface roughness (Rmax) for all P91:A samples with varying surface roughness finishes plotted on log-log scale, showing the impact of sample surface finish on the inductance value

5.3. Differentiating CHT from MHT material

In practise components can have various surface finishes, leading to varying surface roughness profiles, which are not always easy to control and has been shown in Section 5.2 to impact the inductance. Depending on the magnitude of the surface roughness, the Rmax parameter has been equated to a lift-off type effect (shown in Figure 5-15). Therefore it can be desirable for a probe type EM sensor to design an in-built lift-off, into the base of the sensor, to desensitise it from any surface features [20]. This investigation would determine what amount of lift-off would negate the impact of the surface roughness such that there is no distinguishable difference between the inductance value for the roughest surface and the smoothest surface. This level of lift-off would then be applied to EM test correctly heat treated (CHT) and mis-heat treated

(MHT) materials, and determine whether the two different microstructures can be determined when applying a lift-off which would negate the effect of surface roughness.

Three different sample surfaces were EM tested at single low frequency of 10 Hz at various lift-off heights. Sample surfaces P91:A-FM1-Milled Surface, P91:A-FM1-Bandsaw Surface and P91:A-MG1-Ground Surface (surfaces shown in Figure 5-1a, Figure 5-1b and Figure 5-1e respectively) were used and the lift-off was controlled using non-conductive spacers; as described in the experimental chapter Section 3.4.5. The results given in Figure 5-16 show that the introduction of a lift-off reduces the inductance as expected and seen in earlier chapters. With no lift-off, the sensor is at its most sensitive and produces the largest difference between the inductance values of the three different surface finishes; where the difference in the inductance values are greater than the samples' respective error bars. At a lift-off of 0.1 mm, samples MG1-Ground Surface and FM1-Bandsaw Surface, cannot be separated since their inductance value error bars are overlapping. At 0.3 mm of lift-off all three surface finishes have an insignificant impact on the EM signal where the variation in inductance values are within the error bars, thus concluding that at 0.3 mm of lift-off there is no distinguishable impact of the surface roughness on the inductance value (for the samples investigated). This means that if the sensor is able to distinguish between CHT and MHT samples at a lift-off of 0.3 mm, then this level of in-built lift-off would be valuable, such that it would negate the impact of surface roughness (for samples tested, between the range 0 – 40 μm Ra), whilst remaining sensitive to the differences in the microstructures. To investigate if CHT and MHT material can still be distinguished using this sensor at a lift-off of 0.3 mm, two P91:A samples were heat treated to produce CHT microstructure (tempered martensitic laths) and MHT microstructure (equiaxed ferrite grains). Samples were designated P91:A-CHT and P91:A-MHT respectively; images of their microstructures have been given in an earlier

chapter, Figure 4-6 in Section 4.3. Details of the heat treatments can be found in Table 3-3, Section 3.2 and images of the samples can be seen in Figure 5-17. The surfaces were prepared with identical mechanically ground finishes using an Al_2O_3 surface grinder to produce smooth mirror-like surface finishes. Single low frequency (10 Hz) EM tests were performed on the samples with varying lift-off to see at what lift-off value the sensor is still able to distinguish the two microstructures from each other, specifically at 0.3 mm, as this amount of lift-off would negate the influence of the surface roughness; results are tabulated in Table 5-5 and plotted in Figure 5-18. Figure 5-18 clearly shows the softer MHT material to have a higher real inductance value than the harder CHT material at 0 mm of lift-off – this is expected and has been explained previously in Section 4.3. As the lift-off increases, the amount of magnetic flux interacting with the samples is reduced (due to the non-conductive gap between the sensor and sample). Thus with increasing lift-off the difference in the inductance value between the two microstructures (CHT and MHT) begins to decrease. At a lift-off of 0.05 mm there is adequate electromagnetic interaction between the sensor and sample for the two microstructures to be distinguishable since the difference in inductance is larger than the SD error bars, but at a lift-off of 0.1 mm, this is no longer the case and the two microstructures are undistinguishable. Therefore it would not be suitable to apply an in-built lift-off of 0.3 mm for this sensor. With a larger sensor, a larger electromagnetic field can be generated and operation at a higher lift-off may then be possible to achieve the higher sensor sensitivity such that the two microstructures (CHT and MHT) can remain distinguishable at higher lift-off. However in this work the amount of Grade 91 material was limited which meant that the sample size was restricted and therefore sensor size was restricted to avoid edge effects, as explained in the experimental chapter Section 3.4.3. Furthermore, the application for this EM sensor within EON is to complement the current NDT techniques of portable hardness and surface replication which are performed on small localised areas (approximately

100 x 100 mm) on large components so an equally small sensor is appropriate. Therefore in order to compare the microstructures of different samples using this sensor, the surfaces would require a minimum surface finish of 1 µm Ra.

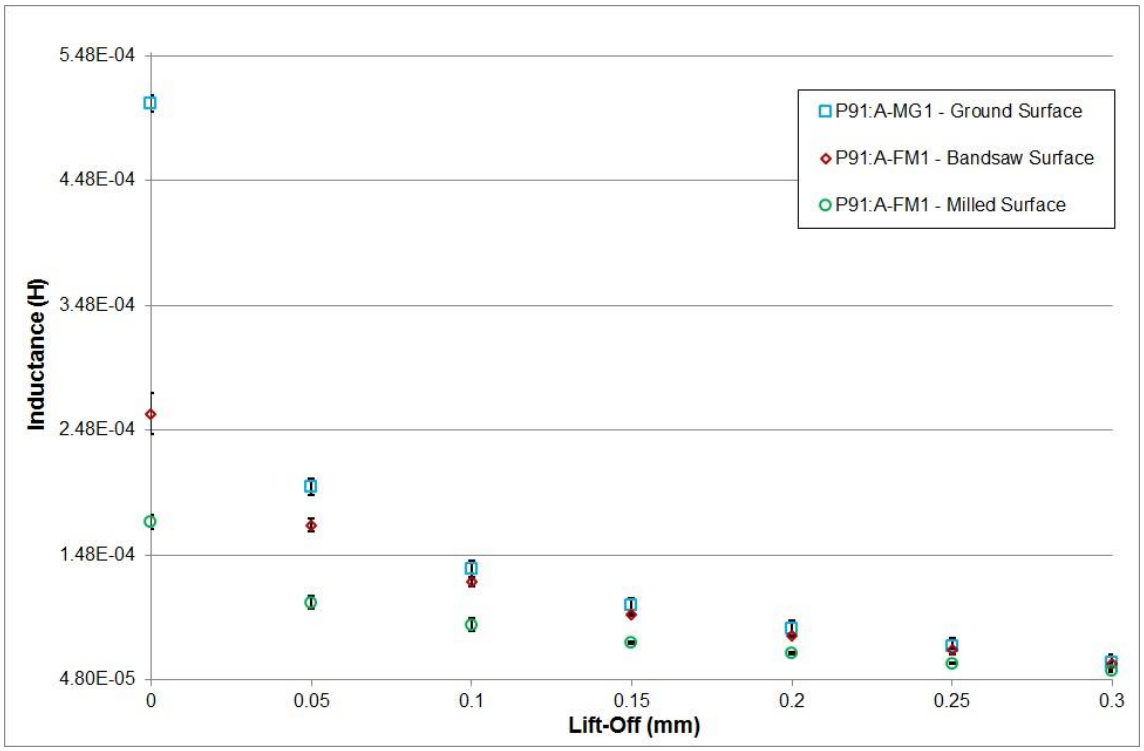

Figure 5-16: Variation of EM signal (10 Hz) with lift-off between sensor and sample surface for P91:A (as-received microstructure) samples with various surface roughness surface finishes

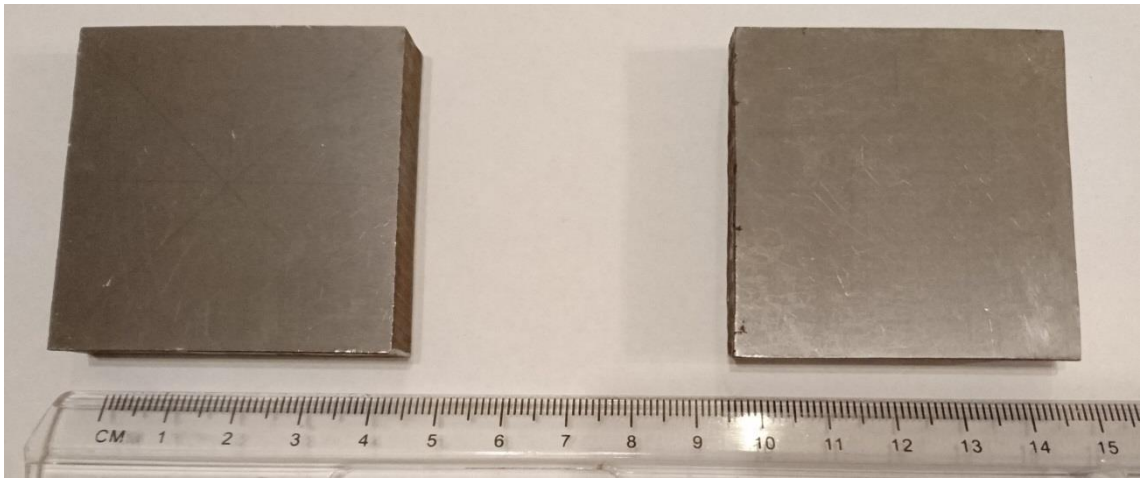

Figure 5-17: Two P91:A samples with identical mechanical grinded smooth surfaces but different microstructures (left) correctly heat treated (CHT) tempered martensite and (right) mis-heat treated (MHT) equiaxed ferrite grains

Table 5-5: Inductance results for samples P91:A-CHT and P91:A-MHT at low frequency (10 Hz) varied with lift-off from the sample surface

Lift-Off (mm)	P91:A-CHT Inductance + SD (E-04 H)	P91:A-MHT Inductance + SD (E-04 H)
0	4.53 ± 0.18	5.74 ± 0.21
0.05	2.04 ± 0.10	2.25 ± 0.07
0.1	1.33 ± 0.06	1.39 ± 0.05
0.15	1.05 ± 0.02	1.09 ± 0.01
0.2	0.87 ± 0.01	0.89 ± 0.01
0.25	0.74 ± 0.01	0.75 ± 0.01
0.3	0.68 ± 0.01	0.69 ± 0.01

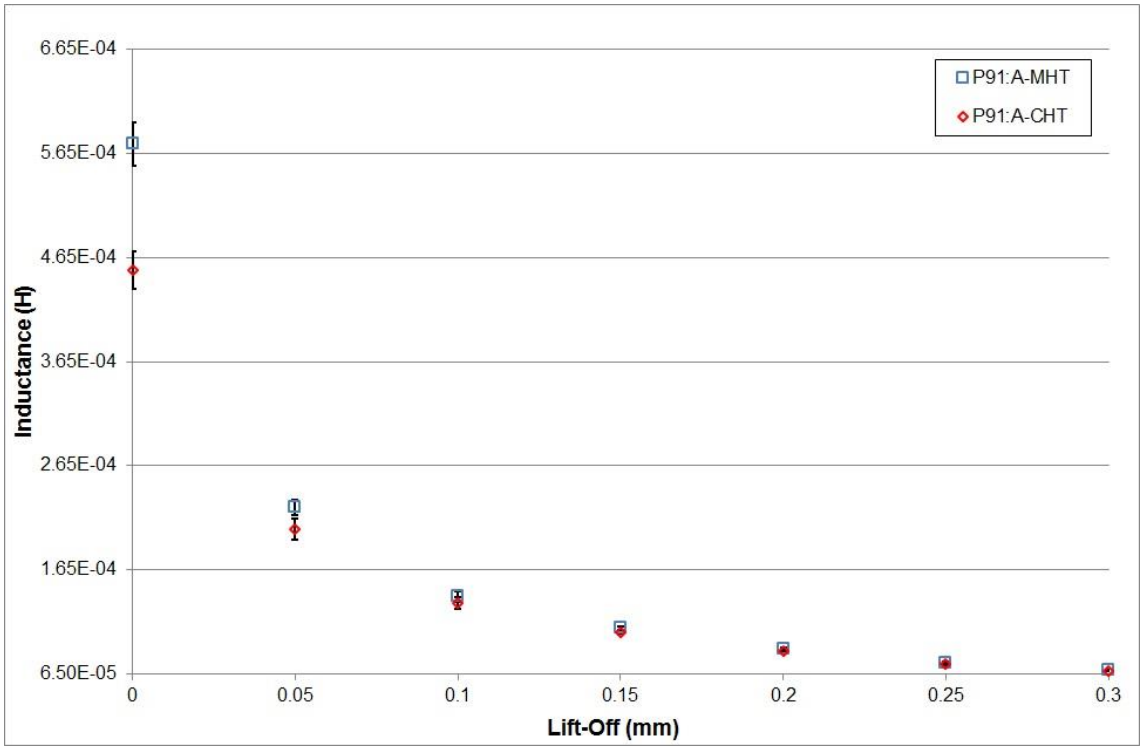

Figure 5-18: Variation of inductance with lift-off between sensor and sample surface for mis-heat treated (MHT) and correctly heat treated (CHT) microstructure samples

5.4. Effect of Surface Preparation

One of the benefits of using EM sensors is the speed with which an inductance result can be produced and analysed (typically minutes) compared with surface replication (typically hours). This speed of testing would benefit industry by deploying the sensor to take numerous measurements across a large component, relatively quickly. The results can then indicate areas of interest (based on the inductance values returned) where the time consuming surface replication tests can be performed to obtain the microstructures. At present portable hardness tests are performed to characterise material leading to possible areas of interest for further investigation, i.e. if the hardness data is out of specification or close to its limits then further investigation may be required. Portable hardness testing requires surfaces to be prepared to a minimum of 120 grit ground surface finish and a smooth mirror like surface is typically required to

apply the surface replication technique. For large in-situ components a Transpol portable grinder is used to prepare surface areas to be inspected for portable hardness testing and surface replication to achieve a smooth mirror-like finish; a number of grinding stages are required (detailed in Table 3-5 in Section 3.2.2.1). It would be useful to understand the minimum surface preparation (i.e. how many of the grinding stages in Table 3-5) that would be required for the EM sensor used in this work, such that the inductance values are unaffected by the surface created. To investigate this P91:C pipe section was used. The pipe section was donated by EON in the as-tempered service entry condition, the microstructure is given in Figure 5-19. Eight different surface finishes (as detailed in Table 3-5 in Section 3.2.2.1) were applied one after another on the same pipe cross-sectional face, as shown in Figure 5-20. These surfaces are typical to the grinding steps followed to prepare a surface for portable hardness and surface replication testing.

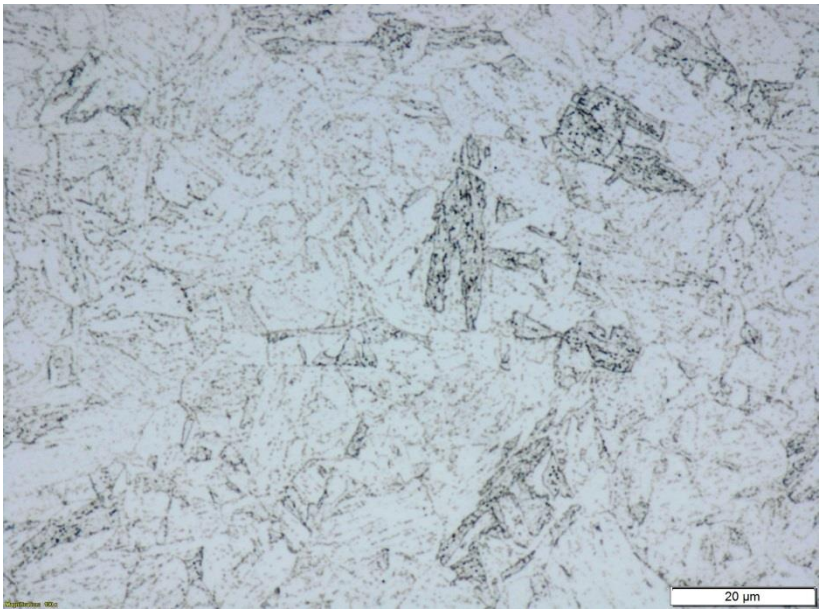

Figure 5-19: P91:C as-tempered material showing martensitic lath microstructure

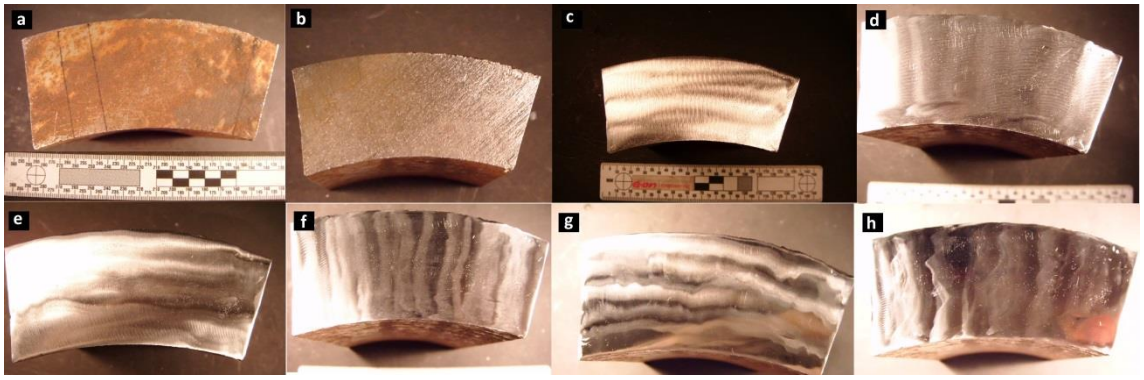

Figure 5-20: Different surface finishes applied to P91:C material received in the as-tempered condition. (a) As-received corroded, (b) Wire brushed. The remainder were all ground using a Transpol surface grinder with varying grit grade; (c) 60 Grit, (d) 120 Grit, (e) 240 Grit, (f) 400 Grit, (g) 600 Grit and (h) 1200 Grit

After each grinding stage, the surface roughness (Ra) and inductance measurements were taken, the results are given in Table 5-6 and graphically in Figure 5-21. The results show a significant reduction in the inductance for the as-received corroded and wire brushed surfaces, where the inductance is approximately half of that, compared with the other ground surfaces (60 – 1200 grit ground). The as-received sample has a significantly corroded and oxidised surface; this will reduce the inductance as the predominant effect of the oxide layer has been shown to be of an effective lift-off [188]. The wire brushed surface has introduced a surface roughness of 6.1 µm (Ra) which also introduces a significant lift-off type effect (as deduced earlier in this chapter), causing a reduction in the inductance. The remaining surface finishes can be seen to have no impact on the inductance since the roughness values for each surface (60 – 1200 grit ground) have a similar or lower surface roughness than that of the sensor's base (1.02 ± 0.32 µm Ra), which was given earlier in this chapter in Table 5-4. This suggests that the application of a 60 grit ground surface finish is adequate to avoid any influence of the surface finish on the inductance value.

Table 5-6: Table of values showing the surface roughness (Ra) and low frequency (10 Hz) inductance results for material P91:C with various surface finishes

Surface	Surface Roughness ± SD, Ra (μm)	Inductance ± SD ($x10^{-4}$ H)
As-received corroded	N/A	1.76 ± 0.24
Wire brushed	6.1 ± 0.40	1.93 ± 0.32
60 grade grit ground	1.2 ± 0.26	3.49 ± 0.20
120 grade grit ground	1.01 ± 0.31	3.55 ± 0.20
240 grade grit ground	0.35 ± 0.09	3.48 ± 0.16
400 grade grit ground	0.25 ± 0.08	3.53 ± 0.18
600 grade grit ground	0.21 ± 0.06	3.51 ± 0.25
1200 grade grit ground	0.13 ± 0.06	3.50 ± 0.24

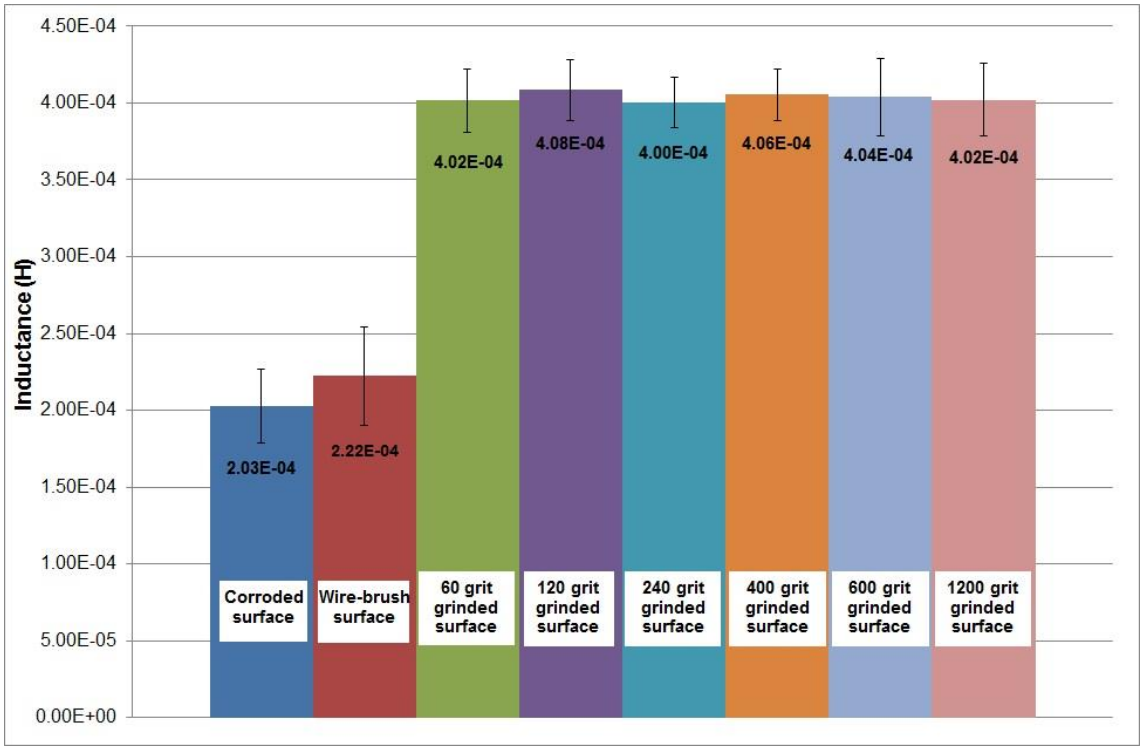

Figure 5-21: Low frequency (10 Hz) EM signal for various surface finishes applied to sample P91:C with an as-tempered microstructure

Samples P91:A-CHT and P91:A-MHT were prepared with surface finishes using the Transpol surface grinder using various SiC grit grades (60 – 1200). The surface roughness values and EM results are tabulated in Table 5-7 and plotted in Figure 5-22. From Figure 5-22 it can be seen that the application of surface ground finishes using the Transpol surface grinder between grit grades 60 – 1200 has no significant impact on the inductance values and hence the sensor's ability to differentiate CHT from MHT material. Previously a plateau region has been shown where the inductance is unaffected by surface roughness for surfaces which have a smaller roughness value than the sensor's base, which was 1.02 ± 0.32 µm Ra. The 60 grit surface finish yields a surface roughness, Ra = 1.11 µm (Table 5-7) and hence there is no significant impact of this surface on the inductance value. Therefore it is recommended that a minimum of a 60 grit ground surface finish, applied using a Transpol grinder, is sufficient to perform EM tests using this sensor, without impacting the sensor's ability to

distinguish CHT from MHT material. This brings the benefit of being able to attain material information with less surface preparation compared to the traditional portable hardness and surface replication techniques. For high accuracy portable hardness tests a finish above 120 SiC grit grade is advised [208] and for the surface replication technique a minimum of 1200 grit ground surfaces is required. With this EM sensor, a minimum application of 60 grit grade surface finish can allow EM tests to be performed with less surface preparation. Hence more tests can be performed across a component covering a greater amount of surface area (quickly) highlighting regions of interest (based on the EM results) where further preparation can be done to allow for surface replication and portable hardness testing, if required. This suggests that the EM sensor can be beneficial if deployed as a principle NDT technique to surface replication and portable hardness.

Table 5-7: Table of values showing the surface roughness (Ra) and low frequency (10 Hz) EM data for samples P91:A-CHT and P91:A-MHT with various surface finishes

Surface Finish	P91:A-CHT		P91:A-MHT	
Different grades of SiC grit ground finishes	Surface Roughness ± SD, Ra (µm)	Inductance ± SD ($x10^{-4}$ H)	Surface Roughness ± SD, Ra (µm)	Inductance ± SD ($x10^{-4}$ H)
60	1.11 ± 0.25	4.47 ± 0.23	1.15 ± 0.12	5.89 ± 0.24
120	0.91 ± 0.24	4.64 ± 0.13	0.79 ± 0.14	5.91 ± 0.17
240	0.41 ± 0.12	4.55 ± 0.09	0.45 ± 0.07	5.92 ± 0.21
400	0.24 ± 0.04	4.52 ± 0.12	0.25 ± 0.07	6.07 ± 0.13
600	0.24 ± 0.05	4.62 ± 0.14	0.27 ± 0.09	6.07 ± 0.29
1200	0.22 ± 0.04	4.65 ± 0.11	0.19 ± 0.03	6.01 ± 0.35

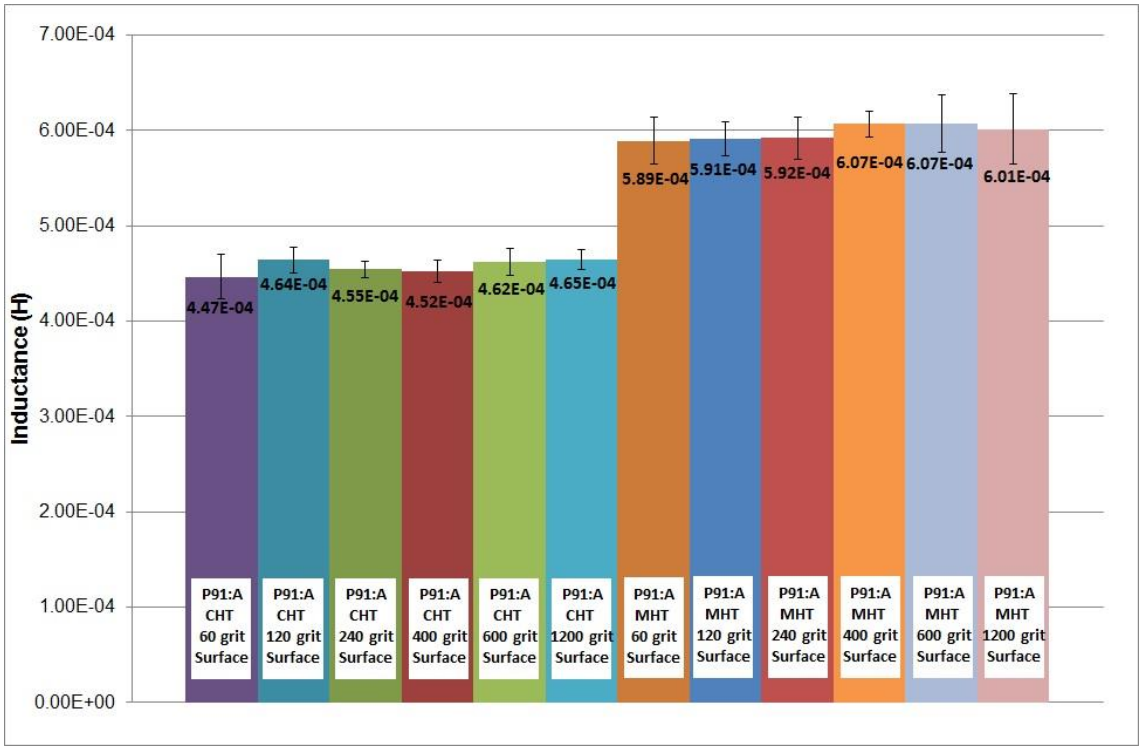

Figure 5-22: Variation of EM signal with various surface grinded finishes applied using a Transpol surface grin on samples P91:A-CHT and P91:A-MHT

5.5.Summary

Grade 91 samples were prepared with different surface roughness profiles, varying from smooth surfaces with arithmetic mean roughness values (Ra parameter) of 0.08 µm to samples with very rough finishes up to 40 µm, These surfaces were created by different machining processes, to determine the impact of surface roughness on the inductance values. The results showed that the impact of surface roughness is negligible for sample surfaces that are smoother than the roughness value of the sensor's base surface (which was determined as 1.02 ± 0.32 µm Ra). The impact of surface roughness on sample surfaces that are rougher than the roughness value of the sensor's base surface is similar to of a lift-off type effect, where the surface roughness value causes the inductance to decrease following an inverse power law relationship. Therefore it is recommended that surfaces should be prepared to an

average surface roughness value lower than that of the sensor's base surface, which is a minimum of approximately 1 µm Ra, for the sensor used in this study. It was also determined that an in-built lift-off of 0.3 mm would be sufficient to negate the surface roughness effect however, at this lift-off the sensor is unable to distinguish between CHT and MHT materials, therefore it is was recommended to not have an in-built lift-off for this sensor. It was shown that a 60-grit SiC ground surface finish, which is typically the first grinding stage (out of six) for power generation utilities when preparing component surfaces for surface replication and portable hardness testing, is suffice for EM sensor tests. Hence, concluding that less surface preparation is required to carry out EM tests in comparison to surface replication and portable hardness testing (which are the current methods). This result means that EON can deploy the EM sensor, not only as a complementary technique to portable hardness testing to screen service entry material as determined in Chapter 4, but as a principle technique. As a principle technique the EM sensor can numerous locations across a component's surface with minimal surface preparation to highlight areas of interest based on the inductance value, where further targeted preparation can be done such that surface replication and hardness tests can be performed. This way, a larger proportion of the component surface area can be scanned, informing the areas of interest where further NDT testing (portable hardness and surface replication) can be carried out, rather than an untargeted general selection of locations.

CHAPTER 6 EFFECT OF WORK HARDENED SURFACES ON THE EM SENSORS ABILITY TO DETERMINE MICROSTRUCTURES

This chapter explores the significance of the work hardened surface layers with respect to the EM sensor inductance values. The chapter studies the influence of grit blasted and shot peened surfaces on the EM sensor by measuring inductance. The results are discussed with respect to the EM sensor's ability to differentiate CHT from MHT bulk microstructures on samples with work hardened surface layers. The chapter concludes by recommending the required surface finish to avoid any influence of the work hardened layers on the components' inductance value, based on the EM sensor used in this study.

6.1. Introduction

During power plant maintenance periods, boiler components can be found with various surface conditions. Refractory and insulating material can adhere to the outer walls of boiler components as a result of in-situ repair and maintenance activity. This can cause difficulty for surfaces to be inspected and non-destructively tested. Oxide scales can also form on component surfaces causing similar issues for NDT inspection. Different utilities use different methods to prepare surfaces for non-destructive testing. The usual method of removing unwanted surface features is to primarily use a metal brush as it is the most time efficient and cost effective method. However metal brushes are not always sufficient in some instances and therefore grit or sand blasting is used to remove unwanted surface features. In conjunction, components within the power generation industry can often undergo surface treatments to improve their mechanical properties such as shot peening. This is a technique which introduces beneficial residual compressive stresses to enhance the mechanical properties and increase the formation of oxidation resistant Cr-rich oxide layers [209]. This operation increases the fatigue and stress corrosion resistance for components which endure dynamic stresses, such as welded joints (common within the power generation industry) [83].

The mechanical deformation of the surface causes a volume of material at the surface to become work hardened. Work hardening and residual stresses have been shown to have an effect on the magnetic properties of steel, in particular the magnetic permeability. A positive elastic strain has been described to increase the interatomic spacing between iron atoms which will cause an increase in the material's magnetic permeability as the mean free path of domain wall movement is increased [210] whereas plastic strain will increase the dislocation density, hence reducing the magnetic permeability, as it is known that dislocations act as pinning points to domain wall movement [27].

6.2. Effect of Grit Blasting

Grit blasting is a cold working process where the surface to be cleaned is impacted continuously with particles of grit for stock removal (cleaning) [211]. The nature of grit blasting is such that it will deform the material at the surface (where the grit impacts the component) introducing a higher dislocation density within the surface layer. Although there is significant literature assessing the effect of mechanical strain on the magnetic properties of various low carbon steel [169, 172, 212], there is none specific to the U-shaped EM sensor techniques in combination with P91 material. To investigate this, P91 material was sectioned and grit blasted using different blasting parameters followed by EM testing to observe the influence of the work hardened surface layer on the samples' inductance values.

Grade 91 material P91:A in the as-received condition was sectioned into sample P91:A-AR:GB (50 x 50 x 10 mm) with an as-ground smooth surface finish (Figure 6-1a). The sample was grit blasted with typical blasting parameters given in Table 3-6 of the experimental chapter Section 3.2.2.2 to produce a work hardened sample with a rougher surface finish (Figure 6-1b). For a similar material (approximately 203 HV)

being subjected to similar grit blasting conditions, a 50-100 µm thick work hardened surface layer would be expected [213]. Figure 6-2 and Figure 6-3 show the microstructural cross-section of the sample's grit blasted surface. Whilst some differences in the martensitic laths at the surfaces of the sample, compared with those laths present within the bulk of the material, can be observed (more irregular and darker at the surface) it is not possible to determine if this is an etching effect or due to the grit blasting process, therefore micro-hardness testing was performed. Figure 6-4 shows the cross-sectional micro-hardness profile for sample P91:A-AR:GB between the grit blasted surface and a depth of 300 µm below the surface. The data clearly shows that the material has been significantly work hardened from the surface down to a depth of 100 µm, as expected [213] since there is a presence of a hardness profile. The hardness at the surface (circa 250 HV) has increased by approximately 40 HV compared to the bulk hardness value, which is approximately 210 HV. The smallest load available for indentations was used (0.01 kg) such that indents could be made as close to the surface as possible; appropriate distances between indents were maintained (see Figure 6-5). The grit blasting process also introduced a significant surface roughness profile, hence to remove this, the sample was ground to a 120-grit SiC ground surface finish (Figure 6-1c); note it has been shown in the previous chapter that the EM sensor, used in this study, is not sensitive to the surface roughness for surface finishes smoother than a 60-grit SiC ground surface finish (Section 5.4). To determine how much of the work hardened layer was removed due to the grinding process, the sample thickness was measured using a micrometer at five locations on the sample, before and after the grinding process, following the arrangement described in Section 3.3.7. The results, given in Table 6-1, show that an average of 16 µm of the surface layer was removed by the grinding procedure resulting in the work hardened layer thickness being reduced from 100 µm to an average of 84 µm. Surface roughness measurements were obtained for each surface finish and given in Table 6-2

along with the single low frequency (10 Hz) inductance values, the multi-frequency inductance results are shown in Figure 6-6.

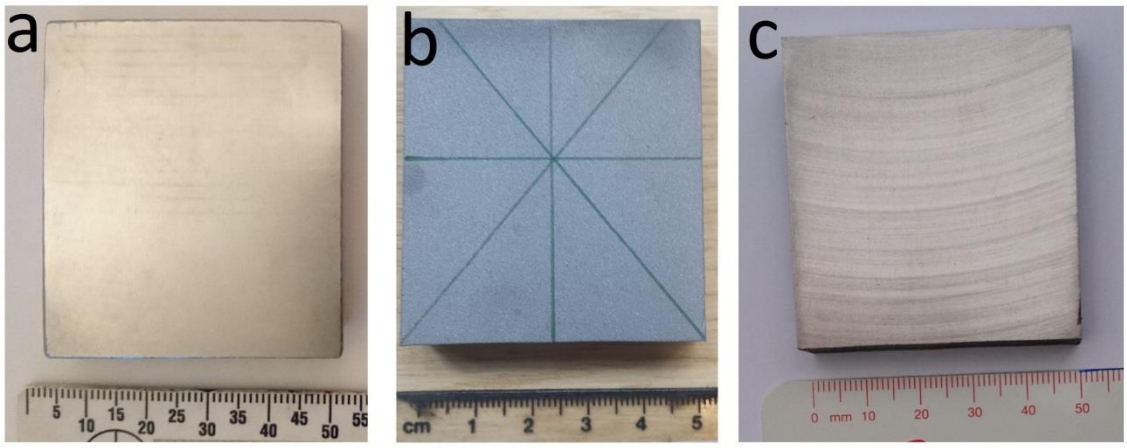

Figure 6-1: Sample P91:A-AR:GB with three different surfaces, (a) smooth mechanically ground surface finish, (b) rough grit blasted surface finish, (c) 120-grit SiC ground surface finish after grit blasting to remove the surface roughness profile

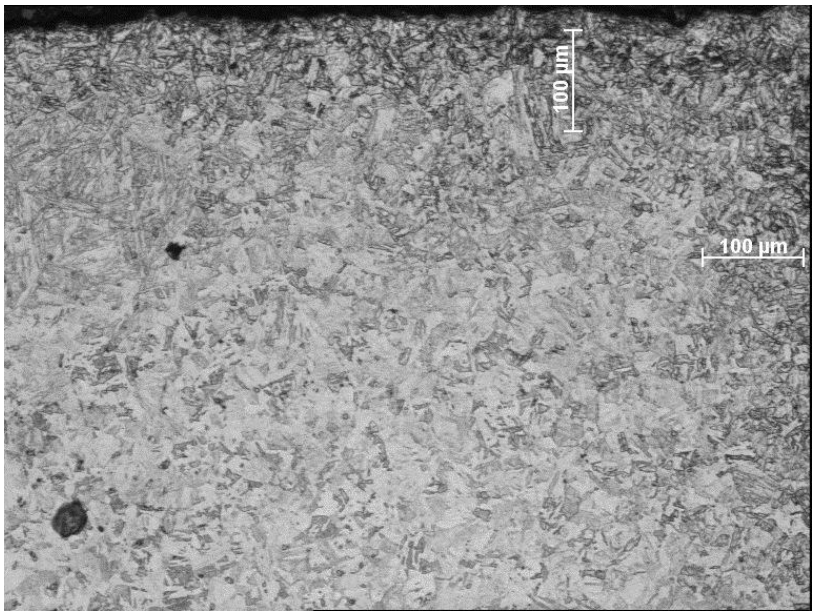

Figure 6-2: LOM image of sample P91:A-AR:GB showing the cross sectional microstructure after grit blasting

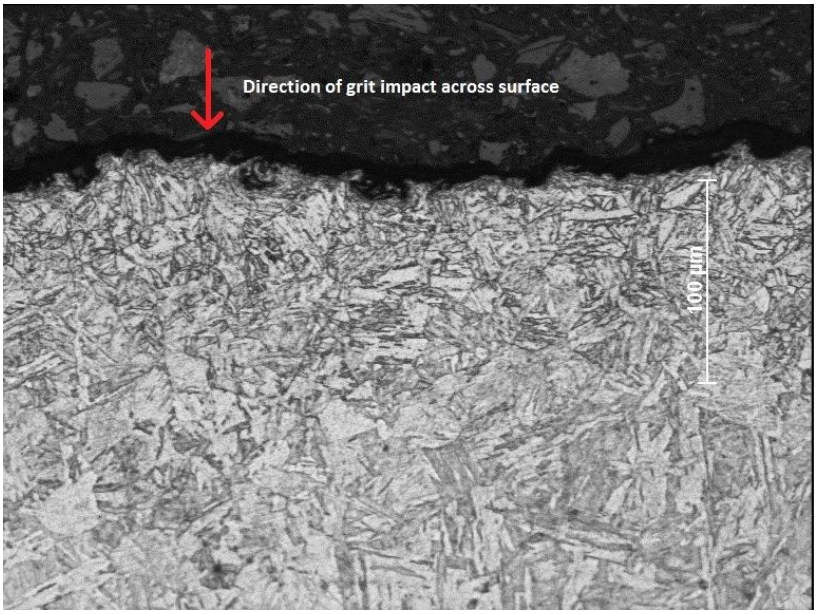

Figure 6-3: Higher mag. LOM image of sample P91:A-AR:GB showing near surface region of the sample which has been grit blasted

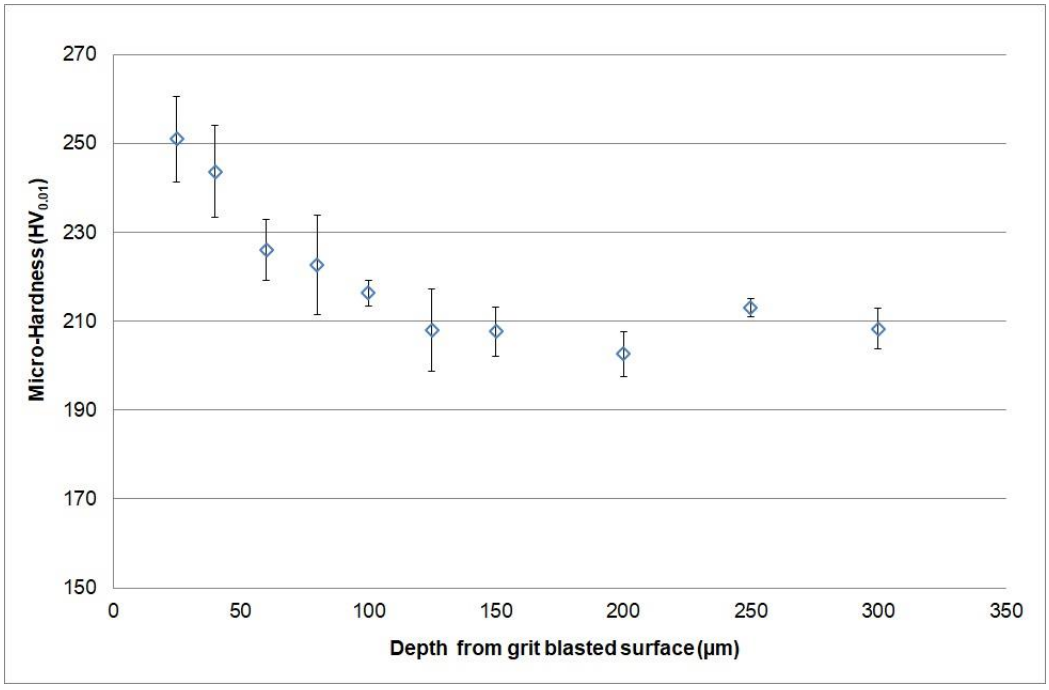

Figure 6-4: Variation of micro-hardness between the surface and a depth of 300 µm below the surface, for sample P91:A-AR:GB

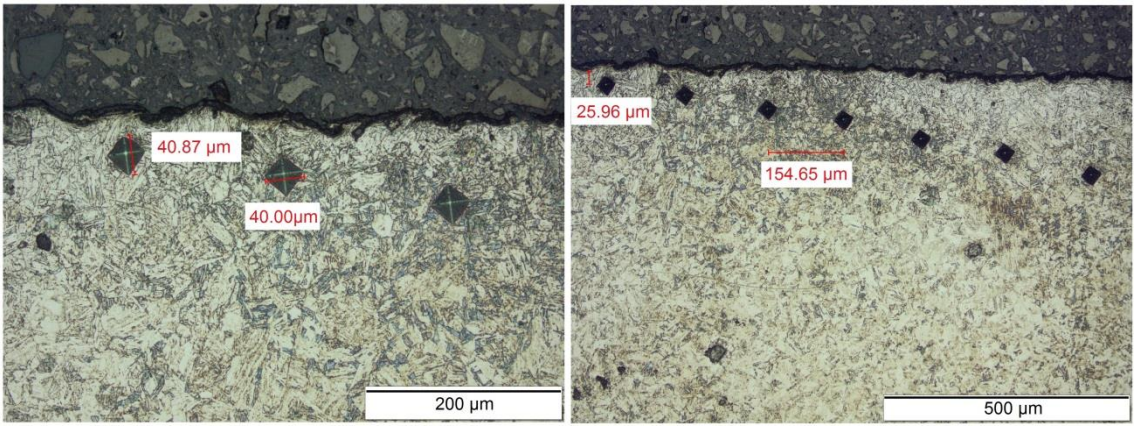

Figure 6-5: Sample P91:A-AR:GB micro-hardness indentations showing diameter of indents and approximate distance between indents

Table 6-1: Thickness measurements for sample P91:A-AR:GB showing material removed due to grinding procedure

	Thickness of material removed at five locations across sample (µm)					
Surface finish	Location 1	Location 2	Location 3	Location 4	Location 5	Avg ± SD
120-grit SiC ground	0	5	15	30	30	16 ± 14

Table 6-2: P91:A-AR:GB samples results for surface roughness and low frequency (10 Hz) EM signal with two different surface finishes; mechanically ground using Al_2O_3 surface grinder and as-grit blasted surface

Surface Finish	Surface Roughness ± SD, Ra (µm)	Surface Roughness ± SD, Rmax (µm)	Inductance ± SD ($x10^{-4}$ H)
Mechanically (Al_2O_3) ground smooth surface	0.08 ± 0.01	3.01 ± 0.24	5.18 ± 0.17
Grit blasted rough surface	4.14 ± 0.17	16.15 ± 2.11	3.31 ± 0.16
Grit blasted + 120 SiC grit ground smooth surface	0.95 ± 0.11	7.26 ± 1.64	4.63 ± 0.20

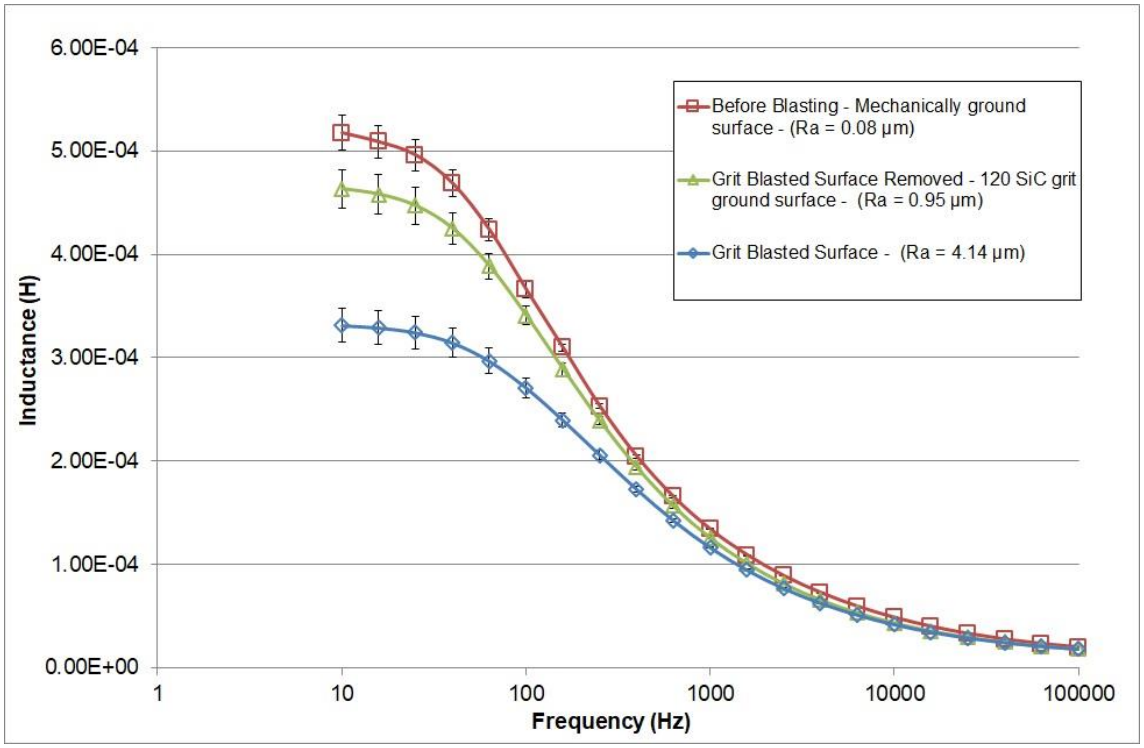

Figure 6-6: Multi-frequency (10 – 100,000 Hz) variation of inductance with various surface conditions for sample P91:A-AR:GB

The multi-frequency results in Figure 6-6 show all three surfaces to display a typical multi-frequency inductance curve whereby the inductance values begin to reduce, and all three curves begin to converge, as the frequency is increased. This is caused by the skin effect due to the formation of eddy currents opposing the induced magnetic field, as explained earlier in Section 3.4.2. At low frequency (10 Hz), where the inductance is strongly dependent on the material's relative permeability, the results show that there is an impact of the grit blasting on the inductance such that it has caused the inductance value to decrease by 36% from 5.18E-04 H down to 3.31E-04 H. This drop in inductance can potentially be attributed to two causes. Firstly the grit blasting process has mechanically deformed the surface and introduced a surface roughness, which has been shown in Chapter 5 to cause a lift-off type effect governed by Eq 5-1; which has a lowering effect on the inductance. Secondly, the grit blasting has introduced a work hardened surface layer (as shown by the micro-hardness profile measured in Figure

6-4) due to the creation of dislocations within the surface layer. The presence of dislocations restricts magnetic domain wall movement, hence having a decreasing effect on the relative permeability and the low frequency inductance as identified in Chapter 4. Considering the surface roughness effect, the surface roughness of the grit blasted surface (Rmax = 16.15 ± 2.11µm, presented in Table 6-2) would be expected to decrease the inductance by 34-42% based on entering the Rmax values into Eq 5-1 as identified in Chapter 5. Thus, the 36% decrease in inductance due to the grit blasted surface, (with the inductance falling from 5.18E-04 H down to 3.31E-04 H), falls within this range and could potentially be masking any effects the work hardened layer may be having on the inductance. Therefore, approximately 16 µm of the surface roughness profile was removed grinding using 120-grit SiC grinding paper to leave a smooth surface finish. This caused the inductance value to increase from 3.31E-04 H to 4.63E-04 H. Interestingly, the surface roughness removed finish has an inductance value (4.63E-04 H) which is 11% lower than the sample with a similar surface roughness but without the work hardened layer (5.18E-04), thus the 11% decrease in signal can be attributed to the effect of the remaining work hardened layer (circa 84 µm) since both the 120-grit SiC ground surface and Al_2O_3 mechanical ground surface have a roughness value which is smoother than that of the EM sensor feet; smooth surfaces have been shown to have a negligible effect on the inductance in Chapter 5. These results suggest that the lift-off type effect caused by the surface roughness of a grit blasted surface (circa 14 – 18 µm) has a more detrimental impact on the inductance than the work hardened layer (circa 84 µm). At higher frequencies, the results (given in Figure 6-7) show that the inductance curves for the Grit Blasted sample and the Grit Blasted Surface Removed samples converge at approximately 60 KHz whereas the inductance value for the Before Blasted sample remains distinguishably higher even up to 100 KHz. This will be due to the influence of the respective resistivity of the surface layers since the EM signal is now penetrating to a

skin depth of circa 120 µm at 100 KHz (methodology for calculating skin depth has been given in Section 3.4.7). As such the resistivity of the Grit Blasted and Grit Blasted Surface Removed samples will be higher than the Before Blasted sample since the surface roughness will create air gaps due to the roughness profile (as identified in Chapter 5 Section 5.2) and the dislocations in the work hardened layer will also contribute to the increased resistivity in the thin skin layer. The resistivity for the Grit Blasted Surface Removed sample will also have a high resistivity compared to the Before Blasted sample but to a lesser extent than the Grit Blasted sample since the rough surface profile has been completely removed and approximately 16 µm of the work hardened layer has also been removed, hence why there is a difference between the Grit Blasted and Grit Blasted Surface Removed samples even at high frequencies up till about 60 KHz when they begin to converge.

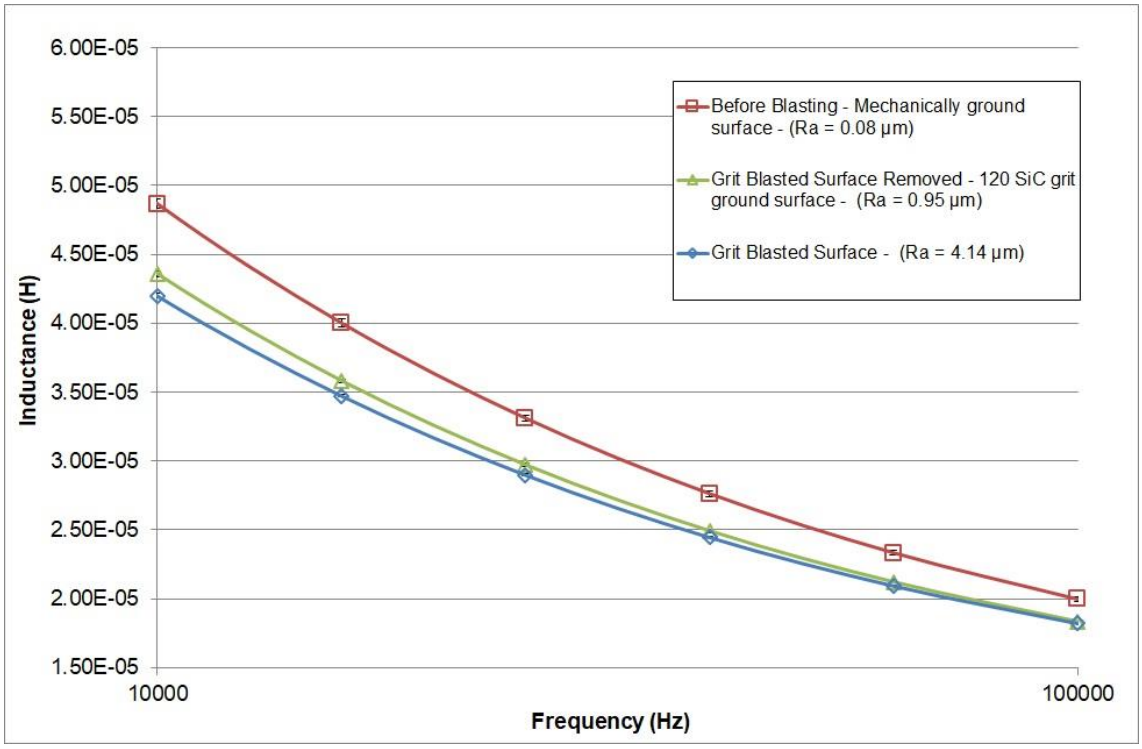

Figure 6-7: High frequency (10 – 100 KHz) variation of inductance with various surface conditions for sample P91:A-AR:GB

6.3. Differentiating CHT from MHT material

The next step was to consider the grit blasting parameters used by EON for cleaning power plant components in preparation for NDT testing, and determine whether the reduction in signal due to grit blasting inhibits the sensor from being able to determine CHT from MHT material. Grade 91 material PL91:A was sectioned to create four samples and then heat treated to produce two correctly heat treated samples (PL91:A-CHT:GB samples) and two mis-heat treated samples (PL91:A-MHT:GB samples) details of heat treatments are given in Table 3-3 within Section 3.2 of the experimental chapter.

Sample surfaces were mechanically ground using an Al_2O_3 surface grinder to produce an identical smooth surface finish (Ra = 0.08 µm) on all surfaces of all four samples. Thereafter, one surface on each sample was grit blasted using nominal grit blasting parameters (detailed in Table 3-7 in Section 3.2.2.2), but the distance between the grit blaster nozzle and the surface was varied. One sample from each pair of CHT and MHT samples was grit blasted from a distance of 30 mm and the other sample from 100 mm. These distances were selected as they are representative of typical distances employed by the technicians at EON for cleaning boiler components, since blasting from a distance further than 100 mm will be too far to achieve stock removal and blasting from a distance closer than 30 mm could result in detrimental mechanical changes to the material. Hardness indentation was performed to determine the amount and depth of work hardening achieved by grit blasting from 30 and 100 mm; the work hardened profiles can be seen in Figure 6-8 which suggests that the distance of the blasting nozzle to the sample has an insignificant effect on the work hardened layer. The hardness at the surfaces of the CHT:GB-30 and CHT:GB-100 samples is approximately 243 HV which gradually decreases to 230 HV which is representative of the bulk of the sample. The hardness at the surfaces of the MHT:GB-30 and

MHT:GB-100 samples is approximately 190 HV which gradually decreases to 150 HV which is representative of the bulk of the sample. The MHT samples would be expected to be softer than the CHT samples since the MHT samples, as shown in previous chapters, has a softer equiaxed ferrite grain structure compared to the harder tempered martensitic lath microstructure of the CHT material.

Low single frequency (10 Hz) EM tests were performed on the four samples before and after the grit blasting procedures, with the results given in Table 6-3 and graphically presented in Figure 6-9. The surface roughness values (given in Table 6-3) showed all four samples to have a smooth surface finish prior to being grit blasted (approximately 0.08 ± 0.01 µm, Ra) which increased to approximately 4.00 ± 0.10 µm, Ra after they were grit blasted. The inductance results (given in Figure 6-9) show that there is a significant impact on the samples due to the grit blasting, as expected and already identified earlier in this chapter, due to a combination of the surface roughness profile and work hardened layer created by the grit blasting procedure (discussed in Section 6.2). The MHT inductance values before and after grit blasting are respectively higher than the CHT values before and after grit blasting; this is also expected since the equiaxed ferrite microstructure of the MHT samples will have a higher relative permeability and hence higher inductance compared to the harder tempered martensitic microstructure of the CHT samples; as identified and discussed in Section 4.3. Interestingly, the grit blasted MHT samples can be clearly distinguished from the grit blasted CHT samples irrespective of whether the grit blasting nozzle is 30 or 100 mm away from the samples. The distance of the grit blasting at either 30 or 100 mm has an insignificant influence on the inductance value, as the difference in inductance is within the error bars, which would be expected since there was no significant impact of these stand-off distances on the work hardened profiles shown in Figure 6-8. Therefore the grit blasting has an insignificant impact on the ability for the

sensor to distinguish between CHT and MHT material if both samples have been grit blasted, irrespective of the grit blasting parameters (within the 30 – 100 mm stand-off range). However the grit blasting will reduce the EM signal by approximately 15 – 30% when comparing non-grit blasted samples to ones which have been grit blasted and this can lead to confusion and mis-identification. For example, from the results given in Table 6-3 and Figure 6-9, it can be seen that the smooth mechanically ground CHT sample (before grit blasting) with an inductance value of 4.87E-04 H and the MHT sample (before grit blasting) sample with the same surface finish has a higher inductance value of 5.77E-04 H (as expected), this would correctly suggest to the technician that the 5.77E-04 material is MHT in comparison to the CHT material. However if the MHT material is grit blasted then the inductance falls to 4.09E-04 H and if prior knowledge of the grit blasted layer was not known, then this result of 4.09E-04 H could be interpreted as a harder CHT bulk material and mask what is otherwise soft MHT bulk material. This has been shown more clearly in Figure 6-10 where a number of PL91:A CHT and MHT samples with varying surface layers and finishes (grit blasted surfaces, smooth and rough surfaces and decarburised layers) have been compared which shows that the MHT - aberrant ferritic bulk sample with a work hardened surface layer and rough surface layer (inductance = 4.09E-04 H) could be misinterpreted as CHT material and mistakenly accepted for service. Similarly, CHT - tempered martensitic bulk with a work hardened and rough surface layer (inductance = 3.26E-04 H) could be confused for un-tempered martensite and mistakenly rejected from service. These results would suggest that there is a need to remove the work hardened surface layer, which is approximately 60 – 100 µm for nominal grit blasting parameters used by EON, before using the EM sensor to avoid any mis-identification or confusion.

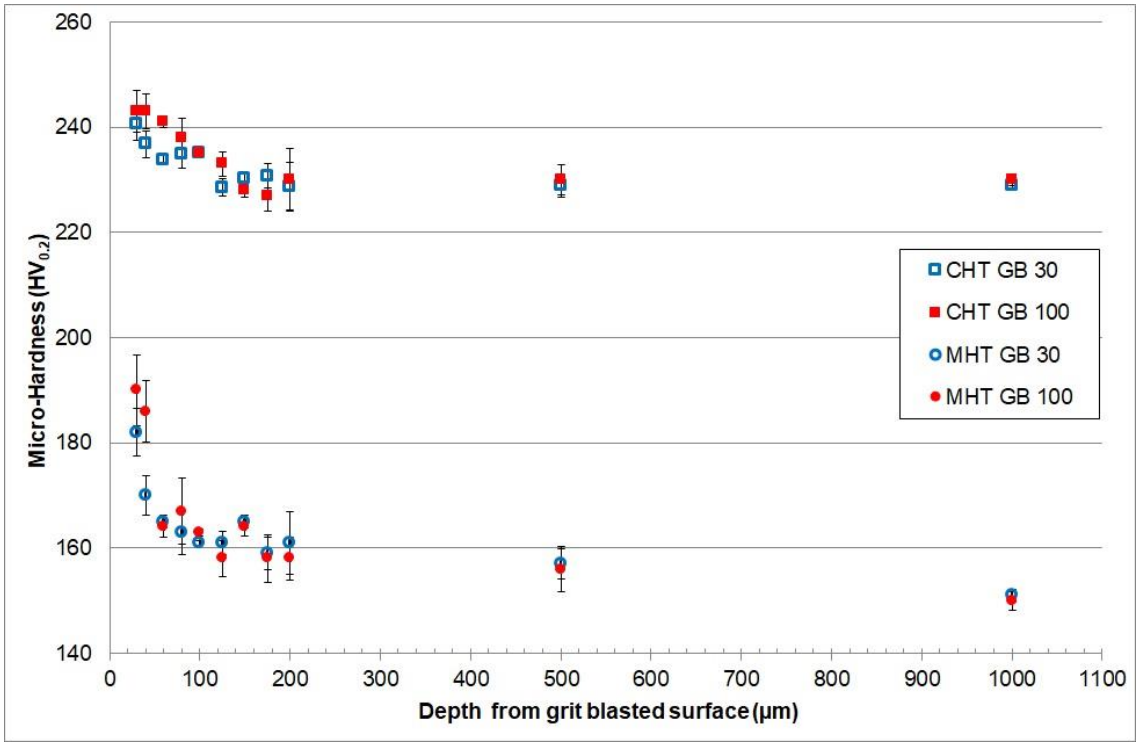

Figure 6-8: Micro-hardness indentation results for two PL91:A-CHT:GB samples blasted at distance of 30 mm and 100 mm and two PL91:A-MHT:GB samples blasted from 30 mm and 100 mm

Table 6-3: Low frequency (10 Hz) inductance and surface roughness results for samples PL91:A-CHT:GB and PL91:A-MHT:GB before and after grit blasting

Sample	PL91:A Inductance, Avg ± SD (x10^{-4} H)		
	Before Blasting (Ra = 0.08 ± 0.01 µm)	After Blasting (Ra = 4.00 ± 0.10 µm)	Reduction in inductance due to grit blasting
CHT:GB 30	4.87 ± 0.07	3.26 ± 0.15	33 %
CHT:GB 100	4.95 ± 0.11	3.33 ± 0.08	33 %
MHT:GB 30	5.77 ± 0.08	4.09 ± 0.06	29 %
MHT:GB 100	5.84 ± 0.10	4.22 ± 0.20	16 %

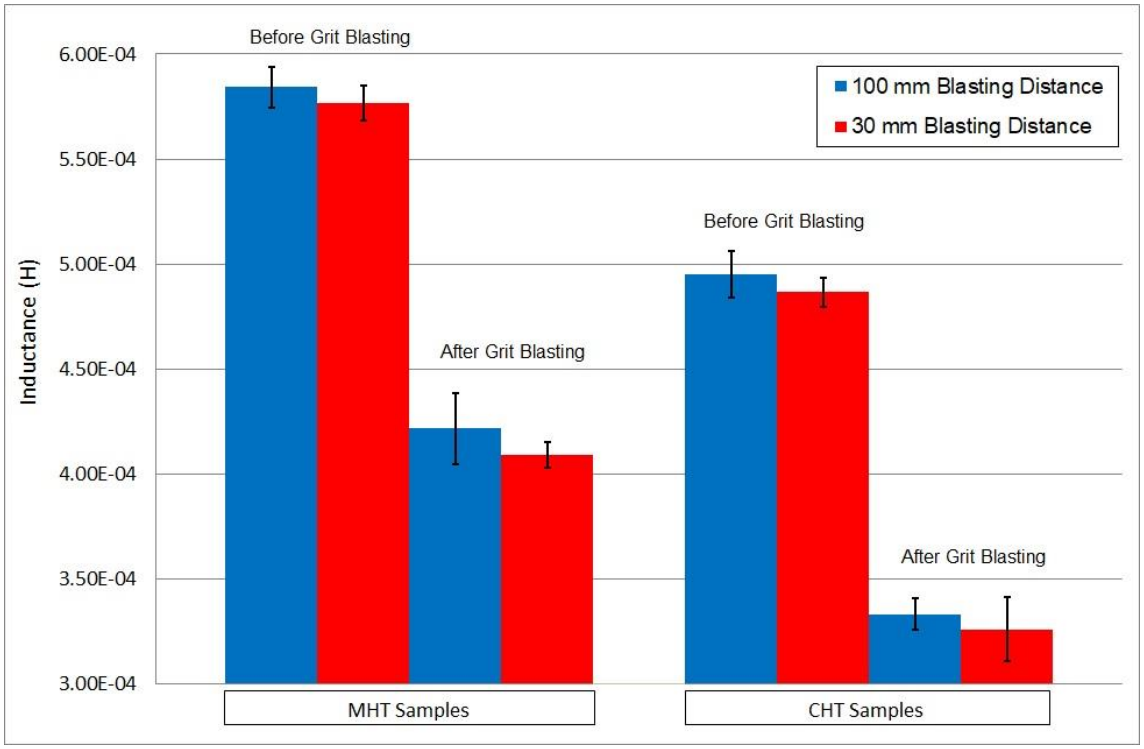

Figure 6-9: Low frequency (10 Hz) inductance variation for PL91:A samples showing the significance of grit blasting CHT and MHT samples from nozzle stand-off of 30 mm and 100 mm

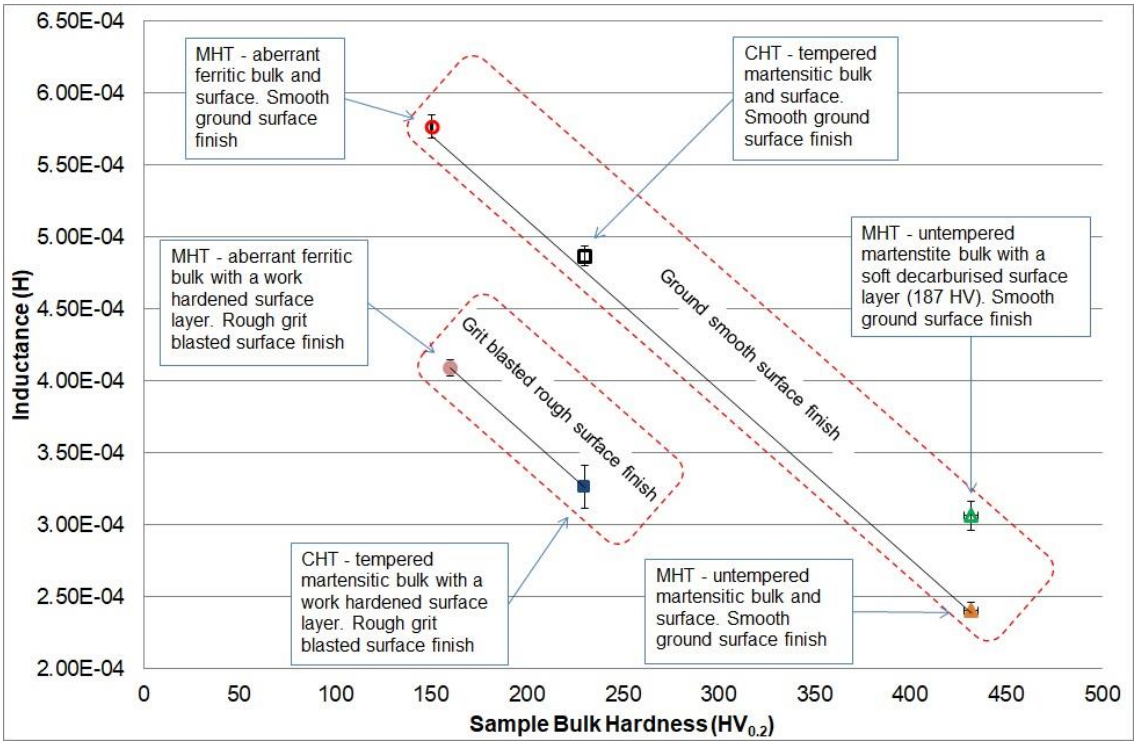

Figure 6-10: PL91:A samples with various bulk and surface microstructures showing a systematic decrease in EM signal for samples that have been grit blasted compared to samples that have been surface ground

6.4. Effect of Shot Peening

A 40 x 50 x 10 mm sample sectioned from PL91:A as-received material with a smooth Al_2O_3 ground surface finish (Figure 6-11a) was shot peened with parameters given in Table 3-8 in Section 3.2.2.3 and designated sample PL91:A-AR:SP (Figure 6-11b). The surface roughness profile was then removed using 120-grit SiC grinding paper (Figure 6-11c) to leave a smooth surface roughness less than 1 µm, Ra; which has been shown to have no impact on the inductance value (see Section 5.4). The sample microstructure after shot peening (Figure 6-12) shows that the martensitic laths at the surface have deformed. The hardness at the surface is approximately 270 HV and falls by 50 HV to 220 HV which then plateaus representing the bulk sample hardness. The hardness profile can be viewed in Figure 6-13, showing an approximately 300 µm thick work hardened layer. The 120-grit SiC surface grinding procedure removed

approximately 70 – 75 µm of material as measured by a micrometer using the methodology described in Section 3.3.7. A small section (10 x 10 x 10 mm) was taken from the sample after the surface roughness profile had been removed by the 120-grit SiC grinding procedure to re-measure the hardness profile (Figure 6-14). From Figure 6-14 it can be deduced that approximately 70 - 75 µm of material has been removed since the bulk hardness (circa 220 HV) plateaued at approximately 300 µm into the material for the shot peened sample and the removal of the surface roughness profile has caused the bulk hardness plateau at approximately 225 – 230 µm. Also the hardness gradient has shifted down as all the red data points are below their blue counterparts suggesting that the blue data points have shifted to the left by 70 – 75 µm.

Surface roughness measurements and multi-frequency EM tests were performed on all three surfaces of sample PL91:A-AR:SP, the results of which are given in Table 6-4 and the multi-frequency inductance data is shown in Figure 6-15. The low frequency (10 Hz) results show that the shot peening process, which induced a 300 µm work hardened layer and a surface roughness profile (Ra = 4.31 µm), equated to a 40% decrease in the inductance, with the value falling from 4.67E-04 H down to 2.78E-04 H. By grinding the surface and removing 75 µm of the work hardened layer, the inductance increases, such that the remnant difference between the before peening surface and the shot peened surface removed is a 4% decrease in inductance from 4.67E-04 H down to 4.47E-04 H. Residual compressive (elastic) stresses in the surfaces of the shot peened and grit blasted samples may be reducing the magnetic permeability in this region since the elastic compressive stresses are reducing the size of the interatomic spacing between the iron atoms. When the surface has been ground to a 120-grit SiC finish, it is likely that this effect has been removed and hence effectively increasing the magnetic permeability within this region leading to an increase in the inductance of both the shot peened surface removed and grit blasted

surface removed samples (seen in Figure 6-15 and Figure 6-6 respectively). It was noticed that the effect of shot peening the surface followed by removing the shot peened surface layer (circa 4% decrease in inductance) is smaller than the effect of grit blasting and removing the grit blasted surface layer (circa 11% decrease in inductance). By grinding the surfaces of both samples the hardest portion and probably the highest volume of residual (elastic) compressive stresses may have been removed. Since a larger depth of material was removed from the shot peened sample (75 µm) in comparison to the grit blasted sample (16 µm), it is likely that the grit blasted sample has a larger volume of compressive stresses at the surface in comparison to the shot peened sample and hence the larger impact on the grit blasted sample's inductance (decrease of 11%) as opposed to the shot peened sample (decrease of 4%). The high frequency data, presented in Figure 6-16, shows a similar trend to the high frequency data observed for the grit blasted samples in Section 6.2; whereby the shot peened and shot peened surface removed samples have a lower inductance at high frequencies than the before shot peening surface which continues to remain distinguishable at 100 KHz unlike the shot peened and shot peened surface removed sample which converge. Similar to previous results, the high frequency behaviour is dictated by the resistivity of the samples within a very small skin depth as the magnetic field is only penetrating to a depth of approximately 120 µm at 100 KHz (methodology for calculating skin depth has been given in Section 3.4.7). The resistivity of the shot peened and as shot peened surface-removed samples will have a higher resistivity, caused by the surface roughness profile introducing air gaps across the roughness profile (as discussed in 3.3.4) and also by the higher dislocation density in the work hardened layer, compared to the smooth ground surface before peening sample.

To determine what the minimum amount of work hardened layer would need to be removed, to avoid such an influence, that the EM sensor was able to determine CHT

from MHT materials; an investigation was performed to EM test surfaces which have a progressively removed work hardened surface layer, this is documented in Section 6.5.

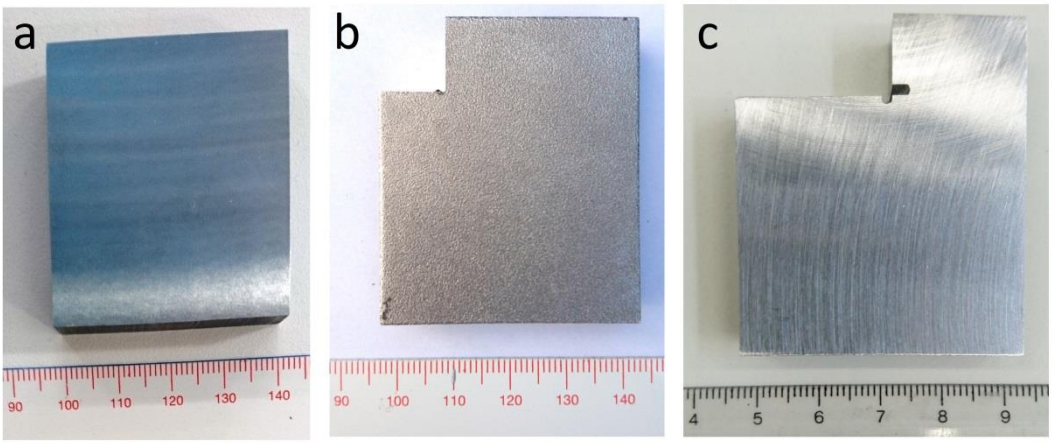

Figure 6-11: PL91:A-AR:SP sample showing (a) before peening with a mechanical ground surface finish, (b) as-shot peened surface finish and (c) 120-SiC grit ground surface finish removing approximately 70 – 75 µm of the shot peened surface

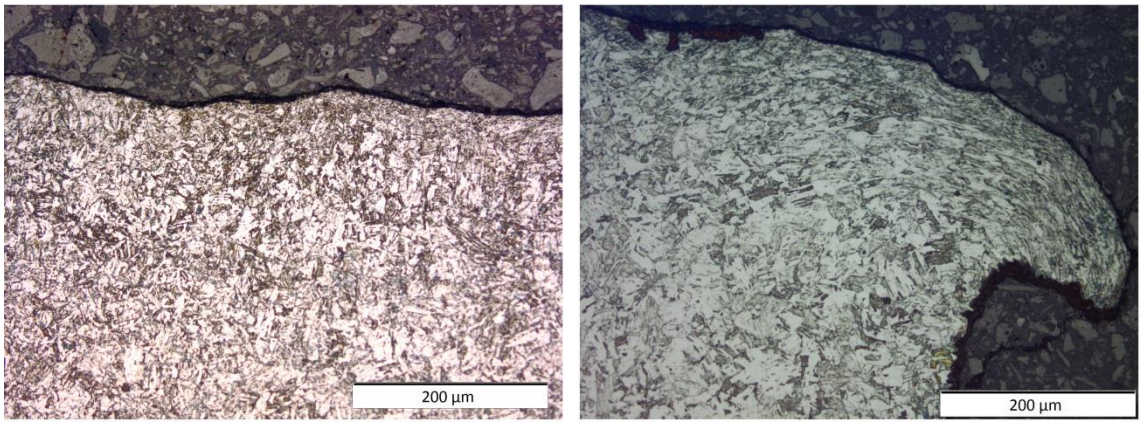

Figure 6-12: LOM images of PL91:A-AR:SP showing deformed martensite laths at the surface (left) and edges (right)

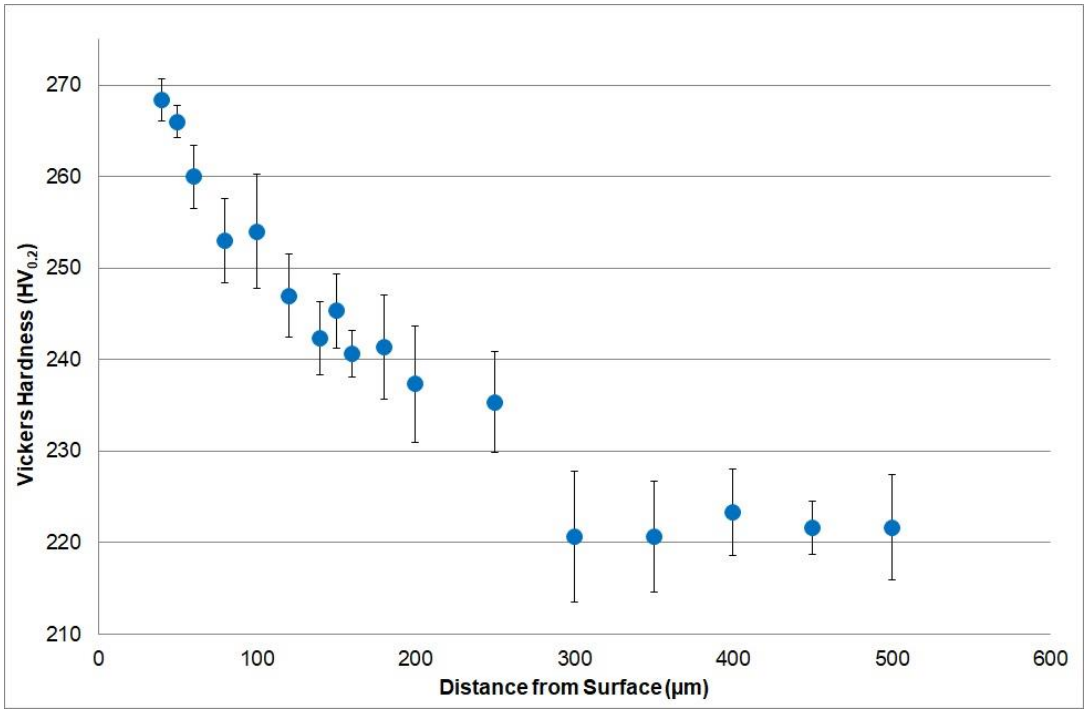

Figure 6-13: Sample PL91:A-AR:SP hardness indent data showing the hardness profile from the surface to a depth of 500 µm

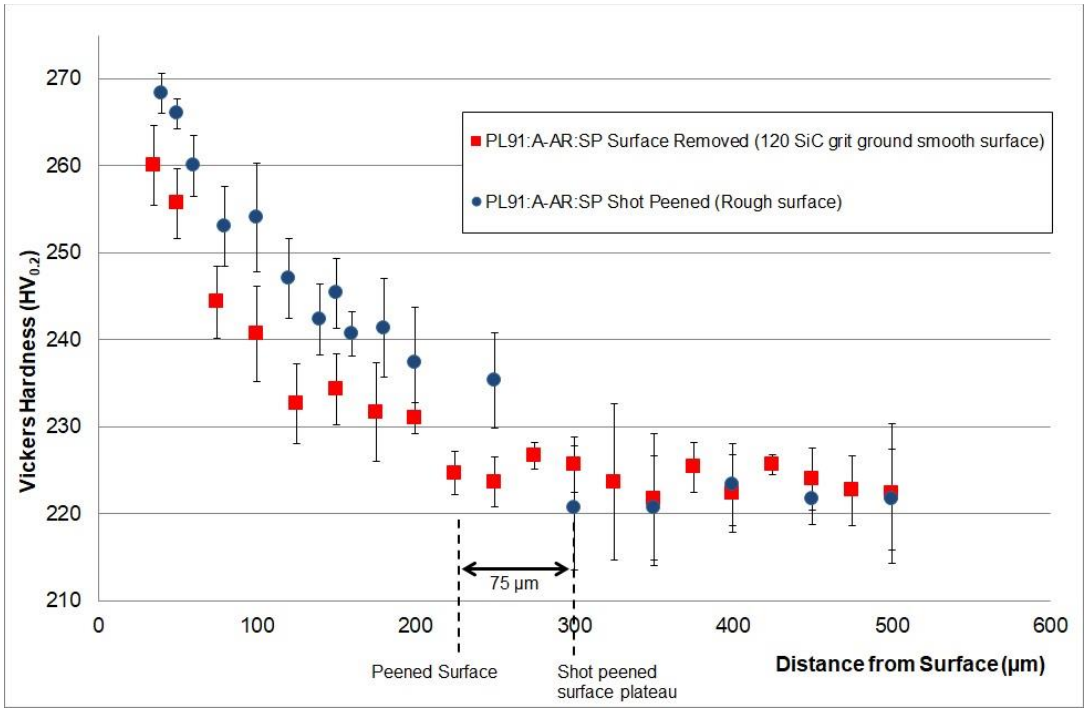

Figure 6-14: Hardness profile between surface and depth of 500 µm for sample PL91:A-AR:SP for as shot peened surface and the 120 SiC grit ground surface removed, showing that the grinding process removed approximately 75 µm of material

Table 6-4: PL91:A-AR:SP sample results of; surface roughness (Ra and Rmax) and low frequency (10 Hz) inductance values for various surface finishes

Sample PL91:A-AR:SP with different surface finishes	Surface Roughness at 8 locations ± SD (µm)		Inductance ± SD (E-04 H)
	Ra	Rmax	
Before Peening (Al_2O_3 mechanical ground surface)	0.06 ± 0.01	4.64 ± 1.09	4.67 ± 0.16
After Peening (Shot peened surface)	4.31 ± 1.62	12.86 ± 4.84	2.78 ± 0.04
Shot peened surface roughness layer removed (120-grit SiC ground surface)	0.89 ± 0.13	6.97 ± 1.55	4.47 ± 0.11

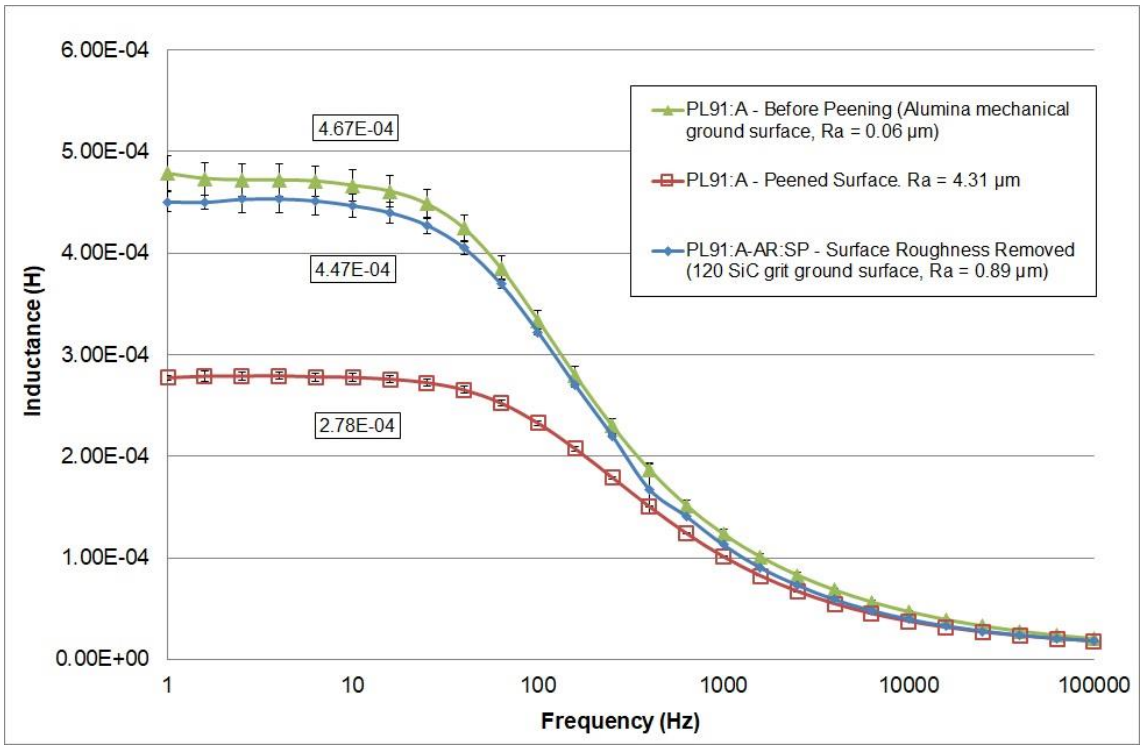

Figure 6-15: Multi-frequency variation of inductance for PL91:A samples with various surface finishes; Before shot peening (Al_2O_3 mechanically ground surface), As-shot peened surface and Surface roughness removed (120 SiC grit ground surface)

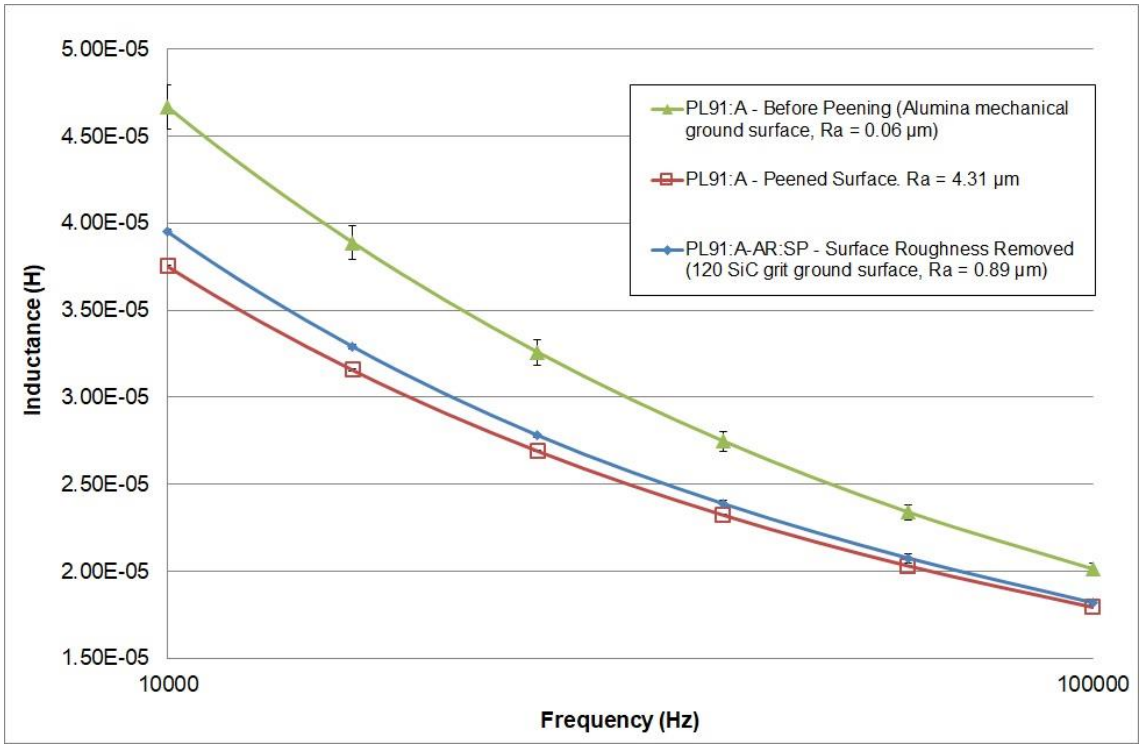

Figure 6-16: High frequency (10 – 100 KHz) variation of inductance for PL91:A samples with various surface finishes; Before shot peening (Al_2O_3 mechanically ground surface), As-shot peened surface and Surface roughness removed (120 SiC grit ground surface)

6.5. Progressively Removed Work Hardened Layer

Sample PL91:A-AR:SP (which had a shot peened surface) had its surface layer progressively removed to determine the impact of different depths of work hardening on the inductance; sample details are given in 3.2.2.3. The sample's surface was progressively ground and the thickness of the sample was measured at each stage to determine the remnant thickness of the work hardened layer (this procedure has been described in more detail in Section 3.3.7). The inductance results at low frequency (10 Hz) were varied against the change in work hardened layer thickness and shown in Figure 6-17 as well as the hardness profile (on a secondary axis) between the surface and the bulk, to a depth of 300 µm. The results show that as the work hardened layer is removed, the absolute hardness (at the newly revealed surface) decreases until the

bulk hardness value is reached (i.e. complete removal of the work hardened layer). Simultaneously the inductance values increase as the work hardened layer is progressively removed, particularly over the removal of the initial 60 – 80 µm of the work hardened layer after which the inductance begins to plateau. After removal of approximately 100 µm (meaning a 200 µm thick work hardened layer still exists) the inductance plateaus. This is because the hardness of the surface after removal of the initial 100 µm of the work hardened layer falls from 270 HV to approximately 250 HV. As such, the difference between the inductance after removal of 100 µm of the work hardened layer and the bulk EM signal at a depth of 300 µm (i.e. when the work hardened layer is completely removed where the bulk hardness is approximately 230 HV) is insignificant. This result would suggest that the EM sensor should be able to determine bulk CHT microstructure from bulk MHT microstructure by removing the initial 100 µm of a work hardened layer for the given range of parameters testing, i.e. work hardened range of 270 HV – 230 HV across 300 µm thick layer. This is beneficial since one of the current techniques of determining the microstructure (portable hardness testing) would require the full 300 µm thick work hardened layer to be removed before getting a true hardness value representative of the bulk microstructure. The sensitivity of the inductance seems to exist over the initial 100 µm of work hardened layer (for the parameters investigated). Therefore it is recommended that if the EM sensor in this investigation is to be deployed for distinguishing CHT from MHT bulk microstructures with grit blasted/ work hardened surfaces, then a minimum of 100 µm of the shot peened surface layer should be removed and the full grit blasted layer (60 – 100 µm) should be removed. Surfaces should be prepared to a minimum surface finish of 120 grade SiC grit ground surface, which produces a surface roughness less than the roughness of the sensor's feet (< 1.0 µm Ra).

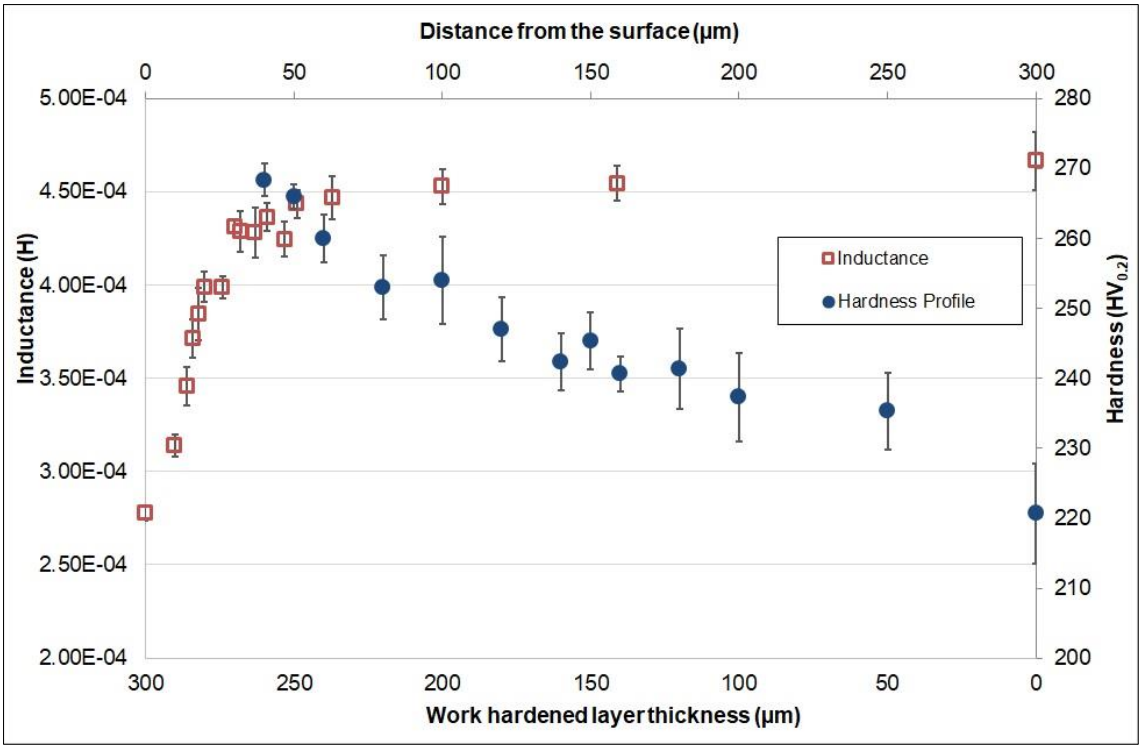

Figure 6-17: Variation of EM signal (10 Hz) with depth of work hardened layer and hardness indentation with distance from the surface

6.6. Summary

The effect of a work hardened surface layer was studied. Grade 91 samples were subjected to grit blasting and shot peening under typical parameters that would be adopted for preparing component surfaces within power plants for NDT inspection. The cold working procedure decreased the inductance by approximately 30 – 35% for the grit blasted samples and by 40% for the shot peened samples. This is probably due to a combination of induced residual compressive stresses from the work hardened layer and a lift-off type affect caused by the surface roughness profile; the effects of which were discussed. Removing a portion of the cold worked surface layer (15 µm for grit blasted and 75 µm for shot peened) reduced the effect, since the surface roughness profile was completely removed, but this was not sufficient to negate the effect entirely

as the remaining work hardened layers still had a decreasing influence on the inductance.

Grit blasting components from 30 or 100 mm (typical grit blasting distances) had no significant impact on the work hardened profiles or the inductance values. The EM sensor was able to distinguish CHT from MHT material if both samples have been grit blasted. However when comparing non-grit blasted surfaces with grit blasted surfaces then the inductance decrease, due to grit blasting, will impact the ability for the EM sensor to differentiate CHT from MHT material – thus the work hardened layer (typically 60-100 µm thick) should be removed.

A shot peened work hardened layer was progressively removed and EM tested to show that the inductance is sensitive to the initial 100 µm of a 300 µm work hardened layer, the removal of which negates the effect of the remaining work hardened layer.

CHAPTER 7 RECOMMENDED APPLICATIONS AND BENEFITS

The results presented and discussed in Chapters 4 – 6 suggest that the U-shaped EM sensor can be used in two different capacities to support the NDT testing of P91 boiler components at EON. However for the EM sensor to be successfully applied then there are some strict procedures that need to be adhered to such that the inductance data is not mis-interpreted by operators. This chapter highlights the specific applications where EON can deploy the EM sensor technique and makes recommendations for operating procedures linked to the discussion chapters summarising the benefits that the EM sensor technique can provide for EON.

7.1. Application 1 – Complementary Technique

From Chapter 4 it was determined that the EM sensor can differentiate correctly heat treated (CHT) microstructures from mis-heat treated (MHT) microstructures. This means the EM sensor can be used to screen service entry components. Currently, surface replication and portable hardness NDT techniques are employed to screen service entry materials. The EM sensor can complement these techniques as it is able to provide the same service. However the portable hardness technique suffers with low accuracy as it has been described as being 'evident' that the technique tends to produce inaccurate results unless used with considerable care [200]. Misleadingly low portable hardness results can be attained for numerous reasons such as inadequate surface preparation, poor calibration technique, incorrect equipment operation, and improper data analysis. These can all present difficulties leading to errors even when a reasonable level of skill and care is involved [208]. The EM sensor has shown to be able to distinguish accurately MHT from CHT microstructures and therefore can be deployed alongside portable hardness testing to provide the technicians with more confidence, particularly for hardness measurements close to the minimum and maximum specification limits 212 HV and 257 HV respectively. Where the EM sensor differentiates itself from portable hardness testing and surface replication is for

components which have a different surface microstructure compared to its bulk microstructure. Chapter 4 identified that for samples with relatively thin decarburised surface layers (circa 300 – 500 µm), the EM sensor is able to determine whether the bulk microstructure beneath the decarburised surface layer is correctly tempered martensite or mis-heat treated ferrite (based on the hardness of the bulk material). In this situation the portable hardness and surface replication techniques would falsely determine the component to be unacceptable soft mis-heat treated material and would require the surface layer to be grinded back and re-tested before determining whether the bulk material is acceptable or not. The EM sensor can provide this differentiation without removing the thin decarburised surface layer.

7.2. Application 2 – Principle Technique

The second application is where the EM sensor is to be applied as a principle technique, to screen in-situ components during maintenance outages. Currently, when carrying out routine plant inspection there are typically two routes to identify which specific locations of a component's surface is to be inspected using surface replication. The primary route is to consult the component's historical data records which identify areas of interest based on past failures, repairs and areas of high stress. The secondary route is based on population statistics, where the utility will have a statistical approach to identify how many component's and which spots on the component's surfaces are to be inspected, e.g. 25% of steam header end caps within a single boiler unit at 8 equidistant circumferential locations. This will usually also factor in the time it takes for surface replicas to be created which can be very expensive; £1500 for 30 surface replicas with each replica taking an experienced operator 30 – 45 minutes to produce [91]. This still leaves the risk of uninspected component's primarily limited for commercial and practical reasons. The EM sensor in this situation can be applied to

relatively quickly (a few minutes per test) attain low frequency inductance data for numerous components and numerous locations on the component's surface; thus achieving a greater coverage of component surface. Where the EM sensor inductance values identify results which infer that bulk microstructure may not be correctly heat treated, it would be sensible for surface replication to be carried out on these select locations.

7.3. Procedural Recommendations

From Chapter 5 it was determined that the surface roughness of a component can have a significant impact on the inductance values measured by the EM sensor. The surface roughness of a component to be inspected must be smoother than the surface roughness of the EM sensor, if the sensor feet are to be in contact with the surface. Hence component surfaces should be prepared with a surface roughness less than 1.0 µm Ra for the surface roughness to have no influence on the inductance measured by the U-shaped sensor used in this study. It has also been shown in Chapter 5 that a surface roughness finish less than 1.0 µm, Ra is achievable with a 60-grit grade SiC grinding procedure.

The effect of lift-off was explored in Chapter's 3 and 5 which showed that by increasing the lift-off between the sensor and the component will cause the sensor to become less sensitive in its ability to distinguish CHT from MHT microstructures and therefore it is recommended that the EM sensor be used in direct contact with the surface being tested.

Chapters 3 – 6 consistently showed that as the testing frequency is increased the eddy currents in the samples dampen the inductance. It was seen that at low frequency (10 Hz) the inductance values were most sensitive to the sample's magnetic permeability, which is the reason why the MHT and CHT microstructures can be

differentiated and therefore it is recommended that a frequency of 10 Hz is used to screen CHT from MHT material for the sensor used in this study.

Chapter 6 explored the effect of work hardened surface layers which can significantly influence the inductance value due to the dislocation density within the work hardened layer and the surface roughness profile created by the grit blasting or shot peening processes. Therefore it is recommended that when components are grit blasted to clean surfaces in preparation for NDT, then 100 µm of the surface layer should be ground using a minimum of 60-grit SiC surface grinding procedure. This will remove the rough surface roughness profile and the bulk of the hardened layer created by the typical work hardening parameters employed by EON as given earlier in Chapter 6.

The recommended parameters for the EM sensor used in this study are summarised in Table 7-1.

Table 7-1: Recommend EM sensor settings for deployment within the power generation industry for Grade 91 material

Recommended settings (for the EM sensor used within this study)	
Sensor type	U-shaped
Frequency	10 Hz
Lift-off	0 mm
Component Surface Roughness, Ra	≤ 1.0 µm
Surface Preparation Finish	SiC grinding 60-grit grade (min)
Typical inductance range for correctly heat treated service entry material	4.0 – 5.5 ($x10^{-4}$ H)
Number of repeated tests in one location to generate statistical error (standard deviation)	8 (for 50 x 50 mm area)

7.4. Benefits

The above applications are recommended for EON's power technology NDT department to consider, based on the experimental research presented in this thesis for the U-shaped EM sensor used to conduct the research. The benefit to EON would be:

- Increased integrity in EON's ability to screen service entry material
- The ability to determine what the bulk microstructures are with the presence of a thin decarburised surface layer
- Less surface preparation to carry out EM tests translating into time savings
- Increased component surface screening for lower time cost compared with surface replication

CHAPTER 8 CONCLUSIONS AND FUTURE WORK

8.1. Conclusions

A small U-shaped EM sensor was manufactured and used to perform a range of tests to measure the multi-frequency (10 Hz – 100 KHz) inductance of numerous Grade 91 power plant materials. The testing was carried out in order to determine the EM sensor's ability to determine whether sample bulk microstructures were either correctly heat treated (tempered martensite laths) or mis-heat treated (equiaxed ferrite grains). A range of samples were produced to understand the influence of the surface condition on the EM sensor inductance measurements based on the possible conditions boiler component surfaces may come across in industry. As such, the influence of surface roughness, decarburised surface layers and work hardened surface layers, on the EM sensor's ability to differentiate correctly heat treated and mis-heat treated bulk microstructures, was researched.

With respect to the EM sensor being able to differentiate correctly heat treated (CHT) from mis-heat treated (MHT) microstructures, the following conclusions have been made:

- The EM sensor used in this study has been shown to be sensitive to the material's magnetic permeability at low frequency (typically 10 Hz) such that the inductance varies with magnetic permeability. The soft MHT material has an equiaxed ferrite grain structure which will have a higher magnetic permeability than the harder tempered martensitic lath microstructure of CHT material since the lath boundaries, dislocations and carbonitride precipitates in the CHT material will pin domain wall movement which influences the inductance

measurements. Thus the EM sensor inductance values were able to significantly distinguish CHT material from MHT material.

- The inductance values of the soft ferritic MHT materials is consistently higher than the inductance values of the harder martensitic CHT materials with the inductance values correlating linearly with the material's hardness value at low frequency (10 Hz)

With respect to the influence of a decarburised surface layer on the EM sensor inductance values, the following conclusions have been made:

- The presence of a decarburised surface layer will lead to an increase in the inductance value. However the EM sensor was still able to provide insight into a material's bulk microstructure through the presence of decarburised layers up to 500 µm in thickness as evidenced in Chapter 4 Figure 4-21
- Sample P91:B-FC+T had a CHT tempered martensitic bulk microstructure with the presence of a 300 – 500 µm thick decarburised surface layer for which the inductance value was distinguishable from a completely MHT bulk material
- With present screening techniques (surface replication and portable hardness testing) used by EON, sample P91:B-FC+T, would be misidentified as soft aberrant material which would require further assessment until the true nature of the bulk microstructure could be determined, whereas the EM sensor was able to determine the bulk microstructure to have an inductance value indicative of a CHT microstructure
- Sample PL91:A-N1100+FC was mis-heat treated to produce an un-tempered martensitic bulk microstructure with the presence of a 1.6 mm decarburised surface layer. The thick decarburised surface layer caused a 28% increase in the inductance, however the inductance value was still significantly lower than the inductance value of the CHT sample (PL91:A-CHT), hence confirming that

the EM sensor can distinguish un-tempered martensitic bulk material with the presence of a thick (1.6 mm) decarburised surface layer from CHT material. Removing 1 mm of the decarburised surface layer (by grinding it down to 600 µm) removed any influence of the decarburised surface layer such that the inductance measured on the sample with the presence of a 600 µm decarburised surface layer was similar to the inductance measured on the sample with no decarburised surface layer.

With respect to the influence of a surface roughness layer on the EM sensor inductance values, the following conclusions have been made:

- A number of samples were machined to create various degrees of surface roughness on sample surfaces in Chapter 5 (ranging from circa 0.1 – 40 µm, Ra – arithmetic mean surface roughness). The research concluded that the surface roughness has a lift-off type effect on the inductance values; such that the inductance value is inversely proportional to the square of the surface roughness Rmax parameter (Rmax parameter represents the peak-to-valley height created by the surface roughness profile).
- For the range of surface roughness profiles examined in this research (circa 0.1 – 40 µm, Ra) the EM sensor inductance value becomes insensitive (i.e. the inductance values of the roughest sample and smoothest sample are similar) with an in-built lift-off of 0.3 mm. However at a lift-off of 0.3 mm, the EM sensor is unable to differentiate CHT from MHT material and therefore it is concluded that an in-built lift-off would not be suitable for this sensor. As such, the EM sensor should be used with the sensor core feet in direct contact with the surface of the specimen being tested.
- The surface roughness has an influence on the inductance only if the surface being tested has a greater surface roughness than the surface roughness

inherent on the EM sensor core feet, which are in contact with the sample. Thus concluding that to negate the influence of surface roughness on the inductance values, surfaces should be prepared to a surface roughness finish smoother than 1.0 µm Ra (for the EM sensor used in this study).

- It was discovered that a surface preparation of 60-grit grade SiC ground surface finish will create a surface roughness smoother than 1.0 µm, Ra and as such concludes that the 60-grit grade SiC ground surface finish is the minimum surface finish required to negate the influence of surface roughness on the measured inductance.

With respect to the influence of a work hardened layer on the EM sensor inductance values, the following conclusions have been made:

- In Chapter 6, a number of Grade 91 samples were subjected to grit blasting and shot peening, using typical parameters that would be adopted for preparing component surfaces within power plants for NDT inspection. The results showed that work hardened layers caused inductance values to decrease due to the dislocations within the work hardened layers having a pinning effect on the domain wall movement which would reduce the layers relative permeability and hence the inductance values. The rough surface roughness profile also contributes to a decrease in the inductance value caused by the work hardened surface.
- For the parameters used and reported in Chapter 6, the grit blasting procedure introduced a 100 µm thick work hardened layer into sample P91:A-AR-GB (with a hardness gradient ranging from 250 HV at the surface to 210 HV in the bulk) and the shot peening introduced a 300 µm work hardened layer into sample PL91:A-AR-SP (with a hardness gradient ranging from 270 HV at the surface to 220 HV in the bulk). The work hardened layers caused the inductance values to

decrease by approximately 30 – 35% for the grit blasted surface and approximately 40% for the shot peened surface.

- Where two components with different microstructures (e.g. CHT and MHT) have been prepared with similar work hardening processing, then the decrease in signal due to work hardening will be similar in both materials and not prevent the EM sensor from being able to distinguish CHT from MHT microstructures.
- Where comparing a component with a non-work hardened surface to a component with a work hardened surface, then the EM sensor was unable to differentiate CHT from MHT material. However the inductance values were sensitive to approximately the initial 100 µm of the work hardened layer in 300 µm thick work hardened layer, removal of which took away the influence of the remaining 200 µm thick work hardened layer. Therefore it was concluded that 100 µm of the surface layer should be removed.

Based on the work undertaken, the EM sensor used in this study has the following potential applications (note consideration should be given to the recommended settings for this sensor given in Chapter 7, Table 7-1):

- The EM sensor can be deployed as a complementary technique to portable hardness testing to help inspectors determine with more confidence whether service entry material is within the specification.
- Where the hardness testing confirms that a decarburised surface layer is present, then the EM sensor can be used to indicate the bulk microstructure efficiently without the need to completely remove the surface layer, given that the decarburised layer is between 300 – 500 µm thick.
- The EM sensor can be utilised as a principle screening technique to screen more components and a greater surface area coverage of components as it is faster than surface replication. The EM sensor can be used with relatively

minimum surface preparation (60-grit SiC surface finish) and the inductance results can indicate the characteristics of the microstructure leading to further investigation with hardness testing or surface replication if required.

- When the EM sensor inductance values are not indicative of a CHT bulk microstructure (i.e. 4.0 – 5.5 $x10^{-4}$ H), the inspector might suspect that there is an aberrant decarburised surface layer. Then hardness and surface replication can be performed to confirm this. This way only a minimal amount of material needs to be removed (up to a maximum of 1.5 mm) before the EM sensor can correctly indicate whether the bulk microstructure's hardness value is within the acceptable range or not, whereas surface replication and hardness testing would require complete removal of the decarburised surface layer.
- When it is known that the component has been shot peened or grit blasted, the EM sensor can be used to indicate what the bulk microstructure is with removal of only 100 µm of the surface layer – thus saving time in comparison to performing hardness testing which would require removal of the full work hardened layer.

8.2. Future work

Following the progress made in this study, to further develop the EM sensor technology to increase its capabilities and make it more accessible across a number of components, future work in this field has been advocated below.

The following suggestions are made with regards to enhancing the validation of the conclusions drawn in Chapter 8:

- The results in Chapter 4 have shown that a thin decarburised surface layer (circa 300 - 500 µm) has an insignificant impact on the EM sensors inductance values being able to determine CHT from MHT bulk microstructures. They have

also shown that a thick decarburised layer (1.6 mm) on an un-tempered bulk microstructure also has an insignificant impact in differentiating between un-tempered bulk martensite and CHT tempered martensite bulk microstructure. However the influence of a thick decarburised surface layer on a tempered bulk microstructure has not been determined. To do this, sample PL91:A-N1100+FC should be heat treated at typical tempering parameters of 760 °C for 3 hours. This should transform the un-tempered martensite bulk microstructure into tempered martensite whilst keeping the thick decarburised surface layer (1.6 mm) intact. EM tests should then be performed in line with the parameters suggested in Table 7-1 using the U-shaped EM sensor to determine the influence of a thick decarburised surface layer on the inductance value when differentiating tempered martensite bulk microstructure from MHT bulk microstructure. This was not achieved during this research due to time limitations.

- Chapter 6 explored the effect of work hardened surface layers on the inductance values and concluded that the EM sensor is able to differentiate CHT and MHT bulk microstructures if both microstructures were subjected to similar work hardening processes. However, if comparing CHT and MHT bulk microstructures such that only one of them had been subjected to work hardening, then the inductances value would be significantly influenced, such that an accurate determination of the bulk microstructure could not be made. In this scenario further work should be carried out to investigate whether introducing an in-built lift-off of 0.05 mm between the work-hardened surface and the EM sensor reduces the influence of the work hardened layer on the inductance values. At a lift-off of 0.05 mm, it was shown in Chapter 5 that the EM sensor is able to differentiate CHT from MHT bulk microstructures, and so if at this lift-off the influence of the work hardening on the inductance values is

reduced, then it may be possible that the work hardened surface layer does not require removing, which is the current conclusion.

The following suggestion is made with regards to the geometry of components and the geometry of the EM sensor:

- The research presented in this thesis considers the EM sensor for applications with flat components surfaces such that the EM sensor core's flat feet can conform flush to the surface of the component being tested. The small U-shaped sensor in this study will conform to steam header end caps (which have a flat surface) and to boiler pipes with very large curvature, such that the small sensor can still be positioned flush with the surface being tested. However, this would not be possible for pipes and tubes with smaller curvature and will prevent use of the U-shaped EM sensor as it would not be able to conform to the curvature. Therefore future work should consider the impact of curved geometries of pipes and tubes on the sensors ability to differentiate MHT components from CHT components. Essentially the consequence of the EM sensor not having flush contact with the test surface will cause the inductance to decrease due to the air gaps that will be created between the sensor and the curved surface of the components. The development of a sensor design or arrangement which could accommodate the geometry effect of different shaped components would greatly enhance the U-shaped EM sensor's application within the power plant industry, allowing the technique to be deployed on more components.

The following suggestion is made with regards to characterising the depth of decarburisation at the surface:

- In Chapter 4, the EM sensor in this study has shown the ability to determine bulk microstructure for samples with a thin decarburised surface layer (300 – 500 µm). The next step would be to develop the technique such that the inductance measurements can determine the depth to which the decarburised surface layer is present. In particular, it would be beneficial to be able to non-destructively determine the depth of the decarburised surface to assess whether its thickness is within specification for acceptable service entry material (max 2 mm) or not. The current conclusions drawn in Chapter 8 recommend that up 1.5 mm of the surface layer would need to be removed before the EM sensor can determine whether the decarburised surface layer is greater than or equal to 2 mm.

The following suggestion is made with regards to making the EM sensor technique portable:

- The experimental set-up for performing EM tests in this study, would not be suitable for portable NDT testing. This is because the impedance analyser used in this research (Solartron 1260A) weighs 18 kg and is a desktop lab based apparatus. Therefore it would be very useful to investigate using a portable impedance analyser and perform in-situ tests within a power plant boiler house to understand the practicalities of deploying the technique in a boiler unit.

The following suggestion is made with regards to developing finite element (FE) modelling capabilities:

- COMSOL Multi-physics FE modelling software was explored to begin developing 3D U-shaped FE models during the research period. Due to time, the models were not able to be fully validated and hence these results have not been reported in the main body of the thesis. Future work to develop this

modelling capability for the U-shaped sensor would significantly increase the variety and speed with which the technique can be developed. FE modelling can be used to explore many of the suggestions within this Chapter such as the influence of component geometries, determining the depth of decarburised surface layers and exploring the influence of surface roughness and work hardened surface layers at wider ranges than those reported within this thesis. Therefore FE modelling can assist in the optimisation of the sensor design for deployment in the field.

LIST OF REFERENCES

1. Spear, B., *James Watt: The steam engine and the commercialization of patents.* World Patent Information, 2008(30): p. 53-58.
2. Muirhead, J.P., *The Life of James Watt: With Selections from his Correspondence*. 1858, John Murray: London.
3. Gooding, D., T. Pinch, and S. Schaffer, *The Uses of Experiment : Studies of Experimentation in the Natural Sciences*. 1989, Cambridge: Cambridge University Press.
4. Scaife, W.G., *Charles Parsons - Manufacturer.* Journal of Materials Processing and Technology, 1992(33): p. 323-330.
5. Sich, J., *100 People who made History*. 2012, London: Dorling Kindersley.
6. Ford, A., *System dynamics and the electric power industry.* System Dynamics Review, 1997. **13**: p. 57-85.
7. Breeze, P., *Chapter 3 - Coal-fired Power Plants*, in *Power Generation Technologies (Second Edition)*, P. Breeze, Editor. 2014, Newnes: Boston. p. 29-65.
8. HMGovernment, *The UK Low Carbon Transition Plan: National Strategy for Climate Change and Energy*. 2009, TSO: Norwich.
9. Campbell, R., *Increasing the Efficiency of Existing Coal-Fired Power Plants*. 2013, Congressional Research Service.
10. *Reheater With 600PCS Nipples*. [Image] 2015 [cited 2015 19/11/2015]; Available from: http://www.made-in-china.com/showroom/product-images/China-Reheater-With-600PCS-Nipples-GlseXp5agb-rMKmAfFHVJcn.html.
11. Marriott, J.B., *Future materials requirements for high temperature power engineering components.* Materials & Design, 1990. **11**(3): p. 122-128.
12. Parker, J. and S. Brett, *Creep performance of a grade 91 header.* International Journal of Pressure Vessels and Piping, 2013. **111–112**: p. 82-88.
13. Parisher, R.A. and R.A. Rhea, *Chapter 2 - Steel Pipe*, in *Pipe Drafting and Design (Third Edition)*, R.A. Parisher and R.A. Rhea, Editors. 2012, Gulf Professional Publishing: Boston. p. 4-12.
14. Lefebvre, B. *V&M Experience in T/P91 Tubes and Pipes*. in *International Workshop on Fabrication and Processing of Grade 91 Material*. 2011. India.

15. ASTM, *Standard Specification for Seamless Ferritic Alloy-Steel Pipe for High-Temperature Service*, in *TABLE 2 Heat Treatment Requirements*. 2015, ASTM International: West Conshohocken, PA.
16. Tokunaga, T., K. Hasegawa, and F. Masuyama, *Phase transformation behavior of Grade 91 ferritic steel.* Materials Science and Engineering: A, 2009. **510–511**: p. 158-161.
17. EPRI, *Service Experience with Grade 91 Components*. 2009.
18. Cohn, M., J. Henry, and D. Nass. *Fabrication, Construction and Operation Problems for Grade 91 Fossil Power Components*. in *ASME/JSME 2004 Pressure Vessels and Piping Conference*. 2004. California: ASME
19. Alstom. *Indoctrination for the Fabrication and Assembly of Grade 91 Material and Hardness Testing Rev. 2.* in *International Workshop on Fabrication and Processing of Grade 91 Material*. 2011. India.
20. Dickinson, S.J., et al., *The Development of a Multifrequency Electromagnetic Instrument for Monitoring the Phase Transformation of Hot Strip Steel.* IEEE Transactions on Instrumentation and Measurement, 2007. **56**(3): p. 879-886.
21. Karimian, N., et al., *Differential permeability behaviour of P9 and T22 power station steels.* Journal of Magnetism and Magnetic Materials, 2014. **352**: p. 81-90.
22. Papaelias, M.P., et al., *Effect of microstructural variations on smart inductive sensor measurements of phase transformation in steel.* Scripta Materialia, 2004. **51**(5): p. 379-383.
23. Liu, J., et al., *Electromagnetic evaluation of the microstructure of Grade 91 tubes/pipes.* International Journal of Pressure Vessels and Piping, 2015. **132–133**: p. 65-71.
24. Zhu, W., et al., *Evaluation of rail decarburisation depth using a H-shaped electromagnetic sensor.* Ndt & E International, 2012. **46**: p. 63-69.
25. Yin, W., et al., *Exploring the relationship between ferrite fraction and morphology and the electromagnetic properties of steel.* Journal of Materials Science, 2007. **42**(16): p. 6854-6861.
26. Davis, C., S. Dickinson, and A. Peyton, *Impedance spectroscopy for remote analysis of steel microstructures.* Ironmaking and Steelmaking, 2005. **32**(5): p. 381-384.

27. Liu, J., et al., *Measurement of microstructure changes in 9Cr–1Mo and 2.25Cr–1Mo steels using an electromagnetic sensor.* Scripta Materialia, 2012. **66**(6): p. 367-370.
28. Yin, W., et al., *Measurement of permeability and ferrite/austenite phase fraction using a multi-frequency electromagnetic sensor.* Ndt & E International, 2009. **42**(1): p. 64-68.
29. Zhu, W., et al., *Modelling and experimental study of an electromagnetic sensor with an H-shaped ferrite core used for monitoring the hot transformation of steel in an industrial environment.* Ndt & E International, 2011. **44**(7): p. 547-552.
30. Yin, W., et al., *Measurement of electromagnetic properties of power station steels.* Ndt & E International, 2012. **51**: p. 135-141.
31. Calderon, F. and J.O.N. Stern, *Better Growth Better Economy: The New Climate Economy Synthesis Report*. 2014: Washington.
32. Hoel, M. and S. Kverndokk, *Depletion of fossil fuels and the impacts of global warming.* Resource and Energy Economics, 1996. **18**(2): p. 115-136.
33. Kverndokk, B.H.S., *Global, Regional and National Carbon Dioxide Emissions 1949-1986*. 1989, Centre for Research in Economics and Business Administration: SNF-Oslo. p. 141-194.
34. Marcucci, A. and P. Fragkos, *Drivers of regional decarbonization through 2100: A multi-model decomposition analysis.* Energy Economics, 2015. **51**: p. 111-124.
35. Pfenninger, S. and J. Keirstead, *Renewables, nuclear, or fossil fuels? Scenarios for Great Britain's power system considering costs, emissions and energy security.* Applied Energy, 2015. **152**: p. 83-93.
36. DECC, *Planning our electric future: a White Paper for secure, affordable and low-carbon electricity*. 2011, TSO: UK.
37. Yoshizawa, M., et al., *Effect of precipitates on long-term creep deformation properties of P92 and P122 type advanced ferritic steels for USC power plants.* Materials Science and Engineering: A, 2009. **510–511**(0): p. 162-168.
38. Ennis, P.J. and A. Czyrska-Filemonowicz, *Recent advances in creep-resistant steels for power plant applications.* Sadhana-Academy Proceedings in Engineering Sciences, 2003. **28**: p. 709-730.
39. Sarver, J.M. and J.M. Tanzosh. *An Evaluation of The Steamside Oxidation of Candidate USC Materials at 650 °C and 800 °C* in *Advances in Materials Technology for Fossil Power Plants*. 2004. South Carolina: ASM International.

40. Potirniche, G., *Predicition and Monitoring Systems of Creep-Fracture Behavior of 9Cr-1Mo Steels for Reactor Pressure Vessels*. 2013, University of Idaho.
41. Di Gianfrancesco, A., *1 - The fossil fuel power plants technology*, in *Materials for Ultra-Supercritical and Advanced Ultra-Supercritical Power Plants*. 2017, Woodhead Publishing. p. 1-49.
42. Masuyama, F., *History of Power Plants and Progress in Heat Resistant Steels.* ISIJ International, 2001. **41**(6): p. 612-625.
43. Viswanathan, R., K. Coleman, and U. Rao, *Materials for ultra-supercritical coal-fired power plant boilers.* International Journal of Pressure Vessels and Piping, 2006. **83**(11-12): p. 778-783.
44. Tabuchi, M., H. Hongo, and F. Abe, *CREEP STRENGTH OF DISSIMILAR WELD USING HIGH B-9CR STEEL FOR A-USC BOILER*. Proceedings of the Asme Pressure Vessels and Piping Conference - 2013, Vol 6a: Materials and Fabrication, ed. D.J. Shim and D. Rudland. 2014, New York: Amer Soc Mechanical Engineers.
45. Dettmer, R., *Coal - the right stuff?* Energize, 2005: p. 50-51.
46. Ehlers, J., et al., *Enhanced oxidation of the 9%Cr steel P91 in water vapour containing environments.* Corrosion Science, 2006. **48**(11): p. 3428-3454.
47. Wu, Q., et al. *Microstructure Characterisation of Advanced Boiler Materials for Ultra Supercritical Coal Power PLants*. in *Advances in Materials Technology for Fossil Power Plants*. 2005. South Carolina: ASM International
48. Nippon. *Nippon Steel & Sumitomo Metal: Seamless Steel Tubes and Pipes for Boilers*. 2015 [cited 2016 09/01/2016]; Available from: https://www.nssmc.com/product/catalog_download/pdf/P008en.pdf.
49. Khanna, A.S., *Introduction to High Temperature Oxidation and Corrosion*. 2002, ASM International: Ohio.
50. Llewellyn, D.T. and R.C. Hudd, *Steels Metallurgy and Applications*. Third ed. 1998, Oxford: Butterworth-Heinemann.
51. Fry, A., S. Osgerby, and M. Wright, *Oxidation of Alloys in Steam Environments*. 2002, NPL.
52. Igarashi, M., et al. *Advances in Materials Technology for A-USC Power Plant Boilers*. in *Advances in Materials Technology for Fossil Power Plants*. 2010. New Mexico: Sumitomo Metals Industries Ltd.
53. Maskell, R., *Advanced PF Power Plant - Improved Materials for Boilers and Steam Turbines*. 2005: UK.

54. Cui, S., et al., *Improvement of Stress-rupture Life for Modified-HR6W Austenitic Stainless Steel.* Journal of Materials Science & Technology, 2011. **27**(11): p. 1059-1064.
55. Orr, J., L.W. Buchanan, and H. Everson. *The Commerical Development and Evaluation of E911, A Strong 9% CrMoNbVWN Steel for Boiler Tubes and Headers*. in *Advanced Heat Resistant Steels for Power Generation*. 1998. San Sebastian, Spain: The Institute of Materials.
56. Ennis, P.J., *Ferritic and Martensitic Steels for Power Plants*, in *Structural Alloys for Power Plants: Operational Challenges and High-Temperature Materials*, A. Shirzadi and S. Jackson, Editors. 2014, Elsevier. p. 188-220.
57. Takahashi, Y., *Study on creep-fatigue evaluation procedures for high-chromium steels—Part I: Test results and life prediction based on measured stress relaxation.* International Journal of Pressure Vessels and Piping, 2008. **85**(6): p. 406-422.
58. Kumar, H., et al., *Evaluation of tempering behaviour in modified 9Cr–1Mo steel by magnetic non-destructive techniques.* Journal of Materials Processing Technology, 2010. **210**(4): p. 669-674.
59. Anderson, R., *Special workshop explores P91/T91 issues, impending ASME Code changes.* Combined Cycle 2005(Third Quarter): p. 3.
60. Ryu, S.H., et al. *The Fracture Behaviours of the Welded Joints in P92, P122 and P23 Pipe Steels for Fossil Power Plans*. in *Advances in Materials Technology for Fossil Power Plants*. 2004. South Carolina: ASM International.
61. Santella, M.L., et al. *Martensite formation in 9Cr-1Mo steel weld metal and its effect on creep behaviour*. in *Proceedings of the EPRI Conference on 9Cr materials fabrication and joining technologies*. 2001. Myrtle Beach, CA.
62. Viswanathan, R., *Damage Mechanisms and Life Assessment of High-Temperature Components*. 1989, Ohio: ASM International.
63. Choudhary, B.K., et al., *Elevated temperature tensile properties of P9 steel towards ferritic steel wrapper development for sodium cooled fast reactors.* Journal of Nuclear Materials, 2013. **443**(1–3): p. 242-249.
64. Scarlin, B., T.-U. Kern, and M. Staubli. *The European Efforts in Material Development for 650 °C USC Power Plants - COST522*. in *Proceedings from the Fourth International Conference on Advances in Materials Technology for Fossil Power Plants*. 2004. South Carolina: ASM International.

65. ASTM, *Standard Specification for Seamless Ferritic and Austenitic Alloy-Steel Boiler, Superheater and Heat-Exchanger Tubes*. 2015, ASTM International: West Conshohocken, PA.
66. Sato, T., et al. *The Practical Application and Long-Term Experience of New Heat Resistant Steels to LArge Scale USC Boilers*. in *Proceedings from the Fourth International Conference on Advances in Materials Technology for Fossil power PLants*. 2004. South Carolina: ASM International.
67. Nutting, J. and R. Viswanathan, eds. *Advanced Heat Resistant Steel for Power Generation*. 1998, University Press Cambridge.
68. Ennis, P.J. *Creep Strengthening mechanisms in 9-12% Chromium Steels*. in *Proceedings from the Fourth International Conference on Advances in Materials Technology for Fossil Power Plants*. 2004. South Carolina: ASM International.
69. Czyrska-Filemonowicz, A., A. Zieliska-Lipiec, and P.J. Ennis, *Modified 9% Cr steels for advanced power generation: microstructure and properties.* Journal of Achievements in Materials and Manufacturing Engineering, 2006.
70. Orr, J. and L. Woollard, *The Development of 9% CrMo Steels from Steel 91 to E911*. Microstructural Development and and Stability in High Chromium Ferritic Power Plant Steels, ed. A. Strang and D.J. Gooch. Vol. 1. 1997, London: The Institute of Materials.
71. Kishore, R., et al., *The morphology and ageing behaviour of δ-ferrite in a modified 9Cr-1Mo steel.* Journal of Nuclear Materials, 1992. **195**(1–2): p. 198-204.
72. Watson, C., *Modelling high integrity steel forgings for turbine applications in the power generation industry*, in *Metallurgy and Materials*. 2015, University of Birmingham.
73. Abe, F., *Precipitate design for creep strengthening of 9% Cr tempered martensitic steel for ultra-supercritical power plants.* Science and Technology of Advanced Materials, 2008. **9**: p. 15.
74. Tenaris. *Introduction to P91/T91 Material*. in *International Workshop on Fabrication and Processing of Grade 91 Material*. 2011. India.
75. King, J.F., et al., *Weldability of Modified 9Cr-1Mo Steel*. 1986: Oak Ridge National Laboratory.
76. Xia, Z.-X., et al., *Laves Phase Formation and Its Effect on Mechanical Properties in P91 Steel.* Acta Metallurgica Sinica (English Letters), 2015. **28**(10): p. 1238-1246.

77. Callister, W.D. and D.G. Rethwisch, *Materials Science and Engineering*. 8th ed. 2011: John Wiley & Sons.
78. Vallourec&MannesmannTubes, *The T91/P91 Book*. 2nd ed, ed. K.V. Haarmaan, J.C. Vandenberghe, B. 2002.
79. Shrestha, T., et al., *Creep rupture behavior of Grade 91 steel.* Materials Science and Engineering: A, 2013. **565**: p. 382-391.
80. Shrestha, T., et al., *Effect of Heat Treatment on Microstructure and Hardness of Grade 91 Steel.* Metals, 2015. **5**(1): p. 131-149.
81. Sanchez-Hanton, J.J. and R.C. Thomson, *Characterization of isothermally aged Grade 91 (9Cr–1Mo–Nb–V) steel by electron backscatter diffraction.* Materials Science and Engineering: A, 2007. **460–461**(0): p. 261-267.
82. Cerri, E., et al., *Evolution of microstructure in a modified 9Cr–1Mo steel during short term creep.* Materials Science and Engineering: A, 1998. **245**(2): p. 285-292.
83. Callister, W.D., *Fundamentals of Materials Science and Engineering: An Integrated Approach*. Second ed. 2005, New Jersey: John Wiley & Sons Inc.
84. Huysmans, S. and J. Vekeman, *Challenging weld repair of grade 91 tubing by avoiding PWHT.* Energy Materials, 2009. **4**(2): p. 76-83.
85. Roberts, S., *5 - Martensitic steels for cast components in ultra-supercritical power plants A2 - Gianfrancesco, Augusto Di*, in *Materials for Ultra-Supercritical and Advanced Ultra-Supercritical Power Plants*. 2017, Woodhead Publishing. p. 121-141.
86. Parker, J., et al., *Guidelines and Specifications for High-Reliability Fossil Power Plants - Best Practice Guideline for Manufacturing and Construction of Grade 91 Steel Components* 2011, EPRI: Palo Alto, CA.
87. Irvine, K.J., M.A. Crowe, and F.B. Pickering, *The Physical Metallurgy of 12% Chromium Steels.* Journal of The Iron and Steel Institute, 1960. **195**: p. 386 - 405.
88. Inskip, N. *The Risk of Material Failure*. 2012 [cited 2017 31/07/17]; Available from: https://www.hera.org.nz/Story?Action=View&Story_id=1667
89. Brett, C., *Personal Communication*. 2012.
90. Kilburn, J. and R. Swanekamp, *Maintenance Workshop Tackles the Challenges of P91/T91 and HRSG Layup*, in *Power Engineering*. 2004, PennWell Energy Group: U.S.
91. Degnan, C., *Personal Communication*. 2014: EON.

92. Shibli, A., *Inspecting Aberrant P91 Components for Integrity*, in *Power*. 2014, Electric Power.
93. Henry, J.F., *Growing experience with P91/T91 forcing essential code changes.* Combined Cycle Journal, 2005.
94. Hao, X.J., et al., *Characterization of Decarburization of Steels Using a Multifrequency Electromagnetic Sensor: Experiment and Modeling.* Metallurgical and Materials Transactions a-Physical Metallurgy and Materials Science, 2009. **40A**(4): p. 745-756.
95. Stupakov, O., et al., *Evaluation of surface decarburization depth by magnetic Barkhausen noise technique.* Journal of Magnetism and Magnetic Materials, 2011. **323**: p. 1692-1697.
96. Siefert, J.A. and J.D. Parker, *Evaluation of the Creep Cavitation Behavior in Grade 91 Steels.* International Journal of Pressure Vessels and Piping.
97. Caminada, S., et al. *Long Term Creep Behaviour and Microstructural Evolution of ASTM Grade 91 Steel*. in *Proceedings from the Fourth International Conference on Advances in Materials Technology for Fossil Power Plants*. 2004. South Carolina, USA: ASM International.
98. Zielińska-Lipiec, A., et al., *The influence of heat treatments on the microstructure of 9% chromium steels containing tungsten.* Journal of Materials Processing Technology, 1997. **64**(1–3): p. 397-405.
99. Zielinska-Lipiec, A., et al., *The evolution of the microstructure of the 9% chromium steel P92 during thermal ageing and creep exposure*, in *Modelling of Microstructural Evolution in Creep Resistant Materials*, A. Strang and M. McLean, Editors. 1999, Iom Communications Ltd: London. p. 79-89.
100. Parker, J. *Practical Experience with Advanced Steels*. in *Proceedings from the Fourth International Conference on Advances in Materials Technology for Fossil Power Plants*. 2004. South Carolina, USA: ASM International.
101. Zurek, J., et al. *Oxidation behaviour of ferritic and austenitic steels in simulated steam environments*. in *Proceedings from the Fourth International Conference on Advances in Materials Technology for Fossil Power Plants*. 2004. South Carolina, US: ASM International.
102. Choudhary, B.K., et al., *On the Reliability Assessment of Creep Life for Grade 91 Steel.* Procedia Engineering, 2014. **86**: p. 335-341.
103. IAEA, *Non-destructive Testing for Plant Life Assessment*. 2005, Vienna.

104. Raj, B., et al., *Assessment of microstructure and mechanical behaviour of metallic materials through non-destructive characterisation.* International Materials Review, 2003. **48**(5): p. 273-325.
105. Shackelford, J., *Introduction to Materials Science for Engineers*. 5th ed. 2000, New Jersey Prentice Hall.
106. Salgado-Lopez, J.M., *In situ metallography as non-destructive test to analyse the microstructural damage in the petrochemical industry*, in *5th Pan American Conference for NDT*. 2011: Cancun, Mexico.
107. Sposito, G., et al., *A review of non-destructive techniques for the detection of creep damage in power plant steels.* NDT&E International, 2010. **43**: p. 555-567.
108. Marder, A.R., *Replication Microscopy Techniques for NDE*. Vol. 17. 1989. 52-56.
109. Salonen, J., et al., *Experience on in-service damage in power plant components.* Engineering Failure Analysis, 2007. **14**(6): p. 970-977.
110. Artamonov, V.V. and V.P. Artamonov, *Nondestructive Examination of Metal Microstructure in Thermal Power Generating Facilities.* Russian Journal of Nondestructive Testing, 2002. **38**(2): p. 105-112.
111. Kan, D., *Analysis of Metal Microstructure in Components of Power Plants without Cutting off Samples.* Energetik, 1968(1): p. 32-33.
112. Gilman, J., *Chemistry and Physics of Mechanical Hardness*. 2009, New Jersey: John Wiley & Sons.
113. Pavlina, E.J. and C.J. Van Tyne, *Correlation of Yield Strength and Tensile Strength with Hardness in Steels.* Journal of Materials Engineering and Performance, 2008. **17**(6): p. 888-893.
114. Aplin, P.F., *CLASSIFICATION AND SELECTION OF PORTABLE HARDNESS-TESTING EQUIPMENT A2 - Boogaard, J*, in *Non-Destructive Testing*, G.M.v. Dijk, Editor. 1989, Elsevier: Oxford. p. 683-688.
115. NASRUL. *Hardness Testing*. 2013 [cited 2016 24th February]; Available from: http://nasruldesign.weebly.com/ndt---brief-overview.html.
116. England, G. *Vickers Hardness Test*. n.d. [cited 2012 29th August]; Available from: http://www.gordonengland.co.uk/hardness/vickers.htm
117. Masuyama, F., *Creep degradation in welds of Mod.9Cr-1Mo steel.* International Journal of Pressure Vessels and Piping, 2006. **83**(11–12): p. 819-825.

118. Blitz, J. and G. Simpson, *Ultrasonic Methods of Non-destructive Testing*. 1 ed. Non-Destructive Evaluation, ed. S. Palmer and W. Lord. 1996, London: Chapman & Hall.
119. Mix, P., *Introduction to Nondestructive testing: A training guide*. 1987, New York: John Wiley & Sons.
120. Freitas, V.L.d.A., et al., *Nondestructive characterization of microstructures and determination of elastic properties in plain carbon steel using ultrasonic measurements.* Materials Science and Engineering: A, 2010. **527**(16–17): p. 4431-4437.
121. Gür, C.H. and B.O. Tuncer, *Characterization of microstructural phases of steels by sound velocity measurement.* Materials Characterization, 2005. **55**(2): p. 160-166.
122. Papaelias, M., *Detection and Measurement of Phase Transformation in Steel using Electromagnetic Sensors*, in *Department of Metallurgy and Materials Science*. 2004, University of Birmingham.
123. Morgan, B.C. and R. Tilley, *Inspection of power plant headers utilizing acoustic emission monitoring.* Ndt & E International, 1999. **32**(3): p. 167-175.
124. Tonolini, F., A. Sala, and G. Villa, *General review of developments in Acoustic Emission methods.* International Journal of Pressure Vessels and Piping, 1987. **28**(1–5): p. 179-201.
125. Runow, P., *The use of acoustic emission methods as aids to the structural integrity assessment of nuclear power plants.* International Journal of Pressure Vessels and Piping, 1985. **21**(3): p. 157-207.
126. Hutton, P.H., *An overview of development and application of acoustic emission methods in the United States.* Nuclear Engineering and Design, 1989. **113**(1): p. 59-69.
127. You, Y., et al., *The effect of hydrogen on the deformation mechanisms of 2.25Cr–1Mo low alloy steel revealed by acoustic emission.* Materials Science and Engineering: A, 2016. **655**: p. 277-282.
128. Allevato, C., *Utilizing acoustic emission testing to detect high-temperature hydrogen attack (HTHA) in Cr-Mo reformer reactors and piping during thermal gradients.* Procedia Engineering, 2011. **10**: p. 3552-3560.
129. Johnson, J.A., et al., *High-Temperature Acoustic Emission Sensing Tests Using a Yttrium Calcium Oxyborate Sensor.* IEEE Transactions on Ultrasonics, Ferroelectrics and Frequency Control, 2014. **61**(5): p. 805-814.

130. Ramos, H.G. and A.L. Ribeiro, *Present and Future Impact of Magnetic Sensors in NDE.* Procedia Engineering, 2014. **86**: p. 406-419.
131. Blitz, J., *Electrical and Magnetic Methods of Non-destructive Testing*. 2nd ed. Non-Destructive Evaluation, ed. S. Palmer and W. Lord. 1997, London: Chapman & Hall.
132. Singh, W.S., et al., *Development of magnetic flux leakage technique for examination of steam generator tubes of prototype fast breeder reactor.* Annals of Nuclear Energy, 2015. **83**: p. 57-64.
133. Hodgson, M., *Comparison of Visual, Eddy Current, Ultrasonic and Magnetic Particle Testing Techniques for Boiler Tube Inspections.* MAterials Evaluation, 2012. **70**(5): p. 508-519.
134. Cartz, L., *Nondestructive Testing: Radiography, Ultrasonics, Liquid penetrant, Magnetic Particle, Eddy Current*. 1995, Ohio: ASM International.
135. Davis, C., M. Strangwood, and A. Peyton, *Overview of non-destructive evalution of steel microstructures using multifrequency electronmagnetic sensors.* Ironmaking and Steelmaking, 2011. **38**(7): p. 510-517.
136. Jiles, D.C., *Magnetic properties and microstructure of AISI 1000 series carbon steels.* NDT International, 1989. **22**(1): p. 56.
137. Wilson, J.W., et al., *Measurement of the magnetic properties of P9 and T22 steel taken from service in power station.* Journal of Magnetism and Magnetic Materials, 2014. **360**: p. 52-58.
138. Das, S.K., A. Joarder, and A. Mitra, *Magnetic Barkhausen emissions and microstructural degradation study in 1.25 Cr–0.50 Mo steel during high temperature exposure.* Ndt & E International, 2004. **37**(3): p. 243-248.
139. Ghanei, S., M. Kashefi, and M. Mazinani, *Comparative study of eddy current and Barkhausen noise nondestructive testing methods in microstructural examination of ferrite–martensite dual-phase steel.* Journal of Magnetism and Magnetic Materials, 2014. **356**: p. 103-110.
140. Ranjan, R., D.C. Jiles, and P.K. Rastogi, *Magnetic Properties of Decarburized Steels: An Investigation of the Effects of Grain Size and Carbon Content.* IEEE Transactions on Magnetics, 1987. **23**(3): p. 1869-1876.
141. Hao, X.J., et al., *Off-line measurement of decarburization of steels using a multifrequency electromagnetic sensor.* Scripta Materialia, 2008. **58**(11): p. 1033-1036.

142. Govindaraju, M.R., et al., *Nondestructive evaluation of creep damage in power-plant steam generators and piping by magnetic measurements.* Ndt & E International, 1997. **30**(1): p. 11-17.
143. Mitra, A., et al., *Magnetic evaluation of creep in modified 9Cr–1Mo steel.* Scripta Materialia, 2007. **57**(9): p. 813-816.
144. Mohapatra, J.N., et al., *Ageing behavior study of 5Cr–0.5Mo steel by magnetic Barkhausen emissions and magnetic hysteresis loop techniques.* Ndt & E International, 2007. **40**(2): p. 173-178.
145. Hyperphysics. *Bar magnet and solenoid*. [cited 2016 19th March]; Available from: http://hyperphysics.phy-astr.gsu.edu/hbase/magnetic/elemag.html.
146. Jiles, D., *Introduction to magnetism and magnetic materials*. 1991, London: Chapman & Hall.
147. *Self inductance and Inductive Reactance*. NDT Resource Center; Available from: https://www.nde-ed.org/EducationResources/CommunityCollege/EddyCurrents/Physics/selfinductance.htm.
148. Spaldin, N., *Magnetic Materials: Fundamentals and Device Applications*. 2003, United Kingdom: Cambridge University Press.
149. Yardley, V.A., *Magnetic Detection of Microstructural Change in Power Plant Steels*, in *Emmanuel College*. 2003, Cambridge.
150. Hubert, A. and R. Schafer, *Magnetic Domains The Analysis of Magnetic Microstructures*. 1998, Berlin: Springer Link.
151. Baldwin Jr, J.A., P.W. Smith Jr, and F. Milstein, *Influence of deformation upon domain wall pinning defect spectrum in 50-50 NiFe.* Solid State Communications, 1975. **17**(8): p. 973-974.
152. Beale, A.D., et al., *TEM studies of domains and micromagnetic processes in structural steels.* Journal of Magnetism and Magnetic Materials, 1992. **104–107, Part 1**: p. 365-367.
153. Dobmann, G., N. Meyendorf, and E. Schneider, *Nondestructive characterization of materials A growing demand for describing damage and service-life-relevant aging processes in plant components.* Nuclear Engineering and Design, 1997. **171**(1–3): p. 95-112.
154. *NDT Resource Center - AE Barkhausen Techniques*. 2016 [cited 2016 28 April]; Available from: https://www.nde-

ed.org/EducationResources/CommunityCollege/Other%20Methods/AE/AE_BarkhausenTechniques.php.

155. Jiles, D.C., *The effect of stress on magnetic Barkhausen activity in ferromagnetic steels : IEEE Transactions on Magnetics, Vol. 25, No. 5, pp. 3455–3457 (Sep. 1989).* Ndt & E International, 1991. **24**(1): p. 41.
156. Ranjan, R., et al., *Grain size measurement using magnetic and acoustic Barkhausen noise : Journal of Applied Physics, Vol. 61, No. 8, pp. 3199–3201 (15 Apr. 1987).* Ndt & E International, 1991. **24**(1): p. 48.
157. Kypris, O., I.C. Nlebedim, and D.C. Jiles, *Measuring stress variation with depth using Barkhausen signals.* Journal of Magnetism and Magnetic Materials, 2016. **407**: p. 377-395.
158. Jiles, D.C., *Dynamics of domain magnetization and the Barkhausen effect.* Czechoslovak journal of physics, 2000. **50**(8): p. 893-988.
159. Moorthy, V., et al., *Evaluation of microstructures in 2.25Cr-1Mo and 9Cr-1Mo steel weldments using magnetic Barkhausen noise.* Materials Science and Engineering: A, 1997. **231**(1–2): p. 98-104.
160. Liu, T., et al., *Comprehensive analysis of Barkhausen noise properties in the cold rolled mild steel.* Journal of Magnetism and Magnetic Materials, 2007. **310**(2, Part 3): p. e989-e991.
161. Błachnio, J., J. Dutkiewicz, and A. Salamon, *The effect of cyclic deformation in a 13% Cr ferritic steel on structure and Barkhausen noise level.* Materials Science and Engineering: A, 2002. **323**(1–2): p. 83-90.
162. Bhattacharyya, D.K., S. Vaidyanathan, and V. Moorthy. *Magnetic Barkhausen Noise analysis for the assessment of microstructures in heat treated 2.25Cr - 1Mo and 17-4 PH steels*. in *Proceedings of the 13th World Conference on Non-Destructive Testing*. 1992. Sao Paulo, Brazil: Elsevier.
163. Saquet, O., J. Chicois, and A. Vincent, *Barkhausen noise from plain carbon steels: analysis of the influence of microstructure.* Materials Science and Engineering: A, 1999. **269**(1–2): p. 73-82.
164. Ranjan, R., *Microstructural characterization of ferromagnetic materials using magnetic NDE techniques.* Ndt & E International, 1996. **29**(5): p. 345.
165. Brett, C. *NDT at 565 °C*. in *British Institute of NDT Condition Monitoring Conference*. 2015. Oxford.

166. Altpeter, I., R. Tschuncky, and K. Szielasko, *8 - Electromagnetic techniques for materials characterization*, in *Materials Characterization Using Nondestructive Evaluation (NDE) Methods*. 2016, Woodhead Publishing. p. 225-262.
167. Volkers, R., *The influence of dislocations on magnetic properties in steel*, in *Materials Science and Engineering*. 2008, Delft University of Technology: Netherlands.
168. Pal'a, J., et al., *Mangetic behaviour of low-carbon steel in parallel and perpendicular directions to tensile deformation.* Journal of Magnetism and Magnetic Materials, 2007. **310**: p. 57-62.
169. Stupakov, O., et al., *Investigation of magnetic response to plastic deformation of low-carbon steel.* Materials Science and Engineering: A, 2007. **462**(1–2): p. 351-354.
170. Chen, Z.J., et al., *Assessment of creep damage of ferromagnetic material using magnetic inspection.* IEEE Transactions on Magnetics, 1994. **30**(6): p. 4326-4328.
171. O'Sullivan, D., M. Cotterell, and I. Meszaros, *The characterisation of work-hardened austenitic stainless steel by NDT micro-magnetic techniques.* NDT&E International, 2004. **37**: p. 265-269.
172. Swartzendruber, L.J., et al., *Effect of plastic strain on magnetic and mechanical properties of ultralow carbon sheet steel.* Journal of Applied Physics, 1997. **81**(8): p. 4263-4265.
173. Iordache, V.E. and E. Hug, *Effect of Mechanical Strains on the Magnetic Properties of Electrical Steels.* Journal of Optoelectronics and Advanced Materials 2004. **6**(4): p. 1297-1303.
174. Garcia-Martin, J., J. Gomez-Gil, and E. Vazquez-Sanchez, *Non-Destructive Techniques Based on Eddy Current Testing.* Sensors, 2011. **11**(3): p. 2525-2565.
175. Ward, C., *Novel NDE Techniques in the Power Generation Industry*, in *Engineering*. 2010, University of Nottingham: Nottingham.
176. Zhou, L., *Non-destructive characterisation of steel microstructures using electromagnetic sensors*, in *Metallurgy and Materials*. 2014, Birmingham.
177. Zhou, L., et al., *The role of microstructure such as phase balance and pearlite lamellar spacing to EM sensor signal*, in *International conference on NDE of steel*. 2011: Jamshedpur, India. p. 208-215.

178. Peyton, A.J., et al., *Monitoring microstructure changes in rod online by using induction spectroscopy.* Ironmaking & Steelmaking, 2010. **37**(2): p. 135-139.
179. Haldane, R.J., et al., *Multi-frequency electromagnetic sensor measurement of ferrite/austenite phase fraction—Experiment and theory.* Scripta Materialia, 2006. **54**(10): p. 1761-1765.
180. Hao, X.J., et al., *Modelling the electromagnetic response of two-phase steel microstructures.* NDT & E International, 2010. **43**(4): p. 305-315.
181. Zhou, L., et al., *Quantification of the phase fraction in steel using an electromagnetic sensor.* Ndt & E International, 2014. **67**: p. 31-35.
182. Libby, H.L., *Introduction to Electromagnetic Nondestructive Test Methods*. 1971, USA: John Wiley & Sons, Inc.
183. Vorst, A.V., A. Rosen, and Y. Kotsuka, *RF/Microwave Interaction with Biological Tissues*. 2006: John Wiley & Sons.
184. Wei, L., et al., *Analysis of the lift-off effect of a U-shaped ACFM system.* Ndt & E International, 2013. **53**: p. 31-35.
185. Papaelias, M.P., et al., *Measurement and Modelling of the Electromagnetic to Phase Transformations in Steels.* METALLURGICAL AND MATERIALS TRANSACTIONS A, 2004. **35A**: p. 965-972.
186. Standardization, I.O.f., *Steels -- Determination of depth of decarburization*. 2003, ISO: Geneva, Switzerland.
187. Yin, W., et al., *Measurement of decarburisation of steel rods with an electromagnetic sensor using an analytical model.* Ndt & E International, 2010. **43**(8): p. 667-670.
188. Zhou, H., *EM Sensor Measurement of Degradation in Steels*, in *Metallurgy and Materials Science*. 2014, University of BIrmingham: UK.
189. Davis, C.L., et al., *Measurement of phase transformation in steels using electromagnetic sensors.* Ironmaking & Steelmaking, 2002. **29**(6): p. 469-476.
190. Yang, H., et al., *In-line Quantitative Measurement of Transformed Phase Fraction by EM Sensors during Controlled Cooling on the Run-Out Table of a Hot Strip Mill*, in *19th World Conference on Non-Destructive Testing*. 2016, WCNDT: Munich, Germany.
191. Streurs. *High Performance Motor*. 2017; Available from: http://www.struers.com/en-GB/Products/Grinding-and-Polishing/Grinding-and-polishing-equipment/Semi-automatic-grinding-and-polishing/TransPol#transpol-features.

192. Marghalani, H.Y., *Effect of filler particles on surface roughness of experimental composite series.* Journal of Applied Oral Science, 2010. **18**: p. 59-67.
193. Hall, R., *Measurement of Recovery and Recrystallation in Interstitial Free Steels Using Electromagnetic Sensors*. 2016, University of Birmingham.
194. Bain, R., *Engineering Safety Newsletter*, in *Safety Lines*. 2007, Department of Labour: Wellington, NZ.
195. Brett, S.J. *The Practical Application of Small Scale Sampling and Impression Creep Testing to Grade 91 Components*. in *Advances in Materials Technology for Fossil Power Plants Proceedings from the 7th Internal Conference*. 2013. Hawaii, USA: ASM International.
196. Totemeier, T.C. and I.J. Perrin. *Effect of Tempering on Microstructure and Properties of Grade 91 Steel*. in *6th International Conference on Advances in Materials Technology for Fossil Power Plants*. 2010. Santa Fe, New Mexico: ASM International
197. EPRI, *Effect of Normalization and Temper and Temper Heat Treatment on P91 Weldment Properties*. 2003: Palo Alto, CA.
198. Shibli, A., *Aberrant P91 and development of inspection and life assessment technologies and methodologies*, in *International conference on experience with the manufacture, welding, quality Control and use of T / P91-92, T / P23-24 steels* 2016: Wuhan, China.
199. Liu, J., et al., *Non-destructive characterisation of N/Al level in P91 steels using electromagnetic sensors.* Materials Science and Technology, 2015. **31**(9): p. 1042-1050.
200. Allen, D.J. and S.J. Turnbull, *Tapada Do Outerio: Metallurgical investigation of P91 steel components*. 1998, EON (PowerGen).
201. *The effect of surface roughness on ultrasonic backscatter monitoring of intrinsic (subsurface) structure: 37082 Bridge, B.; Bollini, G.J. British Journal of Nondestructive Testing, Vol. 29, No. 4, pp. 228–237 (Jul. 1987).* Ndt & E International, 1993. **26**(5): p. 271.
202. Kalyanasundaram, K. and P.B. Nagy, *A simple numerical model of the apparent loss of eddy current conductivity due to surface roughness.* Ndt & E International, 2004. **37**(1): p. 47-56.
203. EON, *Technical Operation Instruction: Ultrasonic Inspection* 2014.

204. Bainbridge, H., *Best Practise for the Procurement and Conduct of Non-Destructive Testing*, in *Part 2: Magnetic Particle and Dye Penetrant Inspection*. 2002, HSE.
205. Brett, C., *Personal Communication*. 2017: EON.
206. Li, J., et al., *Measurement of lift-off using the relative variation of magnetic flux in pulsed eddy current testing.* Ndt & E International, 2015. **75**: p. 57-64.
207. Zhu, W., et al., *Modeling and experimental study of a multi-frequency electromagnetic sensor system for rail decarburisation measurement.* Ndt & E International, 2017. **86**: p. 1-6.
208. Allen, D.J., *Manufacturing Quality of P91 Steel: In-situ Hardness testing - A Review of Recent Experience and Its Implications*. 2002.
209. Haruyama, H., et al. *Effect of shot peening and pre-oxidation treatment in air on steam oxidation resistance of Mod.9Cr-1Mo steel*. in *Advances in Materials Technology for Fossil Power Plants*. 2004. South Carolina, US: ASM International.
210. Zhou, H., *Effect of stress on relative permeability and EM sensor measurements*, in *Metallurgy and Materials Science*. 2012, University of Birmingham: Birmingham.
211. Tosha, K., et al. *Shot Peening and Grit Blasting - Effects on Surface Integrity*. in *International Scientific Committee for Shot Peening*. 2005. Paris, France: shotpeener.com.
212. Stupakov, O. and I. Tomáš, *Hysteresis minor loop analysis of plastically deformed low-carbon steel.* Ndt & E International, 2006. **39**(7): p. 554-561.
213. Chander, K.P., et al., *Effect of grit blasting on surface properties of steel substrates.* Materials & Design, 2009. **30**: p. 2896-2902.

APPENDIX A

THE EFFECT OF TIME AND TEMPERATURE ON THE TEMPERING OF GRADE 91 ALLOY STEEL

prepared for

DR CRAIG DEGNAN, MATERIALS ENGINEER

by N.S. Kahlon

SUMMARY

As part of an Engineering Doctorate being studied at the University of Birmingham sponsored by E.ON Technologies (Ratcliffe) Limited (ETG) the effect of tempering time and temperature on Grade 91 alloy steel was investigated, the results of which are valuable to the materials team at ETG.

The virtuous properties of Grade 91 material are heavily reliant on ascertaining a specific tempered martensitic microstructure which is dependent on the heat treatments performed to produce it. Mis-heat treated Grade 91 components have previously been known to arrive at E.ON to be installed on plant. Quality assurance testing has previous led to the exposure of such aberrant components, which have been traced back to their mis-heat treatments. For the purpose of expanding the knowledge on how tempering heat treatments can affect the production of this specific microstructure in-house tests were performed. The present report provides a summary of the experimental investigation.

CONCLUSIONS

1. An increase in both the temperature and time of the tempering heat treatment will cause the P91 material to soften

2. Between the ranges of parameters tested mis-tempering due to temperature has a more significant effect on the hardness of the material than mis-tempering due to time.

3. At 760 °C over-tempering beyond 3 hours is more detrimental to hardness than under-tempering

RECOMMENDATIONS

1. To achieve a satisfactory hardness for P91 components which require a tempered martensite microstructure, the tempering temperature should not go beyond the range of 740 °C – 760 °C.

2. The target tempering temperature for P91 should be 750 °C

3. When tempering, efforts should be focussed on the tempering temperature to ensure that temperatures do not overshoot or undershoot

CONTENTS

1 INTRODUCTION

Modern operating conditions for power generation are heading towards higher demands from the steam cycle. Modified 9Cr-1Mo alloy ferritic steel, frequently referred to as Grade 91 ("T91" for tubing and "P91" for piping), has the enhanced creep resistant properties that have enabled its selection for the use in critical sections of the steam plant. The improved mechanical properties of Grade 91 have enabled pipes and tubes to be manufactured with thinner wall thicknesses, compared to its weaker predecessor Grade 22 alloy. Reducing the wall thickness of the Grade 91 pipes and tubes significantly reduces the thermal stress, hence increasing the service life [1].

The ability for Grade 91 material to possess better mechanical properties is heavily dependent on the creation of a tempered martensite microstructure with $M_{23}C_6$ type precipitates and MX carbo-nitrides (where M = V/Nb and X = C/N) through controlled heat treatment. Careful maintenance of this specific microstructure, from manufacture through to service, underpins the material's high tensile strength and mechanical performance at elevated temperatures. However, in practise, this is not always achieved. The materials high temperature properties can be degraded due to the failure of producing and maintaining the tempered martensite microstructure. Mis-heat treatment during original component manufacture is an obvious place where the microstructure can be mis-manufactured. However, it is also prone during subsequent processing stages such as forging, pipe-bending or welding during plant fabrication and plant repairs. Intensifying the problem is the inability for standard quality assurance testing to detect the degradation in the materials high temperature properties. [2]

P91 material with the tempered martensite microstructure is used for components such as reheater headers and antler tubes. Hardness testing of these components is an important part of the quality assurance (QA) testing for these components at EON. The standard acceptable hardness range for these components is 210 – 240HV. QA testing which report back results between 200 – 210HV are on the border of the specification limits and therefore require further examination to test for acceptability. Anything below 200HV is below specification and will not be acceptable for service. Therefore it is important to understand the effects of mis-heat treated Grade 91 material with respect to the time and temperature of the heat treatment especially if the temperature and or time are just slightly off specification.

2 PROCEDURE

Vallourec and Mannesmann, a company which manufactures P91 steel, has established a heat treatment procedure which provides the optimum compromise of mechanical properties (toughness, hardness and creep rupture strength). Normalising at 1040 °C – 1080 °C provides dissolution of most carbides without significant grain growth. Tempering at 750 °C – 780 °C allows carbides to precipitate homogenously within the martensitic microstructure, thus contributing to improve the creep behaviour. [2]

The furnaces used for the experiments were at EON Technology Centre Ratcliffe-On-Soar. Samples for this experiment were normalised at 1080 °C for 1hour. For the effect of temperature experiment, the tempering temperature was varied between 700 °C – 800 °C (at 20 °C intervals) at a constant time of 3 hours and for the effect of time experiment, the tempering time was varied between 1 hour – 6 hours (at 1 hour intervals) at a constant temperature of 760 °C (Table 1).

K-type thermocouples were spot welded onto samples to monitor the temperature of the samples. Samples were given time to stabilise at temperature before beginning the experiments (no more than 30 minutes were required for a sample to stabilise at a given temperature).

12 samples of P91 material of size 1 cm^3 cubed was used for this experiment. Within the furnace, samples were positioned equidistance from one another and from the furnace walls to allow for even heat distribution through the samples during the heat treatments. Once all 12 samples had been normalised, 1 sample was sectioned for optical microscopy and hardness testing to determine the normalisation treatment had been successful. The remaining 11 samples were then used for the tempering experiments

2.1 Constant Temperature Trials

For the constant temperature experiments, 6 normalised cubes of P91 were placed into one furnace equidistance from one another. Due to the limit of available thermocouples, only three samples were spot welded with thermocouples. This meant that half the samples had their temperature monitored which was sufficient to represent the batch as all samples were positioned in equidistant locations from one another and the surrounding wall furnaces. The 6 samples were allowed to stabilise at 760 °C within the furnace and then the timer was set. After 1 hour, the furnace door was opened and 1 sample was taken out swiftly, closing the furnace door behind it such that minimum heat was lost, such that the impact on the other samples would be insignificant. Open removal, samples were allowed to air cool to room temperature. Similarly, each hour thereafter another sample would be removed in the same manner until all 6 samples had been removed. The process of opening the furnace door, removing the sample and closing the furnace door was approximately 3 or 4 seconds.

2.2 Constant Time Trials

For the constant time experiments, 3 normalised cubes of P91 were spot welded with thermocouples and placed into 3 different furnaces with different furnace temperatures. Samples were allowed to stabilise at their respective temperatures (See Table 1). Once samples has stabilised at temperature, the timer would be started. The samples were then removed and allowed to air cool after the 3 hour time interval. The remaining 2 samples were heat treated in the same manner at their respective temperatures.

2.3 Material

The material used for the tempering trials was Grade 91 plate received in the as-tempered state from the University of Birmingham (

Table 2). Identical material was used in a previous study [3]

2.4 Heat Treatments

All samples were subjected to a normalisation heat treatment. Samples were placed within a furnace at temperature and allowed to stabilise at 1080 °C. Samples were then held at 1080 °C for 1 hour and taken out of the furnace and air cooled to room temperature (Figure 1).

Figure 2 and Figure 3 show schematics of the constant temperature and constant time heat treatments respectively. For the constant temperature heat treatment samples A-F (after being normalised) were placed in the furnace and allowed to stabilise at 760 °C. Once the samples had stabilise at temperature, they were held at temperature for various times (see Figure 2) between 1 – 6 hours. After the samples respective time had been reached, the sample was taken out of the furnace and allowed to air cool to room temperature. For the constant time heat treatment, samples G – K were entered into separate furnace and allowed to stabilise at their respective temperatures between 700 – 800 °C (see Figure 3). Samples were then held at their respective temperatures for 3 hours before being taken out of the furnace and allowed to air cool to room temperature.

2.5 Microscopy

All samples were metallurgically prepared using SiC grinding paper and diamond polishing paste followed by etching of the surface using Vilella's reagent to reveal the microstructures. Samples were than examined using the optical microscopes at EON Technology Centre, Ratcliffe-on-Soar to view the microstructures produced by the various tempering treatments.

2.6 Hardness Testing

Vickers hardness testing was performed at EON Technology Centre, Ratcliffe-on-Soar using the Zwick/ Roell Indentec machine to see how material hardness changed with tempering parameters.

3 RESULTS & DISCUSSION

3.1 Microstructure

The micrographs in Figure 4 represent the microstructures obtained from the constant time tempering experiment where the samples have all been tempered for 3 hours but at different temperatures. All microstructures are reflective of a tempered martensite microstructure with martensitic laths and the presence of alloy carbides (small black dots). The micrographs in Figure 5 represent the microstructures obtained from the constant temperature tempering experiment where the samples have all been tempered at 760 °C but at different temperatures. All microstructures are reflective of a tempered martensite microstructure with the presence of carbides (small black dots).

3.2 Hardness

Vickers hardness measurements were made using a Zwick/ Roell Indentec hardness machine at EON Technology Centre Ratcliffe-on-Soar. 10 random indents were made with a load of 3Kg across the 1 cm^2 surface area of the samples. The average Vickers hardness was plotted against time and temperature to understand the effects have on the sample hardness (**Error! Reference source not found.**).
The results show that an increase in the time and temperature of the tempering heat treatment will cause the material to soften. The effect of mis-tempering by ± 10 °C from the average tempering temperature (760 °C) has a more significant effect on the hardness of the material than mis-tempering by ± 1 hour. The hardness of the material spans from approximately 290HV – 200HV for the temperature range of 700 °C – 800 °C (at 3hours), this is hardness range of almost 100HV. However the hardness only spans from approximately 230 HV – 210HV for the time range of 1hr – 6hrs (at 760 °C). Therefore over the range of parameters measured the effect of temperature is more significant than time for the tempering of P91. When tempering the material at 760 °C, tempering for more than 3 hours will lower the hardness of the material close to the specification safe limits (210HV). Likewise when tempering a material for 3 hours and mis-tempering over the temperature by of 760 °C will bring your hardness value down towards 210HV.

4 CONCLUSIONS

4.1 An increase in both the temperature and time of the tempering heat treatment will cause the P91 material to soften

4.2 Between the ranges of parameters tested mis-tempering due to temperature has a more significant effect on the hardness of the material than mis-tempering due to time.

4.3 At 760 °C over-tempering beyond 3 hours is more detrimental to hardness than under-tempering

5 RECOMMENDATIONS

5.1 To achieve a satisfactory hardness for P91 components which require a tempered martensite microstructure, the tempering temperature should not go beyond the range of 740 °C – 760 °C.

5.2 The target tempering temperature for P91 should be 750 °C

5.3 When tempering, efforts should be focussed on the tempering temperature to ensure that temperatures do not overshoot or undershoot

8 REFERENCES

8.1 Henry, J.F. *Growing experience with P91/T91 forcing essential code changes*. 2005 [cited 2014 12th December]; Available from: http://www.ccj-online.com/1q-2005/p91-t91/.

8.2 Vallourec&MannesmannTubes, *The T91/P91 Book*. 2nd ed, ed. K.V. Haarmaan, J.C. Vandenberghe, B.2002.

8.3 Jandova, D., J. Kasl, and V. Kanta, *Influence of substructure on creep failure of P91 steel weld joints*, in *ECCC Creep Conference*2009: Zurich.

Tables and Figures

Table 1: Matrix of tempering times and temperatures. Note Experiment C is labelled Constant Temperature and Time because the time of 3hours and temperature of 760 °C are both the constants used in the constant time and temperature experiments respectively. Therefore this experiment can be used in both data sets when analysing the results.

Sample	Type of Experiment	Time (Hours)	Temperature (°C)
A	Constant Temperature	1	760
B	Constant Temperature	2	760
C	Constant Temperature and Time	3	760
D	Constant Temperature	4	760
E	Constant Temperature	5	760
F	Constant Temperature	6	760
G	Constant Time	3	700
H	Constant Time	3	720
I	Constant Time	3	740
J	Constant Time	3	780
K	Constant Time	3	800

Table 2: Chemical composition (wt.%) of P91 plate material used in this experiment

C	Cr	Mo	Mn	Si	V	Ni	Nb	Al	N	P	S
0.11	0.88	0.90	0.41	0.21	0.24	0.11	0.09	0.003	0.066	0.012	0.006

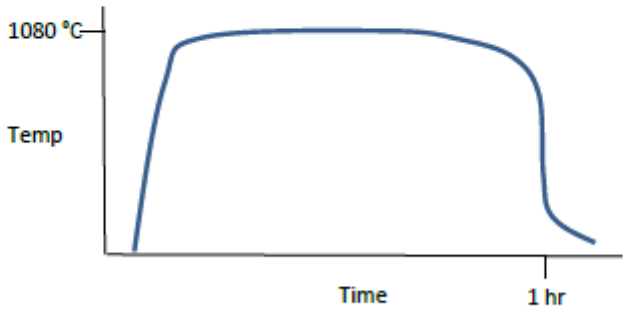

Figure 1: Schematic diagram of the normalisation heat treatment for all samples

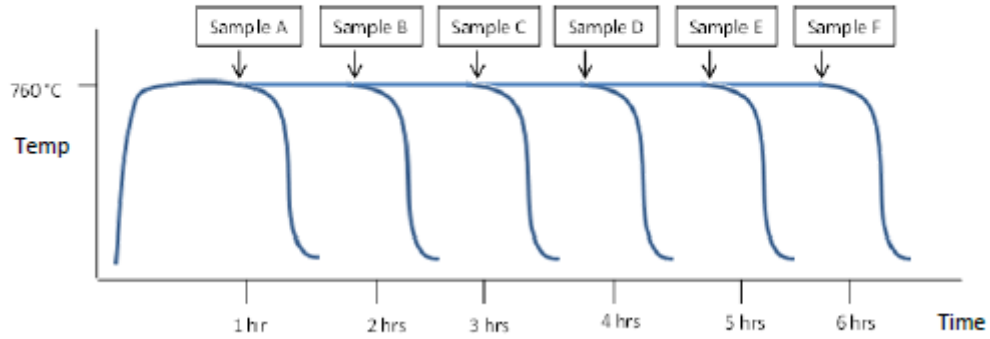

Figure 2: Schematic diagram of constant temperature heat treatment procedure for samples A – F

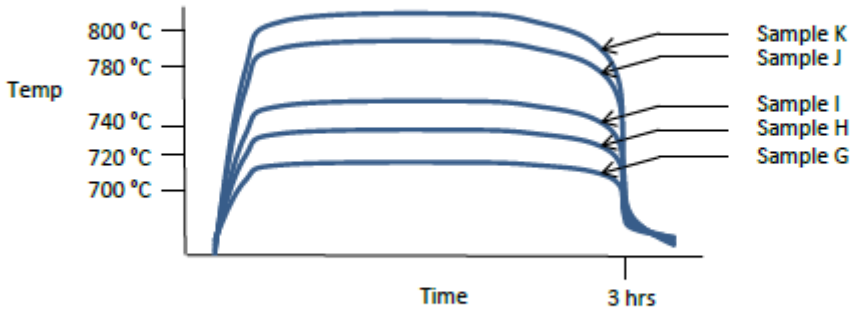

Figure 3: Schematic diagram of constant time heat treatment procedure for samples G – K

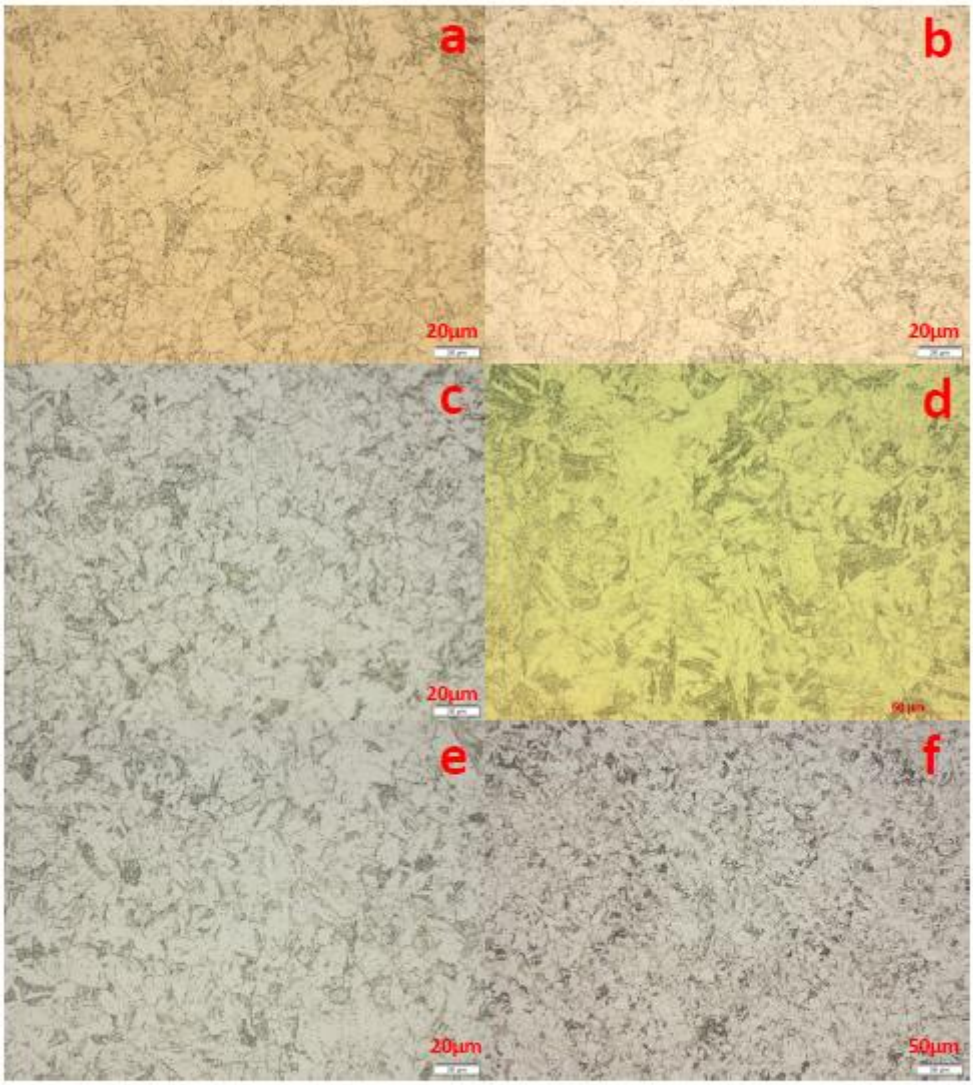

Figure 4: Micrographs 3a – 3f are microstructures of samples tempered for 3 hours at 700°C, 720°C, 740°C, 760°C 780°C and 800°C respectively.

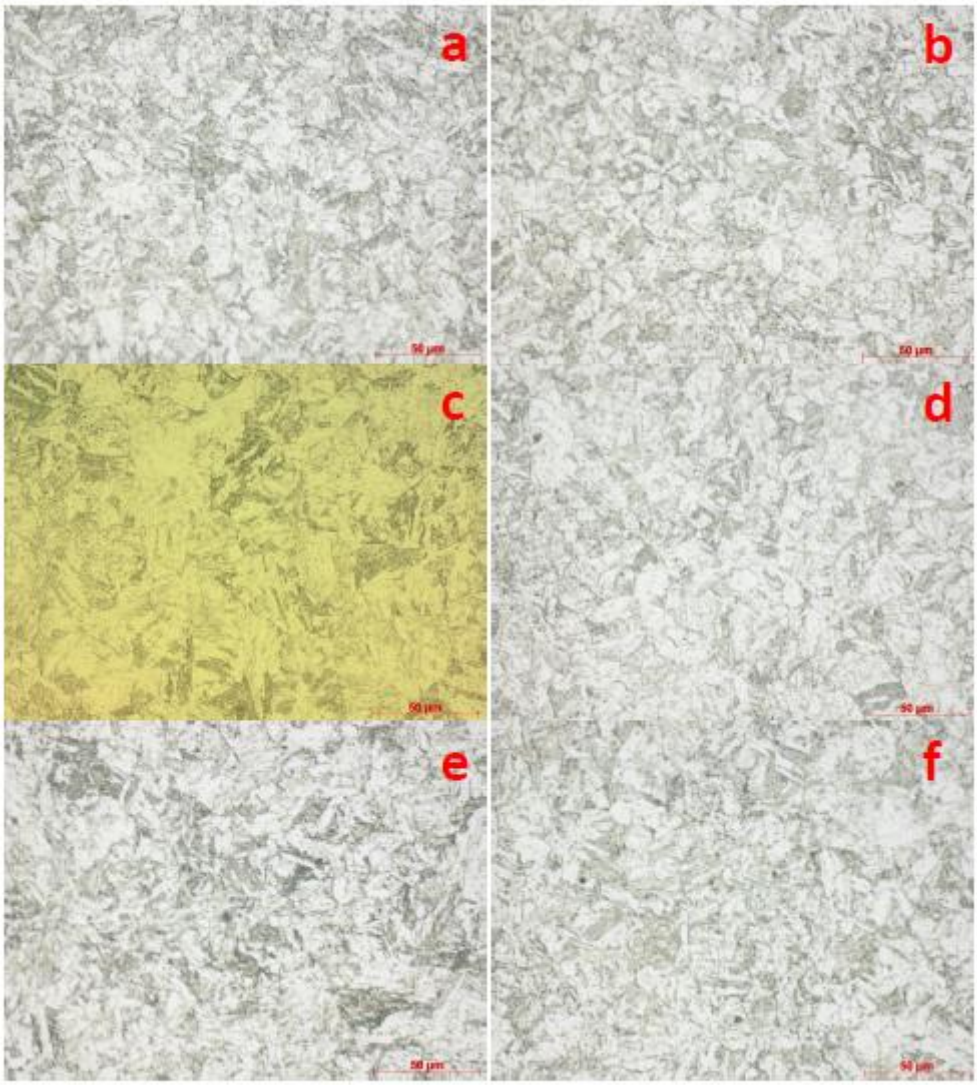

Figure 5: Micrographs 4a – 4f are microstructures of samples tempered at 760°C for 1, 2, 3, 4, 5 and 6 hours respectively.

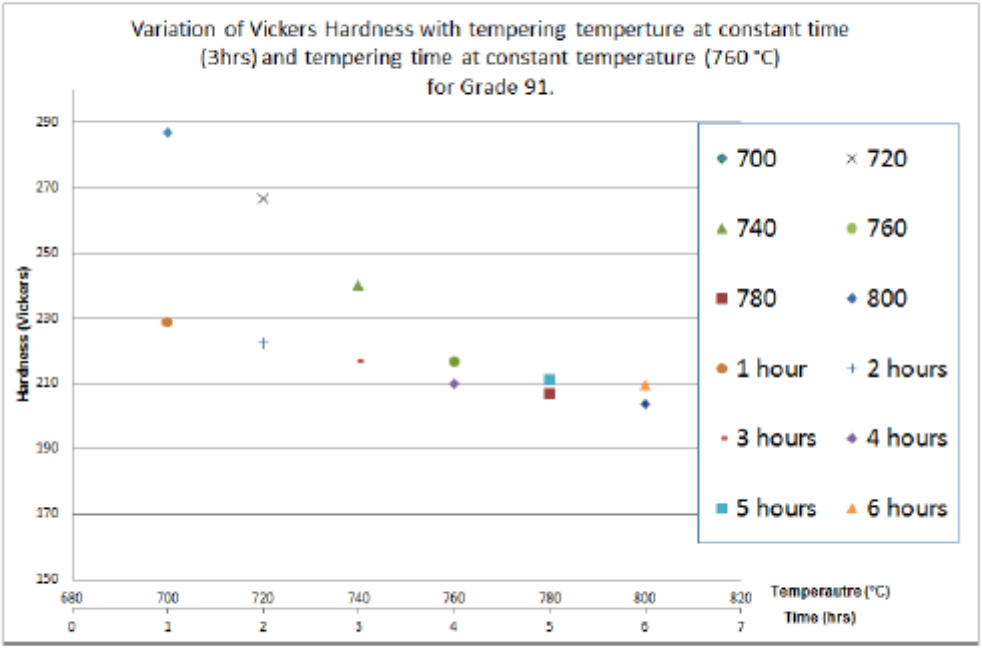

Figure 6: Shows the variation of Vickers hardness with tempering parameters